Structural Mechanisms of Gating at the Selectivity Filter of the human Cardiac Ryanodine Receptor (hRyR2) Channel

Jahn Michael Firth

A thesis submitted for the degree of Doctor of Philosophy

September 2015

Institute of Molecular and Experimental Medicine
Wales Heart Research Institute
School of Medicine
Cardiff University

Funded by the British Heart Foundation



DECLARATION

This work has not been submitted in substance for any other degree or award at this or any other university or place of learning, nor is being submitted concurrently in candidature for any degree or other award.

Signed …… Date ……

STATEMENT 1

This thesis is being submitted in partial fulfillment of the requirements for the degree of PhD.

Signed …… Date ……

STATEMENT 2

This thesis is the result of my own independent work/investigation, except where otherwise stated. Other sources are acknowledged by explicit references. The views expressed are my own.

Signed …… Date ……

STATEMENT 3

I hereby give consent for my thesis, if accepted, to be available online in the University's Open Access repository and for inter-library loan, and for the title and summary to be made available to outside organisations.

Signed …… Date ……

Acknowledgements

I would like to acknowledge several people for their support and guidance throughout my time at the Wales Heart Research Institute.

Firstly, I would like to thank Professor Alan Williams for allowing me to complete my PhD in his lab and for securing funding from the British Heart Foundation. Alan introduced me to the unique nature of single-channel experiments on which this thesis is based.

Secondly, I am especially grateful to my supervisor Dr Joanne Euden. Jo's original idea gave me the opportunity to embark on the PhD project. Jo introduced me to and taught all biological, biochemical and biophysical techniques used to complete my thesis for which I am truly thankful. I would like to thank Jo for her continual support throughout the writing phase and to wish her all the best in her future endeavours.

I would also like to acknowledge Dr Saptarshi Mukherjee and Dr Lowri Thomas who guided me throughout the single-channel analysis for which I am very grateful. I would also like to thank the AJW group and the 2nd floor team for their friendship over the last four years.

My greatest thanks go to my parents, Michael and Annette. They gave me a roof over my head and provided me with an ideal working environment; their love and support has been instrumental in the success of completing this thesis. Lastly, I would like to thank my partner Laura who always helped me see the bigger picture and led me to pursue happiness. Thank you.

Summary

The cardiac ryanodine receptor (RyR2) contains structural elements within the channel pore that function as gates to regulate the release of intracellular calcium, initiating cardiac muscle contraction. The precise regulation of these gates is critical in maintaining normal cardiac function, and channel dysfunction, resulting in altered calcium handling, underlies the mechanisms of arrhythmia and sudden cardiac death.

The enormous size of RyR2 has impeded the gathering of detailed structural information, hence the structural determinants for channel gating remain unknown. Structural modelling studies have revealed similarities between the RyR2 pore and the K^+ channel, KcsA, providing a framework in which to test channel gating mechanisms. A region termed the selectivity filter is a gating component in K^+ channels, involved in inactivation and flicker closings, and its conformation is maintained by a transient hydrogen-bonding network.

This project examined the role of the RyR2 selectivity filter in channel gating by generating mutants at analogous positions to KcsA that either disrupted (Y4813A, D4829A and Y4839A) or maintained (Y4813W, D4829E and Y4839W) a proposed hydrogen-bonding network, and assessed their intracellular Ca^{2+} release, ryanodine modification and biophysical properties. Y4813A and D4829A had drastic effects on channel function, whereas retaining physicochemical properties of conservative mutations, Y4813W and Y4839W, maintained the functional characteristics of WT RyR2. Flicker closings were affected by Y4839A mutation however, in general, single-channel gating for Y4813W, Y4839A and Y4839W was comparable to WT RyR2. Interestingly, monitoring single-channels for prolonged periods revealed novel insights into channel behaviour, characterised by inherent fluctuations in channel activity under steady-state conditions.

This thesis reveals that the selectivity filter region is an important component for RyR2 channel function. However, it remains unclear whether the selectivity filter regulates channel gating, as the proposed hydrogen-bonding network would not be possible due to altered residue distances revealed from recent high-resolution RyR structural models.

Contents

Title……I
Declaration……II
Acknowledgements……III
Summary……...IV
Contents……V
List of figures and tables……..XII
Abbreviations…….. XIX

Structural Mechanisms of Gating at the Selectivity Filter of the human Cardiac Ryanodine Receptor (hRyR2) Channel

Chapter One – Introduction

1.1 – Introduction……1
1.1.1 Cardiac muscle – An electrical system 2
1.1.2 The cardiac myocyte 2
1.1.3 The cardiac action potential 4
1.1.4 The role of Ca^{2+} as a signaling molecule 4
1.2 – Excitation-Contraction Coupling in cardiac myocytes……5
1.2.1 Cardiac muscle contraction – Calcium-Induced Calcium Release 6
1.2.2 Cardiac muscle relaxation – Intracellular Ca^{2+} homeostasis 8
1.2.3 Sympathetic β-adrenergic stimulation of cardiac myocytes 9
1.3 – The Ryanodine Receptor (RyR) channel……11
1.3.1 Ryanodine receptor channel isoforms 11
1.3.2 Ryanodine receptor structure 12
1.3.3 Ryanodine receptor transmembrane domain 14
1.4 – The Cardiac Ryanodine Receptor (RyR2) channel……..16
1.4.1 RyR2 regulation 16
1.4.2 Regulation of RyR2 by Ca^{2+} 18
1.4.3 Pharmacological modulation of RyR channels by ryanodine 19
1.4.4 RyR2 Dysfunction 21
1.4.4.1 Catecholaminergic polymorphic ventricular tachycardia 21
1.4.4.2 CPVT – Molecular mechanisms 22
1.4.4.3 CPVT – Current therapies 24
1.4.4.4 RyR2 dysfunction in Heart Failure 24
1.5 – Structural mechanisms of gating at the selectivity filter of hRyR2…. 26
1.5.1 Research Limitations 26
1.5.2 The Pore-Forming Region Analogy Model 26
1.5.3 The potassium channel KcsA - Crystal structure 28
1.5.4 KcsA as a prototypical ion channel 28
1.5.5 Structural elements of the Pore-Forming Region – Selectivity filter 29
1.5.6 Potassium channel gating mechanisms 31
1.5.7 Potassium channel - C-type inactivation 33

1.5.8 Gating mechanisms at the selectivity filter – Flicker gating 35
1.6 – Aims and Hypotheses…….. 36
1.6.1 Hypotheses 37
1.6.2 Project Aims 38

Chapter Two – Materials and Methods

2.1 – Materials……...40
2.1.1 General Lab Materials 40
2.1.2 Microbiology 40
2.1.3 Molecular Biology 40
2.1.3.1 General Lab reagents 40
2.1.4 Plasmid Vectors 40
2.1.4.1 pcDNA3 Mammalian Expression Vector 40
2.1.4.2 pSL1180 Intermediate Vector – Site-directed mutagenesis 41
2.1.5 Molecular biology reagents 41
2.1.5.1 Media 41
2.1.5.2 Mini/Maxiprep isolation reagents 42
2.1.5.3 Mutant Oligonucleotide Primers 42
2.1.6 Protein biochemistry reagents 42
2.1.6.1 Antibodies 44
2.1.7 Mammalian cell culture 44
2.1.7.1 Mammalian cell culture reagents 44
2.1.8 Electrophysiology reagents 45
2.2 – Methods……46
2.2.1 Microbiology techniques 46
2.2.1.1 Sterilisation procedures 46
2.2.1.2 Transformation of mutant hRyR2 DNA constructs following mutagenesis 46
2.2.1.3 Transformation of recombinant hRyR2 DNA constructs 47
2.2.1.4 Propagation of recombinant hRyR2 DNA constructs 47
2.2.1.4.1 Propagation of pSL1180-NX1 plasmids 47
2.2.1.4.2 Propagation of pcDNA3-RyR2 plasmids 47
2.2.1.5 Small-scale plasmid DNA isolation and purification – Miniprep 48
2.2.1.6 Large-scale plasmid DNA isolation and purification – Maxiprep 48
2.2.1.7 DNA spectrometry - Quantification of DNA concentration 49
2.2.1.8 DNA restriction digest – Verification of DNA preparation 50
2.2.1.9 Agarose gel electrophoresis - DNA analysis 50
2.2.2 Mammalian cell culture 51
2.2.2.1 Human Embryonic Kidney (HEK) 293 cell culture 51
2.2.2.2 Heterologous hRyR2 expression 51
2.2.2.3 Calcium phosphate-mediated transfection 52
2.2.2.4 Determining transfection efficiency using eGFP imaging 53
2.2.3 Protein Biochemistry 53
2.2.3.1 Preparation of hRyR2 mixed-membranes from HEK293 cells 53
2.2.3.2 MicroBCA – Quantification of protein concentration 54

2.2.3.3 Sodium dodecyl sulfate (SDS) - Polyacrylamide gel electrophoresis (PAGE) 55
2.2.3.4 Western blot – Transfer of proteins onto a PVDF membrane 57
2.2.3.5 Western blot – Enhanced Chemiluminsescence (ECL) detection 57
2.2.3.6 Quantification of protein expression by Western blot densitometry 58
2.2.3.6.1 Western blot densitometry analysis example 59
2.2.3.7 Purification of hRyR2 from mixed-membrane preparations 60
2.2.3.7.1 Preparation of Sucrose gradient 60
2.2.3.7.2 Fraction collection 63
2.2.4 Electrophysiology - Single-channel Experiments 65
2.2.4.1 Warner Instruments workstation 65
2.2.4.1.1 Planar lipid bilayer workstation set up 65
2.2.4.1.2 Electronic Bilayer set up 67
2.2.4.2 Bilayer formation 67
2.2.4.2.1 Phosphatidylethanolamine (PE) lipid preparation 67
2.2.4.2.2 Priming the *cis* chamber aperture 67
2.2.4.2.3 Painting a bilayer and measuring lipid bilayer formation 68
2.2.4.2.4 Bilayer integrity 70
2.2.4.3 RyR2 channel incorporation 70
2.2.4.4 RyR2 channel orientation 73
2.2.4.5 Chamber Perfusion 73
2.2.4.6 Single-channel Experiments 74

Chapter Three – Construction and Expression of Selectivity Filter and Pore Helix mutant hRyR2 channels

Chapter Three – Aims……76
3.1 – Introduction……77
3.1.1 A cassette-based strategy for constructing mutant hRyR2 channels - Site-directed mutagenesis 77
3.1.2 Alteration of hRyR2 residues to test a proposed hydrogen-bonding network 77
3.1.3 Amino acid selection - Alanine mutations 78
3.1.4 Amino acid selection - Conservative mutations 79
3.2 – Materials and Methods……80
3.2.1 Generation of mutant pSL1180-NX1-hRyR2 plasmids 80
3.2.1.1 Primer design 81
3.2.1.2 Site-directed Mutagenesis 84
3.2.1.3 *Dpn*I Digest 85
3.2.1.4 DNA Sequencing 85
3.2.1.5 DNA cloning of mutant hRyR2 fragments into WT pcDNA3 vector 86
3.2.1.6 Gel Extraction 87

3.2.1.7 Ligation of mutant hRyR2 fragments into the WT pcDNA3 vector 87
3.2.2 Verification of full-length mutant pcDNA3-eGFP-hRyR2 constructs 88
3.2.3 Propagation of WT and Mutant hRyR2 DNA 90
3.2.4 Protein expression of WT and Mutant hRyR2 91
3.3 – Results……..92
3.3.1 Production of selectivity filter and pore helix mutant hRyR2 plasmids 92
3.3.1.1 Ligation of mutant hRyR2 fragments into WT pcDNA3 vector 93
3.3.2 Verification of full-length mutant pcDNA3-eGFP-hRyR2 constructs 94
3.3.3 Heterologous expression of WT and mutant hRyR2 plasmids – eGFP imaging 97
3.3.4 Quantification of WT and Mutant hRyR2 protein expression 101
3.3.4.1 Western blot protein expression – Densitometry analysis 103
3.4 – Discussion……...105
3.4.1 Construction and Expression of mutant hRyR2 channels 106

Chapter Four – Functional Assessment of Mutant Selectivity Filter and Pore Helix hRyR2 channels

Chapter Four – Aims……..108
4.1 – Introduction…….....109
4.1.1 Techniques to investigate mutant RyR2 functional status 109
4.1.2 Caffeine-induced calcium release assay 109
4.1.2.1 Fluorescent Ca^{2+} indicator – Fluo3 110
4.1.2.2 Fluo3-acetoxymethyl permeation – HEK293 cell loading 110
4.1.2.3 Confocal Laser Scanning Microscopy 110
4.1.3 [^{3}H] ryanodine binding assay measuring mutant RyR2 activity 113
4.2 – Materials and Methods…… 115
4.2.1 Materials – Ca^{2+} imaging reagents and agonists 115
4.2.2 Methods – Caffeine-induced calcium release assay 115
4.2.2.1 Effectene transfection 115
4.2.2.2 Cellular Ca^{2+} imaging – Caffeine-induced calcium release assay 116
4.2.2.3 Caffeine-induced calcium release assay – Analysis 116
4.2.2.3.1 Measuring the maximum Ca^{2+} release from HEK293 cells expressing hRyR2 channels 117
4.2.3 Materials – Ryanodine binding reagents 118
4.2.4 Methods – [^{3}H] Ryanodine binding assay 118
4.2.4.1 Effects of caffeine on [^{3}H] Ryanodine binding assay 119
4.3 – Results……..120
4.3.1 Caffeine-induced calcium release assay 120
4.3.1.1 Mutant hRyR2 caffeine-induced calcium release assay 124
4.3.2 Protein expression of hRyR2 mutants – Densitometry analysis 127
4.3.3 [^{3}H] ryanodine binding assay 131
4.3.3.1 [^{3}H] ryanodine binding - Y4813A vs Y4813W hRyR2 mutations 132
4.3.3.2 [^{3}H] ryanodine binding - D4829A vs D4829E hRyR2 mutations 132
4.3.3.3 [^{3}H] ryanodine binding - Y4839A vs Y4839W hRyR2 mutations 133

4.3.3.4 [^{3}H] ryanodine binding assay – Y4813A caffeine experiment 133
4.4 – Discussion……...135
4.4.1 Caffeine-induced calcium release assay 135
4.4.2 [^{3}H] ryanodine binding assay 136

Chapter Five – Initial Single-Channel Characterisation of Mutant hRyR2 channels

Chapter Five – Aims……..……..141
5.1 – Introduction…….……142
5.1.1 The Single-Channel Electrophysiology technique 142
5.1.2 The role of K^+ as the permeant ion for studying hRyR2 143
5.1.3 Single-channel characterisation of mutant hRyR2 143
5.2 – Methods and Materials…….……145
5.2.1 Electrophysiology reagents 145
5.2.2 Ion handling reagents 145
5.2.3 Methods – Single-channel bilayer experiments 145
5.2.3.1 Initial characterisation of mutant hRyR2 145
5.2.3.2 Mutant hRyR2 channel conductance - Current-Voltage relationship 146
5.2.3.3 Ion handling experiments 146
5.2.3.3.1 Investigating mutant hRyR2 cation-anion discrimination 146
5.2.3.3.2 Examining mutant hRyR2 monovalent-divalent permeability 146
5.2.3.3.3 Investigating mutant hRyR2 ion conduction with changes in K^+ activity 147
5.2.3.3.4 Assessing the dimensions of the pore using monovalent organic cations 147
5.2.3.4 Western blot analysis assessing Y4813A hRyR2 tetramerisation 148
5.2.3.5 Single-channel data acquisition and analysis 148
5.2.3.5.1 Statistical analysis 149
5.3 – Results……..……150
5.3.1 Initial single-channel characterisation of mutant hRyR2 channels 150
5.3.2 Ryanodine modification of mutant hRyR2 channels 152
5.3.3 Investigating altered mutant hRyR2 single-channel function 154
5.3.3.1 Investigating altered mutant hRyR2 single-channel function -Y4813A 154
5.3.3.2 Investigating altered mutant hRyR2 single-channel function - D4829A 156
5.3.3.3 Investigating altered mutant hRyR2 single-channel function - D4829E 158
5.3.4 Ion handling – Assessing mutant hRyR2 channel conductance 161
5.3.5 Ion handling – Assessing altered Y4839A ion conduction properties 164
5.3.5.1 Assessing Y4839A hRyR2 cation-anion discrimination 164
5.3.5.2 Examining Y4839A hRyR2 divalent-monovalent cation permeability 165

5.3.5.3 Assessing Y4839A hRyR2 ion conduction with changes in K^+ activity 167
5.3.5.4 Measuring the pore dimensions and ion conduction properties of Y4839A hRyR2 using monovalent organic cations 168
5.4 – Discussion……...170
5.4.1 Initial single-channel characterisation of mutant hRyR2 channels 170
5.4.2 Structural models of the RyR pore-forming region 170
5.4.3 Initial single-channel characterisation of mutant hRyR2 channels – Y4813 174
5.4.4 Initial single-channel characterisation of mutant hRyR2 channels – D4829 176
5.4.5 Initial single-channel characterisation of mutant hRyR2 channels – Y4839 180
5.4.6 Investigating a potential hydrogen-bonding network in the PFR of RyR 182

Chapter Six – Single-Channel Gating Mechanisms at the Selectivity Filter of WT and Mutant hRyR2 channels

Chapter Six – Aims…….....186
6.1 – Introduction……187
6.1.1 Understanding the mechanisms of hRyR2 channel gating 187
6.1.2 Investigating hRyR2 gating mechanisms using single-channel modelling 190
6.1.3 Describing mechanisms of hRyR2 channel gating in minimised conditions 191
6.1.4 Flicker gating transitions at the selectivity filter of the hRyR2 channel 193
6.1.5 Purpose of investigating single RyR2 channel gating mechanisms 194
6.2 – Materials and Methods…… 195
6.2.1 Materials 195
6.2.1.1 Ca^{2+} Activation experiment 195
6.2.2 Methods 195
6.2.2.1 Single-channel experiments – Ca^{2+} Activation 195
6.2.3 Single-channel data analysis 197
6.2.3.1 Calculating single-channel open probability 198
6.2.3.2 Single-channel modelling 198
6.2.3.3 Data selection for modelling analysis 198
6.2.3.4 Idealisation parameters for modelling analysis 199
6.2.3.5 Constructing kinetic models to describe single-channel gating mechanisms 199
6.3 – Results……..200
6.3.1 Ca^{2+} activation of single WT and mutant hRyR2 channels – Open probability 200
6.3.1.1 Stage #1 – Gating in unbuffered contaminant [Ca^{2+}] solutions 200
6.3.1.2 Stage #2 – hRyR2 channel shutdown 201
6.3.1.3 Stage #3 – hRyR2 Ca^{2+} activation 202
6.3.2 Ca^{2+} activation open probability distributions 204

6.3.3 Categorising the population of WT and mutant hRyR2 channel experiments by open probability threshold 206
6.3.4 hRyR2 Ca^{2+} activation – Modal gating 211
6.3.5 Assessment of hRyR2 mean closed and open times 212
6.3.5.1 The relationship between dwell-time and periods of very high open probability for WT and mutant hRyR2 channels 215
6.3.6 Investigating single-channel gating mechanisms at the selectivity filter of hRyR2 channels 216
6.3.6.1 Justification of hRyR2 modelling analysis 216
6.3.6.2 Data selection criteria for modelling analysis 217
6.3.6.3 Homogenous single-channel data 218
6.3.6.4 Constructing kinetic models to describe the gating behaviour of mutant hRyR2 channels 218
6.3.6.5 Comparing WT and mutant hRyR2 dwell-time distribution histograms 221
6.3.6.6 Assessing individual state transitions between WT and mutant hRyR2 channels 225
6.4 – Discussion……...228
6.4.1 Single-channel Ca^{2+} activation experiments – Biophysical parameters 228
6.4.2 Comparing WT and mutant hRyR2 channel biophysical properties 230
6.4.3 Modelling single-channel gating kinetics and assigning putative structural conformations 232
6.4.4 Comparing gating kinetics and flicker closing transitions between WT and mutant hRyR2 channels 234

Chapter Seven – General Discussion

7.1 Investigating structural mechanisms of gating at the selectivity filter of the hRyR2 channel 238
7.2 Is there a gate at the selectivity filter of hRyR2? 244
7.3 Future work 245
7.3.1 Identifying alternative residue candidates to assess the role of hRyR2 selectivity filter gating 245
7.3.2 What is the physiological relevance of flicker closings in RyR2? 246
7.4 Concluding remarks 247
7.5 Final summary of findings 247

Appendix I – Measuring the maximum Ca^{2+} release from HEK293 cells expressing hRyR2 channels……248
Appendix II – Specific [^{3}H] ryanodine binding values……248
Appendix III – hRyR2 channel gating at negative holding potentials…….. 249
Appendix IV – A representative single hRyR2 channel under steady-state conditions……..... 251

References……262

List of figures and tables

Chapter One……1

Figure 1.1. Cardiac muscle structure. 3
1.2. The main ionic currents responsible for the different phases of the cardiac action potential from ventricular muscle. 5
1.3. Overview of subcellular events occurring in cardiac ventricular muscle contraction in excitation-contraction coupling. 7
1.4. Subcellular events occurring in cardiac muscle relaxation. 8
1.5. Schematic representation of subcellular events occurring in cardiac muscle during β-adrenergic sympathetic stimulation. 10
1.6. Architecture of RyR1 at an overall resolution of 3.8 Å. 13
1.7. Hydropathy plot of the human cardiac RyR channel. 15
1.8. A schematic representation of the six transmembrane segments (S1-S6) of RyR1. 15
1.9. Sequence alignment of the C-terminal pore-forming region of human skeletal and cardiac ryanodine receptors (RyR1 and RyR2). 16
1.10. RyR2 modulators. 17
1.11. The activation of recombinant human RyR2 by cytosolic Ca^{2+}. 18
1.12. Structure of the ryanodine molecule. 19
1.13. Single channel hRyR2 ryanodine modification. 20
1.14. Representative echocardiogram of an episode of bidirectional ventricular tachycardia (VT) observed in a patient with CPVT. 21
1.15. RyR2 polypeptide sequence highlighting four ‘hotspot’ clusters (I-IV) of CPVT channel point mutations. 22
1.16. Schematic representation of a delayed after depolarisation (DAD) following a cardiac action potential. 23
1.17. Schematic representation of the RyR2 Pore Forming Region (PFR) analogy model based on the crystal structure of the potassium channel, KcsA. 27
1.18. Crystal structure of the bacterial potassium channel, KcsA. 28
1.19. Topology diagram of transmembrane ion channels. 29
1.20. Structure of the selectivity filter of KcsA. 30
1.21. Similarity between the architecture of RyR1 pore-forming region and KcsA. 31
1.22. Gating in the potassium channel, KcsA. 32
1.23. The gating cycling of inactivation and recovery in the potassium channel KcsA. 32
1.24. Sequence alignment of KcsA with other K^+ channels. 34
1.25. A cartoon representation of the selectivity filter and pore helix of (A) KcsA and (B) the PFR analogy model of RyR2. 36

Chapter Two……39

Figure 2.1. Linear regression analysis of the relationship between BSA concentration and absorbance at 595 nm. 55
2.2. Representative Western blot densitometry analysis. 59
2.3. Schematic representation depicting the preparation of a sucrose gradient for hRyR2 purification. 62
2.4. Schematic diagram of sucrose gradient fraction collection. 63
2.5. Sucrose gradient fraction collections. 64
2.6. Schematic representation of (A) the styrene cup '*cis*' chamber depicting the 200 µm aperture as a black dot and (B) the copolymer block '*trans*' chamber mounted with the cup. 66
2.7. Schematic representation of the Planar Lipid Bilayer set up. 66
2.8. A modified Pasteur pipette used as a 'painting' stick. 68
2.9. Bilayer formation. 69
2.10. The incorporation of a single hRyR2 channel into a lipid bilayer. 71
2.11. Incorporation of 'junk' into the bilayer. 72
2.12. Dual perfusion manipulator. 74

Table 2.1. Restriction DNA digest reagents. 50
2.2. Calcium-phosphate transfection mixture. 52
2.3. 5 % SDS-PAGE separating gel reagents. 56
2.4. 5 % SDS-PAGE stacking gel reagents. 56
2.5. Mixed-membrane SDS loading preparation for SDS-PAGE. 56
2.6. Representative densitometry analysis of WT and mutant mixed-membrane preparations. 59
2.7. Preparation of sucrose gradients. 60

Chapter Three……75

Figure 3.1. Measuring the distances of residues in the analogy PFR RyR2 model. 78
3.2. Schematic representation of the pcDNA3-eGFP-hRyR2 and pSL1180-NX1-hRyR2 vectors. 81
3.3. Schematic representation of the QuikChange PCR procedure. 83
3.4. A circular sequence vector map of full-length pcDNA3-eGFP-hRyR2. 89
3.5. A template of hRyR2 DNA fragments following restriction digest. 90
3.6. Representative mutant pSL1180-NX1-hRyR2 plasmid digested with *EcoR*I, lanes 1-5. 92
3.7. Mutant pSL1180-NX1-hRyR2 chromatograms. 93
3.8. Restriction digest of full-length pcDNA3-hRyR2 vector (1) and mutant pSL1180-NX1 insert (2). 94
3.9. DNA digest mapping of full-length WT hRyR2 DNA. 95

3.10. Verification of ligated full-length mutant pcDNA3-eGFP-hRyR2 constructs. 96
3.11. WT hRyR2 transfection trial using sodium butyrate. 98
3.12. Transfection of alanine hRyR2 mutation constructs into HEK293 cells. 99
3.13. Transfection of conservative hRyR2 mutation constructs into HEK293 cells. 100
3.14. Western blot comparing protein expression of WT and mutant hRyR2 mixed-membrane preparations between control and the addition of sodium butyrate. 102
3.15. Integrated densitometry analysis to measure hRyR2 protein expression. 103

Table 3.1. Full-length selectivity filter (D4829) and pore helix (Y4813 and Y4839) hRyR2 point mutations. 80
3.2. Mutagenic oligonucleotide forward and reverse primers designed for the generation of selectivity filter and pore helix mutants in hRyR2. 82
3.3. QuikChange XL PCR reagents. 84
3.4. QuikChange XL site-directed mutagenesis PCR thermal cycle protocol. 84
3.5. BigDye Terminator v3.1 reagents. 85
3.6. BigDye Terminator PCR sequencing thermal cycling protocol. 85
3.7. Cloning of full-length pcDNA3-eGFP-hRyR2 vector and mutant pSL1180-NX1-hRyR2 insert. 86
3.8. Ligation of full-length mutant hRyR2 mutations using T4 ligase. 88
3.9. Restriction digest reaction of full-length WT or mutant pcDNA3-eGFP-hRyR2. 88
3.10. Restriction endonuclease recognition sites used for construct verification for full-length pcDNA3-eGFP-hRyR2 and intermediate pSL1180-NX1-hRyR2 vectors. 89
3.11. Comparing the difference in hRyR2 protein expression between control and addition of sodium butyrate using integrated density measurements. 104

Chapter Four…… 107

Figure 4.1. Fundamental principles of confocal optics. 112
4.2. The pore-forming region RyR2 analogy model. 114
4.3. Measurement of maximum Ca^{2+} release in HEK293 cells expressing WT and mutant hRyR2 channels. 117
4.4. Caffeine-induced calcium release assay. 120
4.5. Caffeine-induced calcium release assay examining changes in fluorescence intensity upon addition of caffeine. 121
4.6. Expression of hRyR2 alanine mutations using the Effectene transfection method. 122

4.7. Expression of hRyR2 conservative mutations using the Effectene transfection method. 123
4.8. Caffeine-induced calcium release assay examining HEK293 cells transfected with alanine hRyR2 mutations. 125
4.9. Caffeine-induced calcium release assay examining HEK293 cells transfected with conservative hRyR2 mutations. 126
4.10. Measurement of maximum Ca^{2+} release in HEK293 cells expressing WT and mutant hRyR2 channels. 127
4.11. Quantification of (A) Y4813A and (B) Y4813W protein expression compared to WT hRyR2 using Western blot densitometry analysis. 128
4.12. Quantification of (A) D4929A and (B) D4829E protein expression compared to WT hRyR2 using Western blot densitometry analysis. 129
4.13. Quantification of (A) Y4839A and (B) Y4839W protein expression compared to WT hRyR2 using Western blot densitometry analysis. 130
4.14. An overview of normalised [^{3}H] ryanodine binding of mutant relative to WT hRyR2 mixed-membrane fractions. 131
4.15. Y4813A caffeine [^{3}H] ryanodine binding experiment. 134
4.16. Investigating [^{3}H] ryanodine binding and caffeine response of inner (S6) helix RyR2 mutants. 137

Table 4.1. Representative ryanodine binding reaction. 118
4.2. Normalised Y4813A and Y4813W protein expression levels relative to WT hRyR2. 128
4.3. Normalised D4929A and D4829E protein expression levels relative to WT hRyR2. 129
4.4. Normalised Y4839A and Y4839W protein expression levels relative to WT hRyR2. 130
4.5. Normalised [^{3}H] ryanodine binding results of mutant relative to WT hRyR2 mixed-membrane fractions. 132

Chapter Five…… 140

Figure 5.1. Single-channel recording of unitary current fluctuations from a single hRyR2 channel. 143
5.2. Initial characterisation of recombinant purified single WT and mutant hRyR2 channels incorporated into a planar lipid bilayer. 151
5.3. Ryanodine modification of mutant hRyR2 channels. 153
5.4. Assessing the presence and tetrameric density of Y4813A hRyR2 channels in purified fractions. 155
5.5. Single-channel characterisation of D4829A hRyR2 channels. 157
5.6. Single-channel characterisation of D4829E hRyR2 channels. 159
5.7. Single-channel ryanodine modification of D4829E hRyR2. 160

5.8. Current-Voltage (I/V) relationships of WT and Mutant hRyR2 channels. 162
5.9. Comparing channel conductance between WT and mutant hRyR2. 163
5.10. Cation-anion discrimination in Y4839A hRyR2. 165
5.11. Assessing monovalent-divalent permeability between WT and Y4839A hRyR2 channels. 166
5.12. Assessing channel conductance between WT and Y4839A hRyR2 in response to increasing K^+ activity. 168
5.13. Measuring reversal potential for monovalent organic cations. 169
5.14. Pore-Forming Region models of the ryanodine receptor channel. 172
5.15. Proposed boundary sites of pore-forming region RyR helices. 173
5.16. Comparing the location of residues between (A) the PFR RyR1 model (Yan *et al.,* 2015) and (B) the analogy PFR RyR2 model (Welch *et al.,* 2004). 175
5.17. Single-channel recordings of WT and mutant D4899 RyR1 in symmetrical 250 mM KCl solution. 177
5.18. Comparing the dimensions of the selectivity filter between structural models. 178
5.19. Measuring the distances between residues in (A) the PFR RyR1 model (Yan *et al.,* 2015) and (B) the analogy PFR RyR2 model (Welch *et al.,* 2004). 183

Table 5.1. Assessing WT and mutant hRyR2 channel conductance in symmetrical 210 mM KCl. 163
5.2. Cation-anion discrimination of Y4839A hRyR2. 165
5.3. Assessing the reversal potential and permeability ratios of WT and Y4839A hRyR2 channels under bi-ionic conditions using 210 mM KCl in the *cis* chamber and 210 mM $BaCl_2$ in the *trans* chamber. 167
5.4. Comparing B_{max} and K_D between WT and Y4839A in response to increasing K^+ activity. 168
5.5. Probing the dimensions and conduction properties of WT and Y4839A hRyR2 channels using monovalent organic cations. 169

Chapter Six……...185

Figure 6.1. Structural model of the rabbit RyR1 channel. 188
6.2. Measuring the closed RyR1 channel. 189
6.3. Idealisation of single hRyR2 channel gating events. 190
6.4. A mechanistic description of hRyR2 channel gating. 192
6.5. Gating of single WT hRyR2 channel highlighting rapid flicker closing transitions occuring during periods of high open probability. 193
6.6. Assigning closed and open current levels for single-channel idealisation. 197

6.7. Comparing the open probability of individual WT and mutant hRyR2 channels in unbuffered contaminant [Ca^{2+}]. 201
6.8. Comparing the open probability of individual WT and mutant hRyR2 channels during shutdown. 202
6.9. Comparing the open probability of individual WT and mutant hRyR2 channels during Ca^{2+} activation. 203
6.10. Ca^{2+} activation distribution histograms of WT hRyR2 channels. 205
6.11. Ca^{2+} activation distribution histograms of single WT and mutant hRyR2 channels representing high open probability. 207
6.12. Ca^{2+} activation distribution histograms of single WT and mutant hRyR2 channels representing intermediate open probability. 208
6.13. Ca^{2+} activation distribution histograms of single WT and mutant hRyR2 channels representing low open probability. 209
6.14. Single WT hRyR2 channel modal gating under steady-state conditions. 211
6.15. The relationship between open probability and mean closed times of WT and mutant hRyR2 channels. 213
6.16. The relationship between open probability and mean open times of WT and mutant hRyR2 channels. 214
6.17. Utilising the open probability distribution histograms as a template for modelling data selection. 216
6.18. Representative 30 s extraction of homogenous WT single hRyR2 channel gating for modelling analysis. 217
6.19. Highest ranked kinetic model describing the behaviour of hRyR2 gating when activated by 10 µM $[Ca^{2+}]_{cyt}$. 219
6.20. Constructing a kinetic model to describe the gating behaviour of hRyR2. 220
6.21. Closed dwell-time histograms from a single representative hRyR2 channel activated by 10 µM $[Ca^{2+}]_{cyt}$. 223
6.22. Open dwell-time histograms from a single representative hRyR2 channel activated by 10 µM $[Ca^{2+}]_{cyt}$. 224
6.23. Rate constant from open (O_2) to closed (C_F) between WT and mutant hRyR2. 226
6.24. Comparing the kinetic information between (A) WT and (B) Y4839A hRyR2 channels. 227
6.25. Putative conformational twisting of the S6 helices occurring during opening of the activation gate. 231
6.26. Schematic representation of putative hRyR2 channel conformation transitions when activated by 10 µM $[Ca^{2+}]_{cyt}$. 233
6.27. Schematic representation of putative Y4839A hRyR2 channel conformation transitions during flicker gating. 234
6.28. Structural model of the RyR1 pore-forming region. 235

Table 6.1. Comparing the mean open probability of WT and mutant hRyR2 channels during Ca^{2+} activation experiment. 203
6.2. Categorising the population of WT and mutant hRyR2 channel Ca^{2+} activation experiments by high, intermediate and low open probability thresholds. 206
6.3. The relationship between dwell-time and P_o (0.8 – 1) for WT and mutant hRyR2 channels. 215
6.4. Key biophysical parameters for modelling analysis. 218
6.5. Time constants and relative areas for exponential fits of closed dwell-time distributions. 222
6.6. Time constants and relative areas for exponential fits of open dwell-time distributions. 222
6.7. Rate constants derived from the highest ranked kinetic model. 225

Chapter Seven…… 237

Figure 7.1. A proposed cation-binding site at the luminal mouth of the selectivity filter of RyR1. 242
7.2. Identifying alternative residue candidates to assess the role of side chain interactions to stabilise a putative selectivity filter gate. 245

List of Abbreviations

[^{3}H] ryanodine	Tritiated ryanodine
Å	Ångström
Ab	Antibody
AC	Adenylate cyclase
ADP	Adenosine 5'-diphosphate
APS	Ammonium persulphate
ATP	Adenosine 5'-triphosphate
β-AR	Beta-adrenergic receptor
β-ME	Beta-mercaptoethanol
BSA	Bovine serum albumin
Ca^{2+}	Calcium ion
$[Ca^{2+}]$	Free calcium concentration
$[Ca^{2+}]_{cyt}$	Free cytosolic (*cis*) calcium concentration
$[Ca^{2+}]_{lum}$	Free luminal (*trans*) calcium concentration
$CaCl_2$	Calcium chloride
CaCaM	Ca^{2+}-bound Calmodulin
CaM	Calmodulin
CaMKII	Calcium/Calmodulin-dependent kinase II
cAMP	Cyclic adenine monophosphate
$CaPO_4$	Calcium phosphate
CCD	Central core disease
cDMEM	Complete DMEM
cDNA	Complementary deoxyribonucleic acid
C_F	Flicker closings
C_{NR}	Non-responsive closings
C_R	Responsive closings
CHAPS	3-[(3-cholamidopropyl)-dimethylammonio] 1-propane-sulphonate
CICR	Calcium-induced calcium release
Cl^-	Chloride ion
CM	Cardiac myocyte
CPVT	Catecholaminergic polymorphic ventricular tachycardia
CSQ	Calsequestrin
DAD	Delayed after-depolarisation
dH_2O	Deionised water
ddNTP	Dideoxynucleotide triphosphate
DHPR	Dihydropyridine receptor/ L-type Ca^{2+} channel
DMEM	Dulbecco's modified Eagle's medium
DMSO	Dimethylsulphoxide
DNA	Deoxyribonucleic acid
dNTP	Deoxynucleotide triphosphate
DOPE	1,2-dioleoyl-*sn*-glycero-3-phosphoethanolamine
DR	Divergent region
DTT	Dithiothreitol
EAD	Early after depolarisation

ECC	Excitation-contraction coupling
ECG	Electrocardiogram
ECL	Enhanced chemiluminescent
EDTA	Ethylenediaminetetraacetic acid
EGTA	Ethyleneglycoltetraacetic acid
E_m	Membrane potential
eGFP	Enhanced green fluorescent protein
ER	Endoplasmic reticulum
EtBr	Ethidium bromide
F	Fluo3 signal intensity
F_0	Basal Fluo3 signal intensity
FBS	Foetal bovine serum
FKBP	FK-506 binding protein
HCl	Hydrochloric acid
HEK293	Human embryonic kidney 293 cell
HF	Heart failure
HRP	Horse-radish peroxidase
I_{Ca}	Inward calcium current
ICD	Implantable cardiac defibrillator
Idl	Idealisation single-channel data
IHBC	Inner-helix bundle crossover
IP_3	Inositol 1,4,5-trisphosphate
IP_3R	Inositol 1,4,5-trisphosphate receptor
JCN	Junctin
K^+	Potassium ion
Kb	Kilobase
KCl	Potassium chloride
KcsA	*Streptomyces lividans* potassium (K^+) channel
kDa	Kilodalton
kHz	Kilohertz
LB	Luria-Bertani medium
LTCC	L-Type calcium channel
mA	Milliamp
mDMEM	Minimal DMEM
Mg^{2+}	Magnesium ion
MH	Malignant hypothermia
MOPS	3-(N-morpholino)propanesulfonic acid
MW	Molecular weight
mV	Millivolt
Na^+	Sodium ion
NaB	Sodium butyrate
NaCl	Sodium chloride
NCX	Sodium-calcium exchanger
PAGE	Polyacrylamide gel electrophoresis
PCR	Polymerase chain reaction
PBS	Phosphate buffered saline
pF	Picofarad
PFR	Pore-forming region

PH	Pore helix
PKA	cAMP-dependent protein kinase
PKC	Ca^{2+}-dependent protein kinase
PLB	Phospholamban
P_o	Single-channel open probability
PP1	Protein phosphatase 1
PP2A	Protein phosphatase 2a
PVDF	Polyvinylidene difluoride
QuB	QuB Single-channel analysis software
RCF	Relative centrifugal force
ROI	Region of interest
rpm	Revolutions per minute
RT	Room temperature
RyR	Ryanodine receptor
RyR1	Type 1 Skeletal muscle isoform – Ryanodine receptor
RyR2	Type 2 Cardiac muscle isoform – Ryanodine receptor
RyR3	Type 3 – Ryanodine receptor
SCD	Sudden cardiac death
SDM	Site-directed mutagenesis
SDS	Sodium dodecyl sulphate
SERCA	Sarco/endoplasmic reticulum Ca^{2+} ATPase
SF	Selectivity filter
SOC	Super optimal broth supplemented with glucose
SOICR	Store overload-induced calcium release
SR	Sarcoplasmic reticulum
TAE	Tris-acetate-EDTA
TBS	Tris-buffered saline
TBS-T	Tris-buffered saline with 0.1 % (v/v) Tween-20
T_c	Time closed
T_d	Dead time
TEMED	Tetramethylethylenediamine
T_m	Melting temperature
TM	Transmembrane domain
T_o	Time open
VF	Ventricular fibrillation
VT	Ventricular tachycardia
UV	Ultraviolet
WT	Wild type

Chapter One:

Introduction

Structural Mechanisms of Gating at the Selectivity Filter of the human Cardiac Ryanodine Receptor (hRyR2) channel

1.1 – Introduction

1.1.1 Cardiac muscle – An electrical system

The average human heart will beat 100,000 times per day (Nio *et al.,* 2015). This intrinsic (involuntary) process ensures that blood is pumped around the body to meet the constant demand for oxygen and nutrients whilst removing metabolic waste. In order to trigger the heart muscle to contract, a system is required to send and receive electrical signals. Such a system is established by ion channels that are integral membrane proteins that regulate the flow of ions across a membrane, establishing a potential difference. Ion channels are involved in many physiological processes such as maintaining resting membrane potential (E_m), cell depolarisation, shaping action potentials and regulating signal transduction (Schrempf *et al.,* 1995; Jiang *et al.,* 2002b). Ion channel dysfunction, termed channelopathies, can result in cardiac arrhythmia that may lead to sudden cardiac death (Abriel and Zaklyazminskaya, 2013). It is therefore vital to understand how ion channels function in both health and disease. This thesis focuses on one particular Ca^{2+} ion channel termed the cardiac ryanodine receptor (RyR2) channel and is discussed in detail throughout.

1.1.2 The cardiac myocyte

The heart consists of different cell types such as cardiac myocytes (CM), fibroblasts, pacemaker cells, vascular endothelial cells and smooth muscle cells that contribute to structural, biochemical, mechanical and electrical properties of the functional heart (Xin *et al.,* 2013). CMs are the predominant cell type that form the heart muscle, termed the myocardium, and function to contract and expel blood to the body and lungs (Leri *et al.,* 2015). These cells are typically cylindrical shaped, ~ 10-15 µm in diameter and ~ 100 µm in length, forming striated branching myofibres (Marian *et al.,* 2001). CMs are connected by intercalated disks that contain abundant gap junctions, allowing impulses to spread across the membrane quickly forming an efficient synchronous contracting unit as shown in figure 1.1 (Golob *et al.,* 2014).

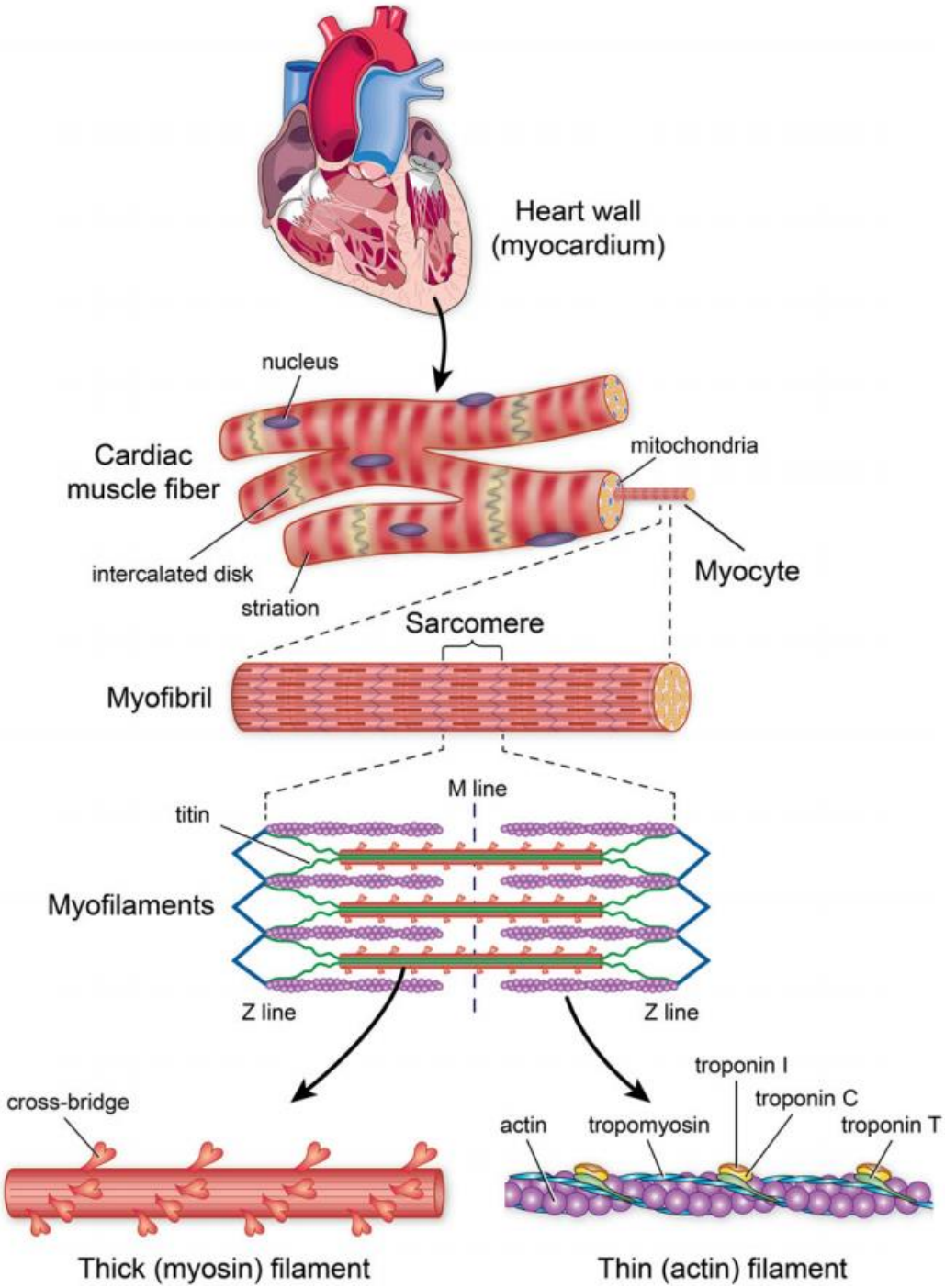


Figure 1.1. Cardiac muscle structure. CMs are composed of sarcomere structures that consist of thick (myosin) and thin (actin) filaments arranged in repeating elements. CMs form muscle fibres connected by intercalated disks that allow for efficient signal transduction. Figure taken from Golob *et al.,* (2014).

1.1.3 The cardiac action potential

An intrinsic, self-generating (automaticity), action potential (AP) arises from specialised CM, termed pacemaker cells (Verkerk *et al.,* 2007). These groups of cells are located in the right atrium and between the atria and ventricles that form the sinoatrial node (SAN) and the atrioventricular node (AVN), respectively. These specialised CMs possess the ability to spontaneously depolarise, providing the electrical excitation required to initiate excitation-contraction coupling (ECC) discussed in section 1.2. The morphology and mechanisms of cardiac APs are different to those seen in neuronal APs due to a prolonged plateau phase (~ 300 ms) as a result of the involvement of calcium channels (Pinnell *et al.,* 2007). A typical representation of a cardiac AP arising from ventricular muscle is characterised by five distinct phases (Phases 0-4), generated by changes in membrane voltage established via a complex interaction of sodium (Na^+), potassium (K^+) and calcium (Ca^{2+}) ion channels and their respective electrical currents, shown in figure 1.2 (Schmitt *et al.,* 2014).

1.1.4 The role of Ca^{2+} as a signaling molecule

Calcium is one of the most versatile signaling molecules in living systems and plays an important regulatory role in a number of cellular processes including muscle contraction, neuronal transmission, cellular motility, fertilisation, cell growth, memory and cell programmed death (Laude and Simpson, 2009). Its ability to fulfil diverse functions is exhibited by highly regulated spatial and temporal dynamics around the cell milieu (Krebs and Michalak, 2007). Responses are dependent on the duration, amplitude, frequency and location of Ca^{2+} transients (Berridge *et al.,* 2003). For example, the duration of a Ca^{2+} signal can be variable lasting milliseconds, for muscle contraction, and up to several hours for fertilisation and cell proliferation (Fearnley *et al.,* 2011).

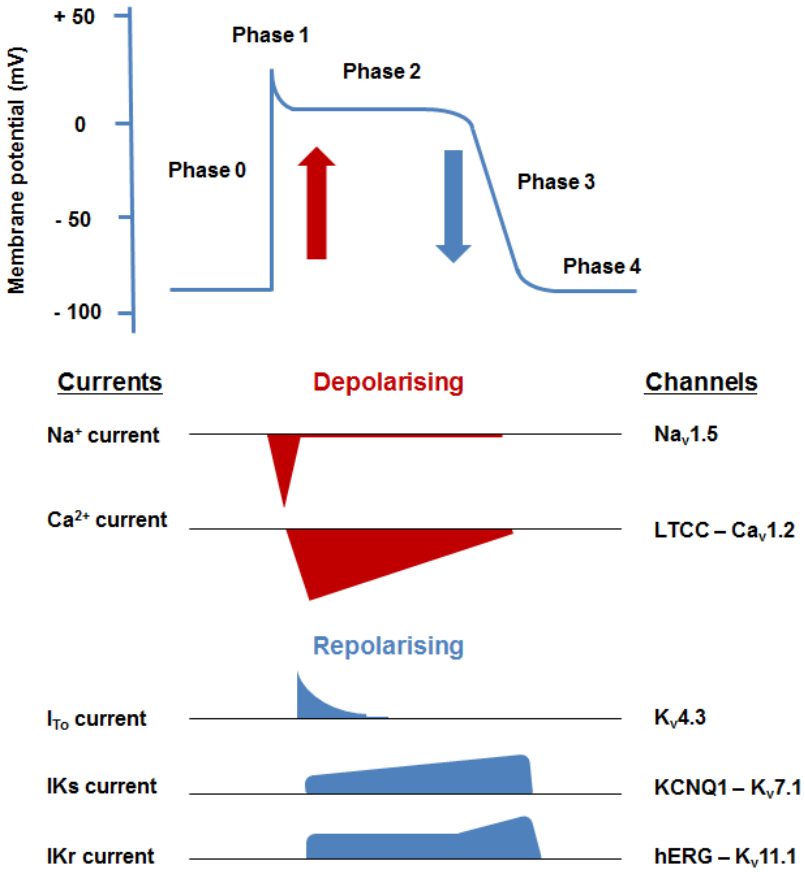


Figure 1.2. The main ionic currents responsible for the different phases of the cardiac action potential from ventricular muscle. Depolarising (red) and repolarising (blue) ionic currents are indicated by relative current amplitude, duration and direction. The shape of the current is aligned with its approximated time of action during the cardiac AP. Figure adapted from Abriel and Zaklyazminskaya, (2013).

1.2 – Excitation-Contraction Coupling in cardiac myocytes

In CMs, ECC is the process of converting an electrical signal into a mechanical response (Bers, 2002). This involves an array of biochemical and biophysical processes that allow the cell to contract. CMs contain highly organised arrays of myofilament proteins comprised of actin (thin) and myosin (thick) filaments and numerous accessory proteins, such as tropomyosin and the troponin complex (troponins T, I and C), which form the contractile apparatus termed the sarcomere shown in figure 1.1 (Golob *et al.,* 2014). Importantly, Ca^{2+} ions are direct activators of the myofilaments and the elevation of intracellular Ca^{2+} within the myocyte cytosol, discussed in section 1.2.1, is essential for the initiation of muscle

contraction. The transient intracellular rise in Ca^{2+} results in binding to troponin C, resulting in a conformational rotation of tropomyosin revealing the myosin-binding sites on actin filaments (Bootman *et al.,* 2006). Effectively, Ca^{2+} unblocks the binding site allowing myosin to bind to actin. This, in conjunction with the hydrolysis of adenosine triphosphate (ATP) to adenosine diphosphate (ADP), provides the energy to begin the cross-bridge cycling process (Leonard and Herzog, 2010).

1.2.1 Cardiac muscle contraction – Calcium-Induced Calcium Release

For ventricular CMs, the initial stage in the ECC process is depolarisation of the sarcolemma transverse tubules (T-tubules) by an inward Na^+ current (I_{Na}) through $Na_v1.5$ channels. This rapid change in membrane potential, shifting the charge within the cell from negative to positive, results in the activation of voltage gated calcium channels located in the plasma membrane termed L-type calcium channels (LTCC) or $Ca_v1.2$ (also termed dihydropyridine receptors (DHPR)) (Nakai *et al.,* 1996). T-tubules are cylindrical invaginations of the sarcolemma that extend into the myocyte and are in close proximity to sarcoplasmic/endoplasmic reticulum (SR/ER) junctional organelles. The intracellular myocyte architecture creates a 10-12 nm gap, termed the dyadic cleft, between the T-tubules and SR membrane expressing RyR2 channels (Franzini-Armstrong *et al.,* 1999; Koh *et al.,* 2005). Depolarisation activates LTCCs and, in conjunction with high extracellular Ca^{2+} concentration, the established electrochemical gradient drives Ca^{2+} into the myocyte (Trafford *et al.,* 1997). The inward Ca^{2+} current (I_{Ca}) increases the Ca^{2+} concentration within the dyadic cleft from ~ 100 nM to ~ 10 µM (Wang *et al.,* 2001). This initial Ca^{2+} influx, termed a Ca^{2+} sparklet, is not sufficient to initiate muscle contraction and accounts for only ~ 15 % of the total increase in intracellular Ca^{2+} (Fearnley *et al.,* 2011). The close spatial proximity in the dyadic cleft ensures that I_{Ca} binds to RyR2, a Ca^{2+} ligand-gated channel, resulting in a large Ca^{2+} release from SR stores through activated RyR2 channels in a process termed calcium-induced calcium release (CICR) shown in figure 1.3 (Fabiato, 1983).

RyR2 channels are packed into elongated clusters in the SR membrane that exhibit a disordered “checkerboard-like” organisation (Franzini-Armstrong *et al.,* 1999; Hayashi *et al.,* 2009b; Baddeley *et al.,* 2009). These clusters of individual RyRs are physically interlocked via specific protein-protein interactions (Yin *et al.,* 2005; Baddeley *et al.,* 2009). A study by Marx *et al* observed multiple RyR2 channels opening and closing in a uniform fashion, supporting the idea of an allosteric

mechanism in channel regulation based on a direct communication among individual RyR channels within an array, termed coupled gating (Marx *et al.,* 2001; Ondrias and Mojzisová, 2002; Liu *et al.,* 2010; Porta *et al.,* 2012; Gaburjakova and Gaburjakova, 2013). The I_{Ca} and activation of individual RyR2 channels functions as a signal amplifier resulting in the release of stored Ca^{2+} through a RyR2-cluster, termed a Ca^{2+} spark (Cheng *et al.,* 1993). As cytosolic Ca^{2+} is the primary ligand for RyR2, adjacent neighbouring RyR2-clusters are activated, resulting in a synchronised release of multiple Ca^{2+} sparks throughout the CM (Ca^{2+} wave) causing a global intracellular Ca^{2+} transient of sufficient magnitude to initiate muscle contraction (Bers, 2004).

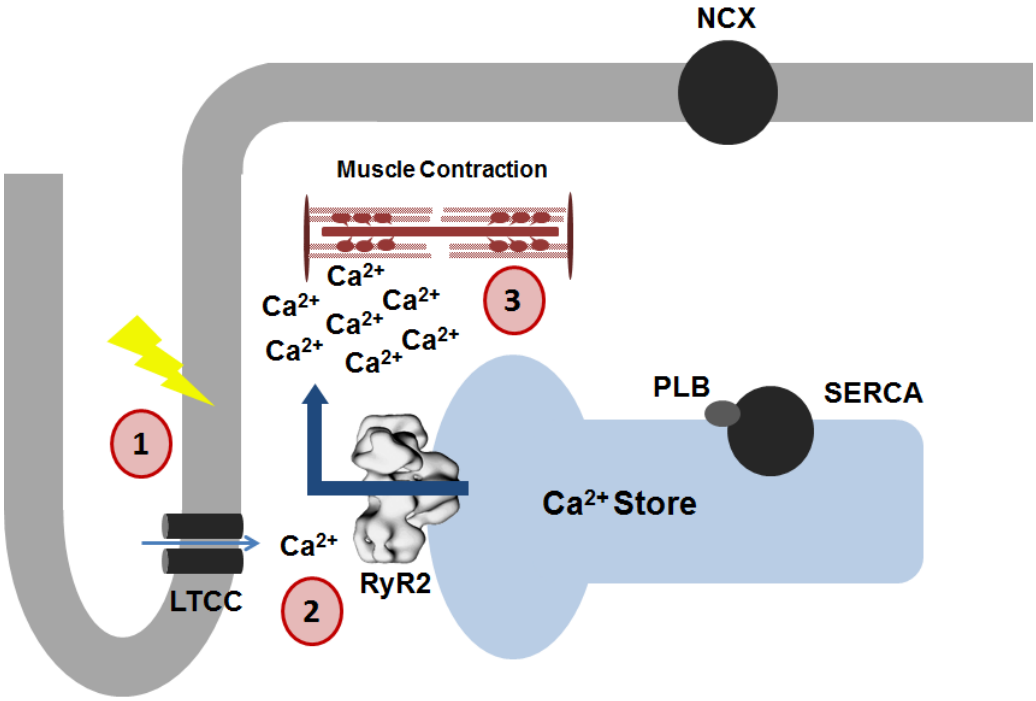


Figure 1.3. Overview of subcellular events occurring in cardiac ventricular muscle contraction in excitation-contraction coupling. Schematic representation of (1) depolarisation of T-tubules, activating L-type calcium channels (LTCCs). (2) Inward Ca^{2+} current (I_{Ca}) activates RyR2 channels (only one RyR2 channel shown) in the SR (Ca^{2+} store). (3) Ca^{2+} release through open RyR2 channels increases the intracellular Ca^{2+} concentration (CICR), Ca^{2+} subsequently binds to myofilaments and initiates muscle contraction.

1.2.2 Cardiac muscle relaxation – Intracellular Ca^{2+} homeostasis

The elevation of intracellular Ca^{2+} is followed by sequestration and extrusion of Ca^{2+} from the myocyte resulting in muscle relaxation (diastole). While the exact initiating trigger of diastole is unknown, it is thought that muscle relaxation occurs through the combination of three predominant processes; (1) closure of LTCCs and RyR2 channels (Györke and Terentyev 2008; Blayney and Lai, 2009), (2) reuptake of Ca^{2+} into the SR through the sarco/endoplasmic reticulum Ca^{2+}-ATPase (SERCA) pump (Schmidt *et al.,* 1998; Periasamy and Kalyanasundaram, 2007) and (3) removal of Ca^{2+} from the myocyte by the Na^{+}-Ca^{2+} exchanger (NCX) (Bers, 2000), depicted in figure 1.4. To a lesser extent the plasma membrane Ca^{2+} ATPase (PMCA) and the mitochondrial uniporter are also involved in the extrusion and uptake of intracellular Ca^{2+}, respectively (Fearnley *et al.,* 2011; Kamer and Mootha, 2015). Cytosolic Ca^{2+} is rapidly removed and Ca^{2+} homeostasis is achieved where systolic influx and SR release of Ca^{2+} are balanced such that there is no net gain or loss of Ca^{2+} with each contraction-relaxation cycle (Scoote and Williams, 2004).

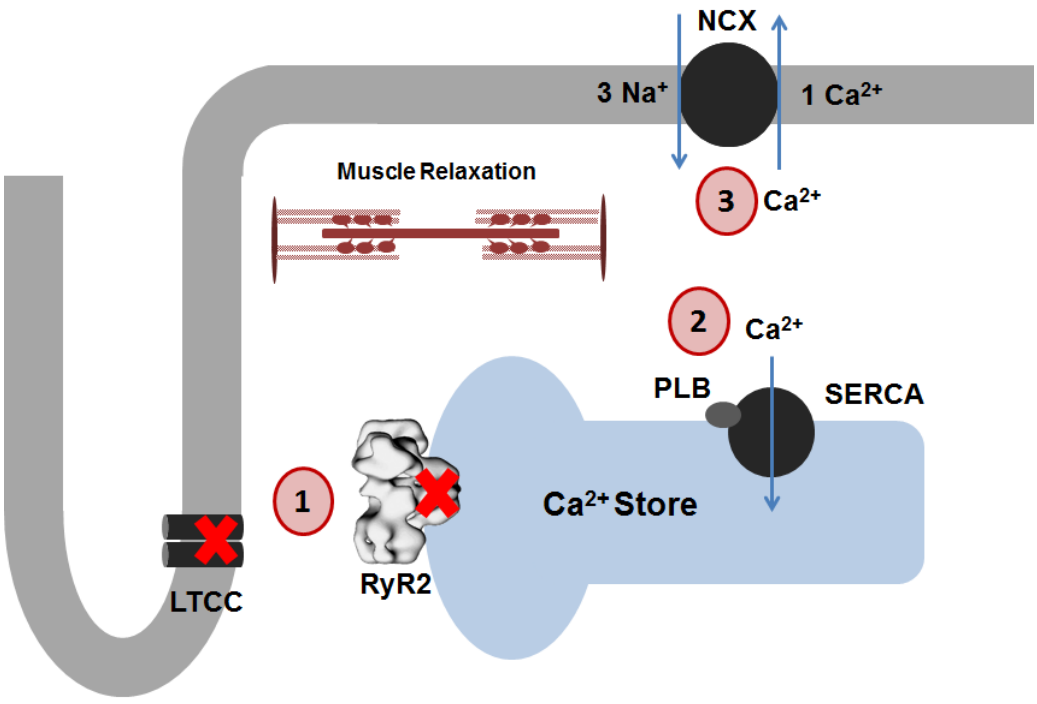


Figure 1.4. Subcellular events occurring in cardiac muscle relaxation. Schematic representation of intracellular Ca^{2+} homeostasis achieved by several membrane proteins that co-ordinate to (1) inhibit Ca^{2+} release, (2) sequester Ca^{2+} into the SR and (3) extrude Ca^{2+} described in section 1.2.2.

1.2.3 Sympathetic β-adrenergic stimulation of cardiac myocytes

Heart rate (chronotropy), strength of contraction (inotropy) and extent of relaxation (lusitropy) increase during periods of stress, exercise or perceived physical threat, resulting in an enhanced cardiac output defined as the amount of blood the heart pumps in one minute (Bers, 2008). This process, termed the fight-or-flight response, is an evolutionary physiological reaction for survival and occurs through the activation of the sympathetic nervous system resulting in an increase of catecholamines epinephrine and, importantly for cardiac myocytes, the neurotransmitter norepinephrine (Hell, 2010; Tank and Wong, 2015).

Myocytes express β–adrenergic receptors (β-AR), which are integral G-protein coupled receptors, on the sarcolemma (Zalewska *et al.,* 2014). Once bound, norepinephrine activates β-AR, initiating a signal transduction cascade that activates adenylyl cyclase (AC), figure 1.5 (1), catalysing the conversion of ATP into cyclic adenosine monophosphate (cAMP) shown in figure 1.5 (2) (Ishikawa and Homcy, 1997). cAMP detaches the regulatory subunits on protein kinase A (PKA), activating the enzyme and allowing PKA to phosphorylate multiple sites in the myocyte, as seen in figure 1.5 (3) (Fu *et al.,* 2013). PKA-mediated phosphorylation of LTCCs and RyR2 enhances inotropy, and increases lusitropy by enhanced dissociation of Ca^{2+} from troponin C (Backx, 2014). In addition, PKA phosphorylation of phospholamban (PLB) releases its inhibition of SERCA, subsequently increasing the activity of SERCA and its ability to sequester Ca^{2+} into the SR (Tada and Katz, 1982; Kranias and Hajjar, 2012). These processes ultimately lead to augmented Ca^{2+} cycling; increasing SR Ca^{2+} content and Ca^{2+} transients, characterised by enhanced cardiac output.

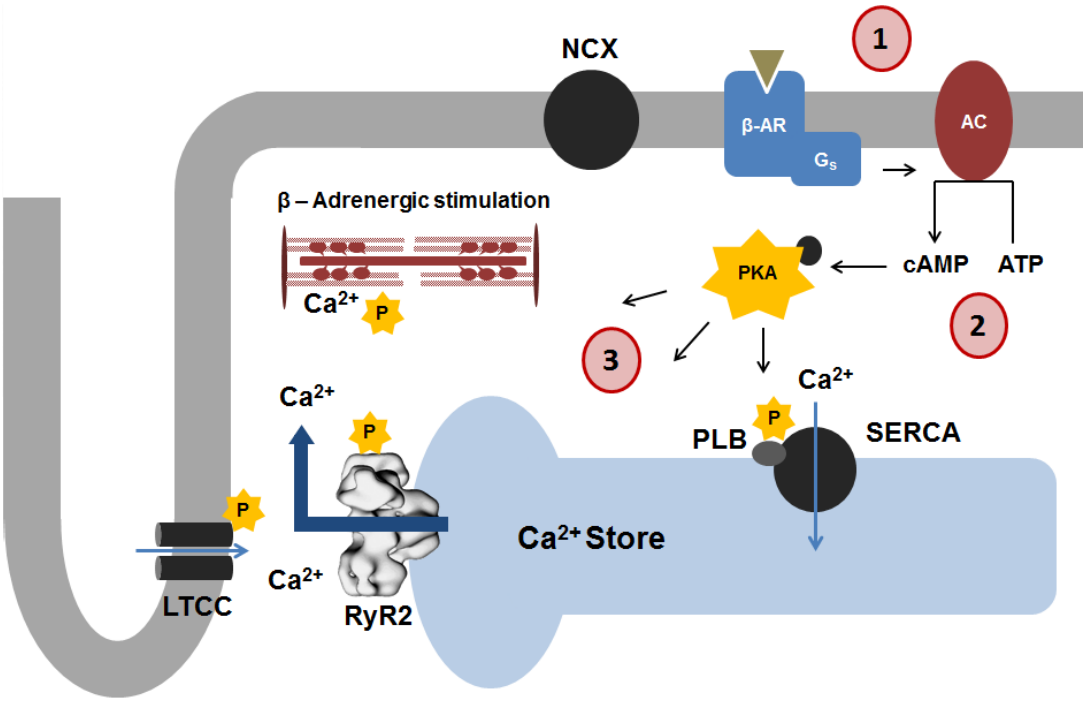


Figure 1.5. Schematic representation of subcellular events occurring in cardiac muscle during β-adrenergic sympathetic stimulation. Protein kinase A (PKA) phosphorylates (highlighted by a yellow 'P') multiple myocyte Ca^{2+} handling proteins including L-type calcium channel (LTCC), RyR2, phospholamban (PLB) and troponin I (Domeier *et al.,* 2012). Figure described in section 1.2.3.

1.3 – The Ryanodine Receptor (RyR) channel

One of the key regulators of the ECC process is the ryanodine receptor (RyR). RyRs are large homotetrameric calcium ion channels with a molecular weight of ~ 2.2 MDa (Yan *et al.,* 2015). These calcium channels are the largest known ion channels found in eukaryotic systems and are responsible for regulating the release of stored Ca^{2+} from intracellular ER/SR organelles, thus playing an essential role in the ECC process, outlined in section 1.2 (Takeshima *et al.,* 1989; Zorzato *et al.,* 1990; Nakai *et al.,* 1990). RyRs were first observed in the 1970s and were originally described as 'feet' structures in electron micrographs of striated muscle localised at the junctions of intracellular SR membranes (Franzini-Armstrong, 1970; Campbell *et al.,* 1980). Dysregulation of RyR has been implicated in acquired and genetic disease such as heart failure, cardiac arrhythmia and skeletal neuromuscular disorders outlined in section 1.4.4. It has therefore emerged over the last decade that RyRs are a therapeutic target and that further research is required to pin point the exact mechanisms of how RyRs function in health and disease.

1.3.1 Ryanodine receptor channel isoforms

Three mammalian RyR isoforms have been identified with each one encoded by a distinct gene residing on separate chromosomes (RyR1, RyR2 and RyR3). RyR1 was first detected in skeletal muscle (Takeshima *et al.,* 1989; Zorzato *et al.,* 1990) where it is abundantly expressed and was termed the skeletal isoform (Marks *et al.,* 1989; Giannini *et al.,* 1995; Ogawa *et al.,* 1999). Subsequently, RyR2 was found to be predominantly expressed in cardiac muscle (Nakai *et al.,* 1990; Otsu *et al.,* 1990) and was termed the cardiac isoform. RyRs are not restricted to striated muscle, RyR3 was initially referred to as the brain isoform (Hakamata *et al.,* 1992) but was found in a variety of other tissues including smooth muscle and diaphragm (Giannini *et al.,* 1995; Marziali *et al.,* 1996). The three isoforms have also been found to be expressed in the ER of neurons, exocrine cells, epithelial cells, lymphocytes and sea-urchin eggs at varying levels (Lanner *et al.,* 2010). Their exact role in these tissues however, is to be determined.

The RyR isoforms share ~ 65 % sequence identity (Hakamata *et al.,* 1992). Despite a high degree of sequence identity, RyRs display an isoform-specific response to some physiological regulators (Meissner, 2002; Fill and Copello, 2002; Bers, 2004).

These differences are important as they are likely to be related to the specialised functions of each tissue-specific isoform (Capes *et al.,* 2011).

This thesis focuses on the human cardiac isoform of the ryanodine receptor channel (hRyR2). On occasion, other isoforms (RyR1), from different species are discussed to draw comparisons between RyR channels or, due to limited availability, of structural/functional information.

1.3.2 Ryanodine receptor structure

RyRs are mushroom shaped with a 'cap' composed of the N-terminal cytoplasmic domain and a 'stalk' consisting of the C-terminal transmembrane domain, shown in figure 1.6. The symmetrical structure arises from four identical monomers each consisting of approximately 5000 amino acids with a molecular weight of 550 kDa (Otsu *et al.,* 1993). The cytoplasmic domain of RyRs constitutes ~ 80 % of the total protein, this large structure has numerous distinctive structural regions and intervening cavities that act as a scaffold suitable for interaction with modulators that bind within the N-terminal region, discussed in section 1.4.1 (Hamilton and Serysheva, 2009; Zalk *et al.,* 2014). When viewed from above, the cytoplasmic domain is square shaped with dimensions of 275 Å x 275 Å and a depth of 120 Å (Efremov *et al.,* 2014). The remaining C-terminal 'stalk', forms the transmembrane (TM) assembly (120 Å x 120 Å x 60 Å) enclosing a central ion-conducting pore (Zalk *et al.,* 2014). The pore-forming region (PFR) of hRyR2, defined as the S5 helix, pore helix, selectivity filter and S6 helix shown in figure 1.17, forms the basis of this thesis and is discussed in detail in sections 1.3.3, 1.5 and chapters 3, 4, 5, 6 and 7.

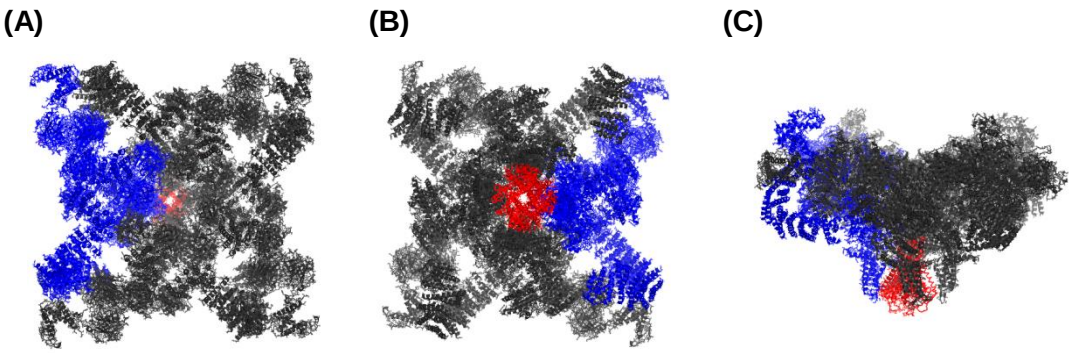


Figure 1.6. Architecture of RyR1 at an overall resolution of 3.8 Å. The structure was generated in PyMol and represents the (A) cytoplasmic view, (B) luminal view and (C) side view of the rabbit RyR1 channel. The homotetramer is composed of four identical monomers encompassing a central pore. One monomer (blue) and pore-forming region (red) are highlighted. This is the highest resolution of the structure of RyR1 to date and has revealed an enormous level of detail. A schematic representation of distinctive structural regions is shown in figure 1.8. The figure was constructed from the PDB file (3J8H) obtained with permission from Chang-cheng Yin (Yan *et al.,* 2015).

The lack of sufficient high resolution structural detail has impeded understanding of RyR gating and regulatory mechanisms discussed in section 1.5.1 (Zalk *et al.,* 2014). Details of RyR structure to date have been obtained through cryo-electron microscopy (cryo-EM) at ~ 10–25 Å resolution (Wagenknecht and Samsó, 2002; Samsó *et al.,* 2005; Ludtke *et al.,* 2005; Samsó *et al.,* 2006; Hamilton and Serysheva, 2009), comparative modelling (Welch *et al.,* 2004; Ramachandran *et al.,* 2009; Ramachandran *et al.,* 2013) and X-ray crystallography of small RyR N-terminal segments (Lobo and van Petegem, 2009; Tung *et al.,* 2010; Lau and van Petegem, 2014). These structures have been invaluable in determining the overall dimensions and approximate domain boundaries of the channel but have been insufficient to allow determination of secondary structural elements or identification of key domains (Yan *et al.,* 2015). Recent years have seen improvements in protein preparation, instrumentation, image processing, and three-dimensional reconstruction techniques enabling several breakthroughs in resolving high-resolution structures (Fernández *et al.,* 2013). Recent cryo-EM structures of the rabbit skeletal RyR1, in the closed-state, are the highest resolution images to date, solved at an overall resolution of 3.8 Å (Yan *et al.,* 2015) and 4.8 Å (Zalk *et al.,* 2014). In addition, Efremov *et al* resolved the rabbit RyR1 in an open-state structure

at a resolution of 8.5 Å (Efremov *et al.,* 2014). These current structures are however models constructed using data obtained from cryo-EM together with single particle analysis. The validity of these models must be tested to assess their credibility as described in chapters 5, 6 and 7.

1.3.3 Ryanodine receptor transmembrane domain

The C-terminal TM region encompasses ~ 20 % of the RyR protein and contains the channel's PFR. The end portion of the C-terminal tail serves a critical functional role, controlling RyR2 oligomerisation, enabling the protein to form a functional Ca^{2+} release channel (Stewart *et al.,* 2003). This was first observed in 1997 when small tetrameric RyR complexes (~ 130 kDa) consisting of the C-terminal region were constructed using trypsinisation and were found to be cation-selective channels that were activated by calcium and modulated by ryanodine (Bhat *et al.,* 1997). An additional study by Euden *et al* showed that the PFR of RyR2 could function as a separate entity, forming a functional tetrameric ion conducting channel (Euden *et al.,* 2013a). When characterised in planar lipid bilayers, differences in gating and ion handling were observed between full-length RyR2 and the separately expressed RyR2 PFR channel, suggesting that domains encoding the cytoplasmic region are important for mechanisms governing channel function (Euden *et al.,* 2013a).

The N- and C-terminal fragments of RyR reside on the cytoplasmic side of the membrane, suggesting that the transmembrane domain contains an even number of membrane-spanning segments (Grunwald and Meissner, 1995). Previous models predicted that the TM was composed of four (Takeshima *et al.,* 1989), six (Tunwell *et al.,* 1996), six to eight (Du *et al.,* 2002) or 12 (Zorzato *et al.,* 1990) membrane-spanning regions per monomer. Recently, using high resolution cryo-EM it has been confirmed that RyR channels are comprised of six TM regions, shown in figures 1.7 and 1.8 (Zalk *et al.,* 2014; Efremov *et al.,* 2014; Yan *et al.,* 2015).

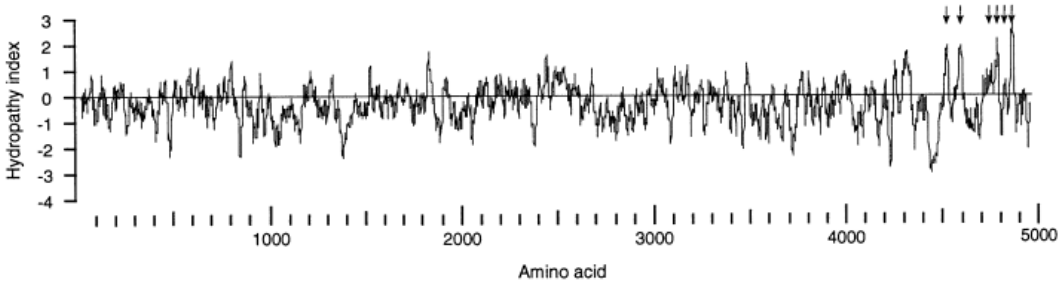


Figure 1.7. Hydropathy plot of the human cardiac RyR channel. Initial identification of six conserved hydrophobic regions of the protein that constitute the membrane-spanning segments, indicated by vertical arrows. Figure taken from Tunwell *et al.,* (1996).

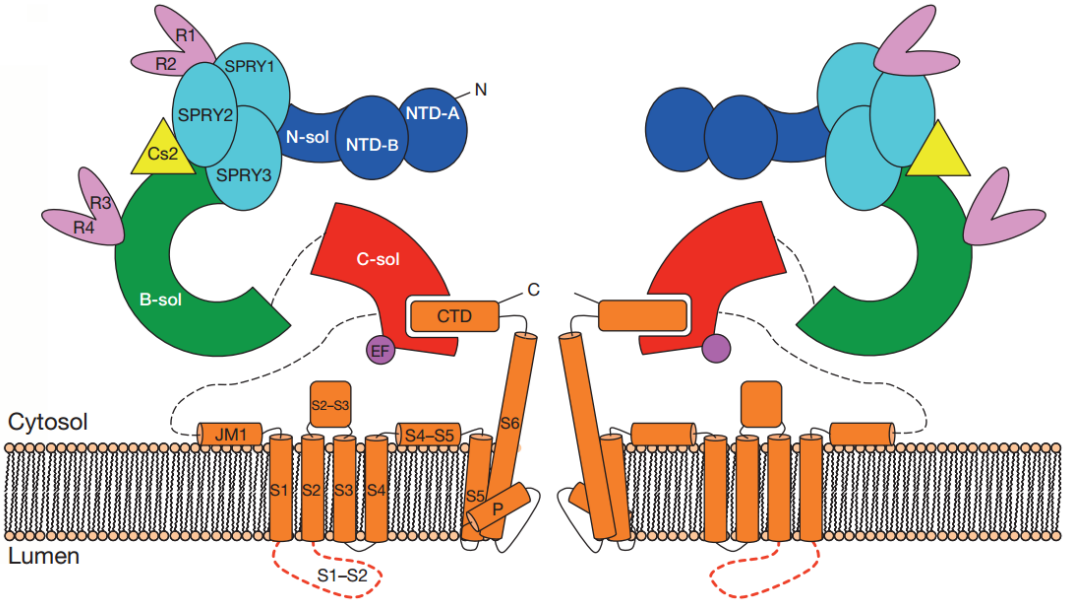


Figure 1.8. A schematic representation of the six transmembrane segments (S1-S6) of RyR1. The structure of the 6TM, inter-helical linkers and PFR are highlighted in orange. The cytoplasmic domains are colour-coded; N-terminal domains-A, B and N-solenoid (blue), SPRY1, 2 and 3 (cyan), Calstablin/FKBP12 binding site (yellow), R12 (clamp)/R34 (phosphorylation) repeats (magenta), bridge-solenoid/helical domain (green), core-solenoid/central domain (red), EF-hand domain (purple) and C-terminal domain/CTD (orange). Figure taken from Zalk *et al.,* (2014).

Interestingly, the region encoding the RyR1 and RyR2 channel pore share almost identical homology with 93.4 % sequence alignment, shown in figure 1.9, suggesting analogous structural and functional channel gating mechanisms, discussed in section 1.5.

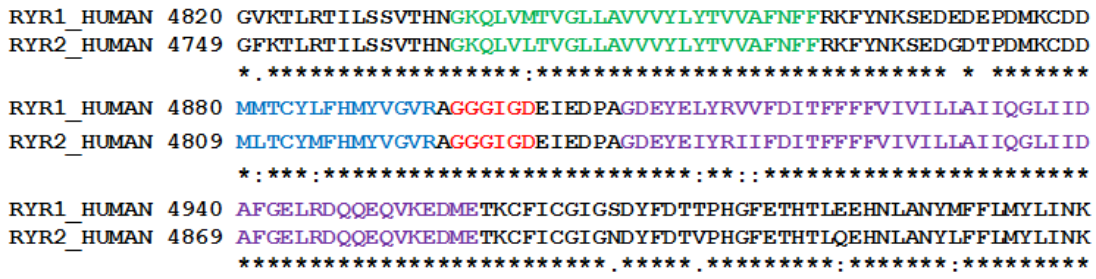


Figure 1.9. Sequence alignment of the C-terminal pore-forming region of human skeletal and cardiac ryanodine receptors (RyR1 and RyR2). Highlighted residues represent the S5 helix (green), pore helix (blue), selectivity filter (red) and S6 helix (purple) based on the RyR2 analogy model (Welch *et al.,* 2004) discussed in section 1.5.2. Figure was constructed using a web-based software, aligning entry codes P21817 (RyR1) and Q92736 (RyR2) (http://www.uniprot.org/align).

1.4 – The Cardiac Ryanodine Receptor (RyR2) channel

1.4.1 RyR2 regulation

The primary role of the RyR2 channel is to release large amounts of Ca^{2+}, from the SR, within several milliseconds to induce cardiac muscle contraction in a process termed CICR (Fabiato, 1983; Baylor and Hollingworth, 2003). This process must be strictly regulated to ensure appropriate duration and amount of Ca^{2+} release as altered Ca^{2+} handling may lead to pathology such as arrhythmia, discussed in section 1.4.4. The sustainability of this cycle is crucially dependent upon precise regulation of RyR2 by numerous cytosolic and luminal ligands and accessory proteins (Capes *et al.,* 2011). Within the myocyte milieu, RyR2 forms a macromolecular complex composed of, but not limited to, triadin, junctin and calsequestrin on the luminal side, and FKBP12.6, calmodulin, protein kinases and protein phosphatases on the cytoplasmic side (Meissner, 2002; Berridge *et al.,* 2003; Lanner *et al.,* 2010). The interaction of these ligands with both the cytoplasmic and luminal sides of RyR2 creates a complex functional structure that

exceeds 3 MDa (Zalk *et al.,* 2014). The majority of these modulators, depicted in figure 1.10, interact with the cytoplasmic domain of the protein at locations some distance from the channel pore (Yan *et al.,* 2015). This suggests that RyR2 channel gating is regulated by an allosteric mechanism with a complex coupling network of inter- and intra-subunit interactions.

There are many other modulators that interact with RyR2 which are not listed in figure 1.10, the figure does however illustrate the enormous complexity of RyR2 regulation and highlights one of the challenges in studying RyR2 function. The regulation of RyR2 by these modulators and accessory proteins is not the focus of this thesis and is discussed in detail elsewhere (Berridge *et al.,* 2003; Györke and Terentyev, 2008; Lanner *et al.,* 2010; Dobrev and Wehrens 2014).

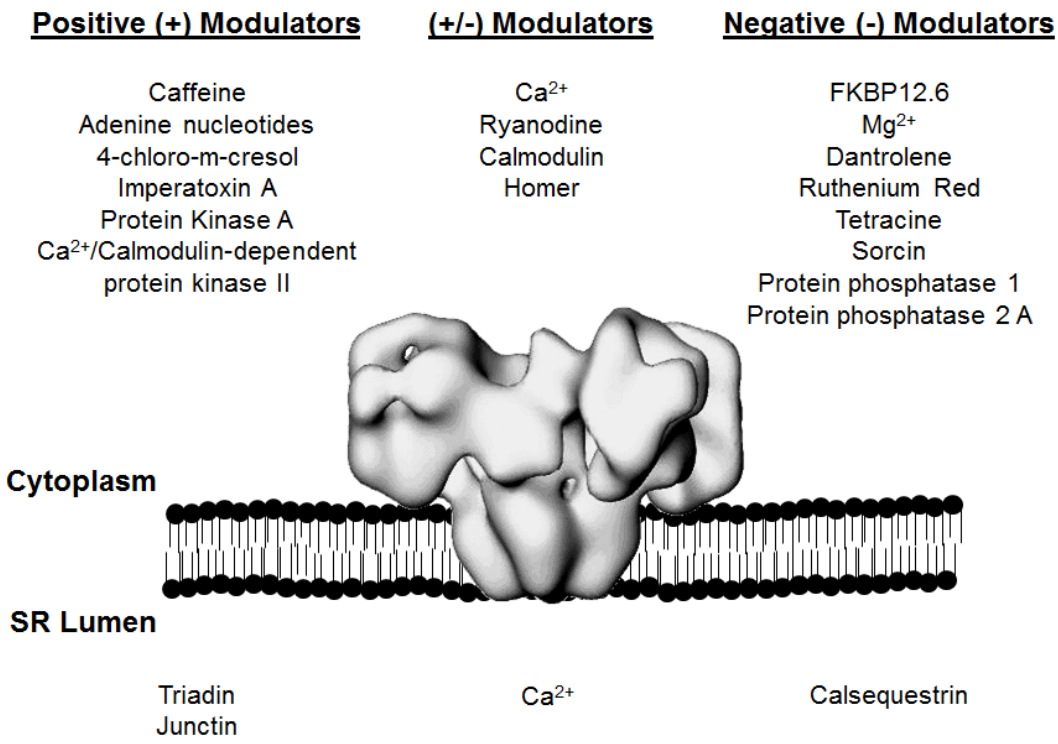


Figure 1.10. RyR2 modulators. A schematic representation of small molecule and protein modulators that provide either positive (+) or negative (-) input signals. Some of these modulators are concentration dependent, such as Ca^{2+} and ryanodine, and fall in to both categories. Figure adapted from van Petegem., (2012).

1.4.2 Regulation of RyR2 by Ca^{2+}

Aside from accessory proteins, RyR2 channel function is regulated by various physiological ligands (Ca^{2+}, Mg^{2+} and ATP), the most important being its primary ligand Ca^{2+} (Endo *et al.,* 1970; Fabiato, 1983; Meissner, 1994). It is well established that cytoplasmic levels of Ca^{2+} are critical for the regulation of channel activity (Fabiato, 1983; Cheng *et al.,* 1993; Williams *et al.,* 2001; Bers, 2002; Scoote and Williams, 2004; Fearnley *et al.,* 2011). Mukherjee *et al* investigated the effects of cytosolic Ca^{2+} concentration ($[Ca^{2+}]_{cyt}$) activation on recombinant hRyR2 channels reporting that elevated Ca^{2+}, ranging from 0-500 µM, increased channel P_o shown in figure 1.11 (Mukherjee *et al.,* 2012). The dependence of RyR2 P_o on $[Ca^{2+}]_{cyt}$ is a physiological necessity and essential for the initiation of cardiac cell contraction by activation of RyR2-clusters and subsequent amplification of Ca^{2+} sparks, described in section 1.2.1 (Wang *et al.,* 2001; Williams *et al.,* 2001).

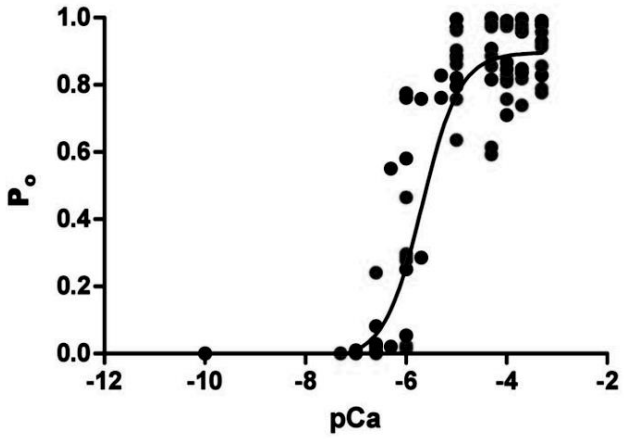


Figure 1.11. The activation of recombinant human RyR2 by cytosolic Ca^{2+}. Figure depicts the sigmoidal relationship between hRyR2 activation by increasing cytosolic Ca^{2+}, ranging from 0-500 µM, and channel P_o. EC_{50} 1.65 ± 0.43 µM. Figure taken and adapted from Mukherjee *et al.,* (2012).

Recently, it has been demonstrated that luminal (intra-SR) Ca^{2+} may also play a key role in regulating Ca^{2+} release (Radwański *et al.,* 2013; Bers, 2014). Early observations reported that spontaneous Ca^{2+} release occurred when the SR Ca^{2+} content reached a particular threshold in a process termed store-overload-induced Ca^{2+} release (SOICR) (Jiang *et al.,* 2004). In addition, luminal Ca^{2+} has been shown to increase RyR2 channel P_o (Sitsapesan and Williams, 1994; Sitsapesan and Williams, 1995; Györke and Györke, 1998; Tencerova *et al.,* 2012; Chen *et al.,*

2014). The regulation of RyR2 by luminal Ca^{2+} is proposed to occur through a variety of mechanisms; activation of different high and low affinity cytosolic sites by permeant Ca^{2+} ions through the channel, termed 'feed-through' (Laver, 2007; Laver, 2009), regulation of luminal accessory proteins (junctin-triadin-calsequestrin complex) (Györke and Terentyev, 2008), or luminal Ca^{2+} sensing at the proposed inner-helix bundle crossover (IHBC) gate (Chen *et al.,* 2014). Understanding the regulation of RyR2 channels by luminal Ca^{2+} is of therapeutic significance, as SOICR is one of the proposed mechanisms prominent in cardiac disease described in section 1.4.4.2.

1.4.3 Pharmacological modulation of RyR channels by ryanodine

The plant alkaloid, ryanodine, found in the stem and roots of the *Ryania speciosa* plant was first isolated as a plant insecticide and was later identified to induce rigid and flaccid paralysis in skeletal and cardiac muscle, respectively (Jenden and Fairhurst, 1969; Nayler *et al.,* 1970; Fairhurst, 1973). The ryanodine molecule, depicted in figure 1.12, was found to bind with high affinity to all three Ca^{2+} release channel isoforms and thus the channel was given the name the ryanodine receptor (RyR1, 2 and 3) (Ogawa, 1994).

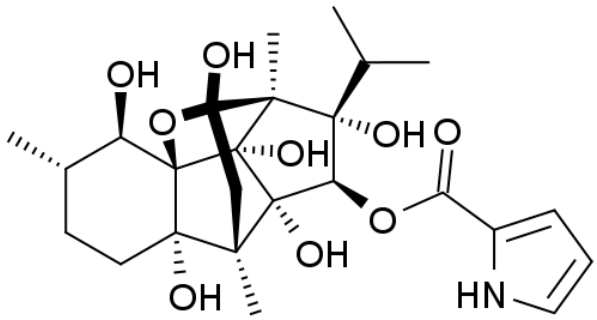


Figure 1.12. Structure of the ryanodine molecule.

The ryanodine molecule can only access its high affinity binding site when the channel is in an open conformation (Lai and Meissner, 1989; Chu *et al.,* 1990; Sutko *et al.,* 1997). Experimental data suggests that the RyR-ryanodine binding site is located within or near the channel pore and is further discussed in chapter 4.1.3 (Tinker and Williams, 1993b; Tu *et al.,* 1994; Callaway *et al.,* 1994). The interaction of ryanodine with RyR is also concentration dependent. At low concentrations (nanomolar to micromolar), binding induces a complex change in single RyR

channel function characterised by reduced unitary conductance and increased open probability (P_o), figure 1.13 (Rousseau *et al.,* 1987; Tinker and Williams, 1993b; Lindsay *et al.,* 1994). A previous study investigating the effects of ryanodine-bound single RyR2 channel gating revealed that the pore adopts an extremely stable open conformation (Mukherjee *et al.,* 2014). In contrast, at high concentrations (> 100 µM), interaction of ryanodine locks the channel in a closed configuration, suggesting that there is a separate low-affinity binding site (Zimányi *et al.,* 1992; Wang *et al.,* 1993).

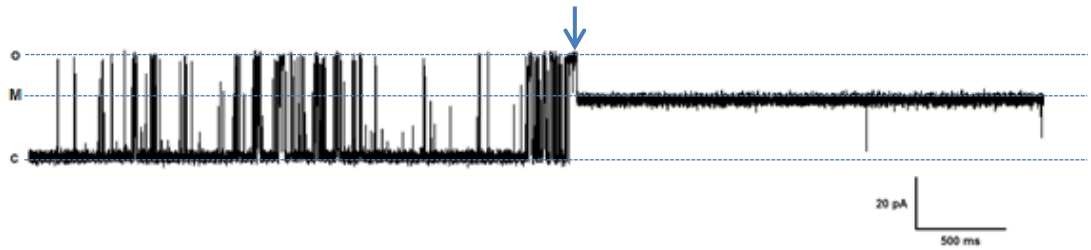


Figure 1.13. Single channel hRyR2 ryanodine modification. (O) Open and (C) closed states denoted by blue line. Typical WT hRyR2 channel gating prior to ryanodine modification in symmetrical 210 mM KCl. (M) Ryanodine modified state, indicated by a blue arrow, is characterised by reduced unitary conductance and increased channel P_o.

The properties of the interaction of ryanodine with RyR channels have enabled it to be used as an important biomarker. Ryanodine has been used to identify the protein during purification (Campbell *et al.,* 1987; Lai *et al.,* 1988; Hymel *et al.,* 1988), to monitor the activity of a population of channels in mixed-membranes (Chu *et al.,* 1990), discussed in chapter 4.4.2, and to study the modulatory effect on single-channel function (Tinker *et al.,* 1996; Wang *et al.,* 2003; Mukherjee *et al.,* 2014), outlined in chapter 5.3.2.

1.4.4 RyR2 Dysfunction

1.4.4.1 Catecholaminergic polymorphic ventricular tachycardia

Catecholaminergic polymorphic ventricular tachycardia (CPVT) is a genetic cardiac disease which is triggered by exercise or emotional stress (Priori *et al.,* 2001; Medeiros-Domingo *et al.,* 2009; Ylänen *et al.,* 2010). Patients with CPVT have structurally normal hearts and at rest display a typical regular electrocardiogram (ECG) (Viskin and Belhassen, 1998). Symptoms arise during sympathetic (β-adrenergic) drive with patients displaying bidirectional ventricular tachycardia (VT) (Napolitano and Priori, 2007), figure 1.14, manifesting as episodes of dizziness, syncope and seizures that may lead to sudden cardiac death if left untreated (Priori *et al.,* 2001; Mohamed *et al.,* 2007). This rare disease, with an estimated prevalence of 1 : 10000, typically presents during childhood and adolescence, and has a high mortality rate with ~ 30 % reported before the age of 30 (Swan *et al.,* 1999; Napolitano *et al.,* 2014). At present CPVT is not curable (Napolitano *et al.,* 2014).

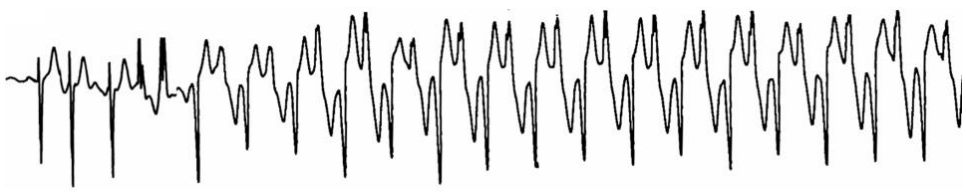


Figure 1.14. Representative echocardiogram of an episode of bidirectional ventricular tachycardia (VT) observed in a patient with CPVT. Bidirectional VT represented by beat-to-beat 180 degrees rotation of the QRS complex. Figure adapted from Mohamed *et al.,* (2007).

CPVT was first described by Reid *et al* and Coumel *et al*, and later by Leenhardt *et al* (Reid *et al.,* 1975; Coumel *et al.,* 1978; Leenhardt *et al.,* 1995). It is now understood that there are five variants of the disease identified from genetic familial investigations. CPVT1, an autosomal dominant form associated with mutations in the gene encoding RyR2 was identified on chromosome 1 (1q42-q43) (Swan *et al.,* 1999; Laitinen *et al.,* 2001; Priori *et al.,* 2001) and CPVT2, a recessive form associated with homozygous mutations in the gene encoding the cardiac isoform of calsequestrin (*CASQ2*), was identified and located on chromosome 1 (1p13-p21)

(Lahat *et al.,* 2001a; Lahat *et al.,* 2001b). Bhuiyan *et al* identified a highly malignant autosomal recessive form of CPVT (CPVT3) that was mapped to a 25 Mb interval on chromosome 7 (7p14-p22), however screening of candidate genes in the region has not revealed a disease-associated gene (Bhuiyan *et al.,* 2007). CPVT4 is caused by a heterozygous mutation in the calmodulin gene (*CALM1*) mapped to chromosome 14 (14q31-q32) (Nyegaard *et al.,* 2012) and CPVT5 is caused by mutation in the triadin gene (*TRDN*) identified on chromosome 6 (6q22) (Roux-Buisson *et al.,* 2012). The highest proportion of CPVT cases (~ 55 %) are accounted for by mutations in RyR2 (CPVT1) (Napolitano *et al.,* 2014).

1.4.4.2 CPVT – Molecular mechanisms

To date, there have been 155 hRyR2 CPVT1-linked mutations reported from the "Gene Connection for the Heart" database (http://www.fsm.it/cardmoc). These point mutations are generally clustered in hot-spots, depicted in figure 1.15, and typically result in a gain-of-function phenotype characterised by spontaneous or inappropriate channel openings (Jiang *et al.,* 2004; di Barletta *et al.,* 2006; George *et al.,* 2007; van Petegem, 2014).

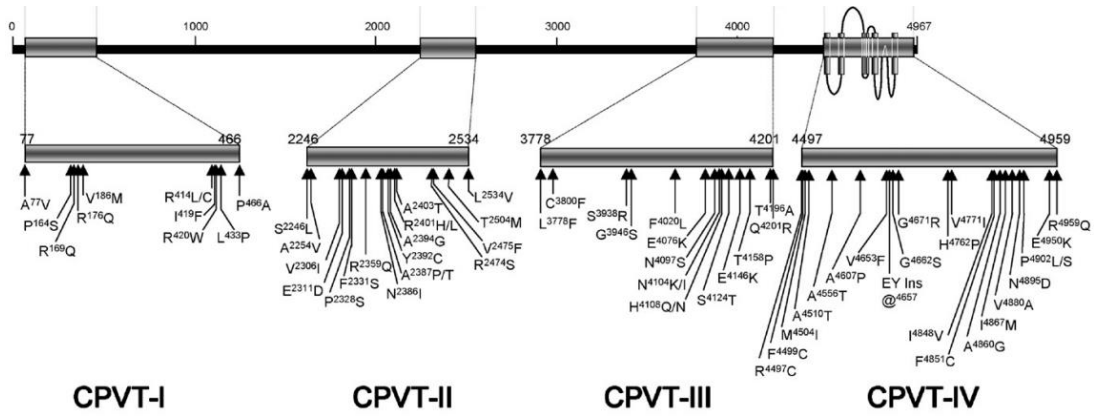


Figure 1.15. RyR2 polypeptide sequence highlighting four 'hotspot' clusters (I-IV) of CPVT channel point mutations. Figure taken and adapted from George *et al.,* (2007).

While the exact mechanism of CPVT is unknown, the likely pathogenic source is a combination of proposed theories such as; 'leaky' RyR2 channels, altered channel Ca^{2+} sensitivity (SOICR), dissociation of accessory proteins (FKPB 12.6) or phosphorylation during sustained β-adrenergic drive (Priori *et al.,* 2001; George *et*

al., 2007; Priori and Chen, 2011). Together these factors result in disrupted Ca^{2+} signaling, whereby Ca^{2+} release during diastole is thought to be the underlying mechanism that gives rise to CPVT (Jiang *et al.,* 2004; MacLennan and Chen, 2009; Priori and Chen, 2011). The augmented intracellular Ca^{2+} concentration during diastole leads to I_{Na} through activation of NCX, functioning in the forward mode and if sufficient, the inward depolarising current results in delayed after depolarisations (DADs) that may cause triggered arrhythmia as shown in figure 1.16 (Reuter *et al.,* 2004; Despa and Bossuyt, 2006).

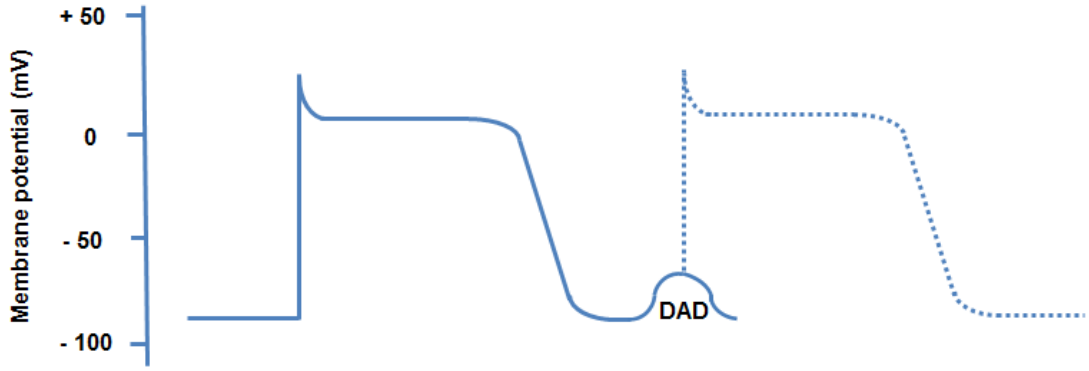


Figure 1.16. Schematic representation of a delayed after depolarisation (DAD) following a cardiac action potential. Abnormal or spontaneous SR Ca^{2+} release through RyR2 during diastole (phase 4) may induce a triggered arrhythmia (dotted line) if the NCX-mediated I_{Na} is sufficient to reach threshold.

Interestingly, point mutations in analogous positions in RyR1 result in skeletal muscle diseases such as malignant hyperthermia (MH) and central core disease (CCD) (Robinson *et al.,* 2006). The similarity between these diseases and CPVT in terms of requiring a 'trigger' highlights common structural defects caused by mutation in RyR1 and RyR2. While the triggering factor may be different, dysfunction in Ca^{2+} signaling through faulty RyR channels may occur through a similar mechanism (Dirksen and Avila, 2002; Brini *et al.,* 2005; Betzenhauser and Marks, 2010). Altogether, approximately 500 missense mutations resulting in disease have been mapped to the primary sequences of RyRs (van Petegem, 2014). In addition, the role of RyR channels in other pathological states such as epilepsy are starting to emerge (Johnson *et al.,* 2010), emphasising the therapeutic potential of RyR as a molecular target.

1.4.4.3 CPVT – Current therapies

β-blockers are considered to be the first-line therapy for patients with CPVT, inhibiting sympathetic drive during periods of stress or exercise (Haugaa *et al.,* 2010). However, 30 % of CPVT patients are reported to be non-responsive to β-blocker therapy, therefore β-blockers are usually used in conjunction with an implantable cardioverter-defibrillator (ICD) (Priori *et al.,* 2002; Sumitomo *et al.,* 2003; Priori and Napolitano, 2005; Hayashi *et al.,* 2009a; Haugaa *et al.,* 2010; Williams and Viswanathan, 2013). Although again, ICDs are not fully protective and can also be proarrhythmic in CPVT patients as both appropriate and inappropriate ICD shocks can trigger catecholamine release (ICD storm) that may subsequently result in arrhythmia and death (Mohamed *et al.,* 2006; Pizzale *et al.,* 2008; van der Werf *et al.,* 2011).

1.4.4.4 RyR2 dysfunction in Heart Failure

In addition to genetic disease such as CPVT, altered RyR2 function has been implicated in heart failure (HF) (Marx *et al.,* 2000; Belevych *et al.,* 2007; Belevych *et al.,* 2013). HF progression is characterised by maladaptive changes in Ca^{2+} homeostasis and at the subcellular level, SR Ca^{2+} and amplitude of Ca^{2+} release is gradually reduced resulting in insufficient activation of the myofilaments (Shannon *et al.,* 2003; Piacentino *et al.,* 2003; Dorn and Molkentin, 2004; Belevych *et al.,* 2007). The amount of Ca^{2+} released from the SR through RyR2 dictates the amplitude of the Ca^{2+} transient, which correlates with the strength of systolic contraction (Wehrens *et al.,* 2005; Dobrev and Wehrens, 2014). The depressed intracellular Ca^{2+} cycling and reduced CICR in HF results in weaker cardiac contractile force that is a common feature of failing hearts (Ather *et al.,* 2013).

A long standing mechanism of HF was proposed that altered Ca^{2+} handling occurred through diastolic SR Ca^{2+} leak (Yano *et al.,* 2000; Ono *et al.,* 2000; Shannon *et al.,* 2003; George, 2007; Belevych *et al.,* 2007). The progressive long-term adrenergic drive that leads to sustained phosphorylation in HF was considered to result in leaky RyR2 channels due to dissociation of FKBP12.6, destabilsing the channel, increasing its P_o (Marx *et al.,* 2000; Lehnart *et al.,* 2005; Shan *et al.,* 2010; Andersson and Marks, 2010; Marx and Marks, 2013). However there is an ongoing debate with studies contradicting these findings showing that PKA phosphorylation

of RyR2-S2808 neither dissociated FKBP12.6 nor substantially modified RyR2 channel gating or open probability (Li *et al.,* 2002b; Jiang *et al.,* 2002a; Stange *et al.,* 2003; Xiao *et al.,* 2006; Benkusky *et al.,* 2007; MacDonnell *et al.,* 2008). The mechanism of RyR2-PKA phosphorylation dysfunction in HF therefore remains unclear.

In addition to PKA-mediated phosphorylation, Ca^{2+}/calmodulin-dependent protein kinase II (CaMKII) phosphorylation of RyR2-S2814 has been identified to promote HF progression (Currie *et al.,* 2004; Ai *et al.,* 2005; Kushnir *et al.,* 2010; Dobrev and Wehrens, 2014). The expression and activity levels of CaMKII in animal models of HF and in failing human hearts are both increased, however the underlying role of CaMKII in HF development is still unclear (Kirchhefer *et al.,* 1999; Hoch *et al.,* 1999; Bers, 2010; Respress *et al.,* 2012). CaMKII-mediated RyR2 phosphorylation has been shown to increase RyR2 P_o at the single-channel level and also in ventricular CMs indicated by an increase in Ca^{2+} spark frequency (Wehrens *et al.,* 2004; van Oort *et al.,* 2010; Bers, 2012). Several groups have identified that CaMKII inhibition is an effective therapeutic strategy in HF, and may be cardioprotective in other arrhythmias by reducing RyR2 channel P_o (Bers, 2010; Li *et al.,* 2012; Swaminathan *et al.,* 2012; Pellicena and Schulman, 2014). The pathogenic effect of sustained PKA and/or CaMKII phosphorylation in HF is likely to be a combination of factors that promote altered RyR2 function and subsequently inappropriate Ca^{2+} handling, contributing to compromised systolic and diastolic cardiac function (Marx and Marks, 2013; Dobrev and Wehrens, 2014).

With the emergence of RyR2 as a potential therapeutic target and emphasis on understanding the underlying pathogenic nature arising from point mutations occurring in CPVT1 and RyR2 dysfunction in HF, it is essential to further elucidate mechanisms involved in channel function, in particular, how channel gating is governed in health and disease.

1.5 – Structural mechanisms of gating at the selectivity filter of hRyR2

1.5.1 Research Limitations

RyR channels play a pivotal role in the ECC process and dysfunction has been observed in both genetic and acquired diseases. The molecular basis of their function is however poorly understood, and is largely due to the absence of atomic-level structural details for the entire channel (Ramachandran *et al.,* 2013; Efremov *et al.,* 2014; Zalk *et al.,* 2014). Hindering efforts to uncover the structure of RyR channels by X-ray crystallography or cryo-EM are their association with the lipid bilayer, the need to extract them from the membrane and the identification of suitable detergents (Baker *et al.,* 2015). There are major challenges in obtaining stable RyR channel protein for structural-functional studies due to the channels' enormous size, inherent flexibility and location within the intracellular SR/ER membrane. In absence of high-resolution structural information; molecular, cellular and biophysical techniques have been tailored over the last three decades to investigate the functional characterisitics of RyR2 channels, discussed in chapters 3, 4, 5 and 6.

It is essential to investigate the effects of disease-linked point mutations, potential therapeutic compounds and physiological regulatory factors on RyR2 channel function, however before this can be achieved, more fundamental information is required on their molecular basis of function. Identifying structural elements involved in RyR2 channel gating remains a key determinant to understand channel function. This project focuses on a particular region of the hRyR2 channel pore termed the selectivity filter and its interactions with the pore helix. It is proposed that interactions between these structural elements are pivotal in mechanisms of channel gating.

1.5.2 The Pore-Forming Region Analogy Model

Molecular modelling and cryo-EM data imply that the PFR of RyR channels are composed of structural elements equivalent to those found in other cation-selective channels (Welch *et al.,* 2004; Samsó *et al.,* 2005; Ludtke *et al.,* 2005; Samsó *et al.,* 2009; Ramachandran *et al.,* 2009; Ramachandran *et al.,* 2013; Efremov *et al.,* 2014; Zalk *et al.,* 2014; Yan *et al.,* 2015). Previous observations comparing the RyR PFR and a prokaryotic potassium channel, KcsA, found striking similarities between

the primary sequences and it was suggested that these structures were likely to have a similar topology (Balshaw *et al.,* 1999). The original RyR2 PFR analogy model described by Welch *et al* was constructed using the 3.2 Å high-resolution crystal structure of KcsA as a template, depicted in figure 1.17 (Doyle *et al.,* 1998; Welch *et al.,* 2004). The PFR model has provided an invaluable framework in which the involvement of domains and individual residues in the processes of ion translocation and gating mechanisms can be predicted and tested.

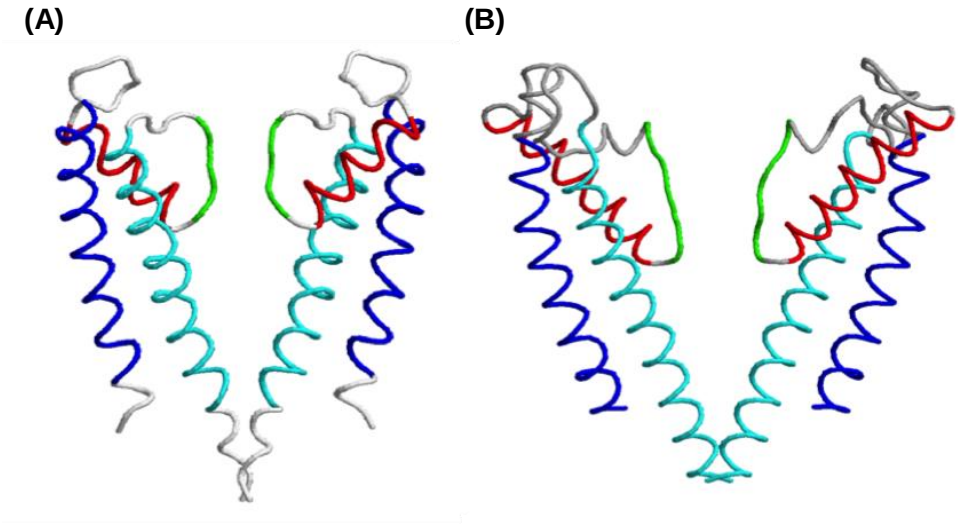


Figure 1.17. Schematic representation of the RyR2 Pore Forming Region (PFR) analogy model based on the crystal structure of the potassium channel, KcsA. (A) KcsA (PDB file: 1BL8) and (B) the RyR2 PFR analogy model. Structural elements are coloured as follows; outer helix or S5 in blue, pore helix in red, selectivity filter in green and inner helix or S6 in cyan. Two monomers are shown for clarity. The four monomers align symmetrically forming a central pore to allow for the selective passage of either K^+ (KcsA) or Ca^{2+} (RyR2) ions across the membrane. Figure was adapted and constructed in PyMol from Welch *et al.,* (2004).

The original analogy model of the PFR hRyR2 (Welch *et al.,* 2004), proposed at the onset of this project, was used as a framework within which predictions of mechanisms of gating occurring at the selectivity filter could be made as (i) a crystal structure of KcsA was resolved at high resolution, section 1.5.3 (Doyle *et al.,* 1998), (ii) physicochemical characteristics and structural elements including the selectivity filter of RyR2 PFR were comparable with KcsA, section 1.5.5 (Welch *et al.,* 2004) and (iii) mechanisms of selectivity filter gating in potassium channels are well known, section 1.5.6 (Cuello *et al.,* 2010a; Cordelo-Morales *et al.,* 2011; Ostmeyer *et al.,* 2013).

1.5.3 The potassium channel KcsA - Crystal structure

The potassium channel, KcsA, from the Gram-positive soil bacteria *Streptomyces lividans* was discovered by Schrempf *et al,* and has been subjected to detailed structural and functional analysis over the last two decades (Schrempf *et al.,* 1995). MacKinnon *et al* were pioneers in obtaining the first high resolution structural images, from KcsA crystals at 3.2 Å, figure 1.18 (Doyle *et al.,* 1998). This was later improved to 2.0 Å by attaching monoclonal Fab fragments to the channel (Zhou *et al.,* 2001). The latter structure by Zhou *et al.,* gave the first in depth visualisation of K^+ ions interacting within the pore and selectivity filter (Zhou *et al.,* 2001).

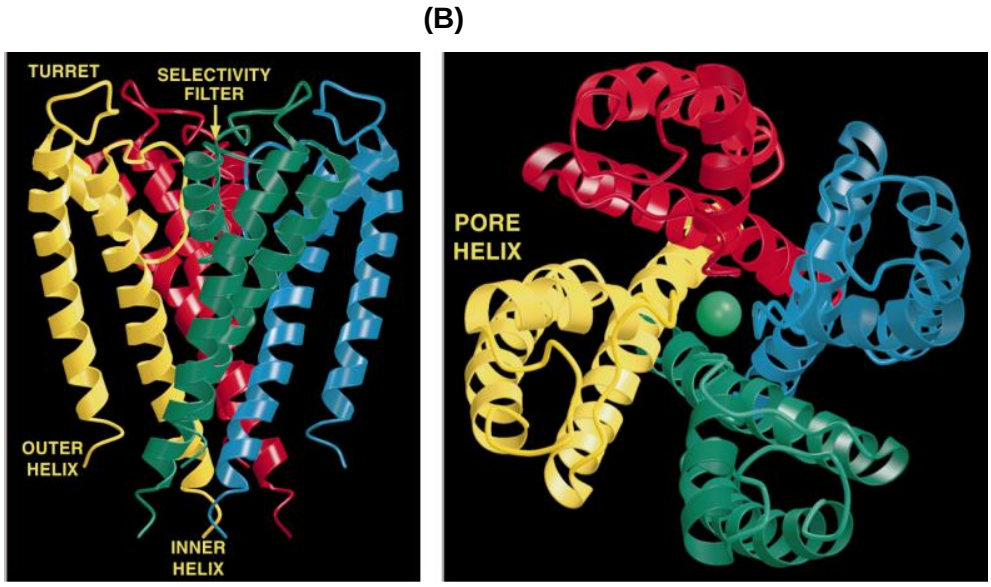


Figure 1.18. Crystal structure of the bacterial potassium channel, KcsA. The K^+ channel is a tetramer with fourfold symmetry encompassing a central pore. View of a ribbon representation illustrating the three-dimensional fold of the KcsA tetramer viewed from the side (A) and extracellular side (B). Four subunits are distinguished by colour. Figure taken and adapted from Doyle *et al.,* (1998).

1.5.4 KcsA as a prototypical ion channel

KcsA is an integral membrane protein that shares high sequence homology and pore architecture with many other K^+ channels including voltage-gated K^+ (K_v), inward rectifier (K_{ir}), Ca^{2+}-activated K^+ (K_{Ca}) and cyclic nucleotide-gated (CNG) channels (Doyle *et al.,* 1988; Yellen, 2002; McCoy and Nimigean, 2012). Compared to K_v channels, that have 6TM depicted in figure 1.19A, KcsA has a simple topology

with only two membrane spanning segments per subunit similar to K_{ir} channels, shown in figure 1.19B.

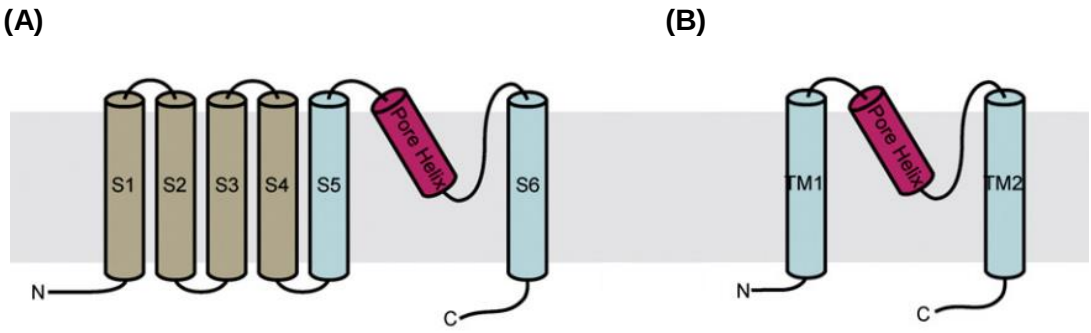


Figure 1.19. Topology diagram of transmembrane ion channels. (A) Voltage-gated potassium (K_v) channel contain six transmembrane helices. Helices S5 and S6 form the pore. (B) Each KcsA subunit is composed of two transmembrane helices connected by a P-loop. Pore forming helices are cyan and the pore-helix in pink. Figure adapted from McCoy and Nimigean, (2012).

KcsA is well characterised, with numerous crystal structures resolved in different conformations (Zhou *et al.,* 2001; Uysal *et al.,* 2009; Cuello *et al.,* 2010b). The structure of KcsA has provided practical insight into the pores of all homologous K^+ channels and has therefore been used as a prototypical ion channel to understand the mechanistic aspects of channel gating and ion permeation (McCoy and Nimigean, 2012).

1.5.5 Structural elements of the Pore-Forming Region – Selectivity filter

In K^+ channels, the selectivity filter is a structural element that controls ion permeation and selectivity and is located at the extracellular end of the pore (Doyle *et al.,* 1998; Zhou *et al.,* 2001). Four identical subunits, containing a highly conserved signature sequence (TVGYGD) are symmetrically aligned to form a central pore (Doyle *et al.,* 1998). This filter forms a backbone of inward facing carbonyl oxygens, shown in figure 1.20, providing an ideal environment for K^+ ion translocation and ensuring high conductance while selectively excluding similar cations such as Na^+ (LeMasurier *et al.,* 2001; Nimigean and Miller, 2002).

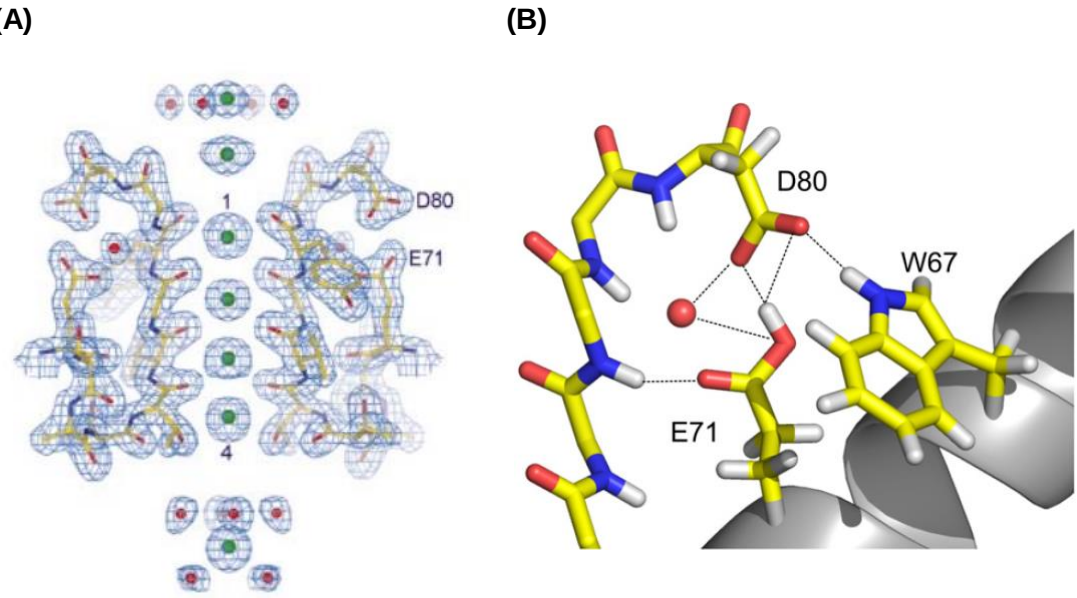


Figure 1.20. Structure of the selectivity filter of KcsA. (A) An electron density view of the selectivity filter of KcsA. Two diagonally opposed subunits are shown with K^+ ions (green spheres) along the ion pathway and water molecules (red spheres). Figure taken from Zhou *et al.,* (2001). (B) A distinct hydrogen-bonding network surrounding the selectivity filter and pore helix of KcsA. The E71-D80 and W67-D80 hydrogen bond interactions between the pore helix and external vestibule are implicated as the driving force for C-type inactivation, regulating gating at the selectivity filter, outlined in section 1.5.7. Figure taken from Cordero-Morales *et al.,* (2011).

The selectivity filter of the PFR of RyR was identified through the recognition of a GIGD sequence similar to the GYGD signature sequence identified in K^+ channels (Doyle *et al.,* 1998; Balshaw *et al.,* 1999; Zhao *et al.,* 1999). The GIGD motif in the PFR analogy model is predicted to be in a location equivalent to the selectivity filter of K^+ channels (Welch *et al.,* 2004). Early biophysical experiments using molecular sieving and electrical distance measurements established that the RyR2 pore radius was 3.5 Å with a length of ~ 10.4 Å (Tinker and Williams, 1993a; Tinker and Williams, 1995). These experimental data are in agreement with recent high-resolution cryo-EM structures, showing that the PFR of RyR is composed of similar structural elements to KcsA and other K^+ channels, shown in figure 1.21 (Welch *et al.,* 2004; Efremov *et al.,* 2014; Zalk *et al.,* 2014; Yan *et al.,* 2015).

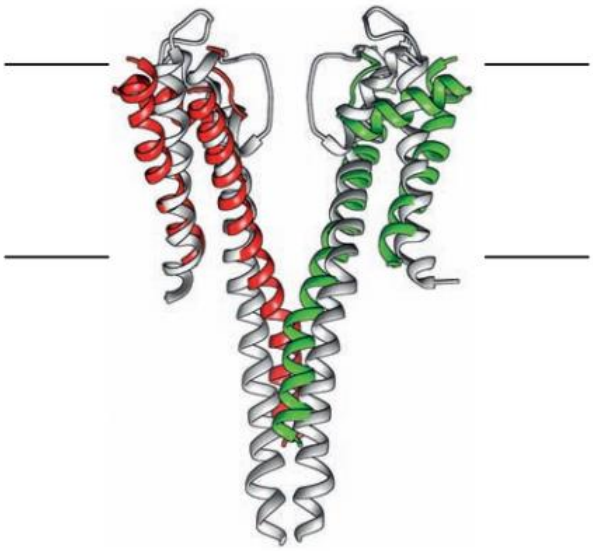


Figure 1.21. Similarity between the architecture of RyR1 pore-forming region and KcsA. Comparison of the backbone of the RyR1 PFR and KcsA superimposed. Two monomers are depicted for each protein, coloured monomers (red and green) represent RyR1 whereas KcsA is depicted in grey. Figure adapted from Efremov *et al.,* (2014).

1.5.6 Potassium channel gating mechanisms

Following the crystallisation of KcsA and other K^+ channels such as MthK, K_vAP and K_v1.2 in various trapped open-conductive, open-inactivated, closed-conductive and closed-inactivated conformations, in combination with experimental evidence it became possible to elucidate gating mechanisms (Doyle *et al.,* 1998; Zhou *et al.,* 2001; Jiang *et al.,* 2002b; Jiang *et al.,* 2003; Long *et al.,* 2005; Cuello *et al.,* 2010b). Transitions between these distinct four states are finely controlled by the coupling of two distinct gates; an activation gate located at the inner-helix bundle crossover (IHBC) (Jiang *et al.,* 2002b) and an inactivation gate situated at the selectivity filter shown in figure 1.22 (Cuello *et al.,* 2010a).

These structures provide an atomic view of the four most important functional states in which the IHBC (activation) gate is either closed or open, and the selectivity filter (inactivation) gate is either conductive or inactivated depicted in figure 1.23 (Zhou *et al.,* 2001; Cuello *et al.,* 2010a; Cuello *et al.,* 2010b).

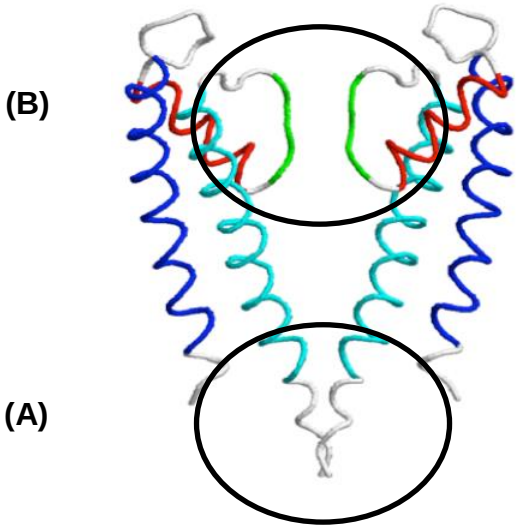


Figure 1.22. Gating in the potassium channel, KcsA. Highlighted regions represented by circles (A) the activation gate at the inner-helix crossover bundle (IHBC) and (B) the inactivation gate located at the selectivity filter.

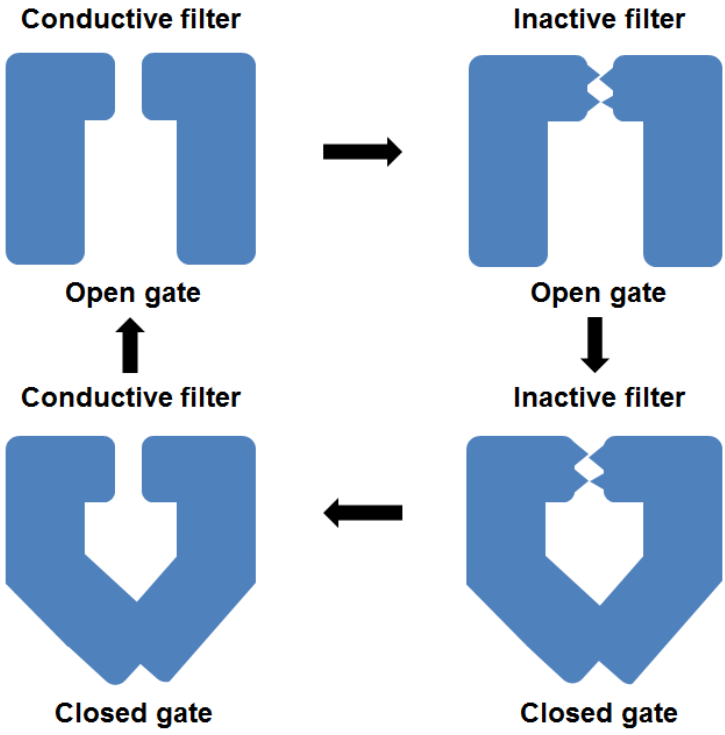


Figure 1.23. The gating cycling of inactivation and recovery in the potassium channel KcsA. Schematic depiction of the four dominant functional states observed from crystal structures and experimental evidence. Figure adapted from Ostmeyer *et al.,* (2013).

1.5.7 Potassium channel - C-type inactivation

A considerable amount of experimental evidence suggests that, as well as the IHBC, a secondary gate exists at the selectivity filter of some K^+ channels (Bernèche and Roux, 2005; Cordero-Morales *et al.,* 2006; Cordero-Morales *et al.,* 2007; Cuello *et al.,* 2010a; Cuello *et al.,* 2010b; van der Cruijsen *et al.,* 2013). The process of gating in the C-terminal region (selectivity filter), known as C-type inactivation, involves conformational changes in the filter structure which alters its relationship with permeant ions (Cuello *et al.,* 2010a). Unlike the fast N-type inactivation which involves a blocking particle linked to the N-terminal region of the channel (the 'ball-and-chain' mechanism), C-type inactivation is a slower process and is characterised by prolonged periods of closed channel events, with the selectivity filter residing in a stable collapsed and inactive conformation (Zagotta *et al.,* 1990; Hoshi *et al.,* 1991; Yellen, 1998; Cordero-Morales *et al.,* 2011). This inactivation displays a wide range of functions from modulating the firing patterns of neurons to regulating the duration and frequency of the cardiac AP (Smith *et al.,* 1996; Spector *et al.,* 1996; Bean, 2007).

The precise mechanisms that govern C-type inactivation are thought to revolve around a distinct hydrogen-bonding network between residues located on the selectivity filter and in the pore helix (PH). In KcsA, an aspartic acid at position 80 (D80), located at the top of the selectivity filter signature sequence, forms a hydrogen bonding network with a glutamic acid and tryptophan residue (E71 and W67), both situated on the pore helix, shown in figure 1.20 (Cordero-Morales *et al.,* 2006). The network of interactions between these three residues holds the selectivity filter in the inactivated state, pinching the central glycine residue of the signature sequence (TVGYGD) (Zhou *et al.,* 2001), thereby preventing K^+ ion occupancy and translocation through the pore (Cuello *et al.,* 2010a). Replacing E71 with alanine (E71A) greatly increases the open probability of KcsA as the channel cannot inactivate (Cordero-Morales *et al.,* 2006; Chakrapani *et al.,* 2007), presumably as a result of disrupting the network as alanine is not capable of hydrogen bonding (Cordero-Morales *et al.,* 2011). Introducing a conservative substitution, tyrosine, to the pore helix (W67Y) at this position retains channel inactivation, similar to WT KcsA, and does not significantly affect the overall kinetics and extent of gating (C-type inactivation) as the ability to form hydrogen bonds is preserved (Cordero-Morales *et al.,* 2011). Likewise, conservative *Shaker* (W434Y) and $K_v1.2$ (W366Y) mutants were also found to retain inactivation currents similar to

their respective WT channels (Cordero-Morales *et al.,* 2011). This underlies the importance of the selectivity filter in the inactivation process and also highlights a proposed conserved mechanism occuring throughout a variety of K^+ channels, figure 1.24.

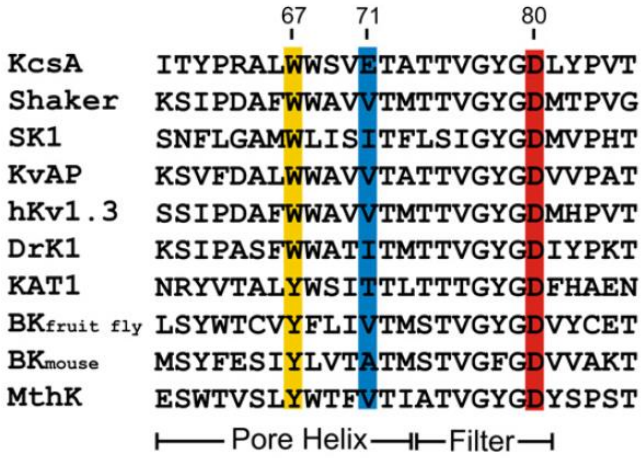


Figure 1.24. Sequence alignment of KcsA with other K^+ channels. The three highlighted columns represent a proposed conservative network between K^+ channels analogous to the E71-D80-W67 interaction established in KcsA. Figure adapted from Cordero-Morales *et al.,* (2011).

The role of the selectivity filter in RyR2 inactivation remains to be established. Data emerging from previous RyR2 investigations indicate that the filter is likely to contribute to channel gating and that mutation of acidic residues in and around the selectivity filter affects both open probability and rates of ion translocation (Mead-Savery *et al.,* 2009; Mukherjee *et al.,* 2012). These observations suggest that the selectivity filter of RyR2 may collapse in a manner analogous to the filter of KcsA during C-type inactivation.

1.5.8 Gating mechanisms at the selectivity filter – Flicker gating

In addition to C-type inactivation outlined in section 1.5.7, another mechanism occurring at the selectivity filter termed flicker gating has been described in K^+ channels such as BK, MthK and KcsA (Ferguson *et al.,* 1993; Talukder and Aldrich, 2000; Piskorowski and Aldrich, 2006; Zadek and Nimigean, 2006; Thomson and Rothberg, 2010; Cuello *et al.,* 2010b). These flicker events are characterised by rapid channel closures switching between conducting and non-conducting states and have been attributed to the dynamic flexible nature of the filter (Shrivastava *et al.,* 2002; Noskov *et al.,* 2004; Welch *et al.,* 2004; Mukherjee *et al.,* 2014). Mutations in the selectivity filter or surrounding structure of K^+ channels have large effects on flicker gating transitions, and have been shown to increase the closed dwell-time duration (Lu *et al.,* 2001; Alagem *et al.,* 2003; Chapman *et al.,* 2006). However, their physiological function is still unknown.

Analysis of recent experimental data of recombinant hRyR2 single channel gating kinetics has revealed fast flicker closing events that are independent of activating ligand concentration (cytosolic Ca^{2+}) (Mukherjee *et al.,* 2012). This mode of gating closely resembles the brief closing transitions reported in K^+ channels that relate to conformational changes in the selectivity filter of these channels (Lu *et al.,* 2001; Alagem *et al.,* 2003; Chapman *et al.,* 2006). Together these observations indicate that the filter of RyR2 is likely to be an important component of the overall gating process and contribute to the regulation of Ca^{2+} release from the SR during ECC.

1.6 – Aims and Hypotheses

Comparing the residues involved in the formation of a hydrogen-bonding network in KcsA (W67, E71 and D80) with those at similar positions in the Welch *et al* analogy PFR model (Y4813, D4829 and Y4839), figure 1.25, highlights the potential for a similar mechanism in RyR2. Residue D4829 (hRyR2) occupies an equivalent position in the selectivity filter signature sequence to D80 in KcsA and is located at an ideal position to form hydrogen bonds with Y4813 and Y4839, analogous to E71 and W67 in KcsA. The PFR analogy model also indicates distances of approximately 2.5 Å which are within the ideal range for hydrogen bond formation (Welch *et al.,* 2004; Hubbard and Haider, 2010).

(A) **(B)**

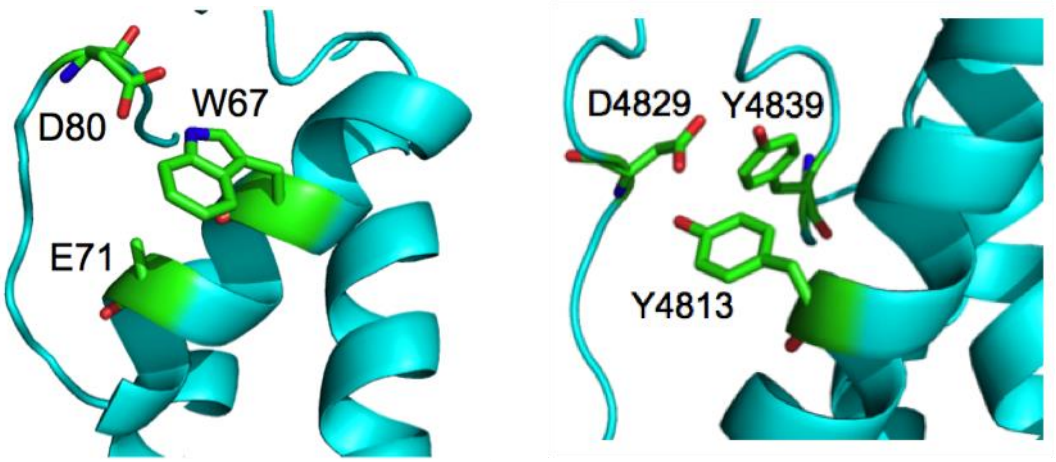


Figure 1.25. A cartoon representation of the selectivity filter and pore helix of (A) KcsA and (B) the PFR analogy model of RyR2. Residues thought to be involved in a hydrogen-bonding network are shown in stick format. The figures were constructed in PyMol using the PDB file 1BL8 for KcsA and the analogy RyR2 model by Welch *et al.,* (2004).

1.6.1 Hypotheses

This project used a variety of biochemical, molecular biological and electrophysiological techniques to assess the importance of the selectivity filter region in the gating process of hRyR2 by testing the following hypotheses:

- That hRyR2 contains an intricate network of hydrogen-bonded residues (Y4813, D4829 and Y4839) at and around the selectivity filter analogous to that seen in KcsA and other K^+ channels.

- That the selectivity filter of hRyR2 is an important gating component. Alanine mutations in and around the selectivity filter will result in altered gating as a consequence of disrupted residue interactions.

- That retaining the physicochemical properties and hydrogen-bonding capabilities of conservative mutants (Y4813W, D4829E and Y4839W) maintains the functional characteristics of WT hRyR2.

1.6.2 Project Aims

To generate three alanine (Y4813A, D4829A and Y4839A) and three conservative (Y4813W, D4829E and Y4839W) mutant hRyR2 channels by site-directed mutagenesis using a cassette based strategy, and to ensure protein expression and transfection efficiencies were comparable with WT hRyR2 for downstream functional assays.

To confirm the functional homotetrameric status of a population of mutant selectivity filter and pore helix hRyR2 channels in a cellular context utilising intracellular Ca^{2+} imaging.

To assess the activity of mutant hRyR2 channels by measuring equilibrium binding of [^{3}H] ryanodine.

To screen purified mutant hRyR2 channels in order to assess their stability and ion conduction properties compared to WT hRyR2 when isolated, solubilised and incorporated into a planar lipid bilayer.

To compare single mutant hRyR2 channel open probabilities and dwell-times with WT hRyR2 under regulated conditions.

To investigate the gating mechanism of WT and mutant RyR2 channels in response to activating Ca^{2+} under minimal conditions.

To identify the prevalence and nature of flicker gating events (thought to originate in the selectivity filter) in mutant hRyR2 channels, to see if substitution has affected this particular conformational transition.

To compare differences between previous and new RyR structural modelling data in regards to residue positioning around the selectivity filter region, and to correlate novel hRyR2 gating information with these models to enhance the credibility of these static structures.

Chapter Two:

Materials and Methods

2.1 – Materials

2.1.1 General Lab Materials

All chemical and reagents used were of analytical grade and were obtained from Sigma-Aldrich, unless otherwise stated. Equipment for electrophoresis, DNA agarose and SDS-PAGE, were supplied from Bio-Rad. All solutions and buffers were dissolved in bottled deionised water (dH_2O) (AnalaR NORMAPUR®, VWR Chemicals) and stored at room temperature (RT) unless otherwise stated. Solutions which required sterilisation were filtered through a 0.22 µm Millex® syringe filter (Merck Millipore).

2.1.2 Microbiology

Bacterial growth media and antibiotics were obtained from Sigma-Aldrich. General sterilised plasticware and glassware were obtained from Greiner and Fisher.

2.1.3 Molecular Biology

2.1.3.1 General Lab reagents

Deionised water (dH_2O): Filter sterilised and autoclaved.
70 % Ethanol: Stock solution 70 % ethanol (v/v).
EDTA 0.5 M stock: 186.12 g/L EDTA, was adjusted to pH 10 with NaOH to dissolve EDTA. Once dissolved, pH was adjusted to 7.5 using HCl.
Ampicillin: 100 mg/mL stock was prepared in bottled dH_2O that was filter sterilised and stored at – 20 °C.

2.1.4 Plasmid Vectors

2.1.4.1 pcDNA3 Mammalian Expression Vector

The pcDNA3 vector (5.446 kb) containing the full-length hRyR2 sequence and an N-terminal eGFP tag, termed pcDNA3-eGFP-hRyR2 (21.229 kb) shown in figure 3.2A, was obtained from George *et al.,* (2003). The full-length hRyR2 sequence encodes 4,967 amino acids (564,567 Da). Human RyR2 accession number: Q92736.

2.1.4.2 pSL1180 Intermediate Vector – Site-directed mutagenesis

The pSL1180 vector (3.422 kb) containing the *Nhe*I/*Xho*I hRyR2 C-terminal DNA fragment, termed pSL1180-NX1-hRyR2 (8.597 kb) shown in figure 3.2B, was used for site-directed mutagenesis. The intermediate vector harbouring the desired point mutation, listed in table 3.1, was reinserted back into the full-length pcDNA3 vector for protein expression and subsequent biochemical and biophysical functional studies.

2.1.5 Molecular biology reagents

Restriction endonucleases: All enzymes (supplied with buffers) were acquired from New England Biolabs (*BamH*I, *Bgl*II, *HinD*III, *EcoR*I, *Xho*I and *Fse*I). Digestion of pSL1180 was performed using the fast *EcoR*I-HF® enzyme. All enzymes were stored at – 20 °C except for *Fse*I that was stored at – 80 °C.
1 kb DNA marker: 1 kb Plus DNA ladder (Invitrogen) was mixed with equal volume of 2 x DNA loading buffer stored at – 20 °C.
TAE, 50 x stock: 2 M Tris, 2 M acetic acid and 50 mM EDTA.
DNA loading buffer (2 x): 5 mL glycerol, 5 mL 1x TAE and 0.25 % (w/v) Orange G. Orange G was used as a tracking dye for nucleic acid electrophoresis to track the DNA front in agarose gels.

2.1.5.1 Media

Luria Bertani (LB) Lennox medium: 10 g/L tryptone, 5 g/L yeast extract and 5 g/L NaCl. Media were autoclaved and incubated at RT until < 50 °C before adding antibiotics (ampicillin 100 µg/mL). Stored at 4 °C.
LB Lennox agar plates: 10 g/L tryptone, 5 g/L yeast extract, 5 g/L NaCl and 15 g/L agar. Agar plates were autoclaved and incubated at RT until < 50 °C before adding antibiotics (ampicillin 100 µg/mL). Plates were poured in a Class 1 containment safety cabinet and allowed to set before parafilming individual plates and storing at 4 °C.
NZY broth: 5 g/L NaCl, 2 g/L $MgSO_4$, 5 g/L yeast extract and 10 g/L NZ amine (casein hydrolysate) adjusted to pH 7.5 with NaOH. Broth was autoclaved before storing at 4 °C, antibiotic-free.

2.1.5.2 Mini/Maxiprep isolation reagents

Qiagen reuspension buffer (P1): 50 mM Tris, adjusted to pH 8.0, 10 mM EDTA and 100 µg/mL RNase A/LyseBlue stored at 4 °C.
Qiagen lysis buffer (P2): 200 mM NaOH and 1 % SDS (w/v).
Qiagen neutralisation buffer (P3): 3 M potassium acetate, adjusted to pH 5.5.
Qiagen column equilibration buffer (QBT): 750 mM NaCl, 50 mM MOPS, adjusted to pH 7.0, 15 % isopropanol (v/v) and 0.15 % Triton® X-100 (v/v).
Qiagen column wash buffer (QC): 1 M NaCl, 50 mM MOPS and 15 % isopropanol (v/v), adjusted to pH 7.0.
Qiagen elution buffer (QF): 1.25 M NaCl, 50 mM Tris and 15 % isopropanol (v/v) adjusted to pH 8.5.

2.1.5.3 Mutant Oligonucleotide Primers

Mutant hRyR2 primers were designed following the guidelines outlined in section 3.2.1.1, and were ordered from Sigma-Aldrich. Primers were supplied as lyophilised pellets which were resuspended in 250 µL bottled dH_2O to form a stock solution, and stored at – 20 °C. The stock solutions were diluted to form working concentrations (125 ng/µL) for site-directed mutagenesis PCR amplification. The list of primers is detailed in table 3.2.

2.1.6 Protein biochemistry reagents

Protease inhibitors: Serine, cysteine and metalloprotease protease inhibitors were used during protein extraction and isolation. Complete EDTA-free protease inhibitor cocktail tablets were obtained from Roche, and stored at 4 °C. In addition, protease inhibitor cocktail solution for solubilisation buffer was obtained from Sigma-Aldrich, and stored at – 20 °C. Both inhibited serine
Hypo-osmotic cell lysis buffer: 20 mM Tris and 1 mM EDTA was adjusted to pH 7.4 using HCl. One protease inhibitor tablet (Roche) per 50 mL buffer was prepared immediately before use.
Microsomal resuspension 'Solution C' buffer: 0.4 M sucrose and 20 mM HEPES stored at – 20 °C.
CHAPS/PC stock: 10 % (500 mg) 3-[(3-cholamidopropyl)-dimethylammonio] 1-propane-sulphonate (CHAPS) and 5 % (250 mg) phosphatidylcholine (PC) in 5 mL

bottled dH_2O was prepared on day of hRyR2 purification and incubated at 4 °C until required.

KCl solution: 0.4 M KCl solution stored at 4 °C.

Solubilisation buffer: 1 M NaCl, 0.15 mM $CaCl_2$, 0.1 mM EGTA and 25 mM PIPES was adjusted to pH 7.4 and stored at – 20 °C. Protease inhibitor cocktail solution 1:1000 (v/v) prepared immediately before use.

Gradient buffer: 300 mM NaCl, 25 mM Tris, 50 mM HEPES, 0.3 mM EGTA, 0.3 % CHAPS/PC (from 10 % stock) and 82.24 mL bottled dH_2O. One protease inhibitor tablet (Roche) per 25 mL buffer was prepared immediately before use.

MicroBSA reagents: Obtained from Thermo Scientific.

BSA standards: 2 mg/mL BSA stock diluted to 500, 200, 100, 50, 20 and 10 µg/mL in dH_2O stored at – 20 °C.

SDS-PAGE separating buffer: 1.5 M Tris stock solution, adjusted to pH 8.8 with HCl.

SDS-PAGE stacking buffer: 0.5 M Tris stock solution, adjusted to pH 6.8 with HCl.

Ammonium persulphate (APS): 10 % APS (w/v) solution.

Sodium dodecyl sulfate (SDS): 10 % SDS (w/v) solution.

SDS-running buffer 1x: 25 mM Tris, 250 mM glycine and 0.1 % (w/v) SDS.

SDS-loading buffer 2x: 100 mM Tris pH 6.8, 20 % (v/v) glycerol, 4 % (w/v) SDS, 10 % (v/v) β-mercaptoethanol and 0.2 % (w/v) bromophenol blue.

Protein molecular weight ladder: Kaleidoscope prestained standard (Bio-Rad) stored at – 20 °C.

Tris-buffered saline (TBS) 1x: 137 mM NaCl and 20 mM Tris, adjusted to pH 7.6 with HCl.

TBS-T 1x: 1x TBS and 0.1 % (v/v) Tween-20.

Blocking solution: 5 % (w/v) non-fat dried milk (Marvel) dissolved in 1x TBS-T.

Blocking Ab solution: 2.5 % (w/v) non-fat dried milk (Marvel) dissolved in 1x TBS-T. Primary and secondary antibodies, stated in section 2.1.6.1, were applied to the membrane as a 1:5000 dilution.

2.1.6.1 Antibodies

Primary Antibody: GFP (B-2) SC-9996 mouse monoclonal IgG_{2a}, 200 µg/mL stock, raised against amino acids 1-236 of full length GFP was obtained from Santa Cruz Biotechnology.
Secondary Antibody: Anti-mouse IgG (whole molecule)-Peroxidase antibody produced in goat was obtained from Sigma-Aldrich.

2.1.7 Mammalian cell culture

All growth media and reagents were supplied by Invitrogen and chemicals were obtained from Sigma unless otherwise stated. Sterile culture flasks and plates were supplied by Greiner.

2.1.7.1 Mammalian cell culture reagents

Dulbecco's Modified Eagle Medium (DMEM): DMEM obtained from Gibco ® Invitrogen supplemented with 4.5 g/L glucose, 10 % (v/v) foetal calf serum and 4 mM glutamine. For tissue culture media, complete DMEM (cDMEM) was supplemented with antibiotics, 100 µg/mL penicillin/streptomycin. For Ca^{2+} imaging, minimal DMEM (mDMEM) was antibiotic-free. All solutions were filtered sterilised and stored at 4 °C.
Saline solution: 0.9 % (w/v) NaCl.
HEPES buffered saline (HBS) 2x: Ready-made HBS 2x was obtained from Alfa Aesar containing 280 mM NaCl, 10 mM KCl, 1.5 mM $NaPO_4$, 12 mM dextrose and 50 mM HEPES, pH 7.0.
Calcium chloride solution: 1 M $CaCl_2$ stock solution filtered sterilised.
Effectene transfection reagent: Effectene reagents were obtained from Qiagen and stored at 4 °C.
Laminin: Mouse laminin (1 mg/mL) was obtained from Sigma.

2.1.8 Electrophysiology reagents

All buffers and solutions were prepared in bottled dH_2O (AnalaR NORMAPUR®, VWR Chemicals), produced by reversed osmosis and capacitive deionisation, that was subsequently filter sterilised before use.

DOPE lipid: 1,2-dioleoyl-*sn*-glycero-3-phosphoethanolamine, 18:1 (9-Cis), PE, was obtained from Avanti Polar Lipids Inc. PE lipid was supplied in powder form which was resuspended in chloroform (50 mg/mL) in a glass vial and stored at – 80 °C.
***n*-decane**: PE lipid was resuspended in *n*-decane to a working concentration of 33 mg/mL.
LiCl solution: 3 M LiCl stock solution was prepared and stored at 4 °C.
KCl solutions: Various KCl solutions were prepared (15, 40, 90, 140, 200, 600, 800 mM) with 20 mM HEPES and adjusted to pH 7.4 using KOH. The addition of hydroxide ions increased potassium concentration by 10 mM. Final KCl solutions concentrations were 25, 50, 100, 150, 210, 610, 810 mM.
KCl gradient buffer: 3 M KCl and 20 mM HEPES solution was adjusted to pH 7.4.

2.2 – Methods

Health and safety training and COSHH assessments were completed at the Wales Heart Research Institute (WHRI). Use of genetically modified organisms (GMO) was carried out in accordance with local GMO guidelines. Microbiology and cell culture procedures were performed in a Class I and Class II containment safety cabinet, respectively. Tritiated ryanodine radioisotope training was received from the WHRI safety officer and disposal of radioisotopes were documented using the IsoStock® software.

2.2.1 Microbiology techniques

2.2.1.1 Sterilisation procedures

Flasks and bottles containing growth media or dH_2O were sterilised by autoclaving at 121 °C, 15 psi for 30 min. Aseptic techniques were performed while working with bacterial cell cultures.

2.2.1.2 Transformation of mutant hRyR2 DNA constructs following mutagenesis

XL10-Gold Ultracompetent *Epicurian coli* cells were used during the cloning stages to transform full-length eGFP-hRyR2, as these cells are endonuclease deficient (*end*A), improving the quality of plasmid DNA, and recombination deficient (*rec*A), increasing insert stability. In addition, these cells exhibit the Hte phenotype which increases the transformation efficiency of ligated and large DNA molecules suitable for RyR2 mutagenesis procedures, outlined in chapter 3. Prior to DNA transformation, the tube containing cells (50 µL) was thawed on ice, 2 µL of β-Mercaptoethanol (β-ME) was mixed gently into incubating on ice for 5 min. 10 µL of the ligation reaction was added and swirled around the tube before incubating the mixture on ice for 30 min. XL10-Gold cells were transformed by incubating tubes at 42 °C in a water bath for 45 s before incubating tubes on ice for 2.5 min. Pre-warmed (30 °C) NZY broth (800 µL) was added to tubes which were incubated at 30 °C, set at 225 rpm, for 1 h. Transformed XL10 cells were spread (50-100 µL) onto LB agar plates containing ampicillin (LB_{amp} 100 µg/mL) and incubated for 16-18 h overnight at 30 °C.

2.2.1.3 Transformation of recombinant hRyR2 DNA constructs

MAX Efficiency® Stbl2™ competent cells were routinely used to transform hRyR2 DNA constructs, as these cells increased RyR2 plasmid yield and quality due to the *end*A1 mutation. Prior to DNA transformation, the tube containing Stbl2 cells (50 µL) was thawed on ice, 2 µL (1-10 ng) plasmid was subsequently added to the tube containing cells which was carefully mixed and incubated on ice for 30 min. Stbl2 cells were transformed by incubating tubes at 42 °C in a water bath for 45 s before incubating tubes on ice for 2.5 min. 800 µL NZY broth (antibiotic-free) was added to tubes which were incubated at 30 °C, set at 225 rpm, for 1 h. Transformed Stbl2 cells were spread (50-100 µL) onto LB agar plates containing ampicillin (LB_{amp} 100 µg/mL) and incubated for 16-18 h overnight at 30 °C (full-length pcDNA3-hRyR2) or 37 °C (intermediate pSL1180-NX1).

2.2.1.4 Propagation of recombinant hRyR2 DNA constructs

2.2.1.4.1 Propagation of pSL1180-NX1 plasmids

Transformed colonies were grown on LB_{amp} plates and stored at 4 °C until required. For DNA cloning procedures using mutant NX1 plasmids, 10-20 bacterial colonies were picked and added in separate tubes containing 5 mL LB_{amp} broth. Tubes were incubated in a 37 °C shaker, set to 225 rpm, for 16-18 h overnight.

2.2.1.4.2 Propagation of pcDNA3-RyR2 plasmids

For large-scale propagation of full-length hRyR2 plasmids, 5-10 colonies were picked and added in separate tubes containing 5 mL LB_{amp} broth. Tubes were incubated in a 30 °C shaker, set to 225 rpm, for 16-18 h overnight. Plasmid DNA was isolated from 3 mL of the overnight culture and verified by *EcoR*I digest, described in sections 2.2.1.5 and 2.2.1.8. The remaining 2 mL was added into tubes containing 6 mL fresh LB_{amp} broth and grown for a further 6-8 h at 30 °C, 225 rpm. 4 mL of the bacterial culture was added to flasks containing 400 mL LB_{amp} broth (1/100 ratio), these flasks were subsequently incubated overnight at 30 °C, 225 rpm for 16-18 h. Bacterial cultures were harvested by centrifugation Avanti® in a J-26 XP centrifuge (Beckman Coulter) at 6000 x *g* for 20 min in 1 L centrifuge tubes (JLA 8.1000 rotor Beckman). Pellets were taken straight through to DNA isolation (maxiprep see section 2.2.1.6) or, alternatively, were stored at – 20 °C.

2.2.1.5 Small-scale plasmid DNA isolation and purification – Miniprep

Small-scale plasmid DNA isolation and purification was performed using the QIAprep Spin miniprep kit (Qiagen). A 3 mL bacterial culture, section 2.2.1.4, was harvested at 17,900 x *g* for 1 min at RT using a bench top minispin 'plus' Eppendorf centrifuge. The bacterial pellet was resuspended in 250 µL Buffer P1 (+RNase A (100 µg/mL) and LyseBlue) ensuring a homogenous solution containing no cellular clumps. The bacteria were lysed by the addition of 250 µL Buffer P2. Samples were inverted 4-6 times or until the cell suspension became viscous and changed to a blue colour. Cell lysis was neutralised by the addition of 350 µL Buffer N3 mixing immediately by inverting 4-6 times or until the cell debris and SDS from Buffer P2 had precipitated to form a cloudy colourless solution. Precipitant material was removed by centrifugation at 17,900 x *g* for 10 min. The supernatant was carefully decanted into QIAprep spin columns and centrifuged for 1 min. The spin columns were washed by the addition of 500 µL Buffer PB and centrifuged again for 1 min. An additional wash step was performed by adding 750 µL Buffer PE (+ ethanol) into the columns which were centrifuged twice for 1 min to ensure that residual wash buffer had been completely removed. The DNA was eluted by adding 30 µL dH_2O to the QIAprep columns which were placed in a 1.5 mL Eppendorf tube and incubated at RT for 1 min. Columns were then centrifuged for 1 min to isolate the DNA which was then stored at – 20 °C.

2.2.1.6 Large-scale plasmid DNA isolation and purification – Maxiprep

Large-scale plasmid DNA isolation and purification was performed using the Qiagen plasmid Maxi kit. As described in section 2.2.1.4.2, 800 mL of transformed Stbl2 cell culture containing plasmid DNA was harvested by centrifugation at 6000 x *g* for 20 min at 4 °C. The bacterial pellet was resuspended in 30 mL Buffer P1 containing RNase A (100 µg/mL) and LyseBlue, before aliquoting the cell suspension in 3 x 50 mL falcon tubes (3 x 10 mL). If the 30 mL bacterial pellet was frozen, the tubes were placed on a roller and allowed to thaw at RT before placing on ice. Cell lysis was completed by the addition of 10 mL Buffer P2 into tubes, inverting 4-6 times or until the cell suspension had turned blue. The 20 mL cell suspension was incubated for 5 min at RT, before the addition of 10 mL neutralisation Buffer N3 to stopped further cell lysis/genomic shearing due to SDS. The samples were inverted 4-6 times or continued until the cell debris and SDS precipitated, forming a cloudy colourless

solution. The precipitated cell suspension was incubated on ice for 20 min, before centrifugation at 20,000 x *g* for 30 min at 4 °C (Avanti J-25 centrifuge Beckman) to remove unwanted cell debris, isolating the plasmid DNA in the supernatant. The supernatant was centrifuged again at 20,000 x *g* for 15 min at 4 °C to ensure that precipitated material was completely removed. Prior to the addition of supernatant to the QIAGEN-tip 500, the column was equilibrated by the addition of 10 mL Buffer QBT. The clear supernatant containing plasmid DNA was added to the QIAGEN-tip and left to pass through the resin by gravity flow. The QIAGEN-tip was washed twice with 30 mL Buffer QC. The DNA was eluted from the tip by the addition of 15 mL buffer QF which was collected in a falcon tube. The addition of 10.5 mL isopropanol (stored at RT) to the eluate initiated DNA precipitation. The sample was mixed by inverting the tube 4-6 times before centrifugation at 15,000 x *g* for 30 min at 4 °C. The supernatant was carefully discarded leaving the DNA pellet which was washed with 5 mL of 70 % ethanol (stored at RT) and centrifuged at 15,000 x *g* for 10 min. The ethanol supernatant was discarded and, the centrifuge tubes containing DNA were air-dried for 10 min to allow for remaining residual ethanol to evaporate. The DNA pellet was resuspended in 1 mL dH_2O, followed by DNA quantification (section 2.2.1.7) and verification (section 2.2.1.8) by restriction digest.

2.2.1.7 DNA spectrometry - Quantification of DNA concentration

Spectrophotometric analysis of plasmid DNA, prepared from large-scale maxiprep, was performed to determine DNA concentration and purity. The spectrophotometer absorbance was set at 260 nm (Abs_{260}), the wavelength at which DNA absorbs UV light, and a 1:50 dilution factor that enabled the calculation of DNA concentration according to the equation stated below:

$$Abs_{260} \text{ x dilution factor x } 50 = [\text{DNA}] \text{ (ng/µL)}$$

Plasmid DNA (20 µL) was mixed with 980 µL dH_2O before calibrating (zeroing) the spectrophotometer using a cuvette containing 500 µL dH_2O. 2 x 500 µL of the DNA dilution was added to the cuvette to assay concentration. A typical DNA yield from 800 mL pellet ranged from 200-800 ng/µL. The sample purity was determined by the absorbance at 280 nm (Abs_{280}) which measures aromatic residues such as tyrosine and tryptophan. The Abs_{280} is an indicator of protein contamination levels within samples, whereby an $Abs_{260:280}$ ratio of > 1.8 was deemed to be of high DNA purity.

2.2.1.8 DNA restriction digest – Verification of DNA preparation

Both intermediate (pSL1180) and full-length (pcDNA3) hRyR2 plasmids were verified by restriction digest to ensure that transformation and DNA propagation was successful. The recognition of specific nucleotide sequences and generation of correct digest patterns ensured that known DNA fragments with particular base pair length were generated and confirmed that plasmid rearrangements had not occurred (George *et al.,* 2003). Four restriction endonucleases were used to digest the full-length pcDNA3-hRyR2 plasmid, described in chapter 3.2.2 with predicted DNA patterns depicted in figure 3.5B. *Eco*RI-HF® was used to digest the intermediate pSL1180-NX1 constructs, as the enzyme recognises two restriction sites, forming two distinct DNA fragments with identifiable base pair lengths (5370 and 3227 bp), shown in figure 3.5A. DNA plasmids were incubated at 37 °C for 1.5 h (full-length plasmid) or 15 min (intermediate plasmid) with the reagents listed in table 2.1. The digested DNA fragments were loaded onto an agarose gel and electrophoresed to analyse DNA patterns described in section 2.2.1.9.

Reagents	**Volume**
DNA (1-2 µg)	5 µL
dH_2O	2 µL
Buffer	1 µL
BSA (10 x)	1 µL
Enzyme (5-10 U)	1 µL

Table 2.1. Restriction DNA digest reagents.

2.2.1.9 Agarose gel electrophoresis - DNA analysis

DNA plasmids were digested using the restriction endonucleases listed in table 3.10 and analysed by agarose gel electrophoresis. 1 % (w/v) agarose gels were prepared by dissolving an appropriate amount of agarose in TAE (1 x) buffer before heating in a microwave oven for (1-2 min). The dissolved agarose solution was cooled at RT for 5 min before the addition of 0.1 µg/mL ethidium bromide (EtBr). A gel tray was set up according to the instructions provided by the manufacturer (Bio-Rad). The agarose EtBr solution was poured into the tray and allowed to cool at RT for the gel to set. The agarose gel tray was placed into a Bio-Rad tank filled with 1x

TAE to allow for the current to pass through. DNA samples were mixed with an equal volume of DNA loading buffer (2 x) and added to the wells alongside a 1 kb Plus DNA ladder (Invitrogen). Gels were electrophoresed for 30-45 min at 100 V or until the dye had migrated to the end of the gel. Agarose gels containing migrated DNA was visualised under UV light using a trans-illuminator Red™ SA – 1000 (Alpha Innotech). DNA samples were compared with the known 1 kb Plus DNA ladder.

2.2.2 Mammalian cell culture

2.2.2.1 Human Embryonic Kidney (HEK) 293 cell culture

Human Embryonic Kidney (HEK) 293 cells were routinely cultured in CellStar® cell culture 75 cm^2 flasks containing complete Dulbecco's Modified Eagles Medium (cDMEM) in a 37 °C, 5 % CO_2 incubator (Thermo Scientific). HEK293 cells were passaged every 72-96 h or until cell density reached 80-95 % confluency. Cells were washed twice with 10 mL 0.9 % saline, before harvesting. The cell suspension was mixed to disrupt any cellular aggregates before counting the cells on a haemocytometer. A glass coverslip was fixed to the haemocytometer under determined counting chambers (4 x 4) with a volume of 1 x 10^{-4} mL. The average cell count was multiplied by 1 x 10^4 to determine cell density (cells / mL) before pelleting the known amount of cells at 1000 x *g* for 5 min. The HEK293 cell pellet was resuspended in a volume adjusted to 1 x 10^6 cells/mL and mixed with 20 mL pre-warmed (37 °C) cDMEM before incubating the flasks.

2.2.2.2 Heterologous hRyR2 expression

Two transfection methods were routinely used to express hRyR2 protein in HEK293 cells which are discussed in detail in section 2.2.2.3. Briefly, the calcium phosphate ($CaPO_4$) method generated increased protein expression valuable for protein biochemical and biophysical assays. However due to increased hRyR2 expression HEK293 cytotoxicity was high and was therefore not ideal for cellular assays. Alternatively, the Effectene transfection method was used in studying the function of hRyR2 in a cellular environment. The Effectene method provides increased transfection efficiency and reduces cell cytotoxicity, ideal for confocal microscopy fluorescent based imaging in HEK293 cells, described in chapter 4.2.2.1.

2.2.2.3 Calcium phosphate-mediated transfection

HEK293 cells were seeded at a density of 1.5 x 10^6 cell/mL into CellStar® 100 x 20 mm Greiner bio-one plates which were incubated for 24 h at 37 °C, 5 % CO_2 prior to transfection. A DNA mix, containing full-length pcDNA3-eGFP-hRyR2 DNA 12 µg/plate, 124 mM $CaCl_2$ and bottled dH_2O was prepared as stated in table 2.2 and ready-made 2x HEPES-buffered saline (HBS) was pre-warmed to 37 °C in a water bath.

HEK293 transfection mixture				
	Reagents	**[Stock]**	**Required amount**	**Volume**
DNA mix	DNA	500 ng/µL	12 µg/plate	24 µL
	$CaCl_2$	1 M	124 mM	124 µL
	dH_2O			up to 500 µL
2x HBS	Equal volumes			500 µL

Table 2.2. Calcium-phosphate transfection mixture. An example of calcium-phosphate reagents and quantities required to transfect HEK293 cells on a 100 mm plate.

The DNA mix was added dropwise into the 2 x HBS solution while vortexing, followed by a 20 min incubation to initiate DNA precipitation. Fresh, pre-warmed cDMEM (20 mL) was added to each plate followed by the addition of the transfection mixture (1 mL added dropwise). Each plate was carefully mixed before returning the plates to the 37 °C, 5 % CO_2 incubator, for 48 h. Protein expression was enhanced by the addition of 2 mM sodium butyrate (NaB), described in chapter 3.3.3. The protocol was adjusted to replace the transfection media 24 h post-transfection with pre-warmed 20 mL cDMEM supplemented with 2 mM NaB. Plates were incubated for a further 24 h before assessing transfection efficiency by eGFP imaging, described in section 2.2.2.4, and cell harvesting for mixed-membrane preparations, outlined in section 2.2.3.1.

2.2.2.4 Determining transfection efficiency using eGFP imaging

The success and efficiency of hRyR2 transfection was determined by eGFP imaging. Plates were carefully mounted onto a 37 °C holding stage and were imaged using an Axiovert 200 microscope (Zeiss) with 10 x objective magnification. A field of view (FOV) was selected that contained a homogenous cell density using a bright-field (BF) light source. Subsequently, the same FOV was visualised using a xenon light source, applying peak excitation at ~ 488 nm, and a 520 ± 28 nm band pass filter to capture eGFP fluorescence, which confirmed hRyR2 protein expression. Image acquisition and processing were completed in AxioVision Rel. 4.3 that were subsequently saved as .tiff files. Transfection efficiency was calculated by the total sum of fluorescent green cells by the total cell count per FOV. Transfected HEK293 cells containing hRyR2 proteins (efficiency > 30 %) were harvested for downstream applications as described in section 2.2.3.1.

2.2.3 Protein Biochemistry

2.2.3.1 Preparation of hRyR2 mixed-membranes from HEK293 cells

HEK293 cells containing hRyR2 protein were harvested 48 h post-transfection. The transfection media was discarded and replaced with pre-heated (37 °C) fresh cDMEM (1 mL); cells were harvested by scraping each plate with a Fisherbrand™ cell scraper, collecting the cell suspension in a 50 mL falcon tube. The aforementioned process of collecting cells from plates was repeated twice to ensure maximal cell harvest. The cell suspension was pipetted to form a homogenous solution that contained no cellular clumps to improve cell count, described in section 2.2.2.1. HEK293 cells were isolated by centrifugation at 1000 x *g* for 5 min RT, before incubating the pellet on ice. Cells were lysed by the addition of hypo-osmostic buffer (1 mL/10^6 cells), containing one protease inhibitor tablet per 50 mL of buffer, which was stored at 4 °C. The lysed HEK293 cell suspension was homogenised in a 30 mL glass homogeniser on ice before aliquoting 15 mL into 50 mL falcon tubes. The aliquots were further homogenised through a 23 G needle (10 strokes) performed by a purpose built homogeniser constructed by Richard Montgomery (Montygeniser) to ensure complete cell lysis. Cell debris (organelles) was removed by centrifugation (2,700 rpm, 4 °C for 15 min) in an Allegra 6R centrifuge (Beckman Coulter). The supernatant containing the mixed-membrane

preparation was isolated by a further centrifugation step (28,000 rpm, 4 °C for 1 h) using a Optima XPN-100 ultracentrifuge (Beckman Coulter). The microsomal pellet was resuspended in solution C (0.4 M sucrose and 20 mM HEPES) at 20 µL/10^6 cells and homogenised in a 3 mL glass homogeniser. The mixed-membrane preparation was quantified by microBCA protein assay, described in section 2.2.3.2 before freezing 4 mg aliquots in liquid nitrogen and storing at – 80 °C.

2.2.3.2 MicroBCA – Quantification of protein concentration

The colourimetric BCA assay mix is a highly sensitive detection reagent that forms a purple-coloured reaction when Cu^{2+} are reduced by protein in an alkaline environment (Smith *et al.,* 1985), which exhibits a strong linear absorbance directly proportional with increasing protein concentration. Mixed-membrane preparations were quantified by a Thermo Scientific™ Pierce™ Micro BCA™ protein assay kit (Fisher Scientific). Protein standards were prepared from a 2 mg/mL bovine serum albumin (BSA) stock (10, 20, 50, 100, 200, 500 µg/mL) and the BCA assay mix containing Reagent A, Reagent B and Reagent C combined in a 50:48:2 ratio, respectively. The mixed-membrane preparations were diluted in bottled dH_2O (1:50, 1:100, 1:200). The dilutions were added to 96-well plates in duplicates of 100 µL alongside BSA standards (100 µL). The BCA assay mix was added into all wells containing protein samples which were incubated for 20 min in a dark area. A multiskan EX spectrophotometer (Labsystems) was set at absorbance 595 nm (Abs_{595}) to quantify protein concentration. A standard curve was generated from the known BSA protein concentrations and used to determine the mixed-membrane concentrations by linear regression, shown in figure 2.1. A typical mixed-membrane protein yield containing hRyR2 from 100-150 x 10^6 cells harvested 48 h post-transfection was approximately 10-20 mg.

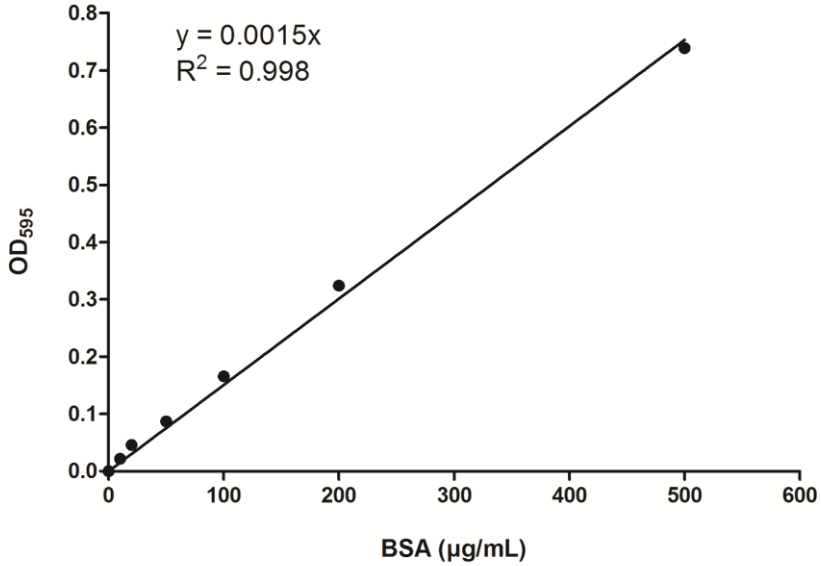


Figure 2.1. Linear regression analysis of the relationship between BSA concentration and absorbance at 595 nm. Diluted mixed-membrane protein samples (1:50, 1:100, 1:200) were estimated from the standard curve.

2.2.3.3 Sodium dodecyl sulfate (SDS) - Polyacrylamide gel electrophoresis (PAGE)

hRyR2 proteins were separated on a discontinuous SDS-PAGE to assess protein expression by western blot, described in sections 2.2.3.4 and 2.2.3.5. Dissociation of homotetremeric hRyR2 channels to monomers (molecular weight 565 kDa) by SDS ensured proteins were denatured and coated in negative charge for electrophoresis. A 5 % (v/v) acrylamide separating gel was prepared according to table 2.3 to resolve the high MW monomers. The polyacrylamide gel mixture was poured into the gel casing (Bio-Rad) and layered with bottled dH_2O. The ammonium persulfate (APS) and TEMED initiated polymerisation, the polyacrylamide mixture was incubated at RT for 20 min to allow the gel to set. The dH_2O was removed from the separating gel and replaced with 5 % stacking gel prepared as stated in table 2.4, followed by the insertion of a pre-set 10 lane comb. The mixed-membrane preparation containing hRyR2 protein (100 µg) was prepared according to table 2.5, incubating the samples at 42 °C for 30 min.

Reagent	Volume
dH_2O	12.16 mL
40 % bis-Acrylamide	2.5 mL
Tris 1.5 M pH 8.8	5 mL
SDS 10 % (w/v)	160 µL
APS 10 % (w/v)	160 µL
TEMED	20 µL
Total	**20 mL**

Table 2.3. 5 % SDS-PAGE separating gel reagents.

Reagent	Volume
dH_2O	4.73 mL
40 % bis-Acrylamide	583 µL
Tris 0.5 M pH 6.8	1.25 mL
SDS 10 % (w/v)	50 µL
APS 10 % (w/v)	50 µL
TEMED	8.3 µL
Total	**6.67 mL**

Table 2.4. 5 % SDS-PAGE stacking gel reagents.

Reagents	Volume
MM Sample (100 µg)	X µL
6 x SDS sample buffer	6 µL
dH_2O	up to 30 µL

Table 2.5. Mixed-membrane SDS loading preparation for SDS-PAGE.

Gels were loaded into gel tanks (Bio-Rad) and topped up with 1 x SDS running buffer. Samples (30 µL) were loaded in pre-cast lanes alongside a 20 µL kaleidoscope protein ladder (Bio-Rad). Electrophoresis was performed at constant current starting at 20 mA, for the first 30 min, before increasing to 30 mA until the myosin (pre-stained protein ladder 216 kDa) migrated to the bottom of the gel (~ 3-4 h). The SDS-gel containing the separated proteins was transferred to a PVDF membrane for Western blot analysis, section 2.2.3.4.

2.2.3.4 Western blot – Transfer of proteins onto a PVDF membrane

Western blotting was performed using the iBlot® Dry blotting system (Invitrogen). Proteins were separated on SDS-PAGE gels and transferred onto a ready-made iBlot Gel Transfer stack (regular or mini), containing the polyvinylidene difluoride (PVDF) membrane. The iBlot was set up as described in the manufacturer's instructions. The anode stack (Bottom) was unsealed and placed into position, aligning with the gel barriers. The SDS-gel was transferred to the anode stack containing the PVDF membrane and a pre-soaked iBlot filter paper was placed on top of the SDS-gel. The cathode stack (Top) was unsealed and placed onto the filter paper with the electrode side facing up, air bubbles were removed using the blotting roller. A disposable sponge was aligned with the metal contact before the lid was secured shut. The proteins were transferred by selecting program 3, for 13 min at 20 V. Once completed, the PVDF membrane containing transferred proteins was placed in blocking buffer overnight.

2.2.3.5 Western blot – Enhanced Chemiluminsescence (ECL) detection

hRyR2 proteins were transferred to a PVDF membrane using the method described in section 2.2.3.4 and were incubated in 5 % (w/v) non-fat dried milk protein (Marvel) in 0.01 % TBS-T buffer (blocking buffer) overnight at 4 °C. The PVDF membrane was washed three times using 20 mL TBS-T buffer for 5 min at RT. A GFP-specific (B-2) SC-9996 mouse monoclonal IgG_{2a} primary antibody, section 2.1.6.1, raised against the N-terminal RyR eGFP tag (amino acids 1-236), was diluted 1:5000 (v/v) in 2.5 % blocking buffer and applied to the membrane for 1.5 h at RT. The membrane was washed again three times using 20 mL TBS-T buffer for 5 min at RT. A horseradish peroxidase (HRP)-conjugated anti-mouse secondary antibody (produced in goat) was diluted 1:5000 (v/v) in 2.5 % blocking buffer before applying to the membrane that was subsequently incubated for a further 1.5 h at RT. The membrane was washed (3 x 5 min RT) before being visualised by enhanced chemiluminsescence (ECL) detection (GE Healthcare). The HRP catalyses the oxidation of luminol into a reagent which emits light (428 nm), the ECL kit increases light emission more than 1000-fold from the presence of enhancer molecules, including phenols (Thorpe *et al.,* 1985). Therefore the location and amount of light produced directly correlated with the amount of protein on the membrane. The PVDF membrane was placed into a cassette containing a plastic

folder, ECL reagent 1 and reagent 2 were mixed in equal volumes before applying to the cassette containing the membrane. An x-ray film (Hyperfilm, GE Healthcare) was aligned with the cassette in the dark room and was exposed for 2-5 min. The x-ray film was developed using a Compact X4 X-OGraph imaging system.

2.2.3.6 Quantification of protein expression by Western blot Densitometry

WT and mutant RyR2 protein expression was determined by Western blot densitometry analysis (outlined in chapter 3) and was used to quantify the relative amounts of RyR2-membrane preparations for the [^{3}H] ryanodine binding assay described in chapter 4. Western blots were scanned into a computer using a Canon CanoScan LiDE 100, achieving 300 dpi. ImageJ, an open source image processing program (http://imagej.net/Welcome), was used to perform densitometry measurements on exposed films. The integrated density tool (ROI area and mean grey value) was used to analyse bands, figure 2.2. A lower integrated density value, determined by a darker ROI, indicated greater protein expression. The area of ROIs remained constant for all band measurements with a working example outlined in section 2.2.3.6.1. To compensate for the differences in RyR2 expression levels, integrated densitometry values were calibrated to 100 µg WT hRyR2 mixed-membrane to ensure that equivalent quantities of mutant and WT RyR2 were added for each [^{3}H] ryanodine binding assay described in chapter 4.2.4.

2.2.3.6.1 Western blot densitometry analysis example

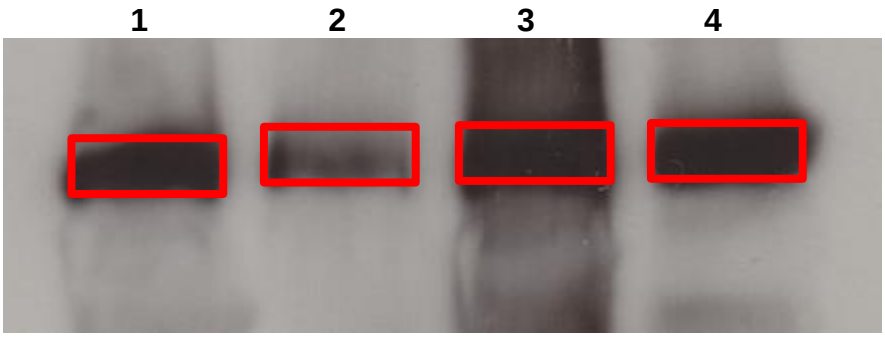


Figure 2.2. Representative Western blot densitometry analysis. (1) WT hRyR2 and representative mutant RyR2 bands (2, 3 and 4). Region of interest (ROIs) are highlighted by red boxes.

ROI		IntDen	Normalised IntDen		Relative Volume (µL)
1	WT hRyR2	**51.23**	51.23/51.23	1	10
2	Mutant #1	**86.83**	86.83/51.23	1.694	16.94
3	Mutant #2	**45.51**	45.51/51.23	0.888	8.88
4	Mutant #3	**45.74**	45.74/51.23	0.892	8.92

Table 2.6. Representative densitometry analysis of WT and mutant mixed-membrane preparations. Mutant hRyR2 preparations were adjusted and normalised to compensate for the differences in hRyR2 expression levels as shown in figure 2.2.

2.2.3.7 Purification of hRyR2 from mixed-membrane preparations

hRyR2 protein was purified from mixed-membrane preparation (12 mg) using continuous sucrose density centrifugation. Aliquots containing 4 mg hRyR2 mixed-membrane (3 x 4 mg aliquots) were thawed on ice. A 10 % : 5 % CHAPS : PC stock was prepared in 5 mL bottled dH_2O, and stirred for 2 h at 4 °C. The mixed-membrane preparation was diluted at a 1 : 4 ratio with 0.4 M KCl and centrifuged at 100,000 x *g* for 30 min at 4 °C using an Optima™ MAX-XP ultracentrifuge (Beckman Coulter). The mixed-membrane pellet (12 mg) was resuspended at 3 mg/mL, adding 3756 µL solubilisation buffer containing 4 µL (1:1000 ratio) protease inhibitor cocktail through a 23 G needle (10 strokes). Once resuspended, the 10 % CHAPS/PC stock was added at a final detergent concentration of 0.6 % (240 µL) and the microsomal suspension was solubilised for 1 h at 4 °C with continuous stirring. The insoluble material from the lysate was removed by centrifugation (14,000 x *g* for 30 min at 4 °C) using an Eppendorf 5417R centrifuge. The supernatant containing the solubilised hRyR2 protein and other cellular components was carefully layered onto one sucrose gradient, described in section 2.2.3.7.1. Solubilised hRyR2 was purified from other membrane proteins and cellular components by continuous density gradient centrifugation using a SW 32.Ti swing out rotor at 100,000 x *g* for 16-18 h at 4 °C.

2.2.3.7.1 Preparation of Sucrose gradient

Gradient buffer was prepared as outlined in section 2.1.6, which was added to three prepared sucrose concentrations (40, 25 and 5 %) according to table 2.7.

Sucrose Concentration % (w/w)	**Sucrose (g)**	**Gradient buffer (g)**
40	7.2	10.8
25	11.25	33.75
5	2.25	42.75

Table 2.7. Preparation of sucrose gradients. The stated amounts form two sucrose gradients.

Falcon tubes containing sucrose and gradient buffer were placed on rollers to mix for > 1 h at 4 °C. Sucrose gradients were prepared in Ultra-Clear™ centrifuge 25 x 89 mm tubes fed from a two chamber pump shown in figure 2.3. The first layer, containing 5 mL 40 % sucrose buffer, acting as a cushion, was added manually. Before the addition of the 25 % sucrose (25 mL), the 5 % sucrose (40 mL) was passed through the inter-connecting chamber to ensure smooth transition and to prevent bubble formation. The stirrer was switched on and the inter-connecting tap was opened, which was immediately followed by switching the pump on to initiate mixing of the two sucrose buffers as detailed in figure 2.3. The buffers were loaded into the tubes layering the continuous sucrose gradient. To ensure sufficient capacity for the solubilised hRyR2 protein, 4-5 mL was left free on top of the gradient. Both gradients were carefully stored at 4 °C until required.

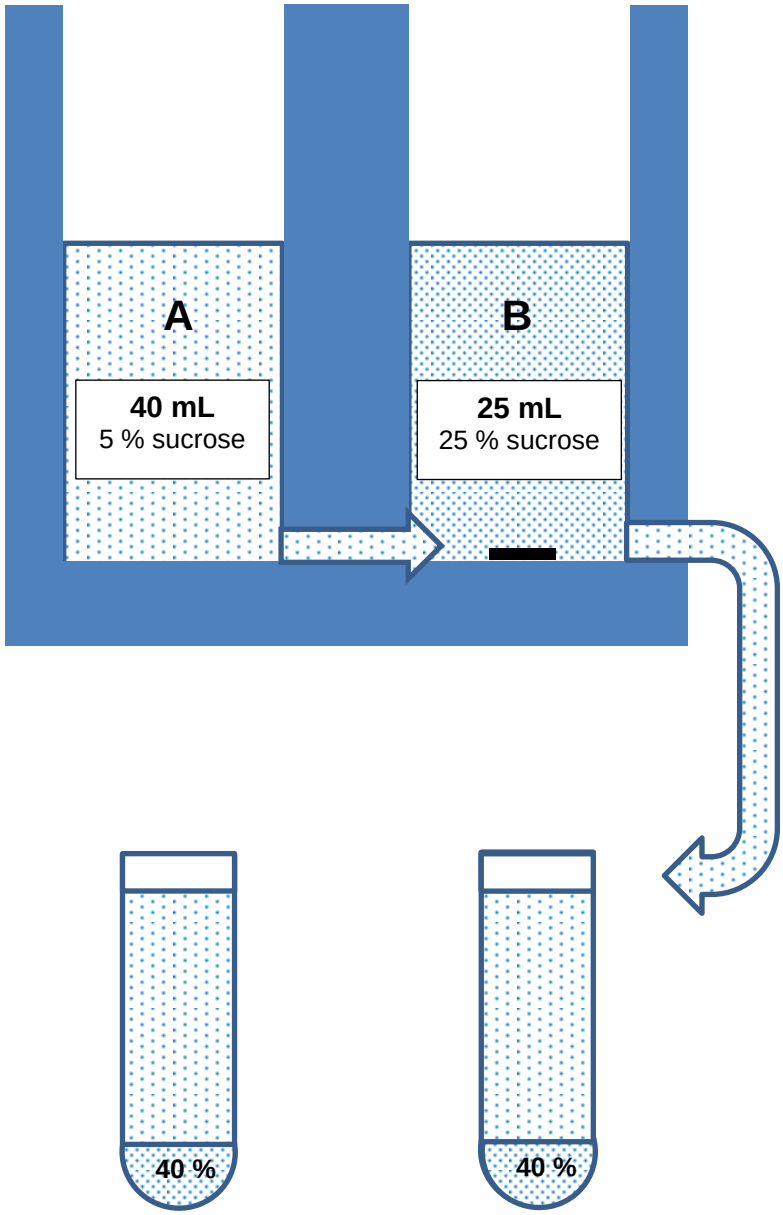


Figure 2.3. Schematic representation depicting the preparation of a sucrose gradient for hRyR2 purification. 40 mL of 5 % sucrose was added in chamber A, allowing sucrose to pass through the inter-connecting chambers to prevent bubble formation. The residual flow-through of 5 % sucrose in chamber B was transferred back into chamber A before adding 25 mL of 25 % sucrose into chamber B. The flow rate was set to 4, the inter-connecting tap was opened, the stirrer in chamber B and pump was turned on to allow the solutions to mix which were fed into the tubes forming a sucrose gradient.

2.2.3.7.2 Fraction collection

Following centrifugation, the gradient tube containing the solubilised hRyR2 protein was carefully placed in a fraction recovery system (Beckman) that was connected to a P-1 pump (Pharmacia Biotech), see figure 2.4. The fraction recovery system pierced the tube to allow the gradient to flow into 15 (~ 1.5 mL) fractions, performed at a flow rate setting of 4 (2 mL/min), for 45 s.

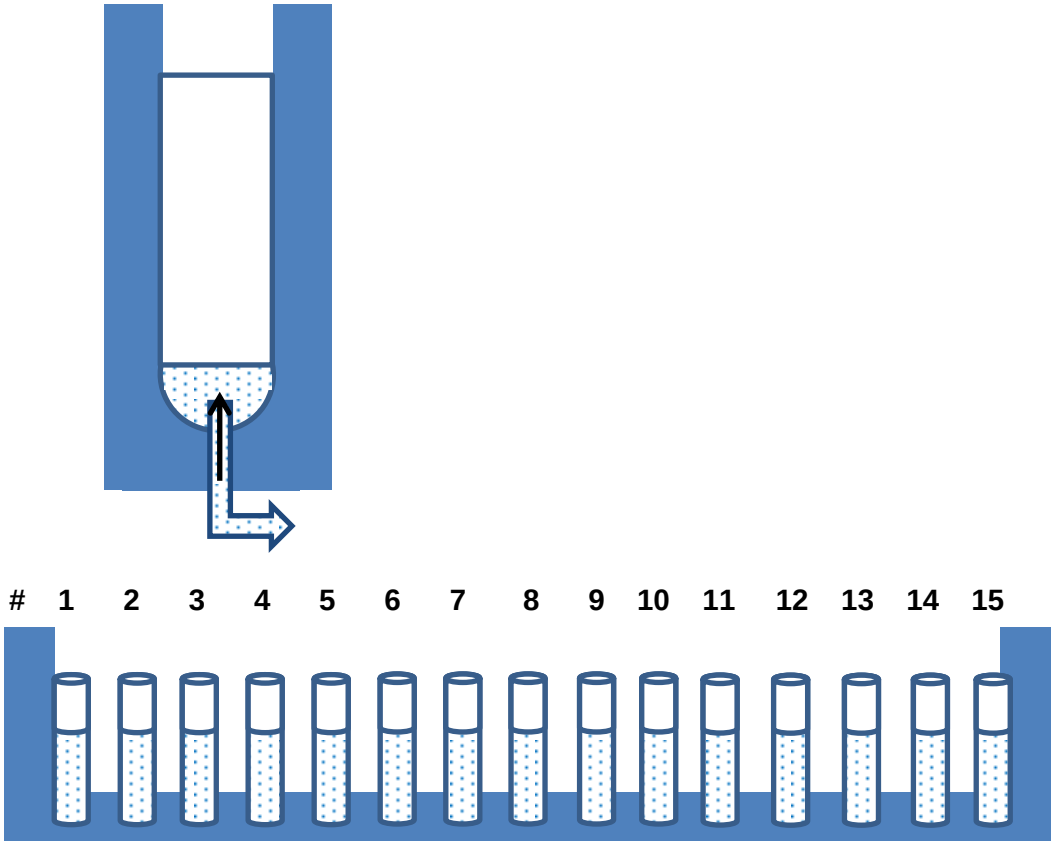


Figure 2.4. Schematic diagram of sucrose gradient fraction collection. Tubes were placed in a fraction recovery system containing a pierced outlet. Fractions 1-15 were manually collected in 45 s intervals using a flow rate setting of 4 (2 mL/min).

Sucrose concentration was measured by the addition of 10 µL fractions to a 0-50 % sugar refractometer obtained from Bellingham & Stanley Ltd. Early purification studies using [^{3}H] ryanodine binding assays, described in chapter 4.1.3, determined the highest proportion of RyR protein in fractions containing 27-29 % sucrose (Campbell *et al.,* 1987; Lai *et al.,* 1988; Hymel *et al.,* 1988). The total concentration of sucrose fractions (1 – 15) from hRyR2 purifications (*n*=29) are represented in

figure 2.5. Typically, fractions 4 (32.9 %), 5 (29.1 %) and 6 (25.8 %), highlighted in blue, containing purified hRyR2 were aliquoted (50 µL) and flash frozen in liquid nitrogen before storing at – 80 °C.

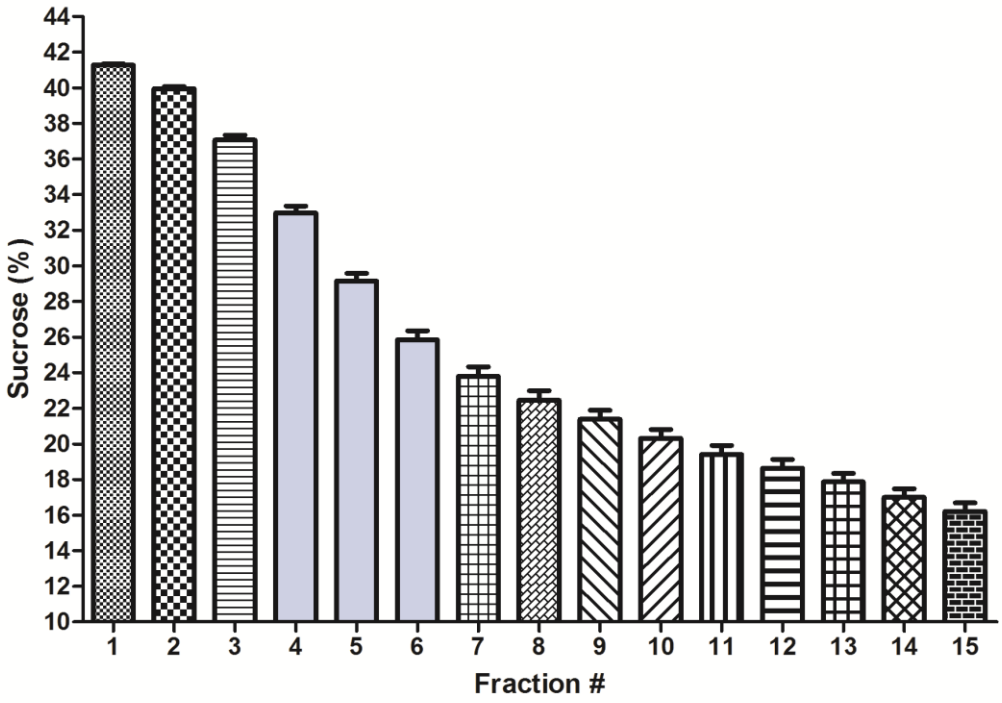


Figure 2.5. Sucrose gradient fraction collections. The sucrose gradient fractions from 1 to 15 were collected, and the percentage of sucrose within fractions was measured by a refractometer. From the total hRyR2 purifications (*n* = 29) the highlighted sucrose fractions, 4, 5 and 6, corresponding to ~ 32 %, ~ 29 % and ~ 26 % sucrose respectively, were routinely aliquoted (50 µL) and frozen in liquid nitrogen stored at – 80 °C and, used for single-channel bilayer experiments.

2.2.4 Electrophysiology - Single-channel Experiments

2.2.4.1 Warner Instruments workstation

All single-channel experiments were completed using the Planar Lipid Bilayer (BLM) workstation from Warner Instruments. Briefly, experiments were completed inside a FC series Faraday cage on a vibration isolation table (Kinetic Systems) to minimise environmental, mechanical and user noise. The components of the single-channel set up, including the cup and block described in section 2.2.4.1.1, were placed on a SPIN-2 bilayer stirplate integrated with a SUN*Stir* rack-mount controller and a SUN-1 halogen lamp.

2.2.4.1.1 Planar lipid bilayer workstation set up

The *in vitro* electrophysiology bilayer technique was first used to study ion channel properties by Miller and Racker, and Alvarez (Miller and Racker, 1976; Alvarez, 1986). A cup and block, depicted in figure 2.6, are two important entities of the set up that allow the study of ion channels in a well-controlled environment. The cup, corresponding to the *cis* chamber, has a cylindrical 500 µL compartment with a centrally located 200 µm aperture. The cup mounted into a pre-casted block establishes a 1000 µL *trans* compartment. Together, the cup and block form two fluid filled chambers that are connected by a small aperture where a planar lipid bilayer was formed, illustrated in figure 2.7. Each chamber was connected via salt bridges which were thin 1 mm capillary tubes containing 3 M LiCl fixed in 2 % w/v agar. The end of each bridge was bathed in the experimental salt solution and a well containing 200 µL 3 M LiCl. These additional wells also contained Ag/AgCl coated electrodes that connected the remainder of the electronic circuit described in section 2.2.4.1.2.

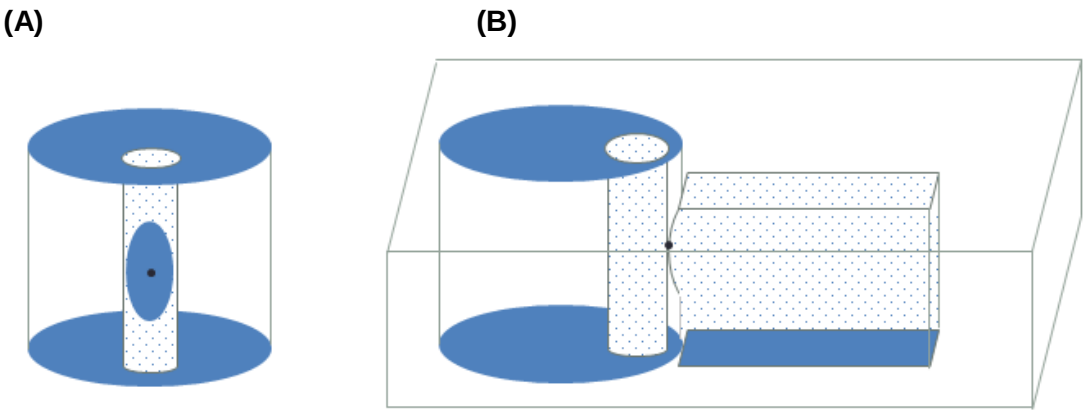


Figure 2.6. Schematic representation of (A) the styrene cup '*cis*' chamber depicting the 200 µm aperture as a black dot and (B) the copolymer block '*trans*' chamber mounted with the cup.

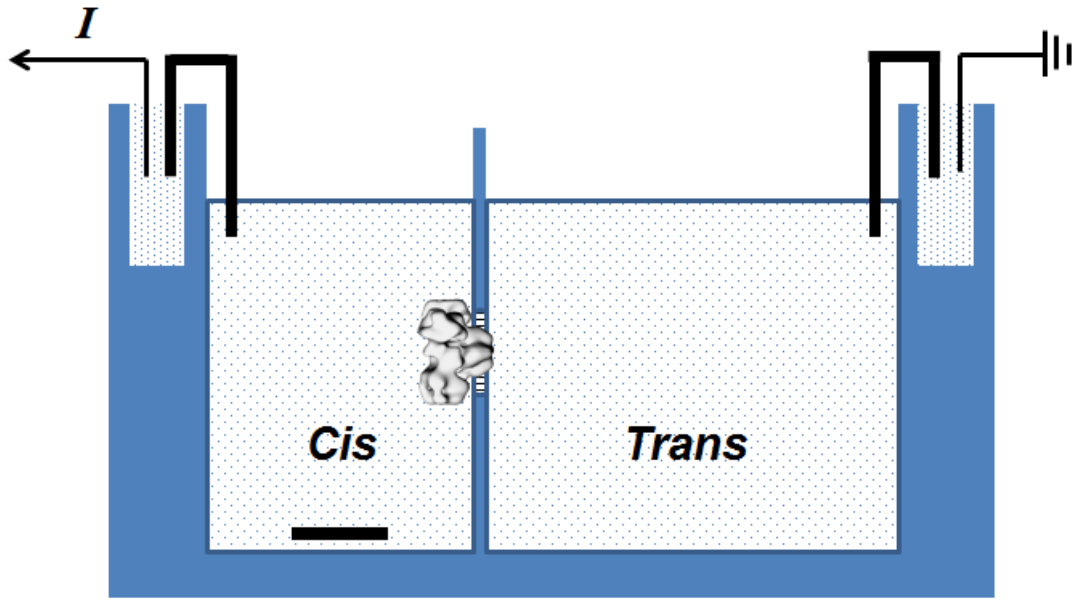


Figure 2.7. Schematic representation of the Planar Lipid Bilayer set up. The two fluid filled chambers, the cup (*cis*) and block (*trans*) are connected by a 200 µm aperture forming two fluid filled chambers. The stirring of the teflon coated magnetic stir-bar, placed at the bottom of the *cis* chamber, facilitated channel incorporation. A representative RyR2 channel is incorporated into a lipid bilayer membrane (not to scale), with the cytoplasmic domain facing the *cis* chamber. Salt bridges and Ag/AgCl electrodes connected the circuit with the head amplifier so that current flowing through the membrane via RyR2 was measured and recorded.

2.2.4.1.2 Electronic Bilayer set up

The electrodes were connected to a head amplifier that held the *trans* chamber at ground relative to the *cis* chamber. The Warner Bilayer Clamp amplifier (BC-535) was used to voltage clamp the *cis* chamber that subsequently dictated the flow of cations. At positive holding potentials (+ mV) cations flowed in the non-physiological direction, from *cis* (cytosol) → *trans* (lumen), and at negative holding potentials (- mV) cations flowed in the physiological direction, from *trans* (lumen) → *cis* (cytosol), as RyR2 incorporates into the bilayer with a fixed orientation outlined in section 2.2.4.4. The operational amplifier transduced the current flow through the bilayer into an analogue voltage signal that was passed through a 5 kHz and 1 kHz multi-step low pass 8-pole Bessel filter (LPF-8). Single-channel data filtered at 5 kHz was used for analysis, whereas data passing through the 1 kHz filter was used for real-time visualisation of current flow in an oscilloscope window. The signal was finally passed through an analog to digital converter (ADC), where the Bruxton software suite (Acquire and Review) was used to record and visualise the data. The QuB software, discussed in detail in chapters 5 and 6, was used for data analysis.

2.2.4.2 Bilayer formation

2.2.4.2.1 Phosphatidylethanolamine (PE) lipid preparation

PE lipid (1,2-dioleoyl-*sn*-glycero-3-phosphoethanolamine, 18:1 (9-Cis), DOPE) was resuspended in chloroform at 50 mg/mL and stored at – 80 °C. The chloroform containing the dissolved PE lipid (10 µL) was evaporated using a stream of nitrogen gas under constant low pressure. The dried lipid was resuspended in 14.5 µL *n*-decane at a final concentration of ~ 33 mg/mL for use in all experiments outlined in chapters 5 and 6.

2.2.4.2.2 Priming the *cis* chamber aperture

Prior to formation of a bilayer, the aperture was primed with excess PE lipid. A bolus of lipid was applied to the aperture and was forced through under pressure. Priming of the *cis* chamber was repeated twice, allowing the lipid to dry between each prime, which ensured that the hole had adequate lipid to facilitate bilayer formation.

2.2.4.2.3 Painting a bilayer and measuring lipid bilayer formation

PE lipid was ‘painted’ across the hole by gentle upward strokes using a modified 3 mL plastic Pasteur pipette as a painting stick shown in figure 2.8.

(A)



(B)



Figure 2.8. A modified Pasteur pipette used as a ‘painting’ stick. A sharp scalpel was used to carve the decanting-end of the pipette to form a curved sharp tip. (A) The tip, highlighted by a black circle, was used to ‘paint’ the 200 µm aperture and (B) the convex outer end, indicated by a black line, was used to prime the aperture with excess lipid.

Lipid was applied to the *cis* chamber side until a change in membrane capacitance was observed. Capacitance, measured in picofarads (pF), was used to assess bilayer formation as the capacity of the membrane to store charge correlated directly to the surface area and thickness of the lipid membrane. Plateau-Gibbs border suction and van der Waals attractions contributed to the spontaneous thinning of the lipid film (Williams, 1994). The spontaneous thinning of the lipid into a bilayer was characterised by an increased surface area that was observed by increased membrane capacitance, which was visualised on the oscilloscope depicted in figure 2.9.

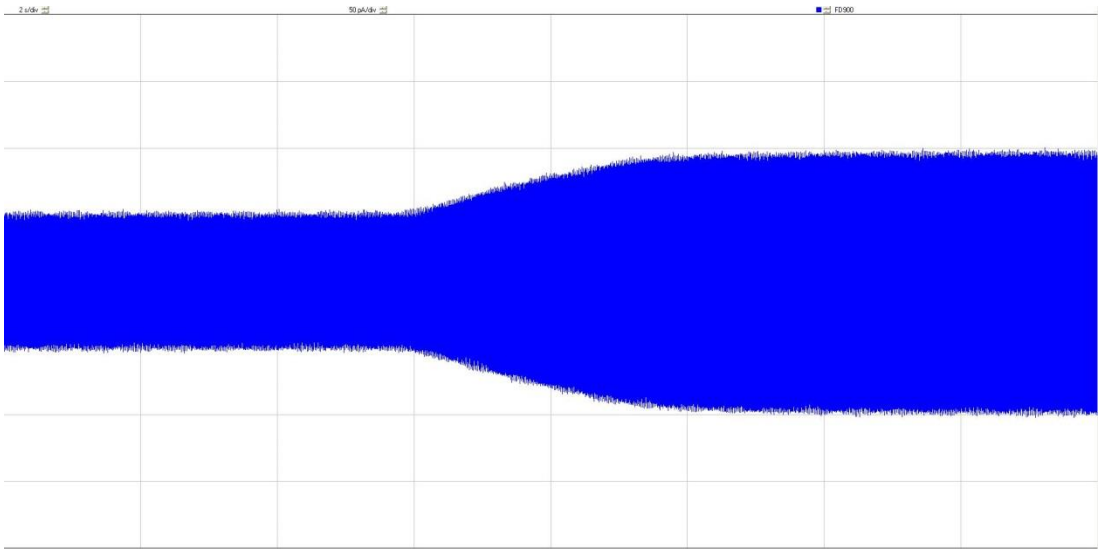


Figure 2.9. Bilayer formation. Spontaneous thinning of lipid to form a bilayer, represented by an increase in membrane capacitance. The ‘CAP TEST’ function depicts the blue trace representing membrane capacitance in the oscilloscope window. Scale bar; 2 s/div and 50 pA/div.

Using the Warner Instruments BLM set up and a styrene cup (200 µm aperture), bilayer formation was confirmed when membrane capacitance ranged from 160-220 pF. High membrane capacitance (> 220 pF) corresponded to a bilayer with a large surface area that was fragile and prone to breaking, furthermore these membranes had a higher probability of multiple channel incorporations. Conversely, low membrane capacitance (< 160 pF) reduced the overall probability of channel incorporation. Thus, membranes with values outside of the preferred capacitance range were terminated to enhance experimental efficiency.

2.2.4.2.4 Bilayer integrity

The success of a single-channel experiment was solely dependent on the stability and integrity of the bilayer. With experiments lasting up to one hour, forming a stable lipid membrane was essential for the long-term psychological and mental health of the user.

"*Planar bilayers can be incredibly frustrating. All of us who have worked with them have, at one time or another, been reduced to irrational acts of anger*."

Stephen H. White (Miller, 1986)

Following bilayer formation (membrane capacitance 160-220 pF) a holding potential of ± 100 mV was applied to challenge the membrane. At high voltages the bilayers stability and integrity was assessed. The incorporation of 'junk', detailed in section 2.2.4.3, or 'leaky' membranes were characterised by altered deflections in current baseline during membrane potential oscillation. A stable baseline ensured that a suitable bilayer was formed, establishing the foundation of a single-channel experiment.

2.2.4.3 RyR2 channel incorporation

Conditions were established to favour micelle fusion. An osmotic gradient was created between the *cis* and *trans* chambers by the addition of a 3 M KCl solution (2 x 100 µL) into the *cis* chamber. The 500 µL volume of the chamber was maintained by removing 2 x 100 µL following each subsequent salt addition. Once the osmotic gradient was established, purified recombinant hRyR2 protein preparation, typically 1-2 µL from fraction # 5, was added into the *cis* chamber. The *cis* solution and protein preparation were stirred, to facilitate micelle fusion, until a single channel was incorporated indicated by large fluctuations in current amplitude representative of channel gating depicted on the oscilloscope, illustrated in figure 2.10.

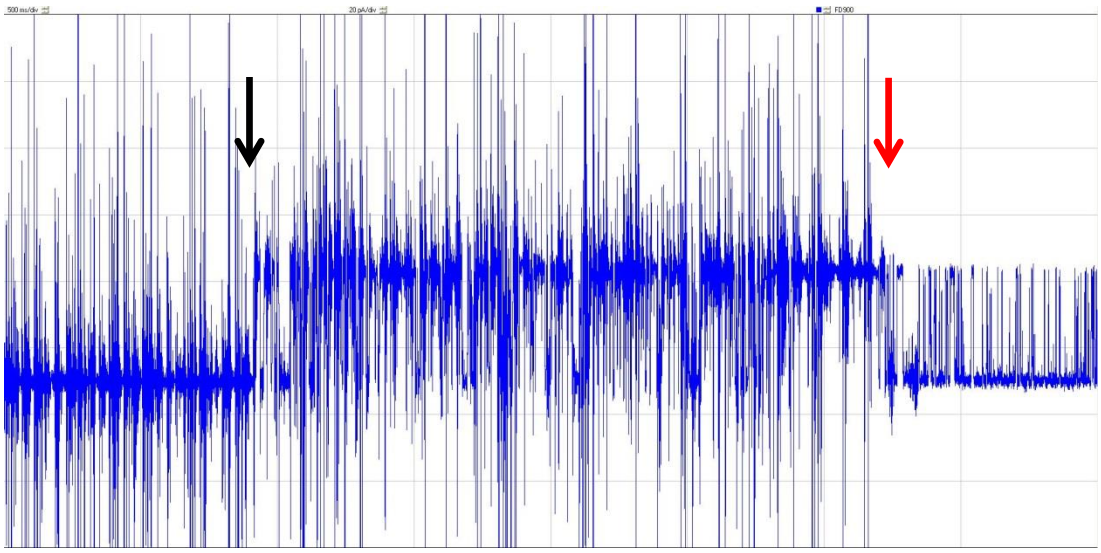
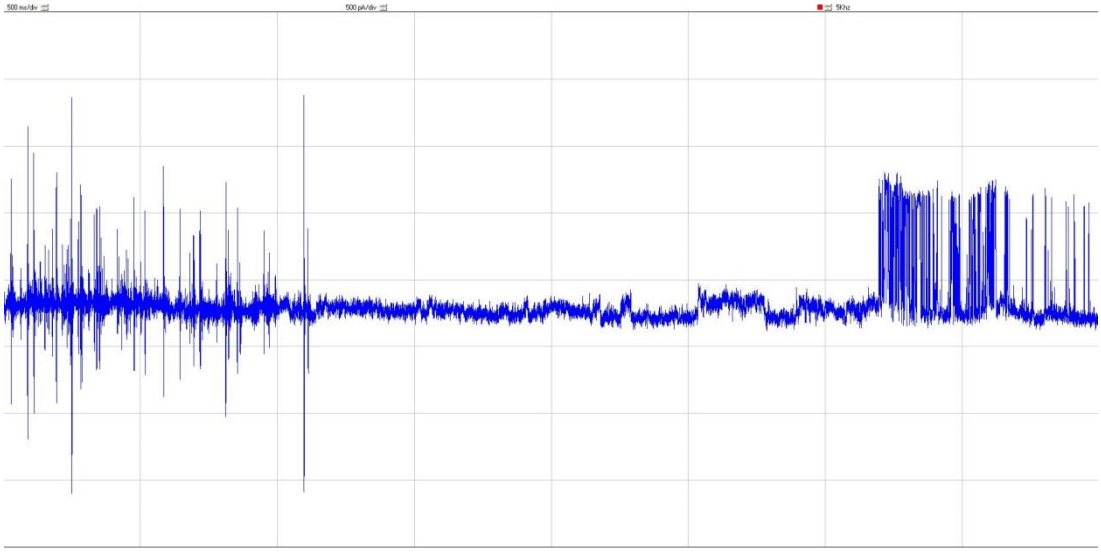


Figure 2.10. The incorporation of a single hRyR2 channel into a lipid bilayer. The oscilloscope depicts the inherent noise generated by stirring. RyR2 channel incorporation was indicated by large ~ 30 pA fluctuations from baseline (highlighted by the black arrow) with clear channel gating events observed when the stirrer was switched off (highlighted by the red arrow). The '*I*m' function displays the current across the bilayer depicted by the blue trace in the oscilloscope window. Scale bar; 500 ms/div and 20 pA/div.

On occasion, damaged proteins from the purification process or unknown foreign objects, termed 'junk', incorporated into the bilayer, depicted in figure 2.11. All experiments with 'junk' were terminated by breaking the bilayer and starting again, repeating the bilayer procedure from section 2.2.4.2.

(A)



(B)

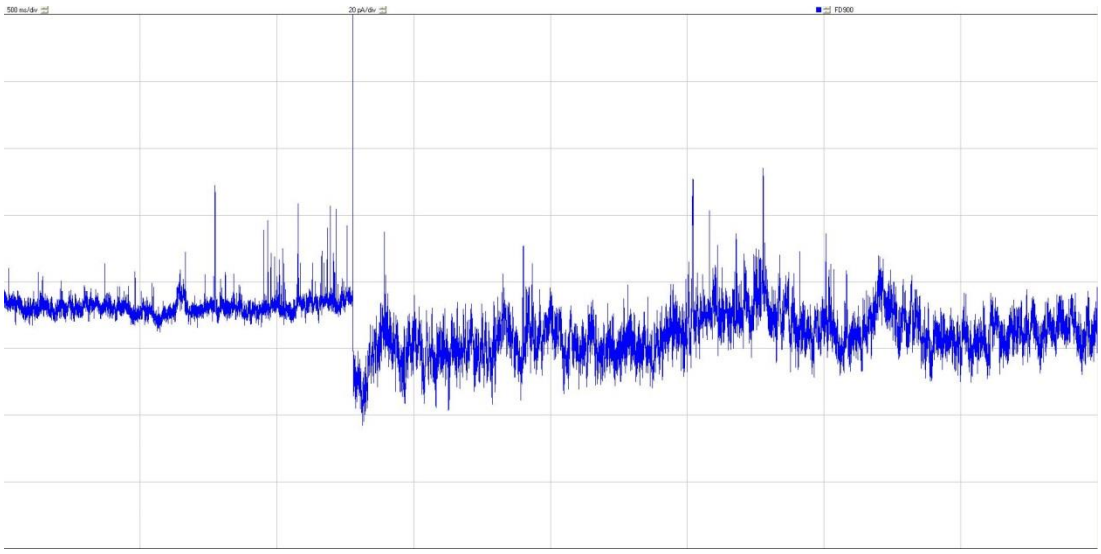


Figure 2.11. Incorporation of 'junk' into the bilayer. (A) Combination of junk and hRyR2 channel incorporated into the bilayer. (B) Junk represented by drastic spontaneous fluctuations in current flowing through the bilayer. Both (A) and (B) experiments resulted in bilayer termination.

2.2.4.4 RyR2 channel orientation

An important consideration of channel incorporation was the orientation of RyR2. Due to the structural asymmetry of the RyR2 molecule shown in figure 1.6, it is physically improbable that the large hydrophilic, cytoplasmic domain would cross the membrane in preference to insertion of the relatively smaller, hydrophobic, TM domain into the membrane. Therefore, channel incorporation into the planar bilayer is in a fixed orientation (Bannister *et al.,* 2015). When the purified hRyR2 protein is added to the *cis* compartment, the cytoplasmic side faces the *cis* chamber while the luminal side faces the *trans* chamber, as shown in figure 2.7. Evidence for RyR2 orientation within the bilayer has been established through cytosolic (*cis*) RyR2 activation and that interaction of blocking molecules with RyR2, such as, but not limited to, ryanodine, flecainide and large tetraalkylammonium (TAA) cations that are side-specific (Lindsay *et al.,* 1991; Tinker and Williams, 1993a; Tinker and Williams, 1993b; Mason *et al.,* 2012; Mukherjee *et al.,* 2012; Bannister *et al.,* 2015).

2.2.4.5 Chamber Perfusion

Upon channel incorporation, the *cis* chamber was immediately perfused using a dual perfusing manipulator, figure 2.12, set at a rate of 2.5 mL/min for 2 min. Perfusion ensured that the *cis* chamber solution was replaced 10 times (5000 µL exchange) with the experimental salt solution. Chamber perfusion ensured that the osmotic gradient and protein suspension was removed preventing further channel incorporation.

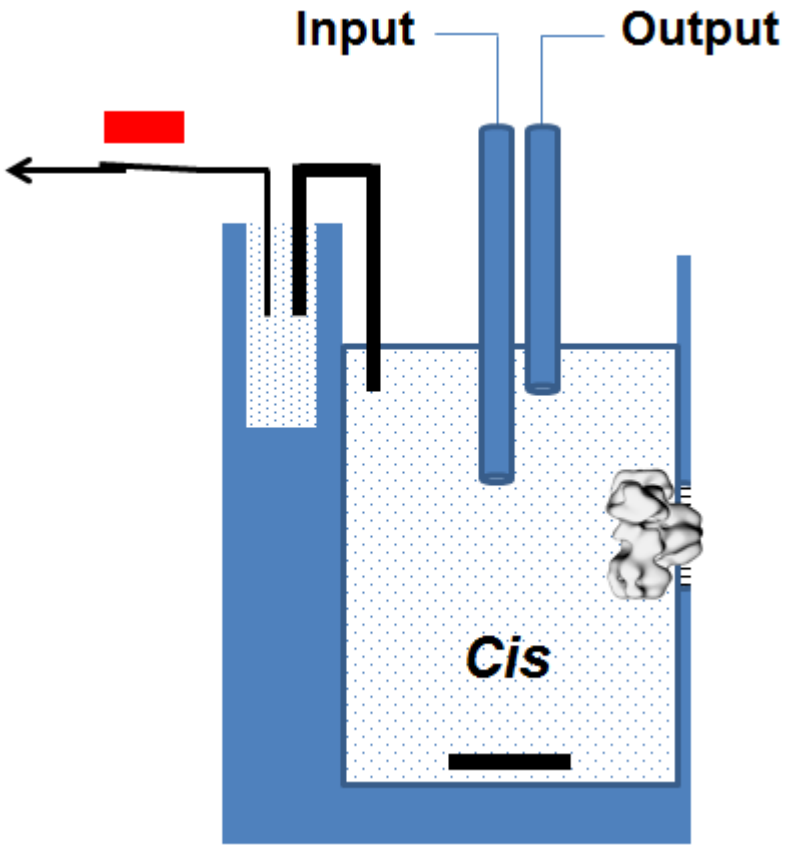


Figure 2.12. Dual perfusion manipulator. An input and output tube, set at different levels, was lowered to a specific point within the chamber. The addition of experimental salt solution occurred through the input while instantaneously excess 'waste' was removed from the output ensuring constant chamber volume. A magnet, indicated by a red rectangle, was placed over the reed switch to isolate the bilayer from the circuit.

2.2.4.6 Single-channel Experiments

Following successful channel perfusion, a range of experiments were completed detailed in chapters 5 and 6. All experiments were completed at room temperature, 20 ± 2 ˚C.

Chapter Three:

Construction and Expression of Selectivity Filter and Pore Helix mutant human RyR2 (hRyR2) channels

Construction and Expression of Selectivity Filter and Pore Helix mutant human RyR2 (hRyR2) channels

Chapter Three – Aims

A mechanism of hRyR2 gating is proposed to arise from interactions between the selectivity filter and pore helix, controlled by a potential hydrogen-bonding network. Before exploring molecular mechanisms occurring at the selectivity filter of hRyR2, structural components formed by residue interactions predicted to be important in channel gating were altered. This chapter describes molecular DNA mutagenesis and cellular biology techniques used to construct and express the proposed single-point hRyR2 mutations. The aims of this chapter were as follows:

- To construct six full-length hRyR2 mutants by site-directed mutagenesis (SDM) using a cassette based method detailed in section 3.2.1.

- To generate three alanine hRyR2 cDNAs, Y4813A, D4829A and Y4839A, to disrupt a proposed hydrogen-bonding network that is hypothesised to stabilise the selectivity filter during channel gating.

- To construct three conservative hRyR2 mutants, Y4813W, D4829E and Y4839W, to introduce residues with similar physicochemical properties that have the potential of forming a hydrogen-bonding network.

- To transfect the six mutant hRyR2 constructs in human embryonic kidney (HEK) 293 cells to ensure that the introduced missense point mutation did not affect protein expression.

3.1 - Introduction

3.1.1 A cassette-based strategy for constructing mutant hRyR2 channels – Site-directed mutagenesis

The manipulation of genetic code, i.e. targeting particular alterations such as mutation, insertion or deletion within DNA sequences has considerably improved, attributed to advances in molecular biology techniques. For example, site-directed mutagenesis (SDM), an *in vitro* procedure, is a common tool utilised to introduce point mutations within DNA templates in order to express desired mutant proteins for structure-function relationships, protein-protein interactions and binding domains of protein/active sites of enzymes for the last three decades (Carrigan *et al.,* 2011).

The full-length pcDNA3-eGFP-hRyR2 plasmid is approximately 21 kb, depicted in figure 3.2, however is unsuitable for polymerase chain reaction (PCR) amplification due to stochastic effects such as premature termination of DNA polymerase affecting product yield and efficiency of PCR. To overcome this challenge, George *et al* and Thomas *et al* constructed five hRyR2 DNA fragments spanning the entire length of the DNA sequence (George *et al.,* 2003; Thomas *et al.,* 2004). These DNA fragments were cloned into intermediate vectors, pSL1180 (Amersham Biosciences, UK), ultimately decreasing the base pair (bp) length of the new plasmid, enabling PCR amplification of the chosen region. These mutagenic cassettes have simplified and permitted the generation of point mutations along the hRyR2 sequence for structural and functional studies (George *et al.,* 2003; Thomas *et al.,* 2004).

3.1.2 Alteration of hRyR2 residues to test a proposed hydrogen-bonding network

The lack of detailed structural hRyR2 information, prompted the generation of the PFR hRyR2 analogy model based on KcsA (Welch *et al.,* 2004), whereby known gating mechanisms in KcsA (and other K^+ channels) can be used to test and refine the model. Comparing residues in KcsA involved in a network with those present at similar positions in the hRyR2 PFR model highlights the potential for a similar mechanism, as discussed in chapter 1.6. Residue D4829 in hRyR2 occupies an equivalent position in the selectivity filter signature sequence to D80 in KcsA and is

located at an ideal position to form hydrogen bonds with Y4839 and Y4813 analogous to W67 and E71 in KcsA, respectively. In further support, the Welch *et al* PFR hRyR2 analogy model indicates distances between Y4813-D4829 of ~ 2.5 and Y4839-D4829 of ~ 3.7 Å, illustrated in figure 3.1B, which are within the ideal range for hydrogen bond formation (Welch *et al.,* 2004; Hubbard and Haider, 2010).

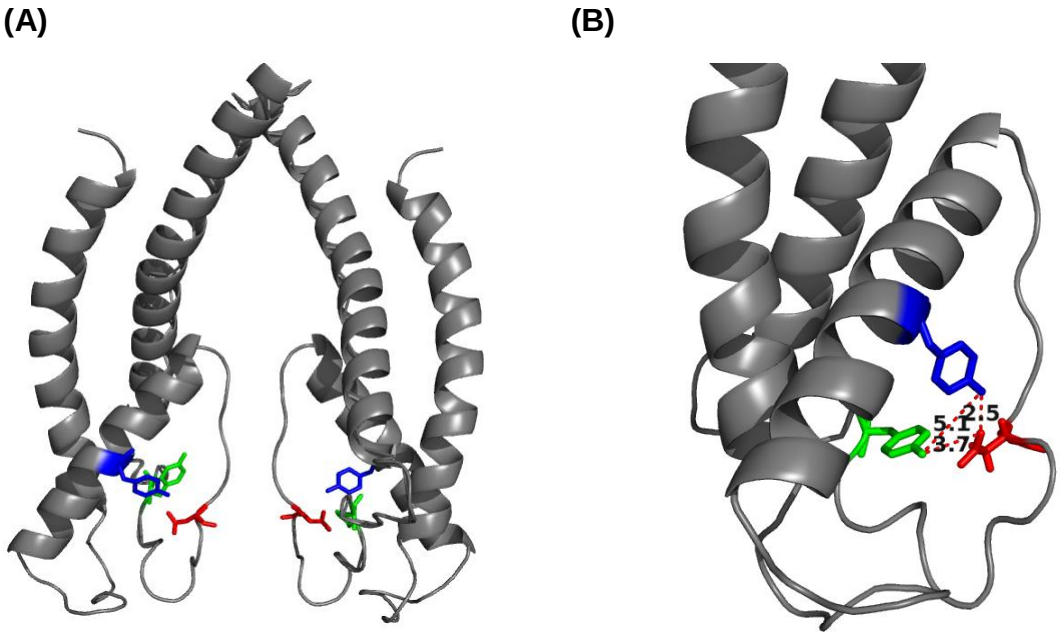


Figure 3.1. Measuring the distances of residues in the analogy PFR RyR2 model. Structure of the Welch *et al* PFR RyR2 analogy model (Welch *et al.,* 2004), highlighted residues are colour coded; Y4813 (blue), D4829 (red) and Y4839 (green). (A) Two monomers of the PFR shown for clarity. (B) Labelled distances (Ångström) were measured and constructed in PyMol, one monomer is shown for clarity.

3.1.3 Amino acid selection - Alanine mutations

To test the hypothesis it was important to select amino acids which would abolish any potential hydrogen-bonding interactions between the selectivity filter and pore helix. Alanine mutations have historically been a popular choice, offering a non-bulky, no charge, chemically inert, methyl side chain (Morrison and Weiss, 2001). In addition, alanine residues form alpha helices to preserve secondary structure and for these reasons, alanine substitution was selected for all three residues listed in table 3.1.

Tyrosine residues are key in providing structural stability in proteins (Hamill *et al.,* 2000), therefore removing a hydrogen-bonding component by alanine substitution is proposed to disrupt local interactions and alter a stabilising conformation of the selectivity filter that is hypothesised to affect hRyR2 channel gating.

3.1.4 Amino acid selection - Conservative mutations

To thoroughly examine channel gating around the proposed selectivity filter region, three conservative mutations at identical positions were constructed, serving as positive controls. Amino acid selection was essential; the chosen residue (side chain) would require aromatic characteristics and physicochemical properties similar to WT to retain hydrogen-bonding interactions.

Tyrosine, with an aromatic phenol side group at Y4813 and Y4839 was substituted by tryptophan. Tryptophan, an aromatic heterocyclic organic compound contains an indole functional group capable of hydrogen-bonding (Cordero-Morales *et al.,* 2011), generating ideal conservative substitutions (Y4813W and Y4839W). The aspartic acid at position D4829, a hydrogen-bonding acceptor, was substituted by glutamic acid (D4829E). Selection of glutamic acid was consistent with the properties of aspartic acid, extending the side chain by one methyl group however retaining the negative charge, acid carboxyl group.

This study focused on constructing six full-length mutant hRyR2 to investigate the role of a proposed hydrogen-bonding network between the selectivity filter and pore helix in hRyR2. The construction and expression of all hRyR2 mutants permitted cellular and electrophysiological characterisation to assess the involvement of residue substitution on channel gating as discussed in chapters 4, 5, 6 and 7.

3.2 – Materials and Methods

3.2.1 Generation of mutant pSL1180-NX1-hRyR2 plasmids

The SDM method was adopted to construct the point mutations listed in table 3.1. The hRyR2 residues Y4813, D4829 and Y4839 are located in the C-terminal of hRyR2, spanning the TM domain. The pSL1180 vector containing the cloned *Nhe*I/*Xho*I C-terminus DNA fragment, figure 3.2, was utilised for the generation of all six full-length mutant pcDNA3-eGFP-hRyR2 cDNA constructs. Unlike the *NheI* site, the *XhoI* site is not part of the coding sequence of hRyR2 and is found in the three prime untranslated region (3'-UTR), therefore an *XhoI* digestion preserves the native stop codon of hRyR2. The pSL1180-NX1-hRyR2 mutagenic cassette, 8597 bp, was a suitable length for PCR amplification. Prior to SDM, 2 µL WT NX1 DNA was transformed into MAX Efficiency® Stbl2™ competent cells, as described in chapter 2.2.1.2, to produce 30 µL template DNA for cloning.

The WT pSL1180-NX1-hRyR2 plasmid was constructed by George *et al.,* (2003), and was made available by Professor Alan Williams' lab.

hRyR2 residue	Amino acid Substitution	Codon change
Y4813	Alanine (A)	TAT → GCT
	Tryptophan (W)	TAT → TGG
D4829	Alanine (A)	GAT → GCT
	Glutamic acid (E)	GAT → GAG
Y4839	Alanine (A)	TAT → GCT
	Tryptophan (W)	TAT → TGG

Table 3.1. Full-length selectivity filter (D4829) and pore helix (Y4813 and Y4839) hRyR2 point mutations.

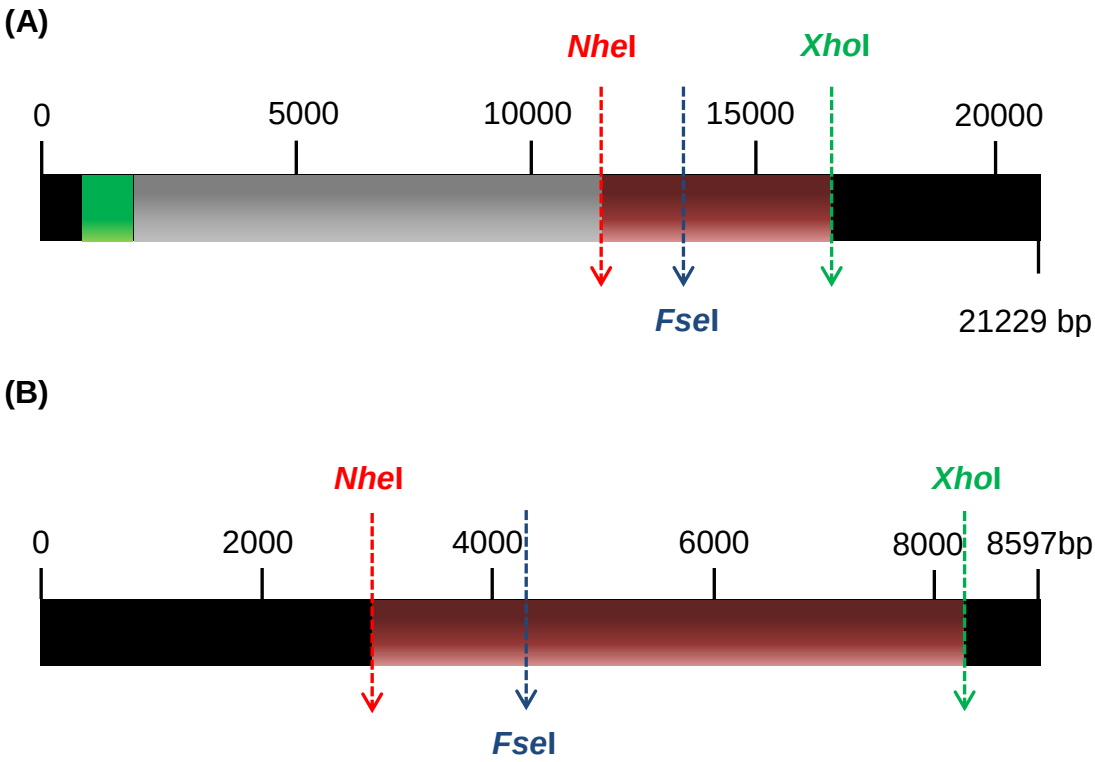


Figure 3.2. Schematic representation of the pcDNA3-eGFP-hRyR2 and pSL1180-NX1-hRyR2 vectors. (A) The pcDNA3 vector containing the N-terminal eGFP tag (green) and the hRyR2 sequence (grey) including the *Nhe*I and *Xho*I (NX1) DNA sequence (red), encoding the C-terminus pore-forming region. (B) The intermediate pSL1180 vector containing the NX1-hRyR2 DNA sequence highlighted in red was used for site-directed mutagenesis. The restriction endonuclease recognition sites for *Nhe*I, *Fse*I and *Xho*I are shown. The sequence encoding the pcDNA3 (5.446 kb) and pSL1180 (3.422 kb) vectors are shaded in black.

3.2.1.1 Primer design

The design of oligonucleotide primers containing a codon substitution and reagents including a DNA polymerase, listed in table 3.3, has enabled the introduction of nucleotide substitution within DNA sequences using PCR amplification. Several factors must be considered when designing primers for SDM. To increase efficiency of mutagenesis the primers should follow certain characteristics: The mutagenic forward and reverse oligonucleotide primers must contain the desired codon substitution, preferably at the centre of the 20-45 nucleotide bases. It is important that primers contain 40-60 % guanine and cytosine (GC) to ensure high melting temperatures (T_m), ideally T_m > 78 °C for efficient annealing and elongation. It is also

essential that they anneal to their complementary sequence on opposite strands of the template and to avoid any possible secondary priming sites. In addition, avoiding primer self-complementarities and direct repeats ensures that primer dimerisation and hairpin formation was prevented (Hyndman and Mitsuhashi, 2003). These guidelines were applied when designing the six hRyR2 mutant primers listed in table 3.2.

Mutation	Direction 5' - 3'	Primer nucleotide sequence	Length (bp)	GC %	T_m °C
Y4813A	Forward	CGATATGCTAACATGCGCTATGTTCCACATGTATGTTGG	39	43.6	79
	Reverse	CCAACATACATGTGGAACATAGCGCATGTTAGCATATCG			
Y4813W	Forward	CGATATGCTAACATGCTGGATGTTCCACATGTATGTTGG	39	43.6	79.3
	Reverse	CCAACATACATGTGGAACATCCAGCATGTTAGCATATCG			
D4829A	Forward	GGAGGAGGGATCGGGGCTGAAATCGAAGACCCAGC	35	62.9	85.8
	Reverse	GCTGGGTCTTCGATTTCAGCCCCGATCCCTCCTCC			
D4829E	Forward	GGAGGAGGGATCGGGGAGGAAATCGAAGACCCAGC	35	62.9	85.2
	Reverse	GCTGGGTCTTCGATTTCCTCCCCGATCCCTCCTCC			
Y4839A	Forward	CCAGCAGGAGATGAAGCTGAGATCTATCGAATCATC	36	47.2	77.6
	Reverse	GATGATTCGATAGATCTCAGCTTCATCTCCTGCTGG			
Y4839W	Forward	CCCAGCAGGAGATGAATGGGAGATCTATCGAATC	34	50	78.2
	Reverse	GATTCGATAGATCTCCCATTCATCTCCTGCTGGG			

Table 3.2. Mutagenic oligonucleotide forward and reverse primers designed for the generation of selectivity filter and pore helix mutants in hRyR2. 'Mutation' codon substitutions are highlighted in red, 'GCT' alanine, 'TGG' tryptophan and 'GAG' glutamic acid. Table includes primer nucleotide base length, guanine and cytosine content percentage and melting temperature. The JustBio 'Oligocalc' web-hosting software was used to calculate T_m, (http://www.justbio.com/index.php?page=oligocalc).

Three main thermal steps were performed with specific time and temperature, repeating in cycles, to ensure the amplification of desired synthesised DNA strands, listed in table 3.4 and depicted in figure 3.3. Optimisation of reagents, such as DNA polymerase, has enhanced proofreading and yield quality ensuring high-fidelity PCR amplification for SDM (Xia *et al.,* 2014).

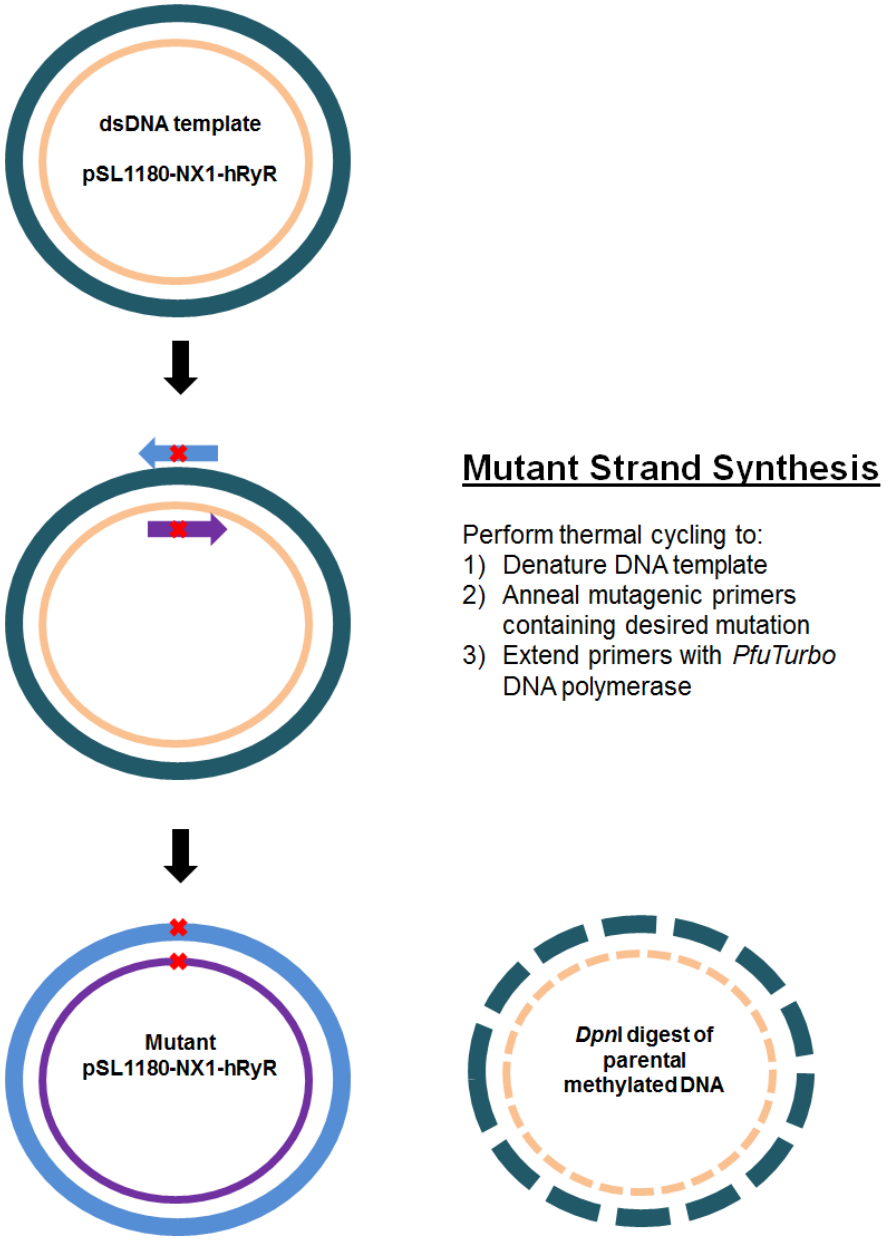


Figure 3.3. Schematic representation of the QuikChange PCR procedure. Figure adapted from QuikChange XL SDM kit instruction manual (Agilent Technologies).

3.2.1.2 Site-directed Mutagenesis

SDM PCR amplifications of pSL1180-NX1-hRyR2 were performed using a GeneAmp® PCR System 9700 thermal cycler (Applied Biosystems). The reaction mixture stated in table 3.3 contains *PfuTurbo* DNA polymerase which is a mixture of *Pfu* DNA polymerase and a thermostable ArchaeMaxx polymerase-enhancing factor. In combination, *PfuTurbo* can amplify vector targets up to 15 kb in length, with increased proofreading activity providing a robust and enhanced high-fidelity PCR product (Cline *et al.,* 1996). The thermal cycling protocol is listed in table 3.4.

Reagent	**Volume**	**Final Concentration**
Reaction buffer	5 µL	1 x
dsDNA template*	1 µL	10 ng
Forward Primer**	1 µL	125 ng
Reverse Primer**	1 µL	125 ng
dNTP mix (10 mM)	1 µL	0.2 mM
QuikSolution	3 µL	1x
dH_2O	38 µL	up to 50 µL
PfuTurbo DNA Polymerase	1 µL	2.5 U

Table 3.3. QuikChange XL PCR reagents. *dsDNA template is WT pSL1180-NX1-hRyR2 plasmid. **Forward and reverse primers are listed in table 3.2.

Step	**Cycles**	**Temperature**	**Time**
Initial Denaturation	1	95 °C	1 min
Denaturation	18	95 °C	50 s
Annealing		60 °C	50 s
Elongation		68 °C	8 min (1 min/kb)
Final Elongation	1	68 °C	7 min
Hold	1	4 °C	Indefinite

Table 3.4. QuikChange XL site-directed mutagenesis PCR thermal cycle protocol.

3.2.1.3 *Dpn*I Digest

Following PCR, 1 µl of *Dpn*I, a restriction endonuclease, was added to the reaction product and incubated at 37 °C for 1 h. *Dpn*I digests methylated 'parental' DNA, leaving the non-methylated, newly synthesised, mutant plasmid DNA. The single-stranded DNA was subsequently transformed into XL10-Gold Ultracompetent cells to generate the double-stranded plasmid as described in section 2.2.1.2.

3.2.1.4 DNA Sequencing

The BigDye Terminator v3.1 Cycle sequencing kit (Applied Biosystems) provides a method of performing fluorescence-based cycle sequencing on DNA templates to verify nucleotide sequence, confirming that SDM codon substitution had been completed. The SDM reaction was prepared according to table 3.5 and tubes were placed in the cycle sequencing ABI Veriti 96 well thermal cycler set to BigDye standard program, listed in table 3.6.

Reagent	Quantity
Better Base (Microzone Ltd)	5 µl
ABI BigDye terminator Ready Reaction mix	1 µl
Mutant template	150-300 ng
Primer*	3.2 pmol
dH_2O	to 15 µl

Table 3.5. BigDye Terminator v3.1 reagents. Sequencing reaction primers flanking boundary sites are stated in section 3.3.2. *Primers stated in section 3.3.2.

Step	Cycle	Temperature	Time
Initial Denaturation	1	96 °C	1 min
Denaturation	25	96 °C	10 s
Annealing		50 °C	5 s
Elongation		60 °C	4 min
Hold	1	4 °C	Indefinite

Table 3.6. BigDye Terminator PCR sequencing thermal cycling protocol.

Unincorporated dye terminators, enzymes and salts were removed from the reaction using the DyeEx 2.0 spin kit (Qiagen). This ensured that sequencing products were eluted in distilled deionised water free from nuclease and ready for DNA sequencing. DNA samples were sequenced using an ABI Prism Genetic Analyser 3130xl sequencer. Confirmation of mutant hRyR2 constructs were analysed by importing sequencing data from Four Peaks (http://nucleobytes.com/index.php/4peaks), a visual sequencing software, to generate chromotagrams. Nucleotide sequences were then exported into JustBio aligner web-hosted software (http://www.justbio.com/index.php?page=aligner) to compare WT and mutant hRyR2 sequences. The intermediate mutant pSL1180-NX1-hRyR2 constructs were further verified by gel agarose electrophoresis using *EcoR*I to digest 1 µg of plasmid DNA, shown in figure 3.5A.

3.2.1.5 DNA cloning of mutant hRyR2 fragments into WT pcDNA3 vector

WT pcDNA3-eGFP-hRyR2 and mutant pSL1180-NX1-hRyR2 plasmids (1 µg) were digested for 2 h at 37 °C as listed in table 3.7. Following digestion, samples were electrophoresed in a 1 % agarose gel for 1.5 h to allow for maximum DNA band separation.

	Vector	**Insert**
	WT pcDNA3-eGFP-hRyR2	Mutant NX1 cassette
cDNA	2 µL	10 µL
*Xho*I (10 U)	0.5 µL	0.5 µL
*Fse*I (3 U)	1.5 µL	1.5 µL
BSA (10 x)	2 µL	2 µL
Buffer 4 (10 x)	2 µL	2 µL
dH_2O	12 µL	4 µL

Table 3.7. Cloning of full-length pcDNA3-eGFP-hRyR2 vector and mutant pSL1180-NX1-hRyR2 insert. Reagents used for restriction endonuclease digest of vector and insert.

3.2.1.6 Gel Extraction

The QIAEX II® Gel Extraction Kit (QIAGEN) was used to excise DNA fragments from the agarose gel following digestion. Two 1.5 mL Eppendorf tubes were weighed and a water bath was pre-heated to 50 °C. The correct DNA fragments were extracted from the agarose gel using a clean, sharp scalpel, illustrated in figure 3.8. The DNA gel slice from pcDNA3-eGFP-hRyR2 and pSL1180-NX1-hRyR2 were weighed in separate tubes. The weight of the DNA gel fragment determined the volume of Buffer QX1 (3 x w/v), and dH_2O (2 x w/v) including 30 µl QIAEXII suspension silica particles. Tubes were incubated at 50 °C for 10 min to solubilse the agarose gel with gentle inversion every 2 min to assist agarose solubilisation and binding of DNA to the QIAEXII silica particles. Samples were centrifuged at 17,900 x *g* for 30 s, the supernatant was carefully discarded and the DNA-QIAEXII pellet was washed by resuspending in 500 µL Buffer QX1. Centrifugation was repeated, the supernatant was discarded and samples were resuspended in 500 µL Buffer PE. The supernatant was carefully discarded following another centrifugation step where the pellet was air-dried for 30 min until the DNA-QIAEXII pellet became white. The DNA was eluted by resuspending the pellet in 20 µL dH_2O, incubating for 5 min at 50 °C and then centrifuging for 30 s to separate the DNA from the QIAEXII beads. The purified sample was transferred to a fresh tube.

3.2.1.7 Ligation of mutant hRyR2 fragments into the WT pcDNA3 vector

The DNA nanodrop Nanovue Plus (GE Lifesciences) was used to determine DNA concentration following gel extraction prior to ligation of the purified NX1 fragment and vector DNA. The ligation reaction was set up at a vector:insert ratio of 1 : 3 as stated in table 3.8. The T4 DNA ligase (Roche) was added to catalyse the formation of phosphodiester bonds between 3'hydroxyl and 5'-phosphate ends of double-stranded DNA, joining mutant pSL1180-NX1 insert and pcDNA3-hRyR2 vector 'sticky'-end DNA fragments together. Reagents were incubated for 16-18 h overnight at 4 °C, allowing for the T4 ligase to join boundary sites to form full length mutant pcDNA3-eGFP-hRyR2 constructs.

Reagents	Quantity
Vector	50 ng
Insert	33 ng
Buffer 2	2 µL
dH_2O	up to 35 µL
Buffer 1	15 µL
T4 Ligase	1.5 µL

Table 3.8. Ligation of full-length mutant hRyR2 mutations using T4 ligase.

3.2.2 Verification of full-length mutant pcDNA3-eGFP-hRyR2 constructs

Following the overnight incubation, 10 µL of the ligation reaction was transformed into XL10-Gold Ultracompetent cells as described in chapter 2.2.1.3. Propagation of mutant full-length pcDNA3-eGFP-hRyR2 constructs was carried out as stated in chapter 2.2.1.4, to generate 30 µL of purified DNA. Full-length constructs were verified by gel agarose electrophoresis using a complement of four restriction endonucleases listed in table 3.10 and illustrated in figure 3.4. Restriction digest reactions were set up as stated in table 3.9 and incubated for 1.5 h at 37 °C. 10 µL of digest reaction was mixed with 10 µL sample buffer and loaded onto a 1 % agarose gel, and was electrophoresed for 30-40 min. The hRyR2 DNA fragments following restriction digest are shown in figure 3.5.

Reagents	Volume
DNA (1-2 µg)	5 µL
dH_2O	2 µL
Buffer	1 µL
BSA (10x)	1 µL
Enzyme (5-10 U)	1 µL

Table 3.9. Restriction digest reaction of full-length WT or mutant pcDNA3-eGFP-hRyR2. Restriction enzymes are listed in table 3.10 and hRyR2 DNA fragments following digestion are illustrated in figure 3.5.

Enzyme	Specificity	Cuts
pcDNA3-eGFP-hRyR2		
***BamH*I**	G•GATC•C	5
***Bgl*II**	A•GATC•T	8
***Hind*III**	A•AGCT•T	3
***EcoR*I**	G•AATT•C	5
pSL1180-NX1-hRyR2		
***EcoR*I**	G•AATT•C	2

Table 3.10. Restriction endonuclease recognition sites used for construct verification for full-length pcDNA3-eGFP-hRyR2 and intermediate pSL1180-NX1-hRyR2 vectors.

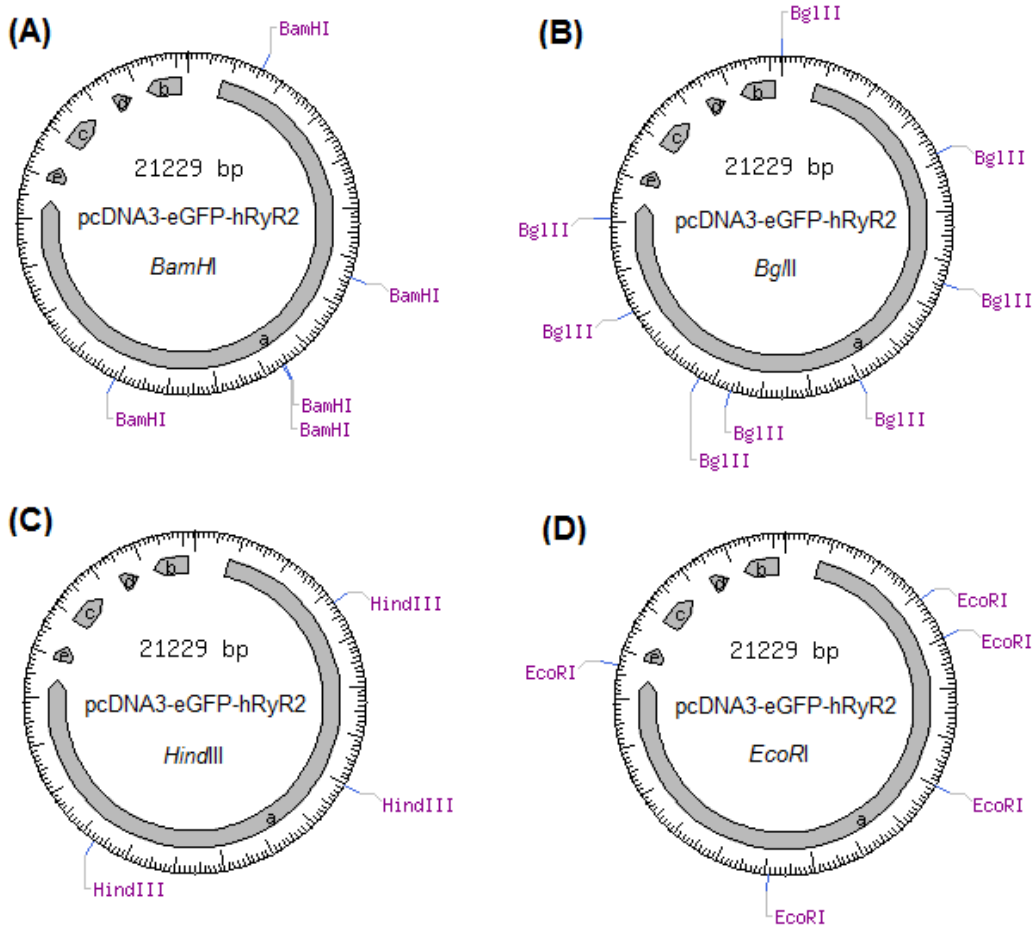
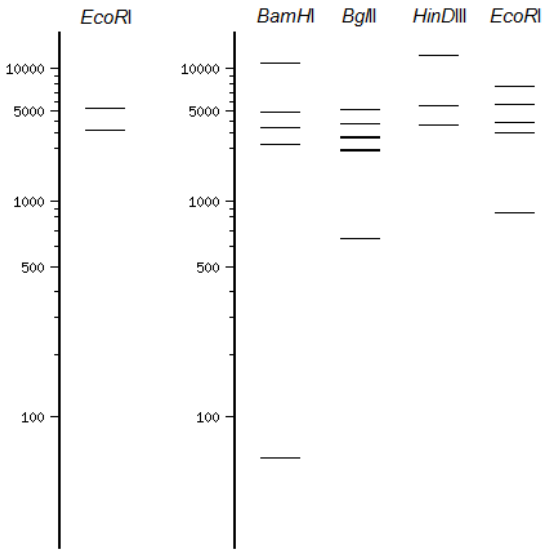


Figure 3.4. A circular sequence vector map of full-length pcDNA3-eGFP-hRyR2. Restriction endonucleases used (A) *BamH*I, (B) *Bgl*II, (C) *Hind*III and (D) *EcoR*I. Figure obtained from New England BioLabs (http://tools.neb.com/NEBcutter2).

(A) **(B)** **(C)**



Plasmid	Enzyme	#	Coordinates	Length (bp)
pSL1180-NX1-RyR2	*EcoR*I	1	2994-8363	5370
		2	8364-2993	3227
pcDNA3-RyR2	*BamH*I	1	12101-1535	10664
		2	1536-6406	4871
		3	8640-12100	3461
		4	6407-8605	2199
		5	8606-8639	34
	*Bgl*II	1	16060-12	5182
		2	13-3817	3805
		3	3818-6449	2632
		4	9023-11632	2610
		5	6450-9022	2573
		6	14155-16059	1905
		7	12282-14154	1873
		8	11633-12281	649
	*Hind*III	1	12708-3237	11759
		2	7008-12707	5700
		3	3238-7007	3770
	*EcoR*I	1	16677-3130	7683
		2	10936-16676	5741
		3	6984-10935	3952
		4	3969-6983	3015
		5	3131-3968	838

Figure 3.5. A template of hRyR2 DNA fragments following restriction digest. A representation of DNA fragments from (A) pSL1180-NX1-hRyR2 and (B) pcDNA3-eGFP-hRyR2 on a 1 % agarose gel (electrophoresed for 30 min), following restriction digest. (C) Restriction enzymes, plasmid coordinate sites and DNA fragment length (bp) are stated. pcDNA3- eGFP-hRyR2 DNA fragments digested by *Bgl*II, 2632 bp, 2610 bp and 2573 bp, and also 1905 bp and 1873 bp were not resolved on the agarose gel and migrated as a single band, respectively. The DNA fragments were created using NEBcutter V2.0 (http://tools.neb.com/NEBcutter2).

3.2.3 Propagation of WT and Mutant hRyR2 DNA

Following full-length mutant pcDNA3-eGFP-hRyR2 DNA sequencing and verification, transformed MAX Efficiency® Stbl2™ cells were propagated containing mutant DNA as outlined in chapter 2.2.1.4. Mutant constructs were isolated from Stbl2 cells by MAXIprep as described chapter 2.2.1.6 and were verified by restriction digest mapping using the enzymes described in section 3.2.2. DNA was used for mammalian HEK293 cell transfection and protein expression.

3.2.4 Protein expression of WT and Mutant hRyR2

The calcium-phosphate ($CaPO_4$) precipitant transfection method was used to transiently introduce WT and mutant pcDNA3-eGFP-hRyR2 constructs into mammalian HEK293 cells, as described in chapter 2.2.2.3. An optimisation trial of WT and mutant protein expression was completed by supplementing the cDMEM media with 2 mM sodium butyrate (NaB). While the exact mechanism of increased hRyR2 expression by NaB remains unknown, NaB is an inhibitor of histone deacetylation, and possibly increases gene transcription by enhancing gene accessibility to transcription factors (Jiang and Sharfstein, 2008). Previous studies have used NaB to improve expression levels of ion channels including voltage gated Na^+ channels (Baines *et al.,* 1992), inward rectifier K^+ channels (Panama *et al.,* 2007) and the cystic fibrosis transmembrane regulator (CFTR) Cl^- channel (Gerçeker *et al.,* 2000). In addition, a study assessed the proposed transcriptional upregulatory properties of NaB for hRyR2 expression and reported that the effect of NaB was both time and concentration dependent (Guzadhur, 2009). The optimisation trial by Guzadhur identified that using 2-5 mM NaB and harvesting cells 24-48 h post-transfection was optimal for hRyR2 protein expression, and was therefore employed in this thesis. Subsequently, RyR2 protein expression was quantified by Western blot as outlined in sections 2.2.3.5 and 2.2.3.6.

3.3 – Results

3.3.1 Production of selectivity filter and pore helix mutant hRyR2 plasmids

Full length, eGFP tagged, hRyR2 cDNA was modified to incorporate the desired selectivity filter and pore helix mutations using Quikchange® XL SDM kit. Primers were designed to incorporate the correct codon missense mutation (alanine (GCT), tryptophan (TGG), glutamic acid (GAG)) following primer guidelines discussed in section 3.2.1.1 and listed in tables 3.1 and 3.2. The PCR protocol stated in section 3.2.1 (tables 3.3 and 3.4) was used to perform SDM on the pSL1180-NX1-hRyR2 template at the desired nucleotide position. Following PCR *Dpn*I digestion, newly synthesised mutant DNA was transformed into XL-10 competent cells and propagated to yield 30 µL mutant DNA. The mutant pSL1180-NX1-hRyR2 plasmid was initially verified by DNA digest using *EcoR*I. The DNA fragments, depicted in figure 3.6, were in accordance to the predicted DNA patterns shown in figure 3.5.

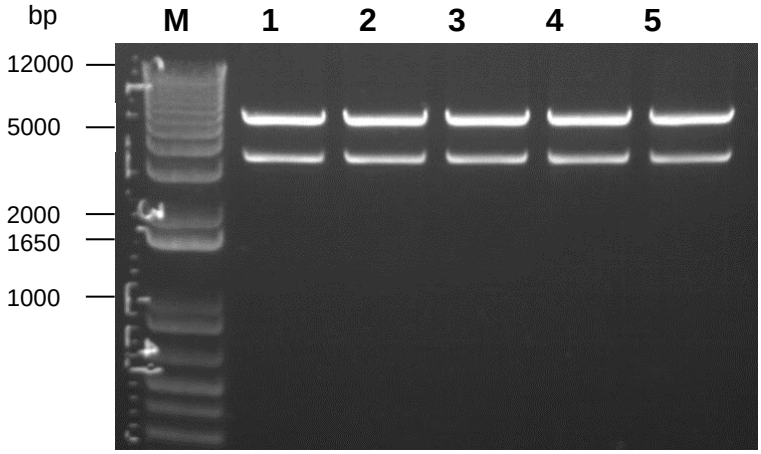


Figure 3.6. Representative mutant pSL1180-NX1-hRyR2 plasmid digested with *EcoR*I, lanes 1-5. (M) 1 kB DNA ladder. DNA fragments were in accordance with the predicted DNA patterns shown in figure 3.5A.

Utilising the BigDye terminator protocol described in section 3.2.1.4, mutant pSL1180-NX1-hRyR2 DNA was sequenced using the SPFOR 14357-79 (3.2 pmol) oligonucleotide primer targeted to the site of mutation. All six intermediate NX1-hRyR2 plasmids successfully contained the desired point mutation, as indicated by the chromatograms in figure 3.7, highlighting the codon substitution to either alanine (GCT), tryptophan (TGG) or glutamic acid (GAG).

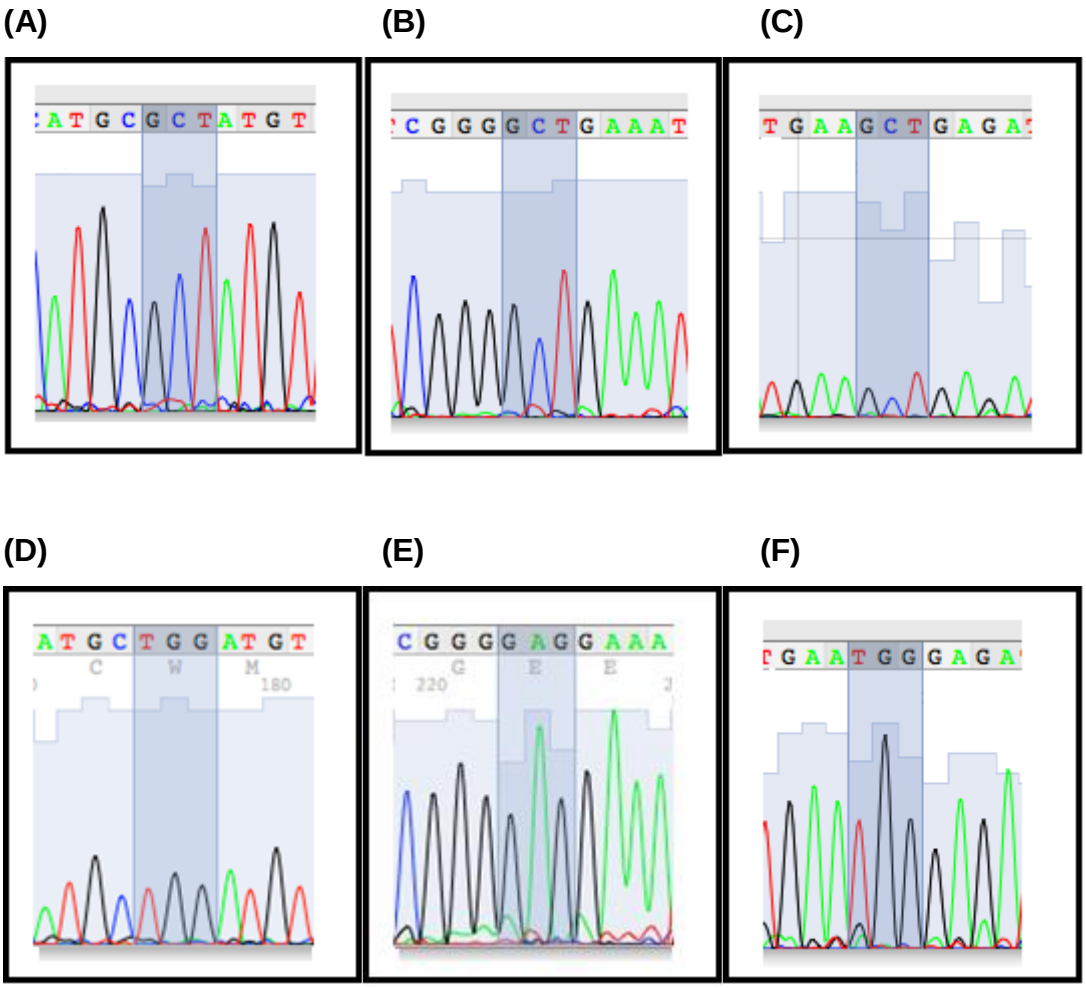


Figure 3.7. Mutant pSL1180-NX1-hRyR2 chromatograms. (A) Y4813A, (B) D4829A, (C) Y4839A, (D) Y4813W, (E) D4829E and (F) Y4839W. DNA sequencing was successful, desired point mutations to alanine (GCT), tryptophan (TGG) or glutamic acid (GAG) were verified, highlighting codon substitution in blue.

3.3.1.1 Ligation of mutant hRyR2 fragments into WT pcDNA3 vector

Full-length hRyR2 mutants were created by reinserting mutant NX1 DNA cassettes into full-length vector using *Xho*I and *Fse*I restriction enzymes, outlined in section 3.2.1.5. Full-length WT pcDNA3-eGFP-hRyR2 vector and mutant NX1-hRyR2 insert were digested using reagents listed in table 3.7. The double digest was electrophoresed for > 2 h to ensure maximum DNA fragment separation for DNA cloning, shown in figure 3.8.

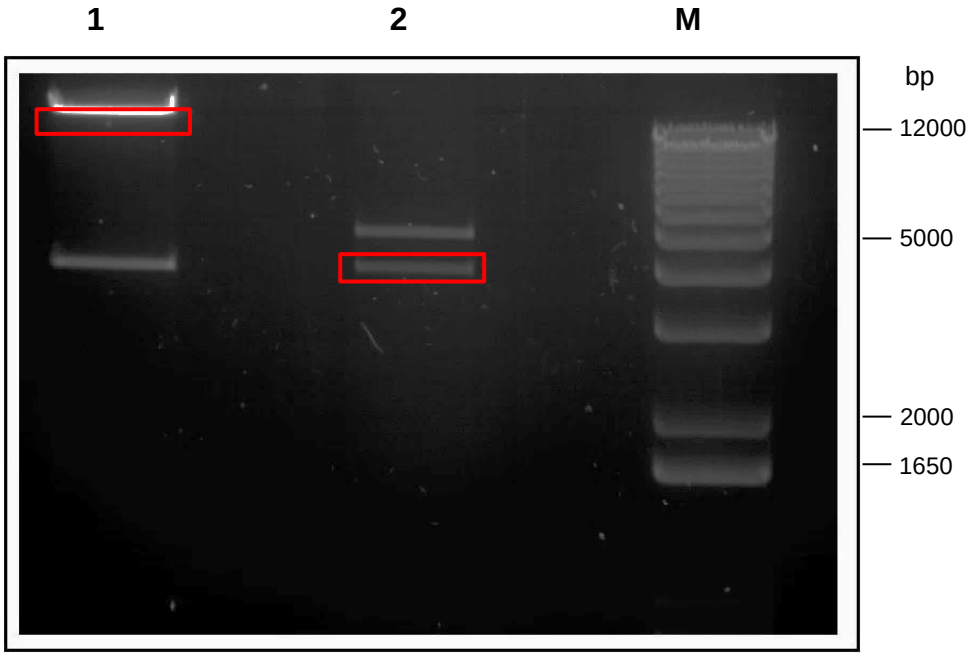


Figure 3.8. Restriction digest of full-length pcDNA3-hRyR2 vector (1) and mutant pSL1180-NX1 insert (2). (M) 1 kb Plus DNA ladder. DNA-gel fragments (red boxes) were excised under UV light using a clean, sharp scalpel and purified using the QIAEXII as described in sections 3.2.1.5 and 3.2.1.6.

3.3.2 Verification of full-length mutant pcDNA3-eGFP-hRyR2 constructs

Mutant NX1-hRyR2 insert and WT pcDNA3-eGFP-hRyR2 vector were ligated using the protocol listed in table 3.8. Transformed MAX Efficiency ® Stbl2™ cells containing mutant pcDNA3-hRyR2 constructs were propagated, yielding 200-800 ng/µl DNA. Full-length hRyR2 constructs were verified by gel agarose electrophoresis using the restriction endonucleases listed in table 3.10. WT hRyR2 (figure 3.9) and the six full-length digested mutant hRyR2 DNA fragments (figure 3.10 A-E) were correct and in accordance to the predicted DNA patterns shown in figure 3.5B when electrophoresed for 30-45 min on a 1 % agarose gel. Mutant constructs were finalised by verifying ligation boundary sites using automated sequencing, described in section 3.2.1.4, using primers SPREV 11923-42 (*Fse*I recognition region), BF 14622-640 (*Xho*I recognition region) and SPFOR 14357-79 (mutation recognition region). However, in the absence of sequencing the entire reading frame, it was not possible to be entirely certain that the only sequence alteration in the hRyR2 plasmid was the intended point mutation.

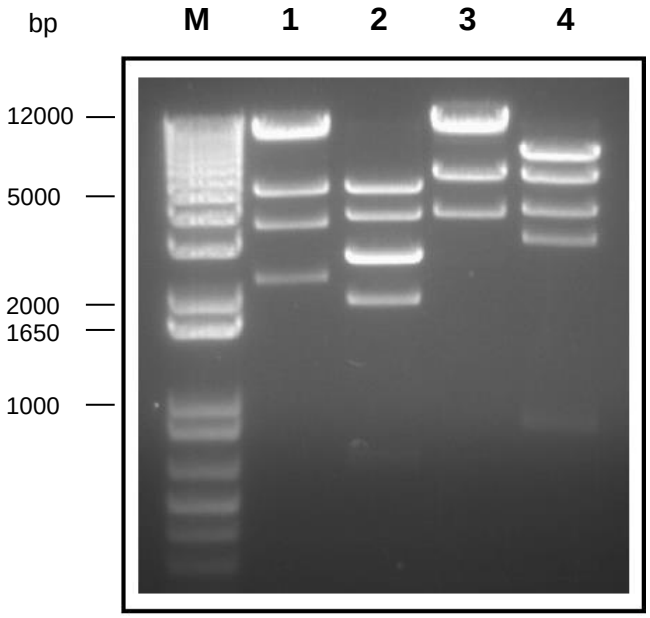


Figure 3.9. DNA digest mapping of full-length WT hRyR2 DNA. Restriction endonucleases (1) *BamH*I, (2) *Bgl*II, (3) *HinD*III and (4) *EcoR*I. (M) 1 kB DNA ladder. WT hRyR2 DNA fragments were in accordance to the predicted DNA patterns shown in figure 3.5B.

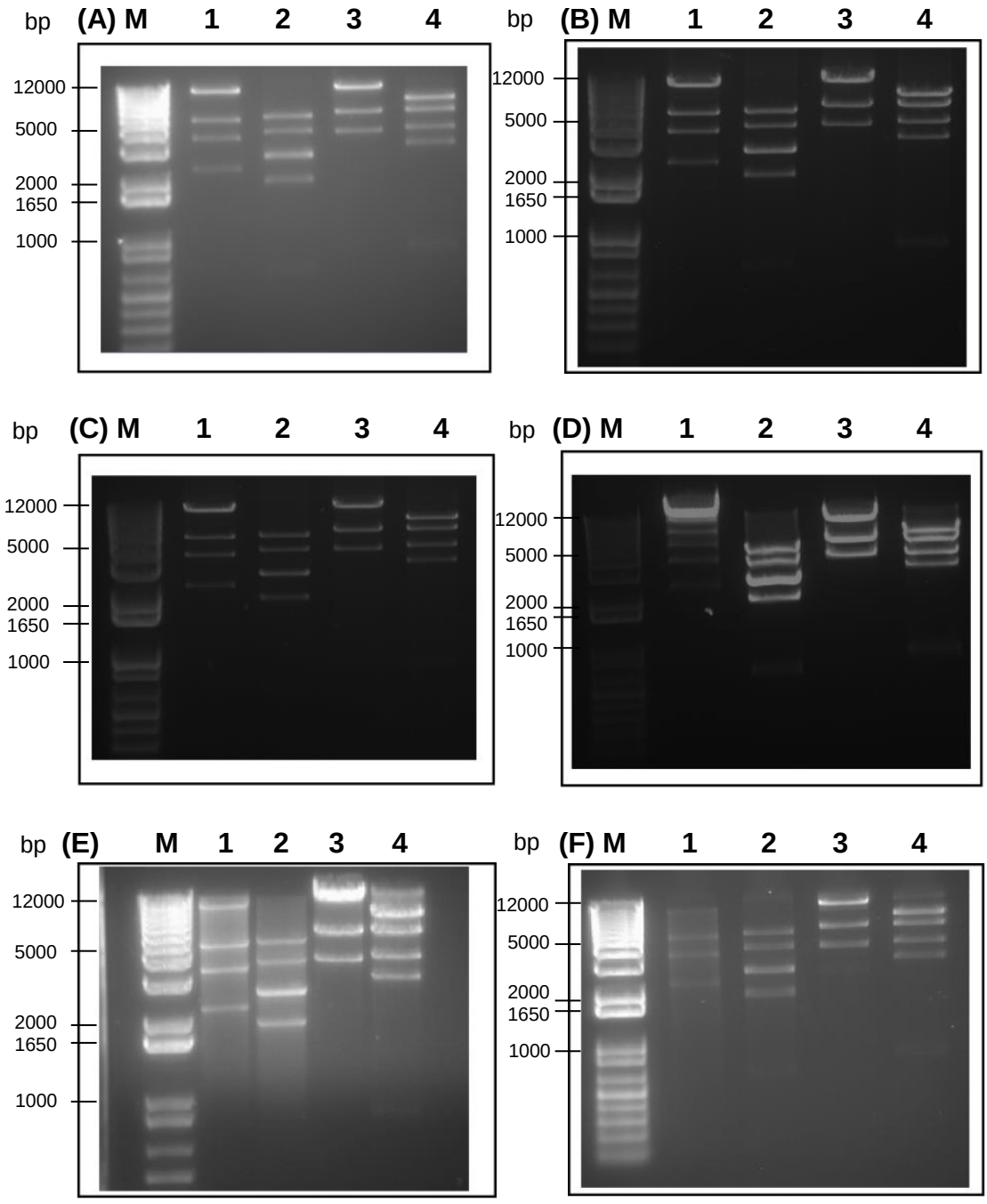


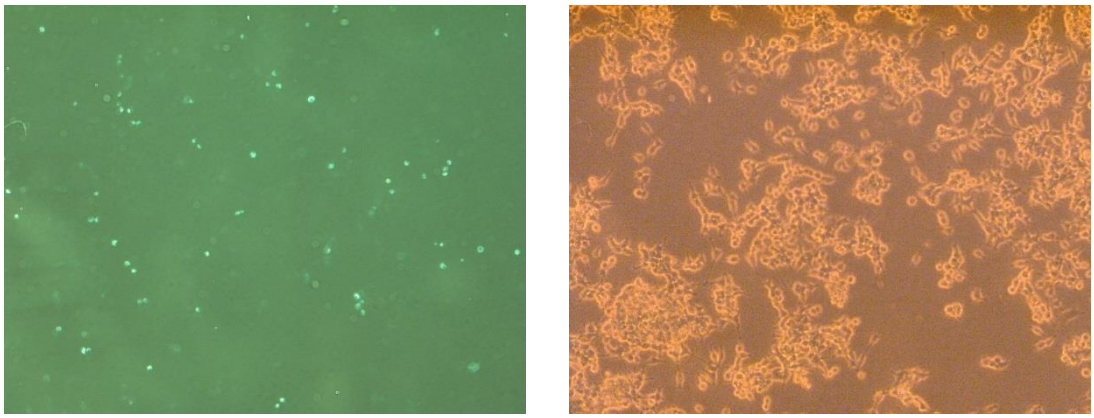
Figure 3.10. Verification of ligated full-length mutant pcDNA3-eGFP-hRyR2 constructs. DNA digest mapping of (A) Y4813A, (B) Y4813W, (C) D4829A, (D) D4829E, (E) Y4839A and (F) Y4839W using restriction endonucleases (1) *BamH*I, (2) *Bgl*II, (3) *HinD*III and (4) *EcoR*I. (M) 1 kB DNA ladder. Mutant DNA fragments were in accordance to the predicted DNA patterns shown in figure 3.5B.

3.3.3 Heterologous expression of WT and mutant hRyR2 plasmids – eGFP imaging

To achieve appropriate levels of hRyR2 protein expression for downstream assays ([^{3}H] ryanodine binding (chapter 4) and single-channel experiments (chapters 5 and 6)), the transfection of both WT and mutant hRyR2 DNA into mammalian HEK293 cells was optimised by the addition of 2 mM NaB, as described in chapter 2.2.2.3. Figure 3.11 depicts the increase in WT hRyR2 protein expression indicated by enhanced 'green' fluorescent cells following the addition of 2 mM NaB compared to control (figure 3.11A).

eGFP imaging 48 h post-transfection indicated that all six full-length mutant pcDNA3-eGFP-hRyR2 constructs were able to express hRyR2 protein verified by green fluorescent HEK293 cells. Transfection efficiencies of the six mutant hRyR2 constructs were comparable to WT hRyR2 shown in figures 3.11B, 3.12 and 3.13.

(A)



(B)

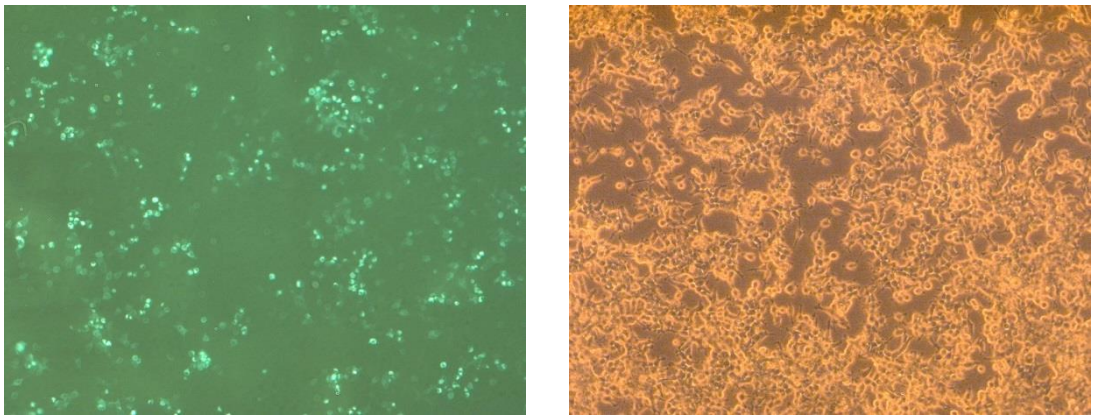


Figure 3.11. WT hRyR2 transfection trial using sodium butyrate. (A) Representative control field of view (FOV) without the addition of 2 mM NaB. (B) Representative FOV with the addition of 2 mM NaB. (*left*) eGFP imaging FOV visualised using a xenon light source (peak excitation ~ 488 nm), and a 520 ± 28 nm band pass filter, outlined in section 2.2.2.4. The green fluorescent cells indicated hRyR2 protein expression. (*right*) Bright field imaging displays the total cell density. Scale: 10 x objective magnification.

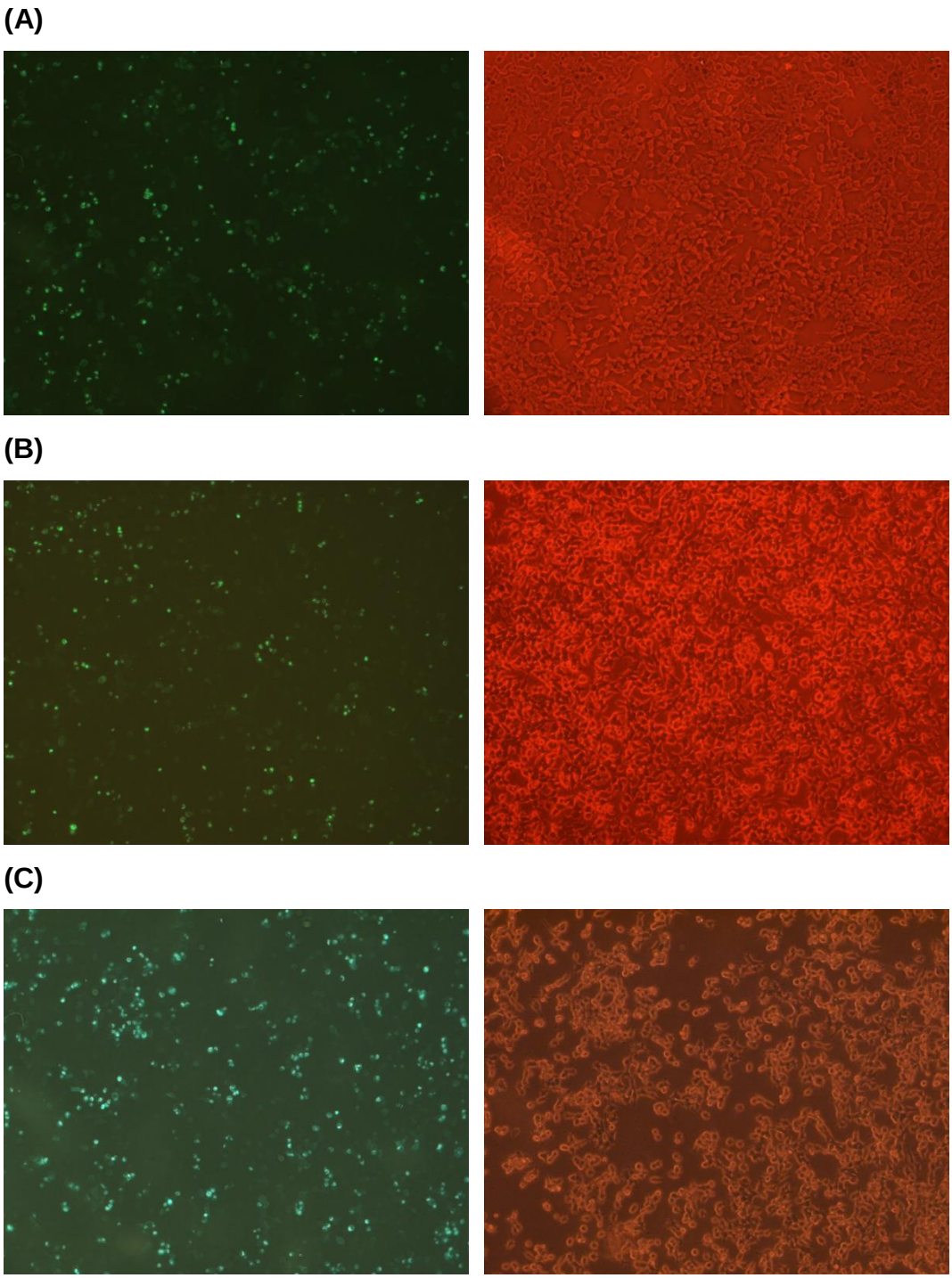
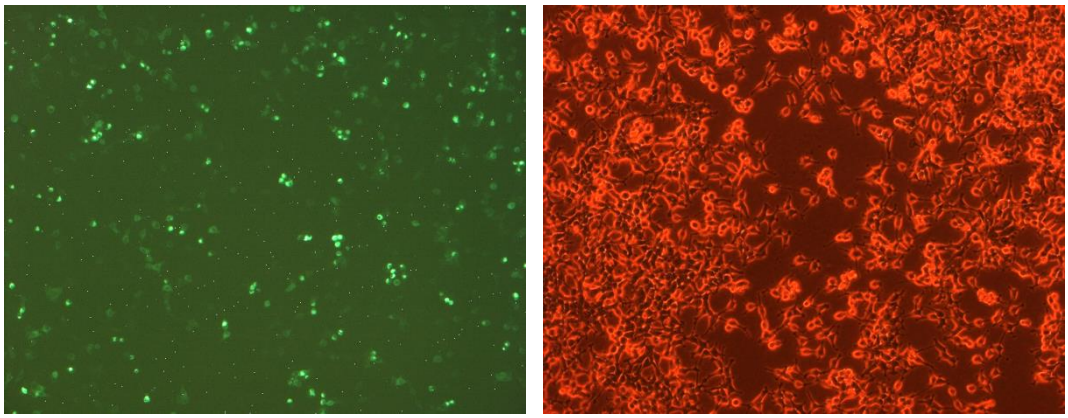
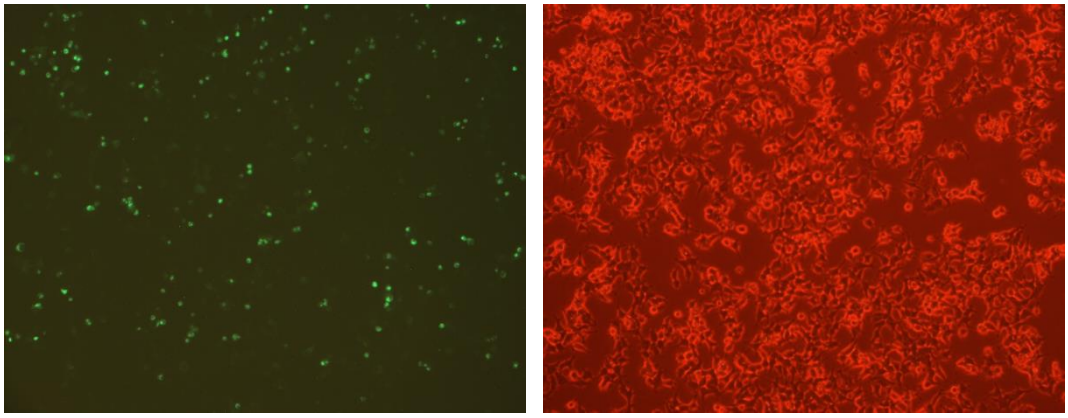


Figure 3.12. Transfection of alanine hRyR2 mutation constructs into HEK293 cells. (A) Y4813A, (B) D4829A and (C) Y4839A. (*left*) eGFP imaging of HEK293 cells outlined in section 2.2.2.4. The green fluorescent cells confirmed hRyR2 protein expression. Transfection media was supplemented with 2 mM NaB 24 h post-transfection. (*right*) A bright field light source applied to the same FOV displays the total cell density. Scale: 10 x objective magnification.

(A)



(B)



(C)

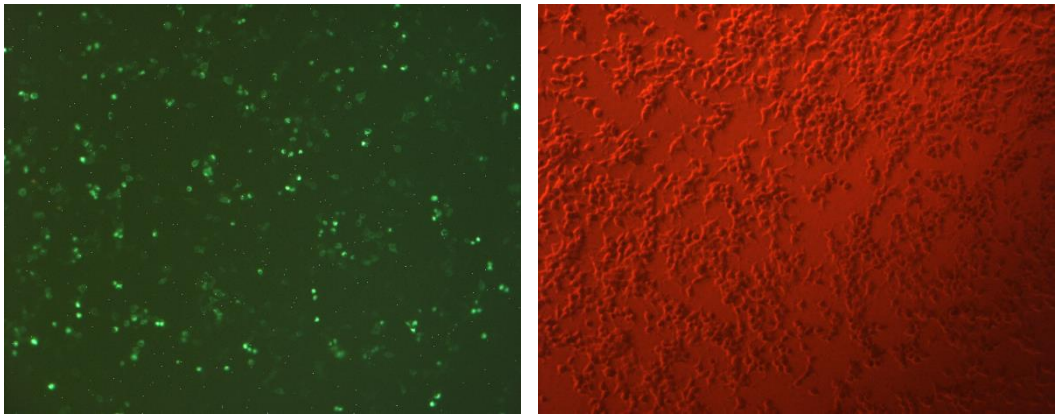


Figure 3.13. Transfection of conservative hRyR2 mutation constructs into HEK293 cells. (A) Y4813W, (B) D4829E and (C) Y4839W. (*left*) eGFP imaging of HEK293 cells outlined in section 2.2.2.4. The green fluorescent cells confirmed hRyR2 protein expression. Transfection media was supplemented with 2 mM NaB 24 h post-transfection. (*right*) A bright field light source applied to the same FOV displays the total cell density. Scale: 10 x objective magnification.

3.3.4 Quantification of WT and Mutant hRyR2 protein expression

Quantification of WT and mutant hRyR2 protein expression was achieved by Western blot densitometry analysis, described in chapter 2.2.3.6. Following microBCA protein assay, 100 µg of mixed-membrane preparations, containing hRyR2 protein, were loaded onto SDS-PAGE gels and subsequently verified by Western blot, shown in figure 3.14. The distinctive upper band highlighted by a black arrow in figure 3.14A and B, represents the monomers of WT and mutant hRyR2 protein (~ 565 kDa) due to dissociation of the tetrameric protein by SDS-PAGE.

Figure 3.15A shows protein expression of hRyR2 channels from control experiments without the addition of 2 mM NaB. In contrast, figure 3.15B represents protein expression performed using a modified transfection protocol that included 2 mM NaB 24 h post-transfection. Comparing figure 3.15A and B, the addition of NaB almost doubled protein expression of WT and mutant hRyR2 channels by 1.82 ± 0.2 fold (n=5, p=0.0085), listed in table 3.11. In addition, mutant protein expression shown in lanes 2-5 in figure 3.15B were comparable to WT hRyR2 in lane 1, demonstrated by relative protein expression (compared to WT hRyR2) of D4829A 0.84, Y4813A 0.82, Y4839A 1.1 and Y4839W 1.02. The two conservative hRyR2 mutations, Y4813W and D4829E, were not used in the protein expression NaB trial. Their expression was subsequently verified by Western blot shown in figures 4.11 and 4.12.

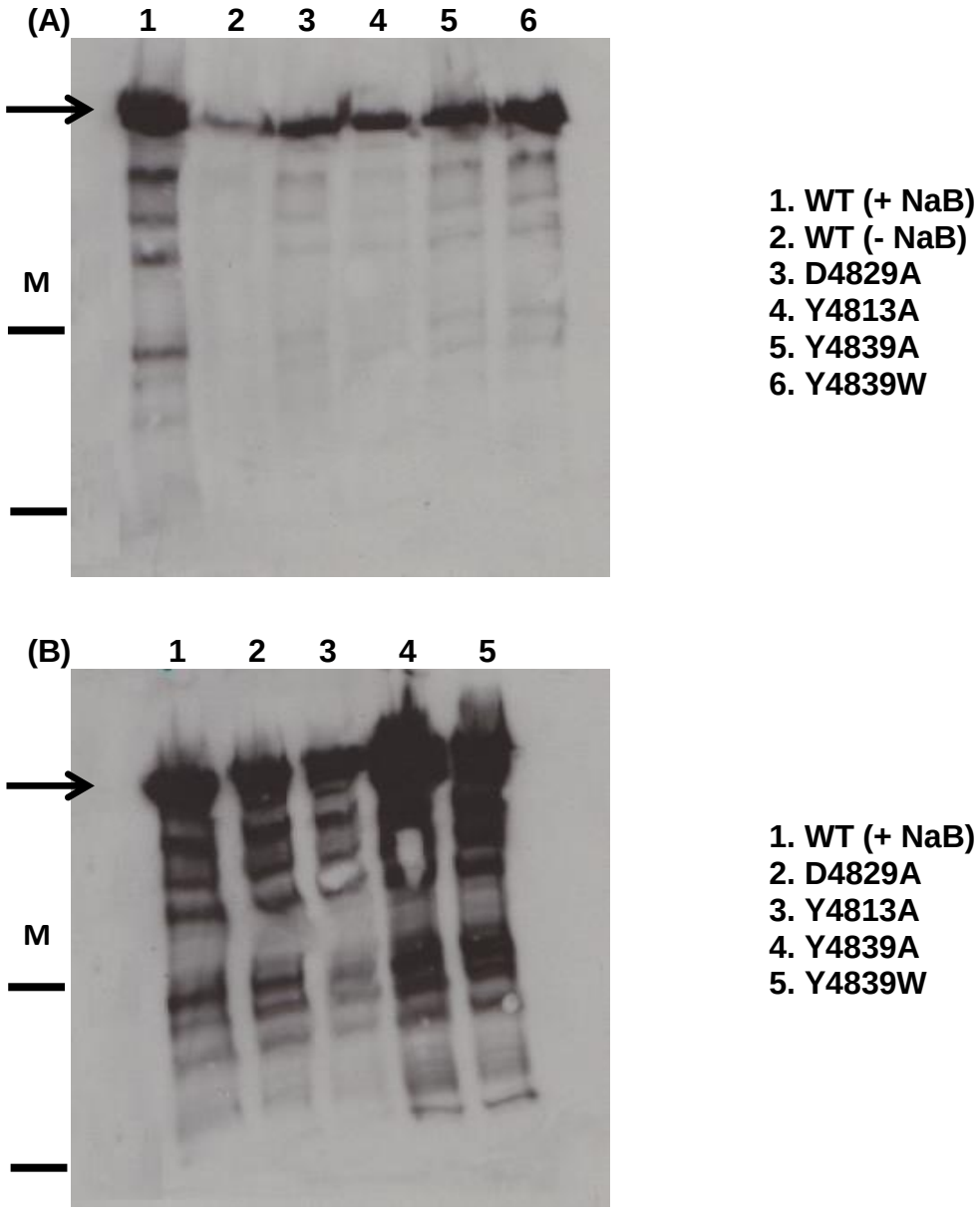
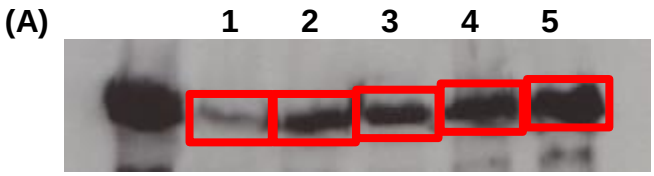
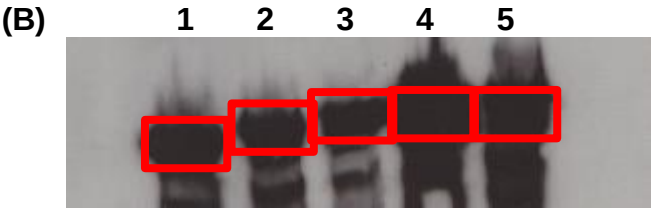


Figure 3.14. Western blot comparing protein expression of WT and mutant hRyR2 mixed-membrane preparations between control and the addition of sodium butyrate. Western blot of hRyR2-eGFP tagged channels, labelled on figure, from (A) control, without the addition of 2 mM NaB, except for lane 1, and (B) with the addition of 2 mM NaB. The hRyR2 monomers detected by eGFP-Ab, as outlined in chapter 2.2.3.4, are indicated by a black arrow. (M) The Kaleidoscope™ prestained markers of myosin, molecular weight (MW) of 216 kDa (top band), and β-galactosidase, MW of 132 kDa (lower band), are depicted by a black bar. Integrated densitometry analysis is shown in figure 3.15.

3.3.4.1 Western blot protein expression – Densitometry analysis



Lane	ROI	Area	IntDen
1	WT hRyR2	756	131.34
2	D4829A	756	93.398
3	Y4813A	756	97.086
4	Y4839A	756	74.360
5	Y4839W	756	64.016



Lane	ROI	Area	IntDen
1	WT hRyR2	756	48.052
2	D4829A	756	56.934
3	Y4813A	756	58.512
4	Y4839A	756	43.566
5	Y4839W	756	46.716

Figure 3.15. Integrated densitometry analysis to measure hRyR2 protein expression. Western blot of (A) control and (B) with the addition of 2 mM NaB. A lower integrated density value, determined by a darker area, indicated greater protein expression. A 1.82 fold increase in hRyR2 protein expression occurred with the addition of NaB listed in table 3.11. Densitometry was assessed as described in chapter 2.2.3.6.

Lane	Control IntDen	NaB IntDen	Factor increase
1	131.34	48.05	2.73
2	93.40	56.93	1.64
3	97.09	58.51	1.65
4	74.36	43.57	1.70
5	64.02	46.72	1.37
Mean ± SEM			**1.82 ± 0.2**

Table 3.11. Comparing the difference in hRyR2 protein expression between control and addition of sodium butyrate using integrated density measurements. A low integrated density value represents a darker area. The addition of NaB increased hRyR2 protein expression by 1.82 ± 0.2 fold (p=0.0085, n=5). Integrated densitometry values are from figure 3.15.

3.4 – Discussion

In order to understand processes of hRyR2 channel gating and how it is regulated during normal and pathogenic states, further information is required on structural mechanisms involved in conformational changes occurring at the proposed selectivity filter. Three residues located in the selectivity filter and pore helix of PFR hRyR2 are predicted to form a hydrogen-bonding network that form a defined structural element within the pore region acting to regulate channel gating analogous to known mechanisms occurring in K^+ channels (Cuello *et al.,* 2010a; McCoy and Nimigean, 2012). The development and introduction of subtle differences in chemical properties of amino acids are invaluable for pinpointing specific traits of side chain function, especially when detailed structural gating elements for hRyR2 remain unknown (Welch *et al.,* 2004; Euden *et al.,* 2013b; Ramachandran *et al.,* 2013; Mei *et al.,* 2015).

The selection of residues for substitution at positions Y4813, D4829 and Y4839 were carefully considered as every amino acid side chain has multiple chemical and physical attributes (valence, hydrophobicity, polarity, hydrogen bonding ability, and size), meaning that point mutation, in particular side chain exchange, would result in numerous chemical and steric alterations in the local protein environment (Pless and Ahern, 2013). The selection process discussed in sections 3.1.3 and 3.1.4 was employed to eliminate a proposed network of interactions by three alanine residues around the pore region. In addition, to comprehensively assess the importance of residue interaction on the stabilisation of the proposed selectivity filter, that is predicted to act as a defined structural element in hRyR2 channel gating (regulated by a network of interactions), three residues with particular side chain chemical and physical attributes (hydrogen-bonding properties) were selected. Tyrosine was replaced by tryptophan at positions Y4813W and Y4839W, and the conserved aspartic acid was replaced by a glutamic acid residue (D4829E) at the proposed selectivity filter.

3.4.1 Construction and Expression of mutant hRyR2 channels

Construction of recombinant mutant hRyR2 cDNA was followed by verification of protein expression. It was necessary to assess whether the introduction of a missense point mutation altered protein expression. A reduced, or absence of, mutant hRyR2 expression would have deleterious consequences on downstream functional assays. It was confirmed that point mutations occurring within the proposed pore region did not alter protein expression when compared to WT hRyR2, shown in figure 3.14. The addition of NaB in this study augmented hRyR2 protein expression, depicted in figure 3.15, supporting previous reports by Guzadhur, (2009). The use of NaB within the transfection protocol was therefore continued throughout future transfections.

This chapter has described molecular and cellular biology techniques used to generate the hRyR2 mutations to test the proposed hypotheses outlined in chapter 1.6. In summary, the successful construction and expression of all six hRyR2 mutants permitted the continuation of the PhD project, whereby cellular and electrophysiological approaches were utilised to fully characterise the effect of point mutations on hRyR2 channel gating, discussed in chapters 4, 5, 6 and 7.

Chapter Four:

Functional Assessment of mutant Selectivity Filter and Pore Helix hRyR2 channels

Functional Assessment of mutant Selectivity Filter and Pore Helix hRyR2 channels

Chapter Four – Aims

This chapter describes functional qualitative and quantitative assays that were used as an initial screen to examine the consequence of generating point mutations in the proposed selectivity filter and pore helix of hRyR2 on protein expression, tetrameric stability and function. The aims of this chapter were as follows:

- To confirm the functional homotetrameric status of a population of mutant selectivity filter and pore helix hRyR2 channels in a cellular context utilising intracellular Ca^{2+} imaging.

- To assess the activity of mutant hRyR2 channels by measuring equilibrium binding of [^{3}H] ryanodine.

4.1 – Introduction

4.1.1 Techniques to investigate mutant RyR2 functional status

The emphasis of this study was to elucidate the consequence of constructing point mutations occurring in critical regions lining the PFR on channel tetramerisation and function. Due to their intracellular location, specific techniques have been developed to study RyR2. A method of investigating RyR2 function has been based on visualising Ca^{2+} signalling in cells. Characterisation of mutant hRyR2 channels has been achieved using fluorescent based markers as tools to examine the functional status of a population of mutant channels, outlined in section 4.1.2. In addition, a subcellular approach, utilising tritiated ([^{3}H]) ryanodine, was used to investigate the activity of mutant hRyR2 channels, detailed in section 4.1.3.

4.1.2 Caffeine-induced calcium release assay

A cellular based assay, termed caffeine-induced calcium release, has been developed to examine the consequences of point mutations in hRyR2 on intracellular Ca^{2+} handling (Thomas *et al.,* 2004). HEK293 cells have been extensively used as a heterologous cellular model for studying hRyR2 function, described in chapter 2.2.2.2, as importantly, these cells lack endogenous RyRs, therefore Ca^{2+} signals from ER stores can confirm channel function (Du *et al.,* 2001; Kong *et al.,* 2008; MacLennan and Chen, 2009; Viero *et al.,* 2012). The elevation of cytosolic Ca^{2+} concentration $[Ca^{2+}]_{cyt}$ as a consequence of RyR2 activation can be used as a biomarker for determining the functional status of wild-type and mutant channels expressed in HEK293 cells. The use of confocal laser scanning microscopy (CLSM) has enabled high resolution imaging of membrane-permeable Ca^{2+} sensitive fluorescent dyes (fluorescent Ca^{2+} indicators) such as Fluo3, to measure overall intracellular Ca^{2+} changes as outlined in section 4.1.2.1.

Activating channels by caffeine, an RyR agonist, provokes a Ca^{2+} response inducing a fluorescent intensity change that can be measured, therefore caffeine has been regularly used to examine Ca^{2+} dynamics in whole cell experimental models that express RyR channels (Mead-Savery *et al.,* 2009; Euden *et al.,* 2013b; Ramachandran *et al.,* 2013; Mei *et al.,* 2015). Although the exact mechanism of RyR2 activation by caffeine is unknown, it is considered to occur through an indirect

action, sensitising RyR2 to activating Ca^{2+} and lowering the luminal Ca^{2+} threshold (Sitsapesan and Williams, 1990; Kong *et al.,* 2008).

4.1.2.1 Fluorescent Ca^{2+} indicator – Fluo3

Fluo3 molecules exhibit an increase in fluorescence upon binding Ca^{2+} revealing spatial dynamics of many elementary processes in Ca^{2+} signalling (Clapham, 1995; Cheng *et al.,* 1996; Bootman *et al.,* 1997). Fluo3 has an absorption spectrum compatible with excitation at 488 nm by Argon-ion laser and emissions when bound to Ca^{2+} from 506 to 526 nm (Rijkers *et al.,* 1990). The Fluo3 molecule shares similar properties with Ca^{2+} chelators such as EGTA (ethylene glycol tetraacetic acid) and BAPTA (1,2-bis(o-aminophenoxy)ethane-N,N,N',N'-tetraacetic acid) binding Ca^{2+} with high affinity (K_D 325 nM) (Grynkiewicz *et al.,* 1985; Paredes *et al.,* 2008). Its high specificity for Ca^{2+}, and sensitivity over an appropriate concentration range with linear output (calcium concentration proportional to fluorescence intensity), ensure that Fluo3 has a large signal-to-noise ratio for imaging analysis.

4.1.2.2 Fluo3-acetoxymethyl permeation – HEK293 cell loading

Efficiency of fluorescent indicator cell loading has improved with the attachment of a modified uncharged acetoxymethyl (AM) ester to Fluo3 (Fluo3-AM), enabling the indicator to permeate cell membranes (Paredes *et al.,* 2008). In addition, the permeation of the fluorescent indicator involves a dispersing agent (Pluronic ® F-127) as AM esters are relatively insoluble in aqueous solutions, therefore Pluronic ® F-127 facilitates the solubilisation of water-insoluble dyes, assisting cell loading. Once passively loaded inside the cell cytosol, nonspecific esterases cleave the Fluo3-AM resulting in a charged Fluo3 fluorescent molecule that decreases the probability rate of indicator leakage from the cell.

4.1.2.3 Confocal Laser Scanning Microscopy

As described above, Ca^{2+} is used as a biomarker for studying the function of RyR2 channels when expressed in fluorescent Fluo3-loaded HEK293 cells by CLSM. CLSM offers many advantages over conventional light microscopy, in particular, it utilises a pair of pinhole apertures to limit the specimen focal plane, removing extraneous light originating in out-of-focus regions, increasing the optical resolution

and contrast (Webb, 1996). Fluorescent based images are prone to photo-bleaching from exposure to light, decreasing the signal-to-noise ratio and image resolution (Bernas *et al.,* 2004). To overcome this, excitation light (488 nm) from a high-powered laser passes through a pinhole filter and is directed towards a series of horizontally and vertically rotating mirrors by the acousto-optical beam splitter (AOBS), shown in figure 4.1. These mirrors allow the excitation light to systematically scan across the sample in a point-by-point fashion preventing global photo-bleaching. For these reasons, and the availability of a SP5 CLSM (Leica), visualisation of Ca^{2+} signalling to functionally characterise mutant RyR2 channels were completed using fluorescent based CLSM.

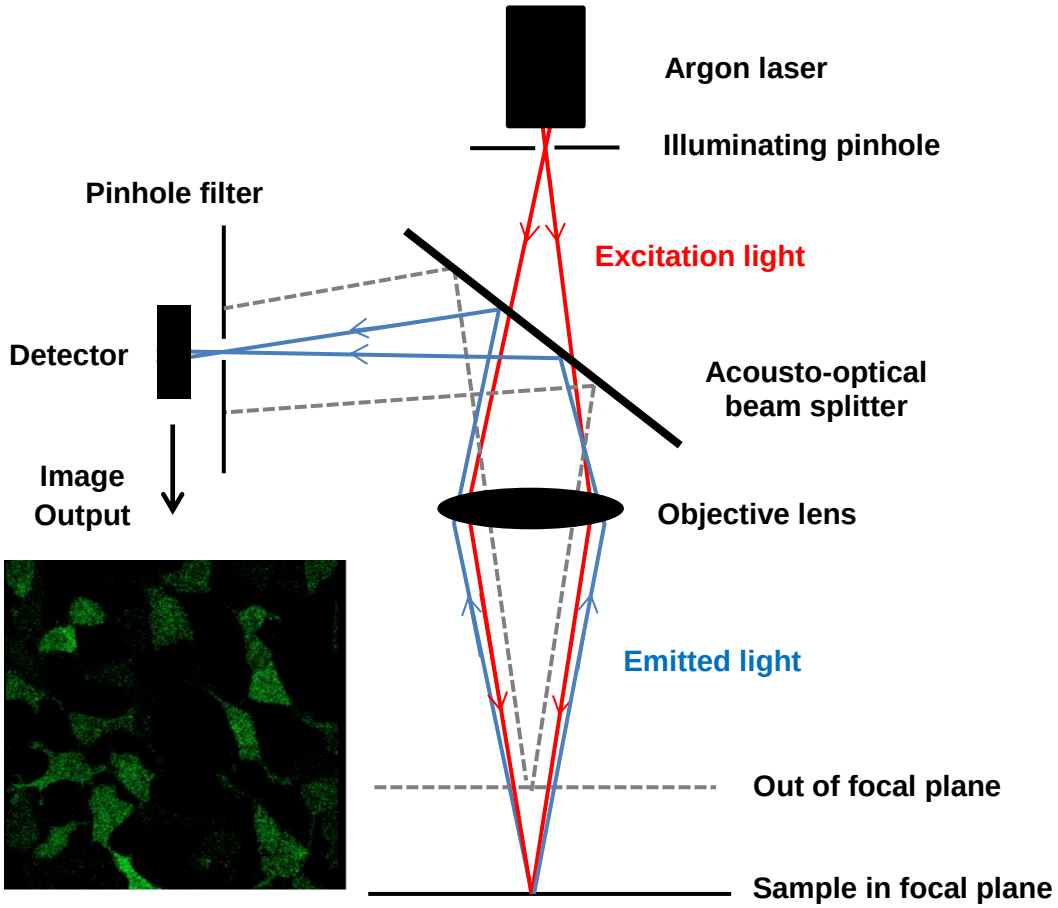


Figure 4.1. Fundamental principles of confocal optics. Schematic representation of confocal microscopy showing excitation (red) and emitted (blue) light in the focal plane. The AOBS directs light from the focal plane through a pinhole filter generating a high-resolution optical image while excluding extraneous light reflected from above the focal plane (grey dotted line). Diagram adapted from Mongan *et al.*, (1999).

4.1.3 [^{3}H] ryanodine binding assay measuring mutant RyR2 activity

Among the macroscopic techniques established to investigate the function of large numbers of RyR channels (section 4.1.1), an approach involving the isolation of mixed-membrane vesicles to monitor mutant channel activity was developed (Chu *et al.,* 1990). The advent of [^{3}H] ryanodine has provided an indispensable tool that was initially used in the identification and isolation of RyR2 (Campbell *et al.,* 1987; Lai *et al.,* 1988; Hymel *et al.,* 1988) and more recently used to assess the activity of RyR channels under particular conditions. The ryanodine molecule can only access its high affinity binding site when the channel is in an open conformation (Lai and Meissner, 1989; Chu *et al.,* 1990; Sutko *et al.,* 1997; Tanna *et al.,* 1998), therefore hRyR2 activity can be assessed by specific radioactive binding measurements.

In previous studies, [^{3}H] ryanodine binding assays have been used to investigate the effect on RyR function of various compounds known to modulate channel activity, including physiological ligands such as Ca^{2+}, Mg^{2+}, ATP, calmodulin and PKA (Holmberg and Williams, 1989; Imredy and MacLennan, 1998; Balshaw *et al.,* 2001; Swan *et al.,* 2003), non-physiological ligands such as caffeine, JTV-519 (K201), dantrolene (Holmberg and Williams, 1989; Jones *et al.,* 2005; Hunt *et al.,* 2007; Seidel *et al.,* 2014), and accessory proteins such as FKBP12.6 (Yano *et al.,* 2003; Zissimopoulos *et al.,* 2012), as binding of ryanodine is enhanced by compounds which activate the channel, and is reduced by other agents that inhibit RyR activity.

While the exact binding site is unknown, proteolytic digestion (Callaway *et al.,* 1994), photo-affinity labelling (Witcher *et al.,* 1994) and observations that ryanodine can only access its site when the channel is in an open confirmation has led to the suggestion that the binding site is located in the C-terminal pore region of the channel (Witcher *et al.,* 1994; Callaway *et al.,* 1994; Wang *et al.,* 2003; Mukherjee *et al.,* 2014). In addition, numerous studies have investigated alanine scanning within the PFR and have identified several residues that effect or even abolish [^{3}H] ryanodine binding, discussed in section 4.4.2 (Zhao *et al.,* 1999; Gao *et al.,* 2000; Du *et al.,* 2001; Li *et al.,* 2002a; Wang *et al.,* 2003; Du *et al.,* 2004; Wang *et al.,* 2004; Ranatunga *et al.,* 2005).

The three residues located in the selectivity filter, D4829, and pore helix, Y4813 and Y4839 depicted in figure 4.2, are in similar positions within the RyR PFR to residues

investigated in previous studies (section 4.4.2) (Gao *et al.,* 2000; Wang *et al.,* 2003; Euden *et al.,* 2013b). Measurements of equilibrium [^{3}H] ryanodine binding were important to assess the consequence of alanine and conservative mutations on channel activity, in particular to assess if the mutations affected channel gating or altered the access to, or affinity of, the ryanodine binding site.

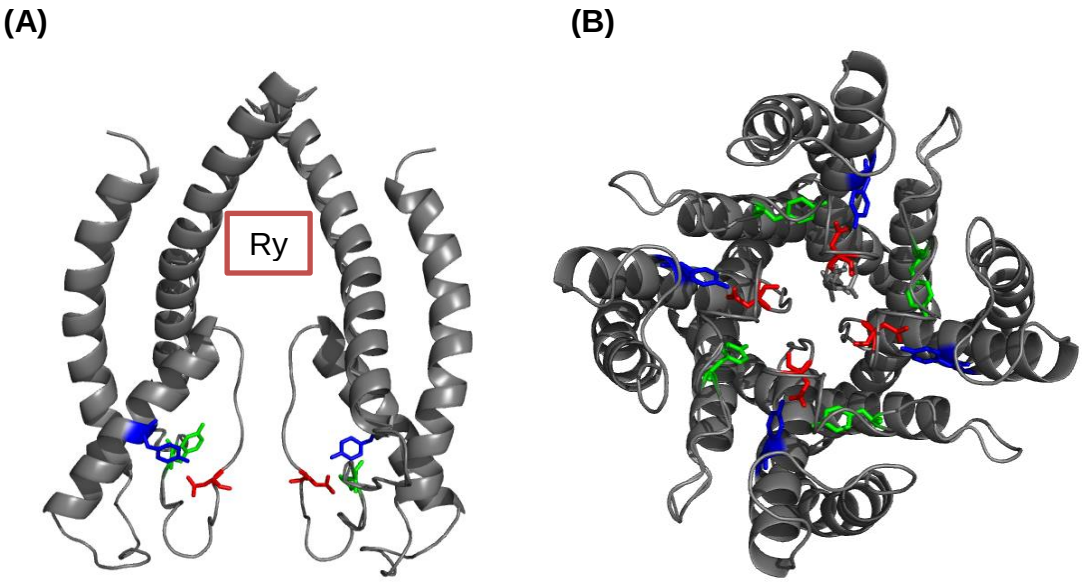


Figure 4.2. The pore-forming region RyR2 analogy model. Highlighted residues correspond to Y4813 (blue), D4829 (red) and Y4839 (green). (A) Side view of the PFR RyR2 highlighting the proposed region of the ryanodine binding site, boxed "Ry" (Witcher *et al.,* 1994; Callaway *et al.,* 1994; Wang *et al.,* 2003), two monomers shown for clarity. (B) Luminal view of the PFR RyR2 channel with central aligned pore. Highlighted residues are at ideal distances to form a hydrogen-bonding network that may support and stabilise selectivity filter regulated channel gating akin to known mechanisms in K^+ channels outlined in chapter 1.5.

4.2 – Materials and Methods

4.2.1 Materials – Ca^{2+} imaging reagents and agonists

20 % Pluronic acid stock: 50 µg pluronic acid was dissolved in 250 µL DMSO to form a 20 % stock.
Fluo3-AM solution: 50 µg Fluo3-AM was added to 44 µL of 20 % pluronic stock to obtain a stock concentration of 1 mM Fluo3-AM.
Fluo3-AM mDMEM solution: 10 µL Fluo3-AM pluronic acid stock was added to 1 mL mDMEM to obtain a 10 µM working concentration.
100 mM caffeine stock: 20 mg caffeine was added to 1 mL mDMEM pre-heated to 37 °C to facilitate solubilisation.

4.2.2 Methods – Caffeine-induced calcium release assay

4.2.2.1 Effectene transfection

RyR2-HEK293 cell transfections for Ca^{2+} imaging was performed using the non-liposomal, lipid-based Effectene kit (Qiagen) due to its high transfection efficiencies and low cell cytotoxicity requiring low DNA concentrations (0.8 µg per experiment). HEK293 cells were seeded at 1 x 10^5 cells/mL in 200 µL menisci onto coverslips (MatTek) coated with 5 µL mouse laminin (1 mg/mL) obtained from Sigma. Laminin was evenly coated onto coverslips using the decanting-end of a 200 µL pipette tip prior to the addition of cells. The coverslips were incubated for 2-3 h at 37 °C, 5 % CO_2, to allow for cell adhesion prior to transfection. A transfection mixture was prepared containing plasmid DNA (0.8 µg for 7 coverslips) made up to 100 µL using buffer EC. A DNA-condensing enhancer was added (6.4 µL) to the mixture before vortexing and incubating at RT for 5 min. 20 µL Effectene was added to the reaction which was further vortexed and incubated at RT for 10 min to produce condensed Effectene-DNA complexes. 600 µL of pre-warmed cDMEM was added to the reaction, mixing twice, before adding 100 µL Effectene-transfection mixture to each coverslip (x 7). The coverslips were returned to the incubator for 24 h. Each coverslip was flooded with 2 mL cDMEM the following day before returning to the incubator for a further 24 h (total 48 h post-transfection). HEK293 cells expressing hRyR2 protein were verified by eGFP imaging prior to determining channel function using light microscopy, described in section 2.2.2.4. For a control, plates were

seeded with untransfected HEK293 cells and were subsequently assessed as described in the following sections.

4.2.2.2 Cellular Ca^{2+} imaging – Caffeine-induced calcium release assay

Cellular Ca^{2+} imaging studies of HEK293 cells expressing hRyR2 channel proteins were performed using a SP5 confocal microscope (Leica). Coverslips containing 2 mL media were removed 48 h post-transfection (Effectene) and dried using tissue. A 10 µM Fluo3-AM working stock was prepared by adding 10 µL Fluo3-AM pluronic acid mix (section 4.2.1) to 1 mL mDMEM. HEK293 cells were loaded (150 µL) with the 10 µM Fluo3-AM mDMEM and then incubated at 30 °C, 5 % CO_2 for 1 h. Coverslips were flooded with 1.2 mL mDMEM to stop Fluo3-AM loading and to initiate de-esterification (20 min). The medium was removed and replaced with 200 µL mDMEM immediately prior to imaging the coverslips using an oil-immersed, 63 x magnification objective and Argon laser (20 %). The Leica LAS AF Lite software was used for confocal imaging and was set up as stated; excitation of Fluo3-AM 488 nm, Argon laser set to 20 %, format 512 x 512 pixels, zoom factor 1.7, time interval 70 ms and frames set to 1000 (1 min recording). A field of view (FOV) containing 10 or more well loaded fluorescent HEK293 cells was chosen for each experiment shown in figure 4.4. Channel function was assessed by the addition of 20 µL caffeine stock (100 mM) to the 200 µL meniscus (final concentration 10 mM) 20-30 s into the recording. Large data files (~ 0.5 GB/1 min recording) were saved onto an external hard drive immediately after use which were analysed as described in section 4.2.2.3.

4.2.2.3 Caffeine-induced calcium release assay – Analysis

Ca^{2+} imaging analysis was performed using the Leica LAS AF Lite software before exporting the raw data into Excel. The change in fluorescent intensity (ΔF) was measured by selecting regions of interest (ROI) within the FOV containing cells loaded with Fluo3 Ca^{2+} indicator that responded to the addition of 10 mM caffeine. ΔF was background corrected by subtracting selected ROI containing background fluorescence. The basal Fluo3 signal intensity (F_0) was calculated as the mean average fluorescence before caffeine addition (first 20 s). Fluorescent transient plots were generated by normalising the data, dividing the background corrected change in fluorescence by the average basal fluorescence ($\Delta F/F_0$) as shown in

figure 4.3. An increase in Fluo3 fluorescent intensity upon caffeine addition corresponded to functional hRyR2 channels.

4.2.2.3.1 Measuring the maximum Ca^{2+} release from HEK293 cells expressing hRyR2 channels

The caffeine-induced Ca^{2+}-transient amplitude was measured in HEK293 cells expressing WT and mutant hRyR2 channels. The maximum Ca^{2+} release was determined by measuring the height of the peak Fluo3 signal (F), shown in figure 4.3, and subtracting the value by the average basal F_0. Due to differences in basal F_0 the maximum Ca^{2+} release peak was normalised and determined by the equation stated; $(F-F_0)/F_0$.

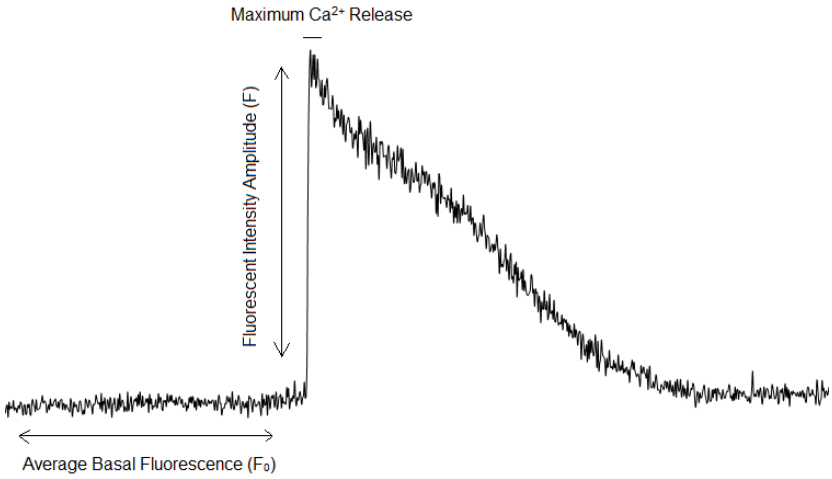


Figure 4.3. Measurement of maximum Ca^{2+} release in HEK293 cells expressing WT and mutant hRyR2 channels. The average basal Fluo3 signal intensity (F_0) was determined over a period of 20 s prior to 10 mM caffeine addition. The maximum Ca^{2+} release was determined by measuring the height of the peak Fluo3 signal (F) and subtracting the basal F_0; $(F-F_0)/F_0$.

4.2.3 Materials – Ryanodine binding reagents

Ryanodine binding buffer: 1 M KCl, 25 mM PIPES and 100 µM $CaCl_2$ adjusted to pH 7.4 with KOH.
[^{3}H] ryanodine: 1 µM stock obtained from Perkin Elmer (95 Ci/mmol).
'Cold' unlabelled ryanodine: 1 mM stock prepared in dH_2O obtained from Abcam.
Ryanodine binding buffer ($CaCl_2$ and caffeine): 1 M KCl, 25 mM PIPES, 100 µM $CaCl_2$ and 10 mM caffeine adjusted to pH 7.4 with KOH.
Ryanodine binding buffer (Caffeine): 1 M KCl, 25 mM PIPES and 10 mM caffeine adjusted to pH 7.4 with KOH.

4.2.4 Methods – [^{3}H] Ryanodine binding assay

To minimise local radioisotope contamination all [^{3}H] ryanodine binding experiments were completed inside a 1 m^2 plastic tray. Assays were prepared as stated in table 4.1, to a total reaction volume of 500 µL in triplicate (3 x hot and 3 x cold reactions). For valid comparison, relative contents of WT and mutant RyR2 protein in membrane preparation fractions were determined by Western blot densitometry analysis described in chapter 2.2.3.6. Mutant hRyR2 bands were calibrated to 100 µg WT protein, adjusting mutant mixed-membrane (MM) volumes accordingly. Cold ryanodine (10 µM) was added into cold reactions and 2 µL (10 nM) of the [^{3}H] ryanodine stock, stored at – 20 °C, was diluted 1 : 10 ratio (v/v) with binding buffer (total 20 µL) to reduce pipetting error. Reaction tubes were vortexed and incubated for 1.5 h at 37 °C in a water bath while Whatman GF-F filter pads were pre-soaked in binding buffer.

		[^{3}H] Ryanodine reaction	**Cold Ryanodine reaction**
Reagent	**[Working]**	**Volume**	
MM Sample	100 µg	X µL	X µL
Binding buffer		up to 500 µL	up to 500 µL
Cold ryanodine	10 µM	N/A	5 µL
[^{3}H] ryanodine	10 nM	20 µL	20 µL

Table 4.1. Representative ryanodine binding reaction. MM samples, completed in triplicate, were calculated by densitometry analysis described in section 2.2.3.6. Volumes were adjusted according to WT hRyR2.

Once the incubation period was complete, the reactions were stopped by the addition of 5 mL binding buffer. The pre-soaked GF-F filter pads were placed onto columns of a vacuum manifold (Hoeffer). Each reaction (5.5 mL) was passed through the filter pads by a vacuum created using a Heto Master Jet pump. The tubes were washed twice with binding buffer (5 mL) and passed through the column by vacuum to remove any unbound radioactive ryanodine. The GF-F filter pads were placed in scintillation vials with 10 mL scintisafe liquid and incubated for 24 h before counting radioactivity (disintegrations per minute - dpm) on a scintillation counter (Packard Tricarb 2100TR Liquid Scintillation Analyser). Specific binding was measured by subtracting 'cold' ryanodine with 'hot' [^{3}H] ryanodine binding results.

4.2.4.1 Effects of caffeine on [^{3}H] Ryanodine binding assay

Ryanodine binding assays were repeated as outlined in the protocol stated above with modification of binding buffers. Two binding buffers were prepared with either 100 µM $CaCl_2$ and 10 mM caffeine, or only 10 mM caffeine as stated in section 4.2.3.

4.3 – Results

4.3.1 Caffeine-induced calcium release assay

An initial qualitative assessment of the functional state of WT and mutant hRyR2 channels was performed by monitoring the release of Ca^{2+} from intracellular stores in response to the application of 10 mM extracellular caffeine. Figure 4.4 shows a representative FOV of transfected HEK293 cells expressing WT hRyR2 before (A) and after (B) caffeine addition. Figure 4.4A depicts the basal F_0 before agonist addition. Upon caffeine addition to the menisci, induction of Ca^{2+} release through activated WT hRyR2 channels was observed as a fluorescence intensity increase shown in figure 4.4B.

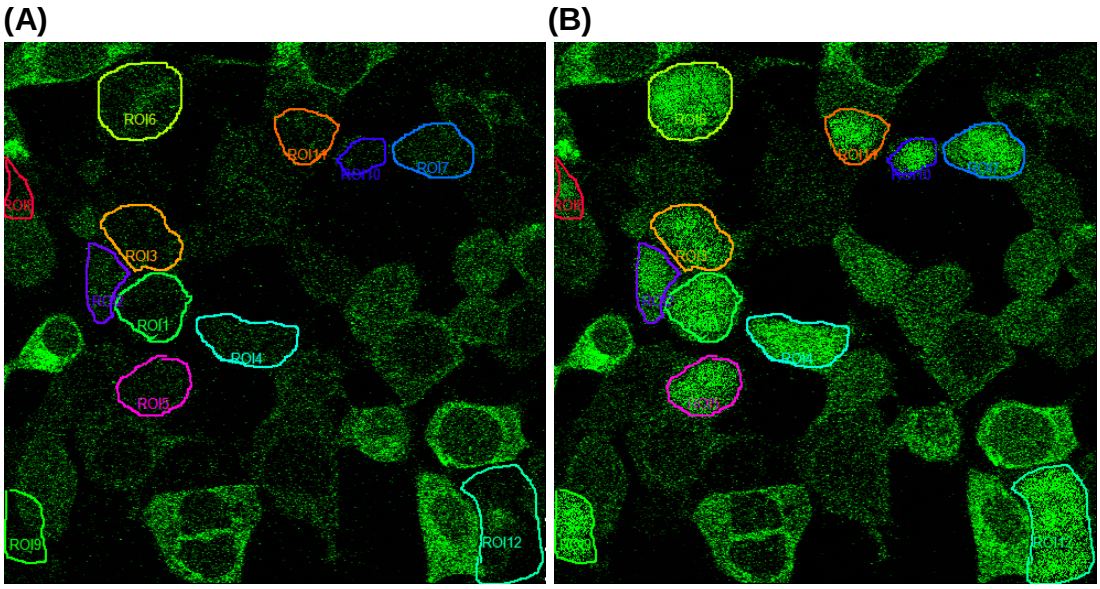
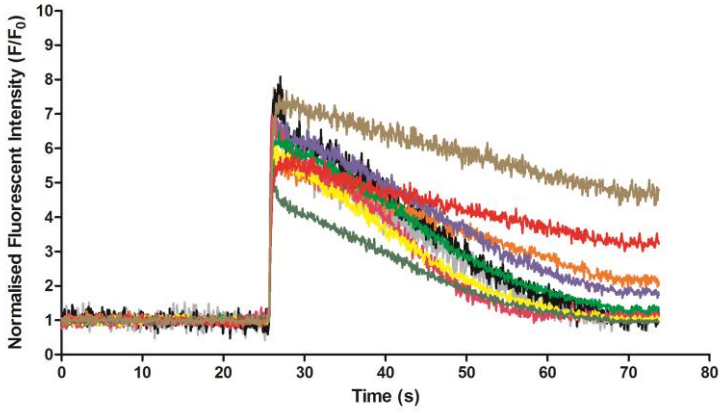


Figure 4.4. Caffeine-induced calcium release assay. Representative FOV of fluorescent Ca^{2+} imaging showing HEK293 cells, loaded with Ca^{2+} indicator Fluo3, expressing WT hRyR2 examined by CLSM. (A) FOV depicts basal F_0 of 10 or more HEK293 cells prior to caffeine addition. (B) Identical FOV following caffeine (10 mM) challenge. Ca^{2+} release through activated WT RyR2 channels is represented by a fluorescent intensity increase, highlighted by regions of interest (ROI). Scale: 63 x objective magnification.

Figure 4.5A represents a typical trace depicting changes in fluorescence intensity of ten HEK293 cells expressing WT hRyR2 channels following caffeine addition. The addition of caffeine, 20-30 s into the experiment, evoked a rapid 3-8 fold increase in fluorescence. The mean maximum Ca^{2+} release of HEK293 cells expressing WT hRyR2 was 5.11 ± 0.28, acquiring data from 55 cells from six separate transfection experiments, shown in figure 4.10. In addition, a control caffeine-induced calcium release experiment of untransfected HEK293 cells was completed. The addition of caffeine did not illicit a fluorescence change 20-30 s into the experiment (figure 4.5B).

(A)



(B)

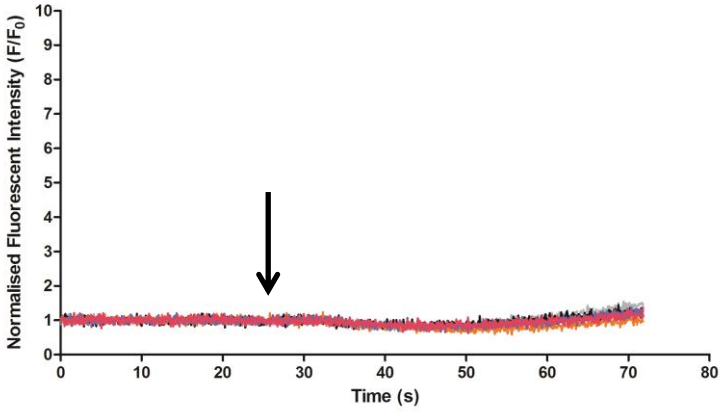


Figure 4.5. Caffeine-induced calcium release assay examining changes in fluorescence intensity upon addition of caffeine. (A) Ten representative ROIs containing Fluo3-loaded HEK293 cells expressing WT hRyR2 channels were monitored. Caffeine stimulation (20-30 s) induced a 3-8 fold increase in fluorescence intensity. (B) Untransfected RyR-deficient HEK293 cells did not illicit a fluorescence change upon caffeine stimulation. The addition of caffeine is indicated by a black arrow.

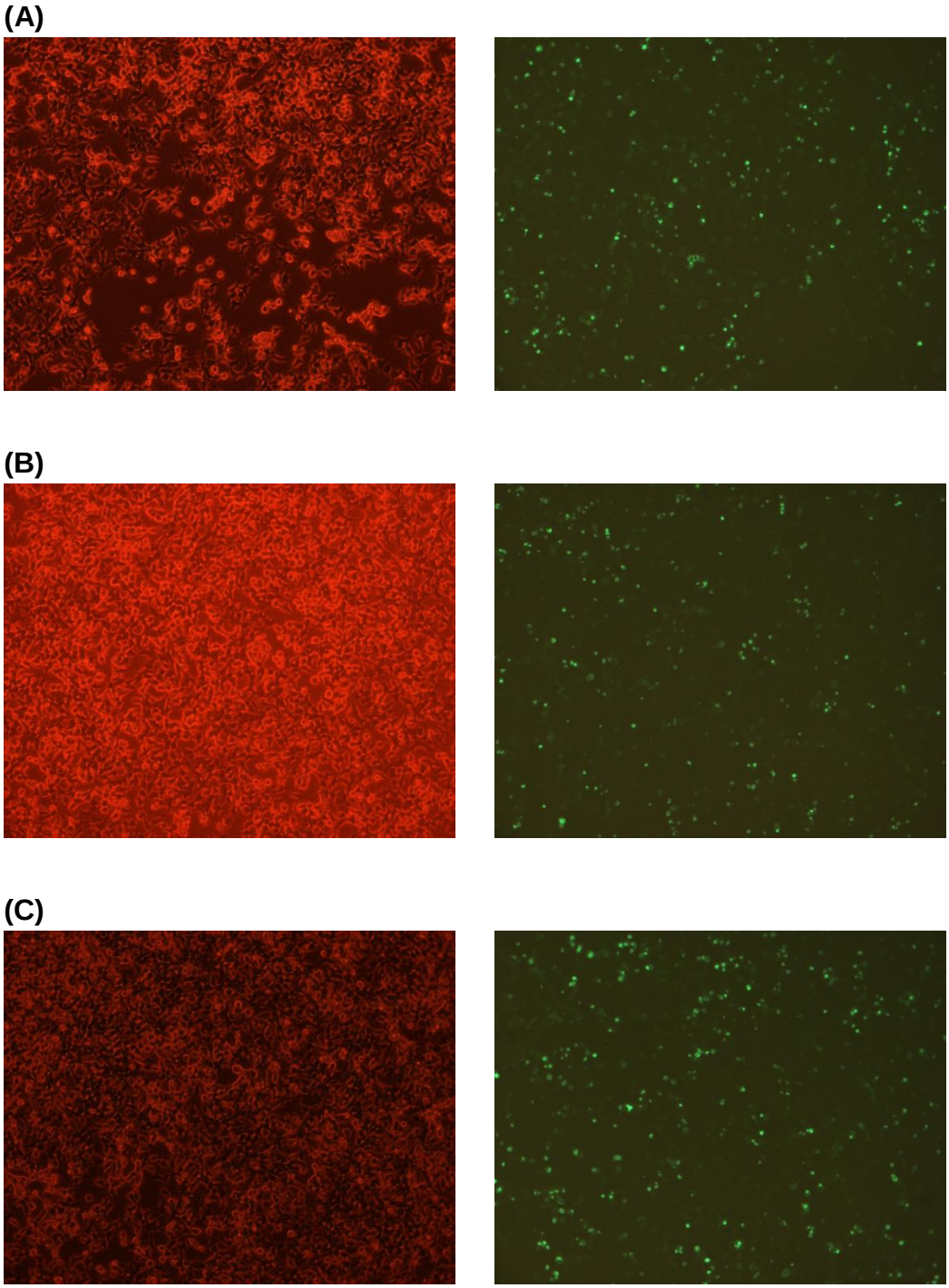


Figure 4.6. Expression of hRyR2 alanine mutations using the Effectene transfection method. Confocal microscopy eGFP imaging demonstrated high transfection efficiency using the Effectene method. (A) Y4813A, (B) D4829A and (C) Y4839A. (*left*) Bright field imaging displays the total cell density and (*right*) eGFP imaging, outlined in section 2.2.2.4, of green fluorescent HEK293 cells confirmed hRyR2 protein expression. Scale: 10 x objective magnification.

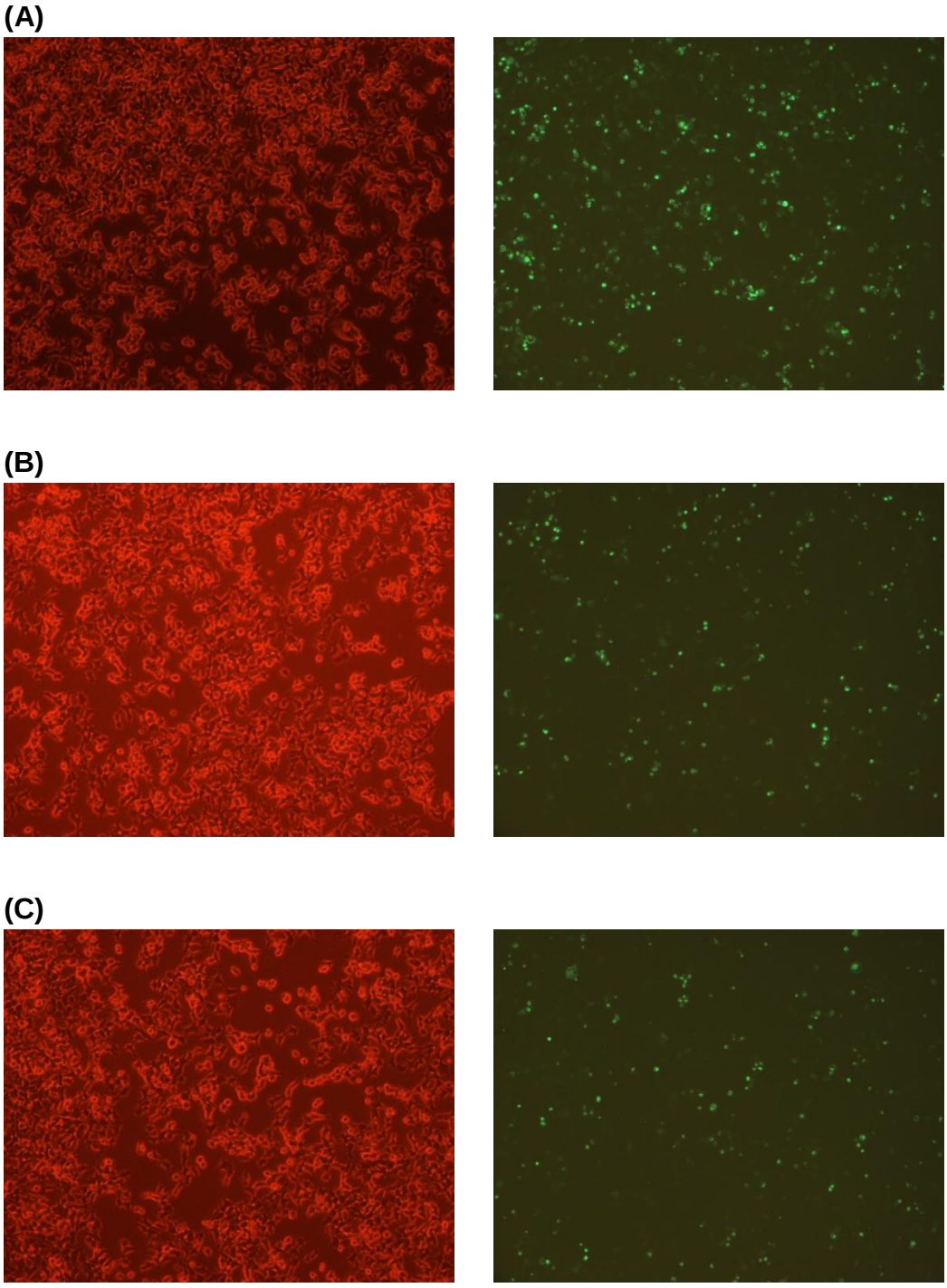


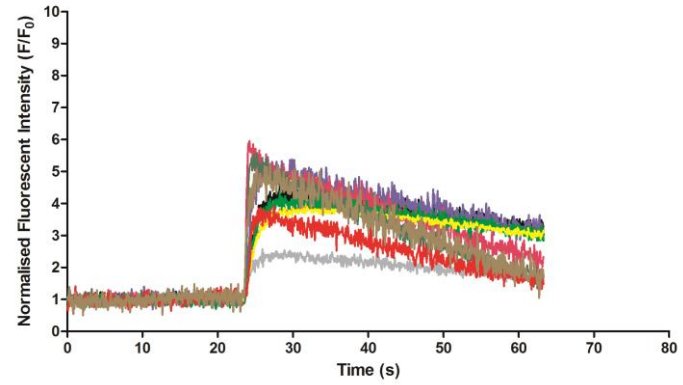
Figure 4.7. Expression of hRyR2 conservative mutations using the Effectene transfection method. Confocal microscopy eGFP imaging demonstrated high transfection efficiency using the Effectene method. (A) Y4813W, (B) D4829E and (C) Y4839W. (*left*) Bright field imaging displays the total cell density and (*right*) eGFP imaging, outlined in section 2.2.2.4, of green fluorescent HEK293 cells confirmed hRyR2 protein expression. Scale: 10 x objective magnification.

4.3.1.1 Mutant hRyR2 caffeine-induced calcium release assay

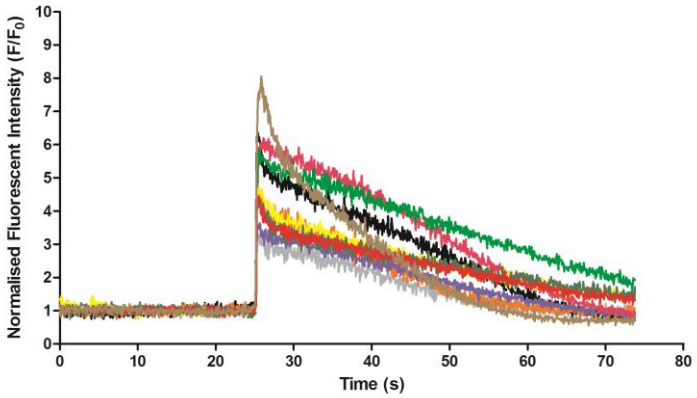
Protein expression of hRyR2 mutants was confirmed by eGFP imaging shown in figures 4.6 and 4.7. Transfection efficiencies observed were high using the Effectene method (> 40 %), ideal for Ca^{2+} imaging using CLSM. All alanine mutants (Y4813A, D4829A and Y4839A) and conservative mutants (Y4813W, D4829E and Y4839W) were sensitive to caffeine stimulation and evoked a rapid increase of fluorescence. Figures 4.8 and 4.9 depict representative responses from ten different HEK293 cells expressing mutant channels. The change in ΔF indicated that all hRyR2 mutations formed functional homotetrameric channels that could release Ca^{2+} from the HEK293 ER stores upon 10 mM caffeine addition.

The maximum Ca^{2+} release in Fluo3-loaded HEK293 cells expressing mutant channels was compared with cells expressing WT hRyR2 channels. Interestingly, the mean maximum Ca^{2+} release, determined by measuring the height of the Fluo3 signal peak (section 4.2.3.3.1), from cells expressing Y4813A (3.81 ± 0.26, p=0.0009) and D4829A (3.95 ± 0.24, p=0.0022) channels were significantly reduced compared to WT hRyR2 (5.11 ± 0.28) by 25.6 % and 22.7 %, respectively, shown in figure 4.10. There were no differences in maximum release between WT and the conservative mutants (Y4813W, D4829E and Y4839W) and Y4839A mutant hRyR2 channels (figure 4.10). The data from mutant channels were acquired from three separate transfection experiments and from a minimum of 39 cells, listed in table I (appendix I).

(A)



(B)



(C)

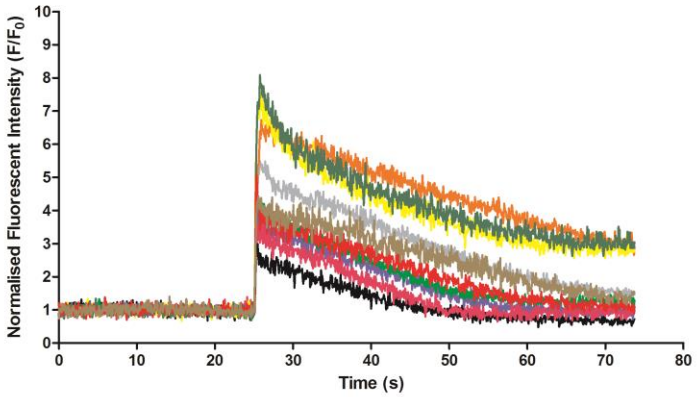
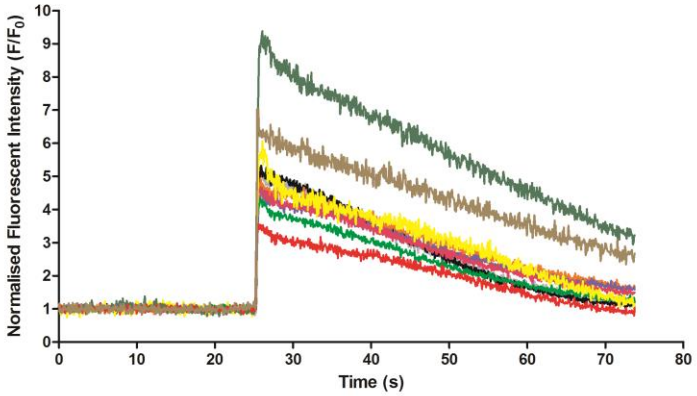
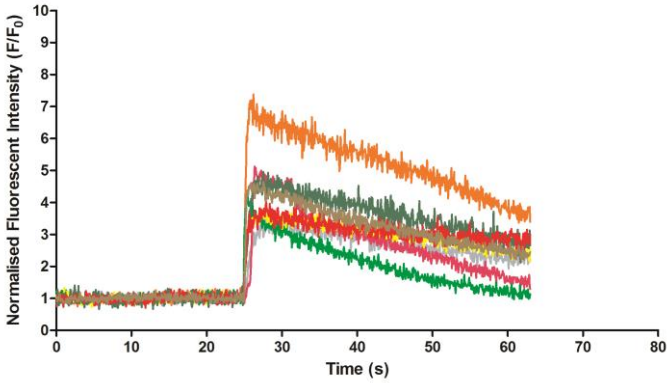


Figure 4.8. Caffeine-induced calcium release assay examining HEK293 cells transfected with alanine hRyR2 mutations. (A) Y4813A, (B) D4829A and (C) Y4839A. Caffeine stimulation induced a rapid increase in fluorescence intensity indicating that alanine mutations formed functional homotetrameric channels.

(A)



(B)



(C)

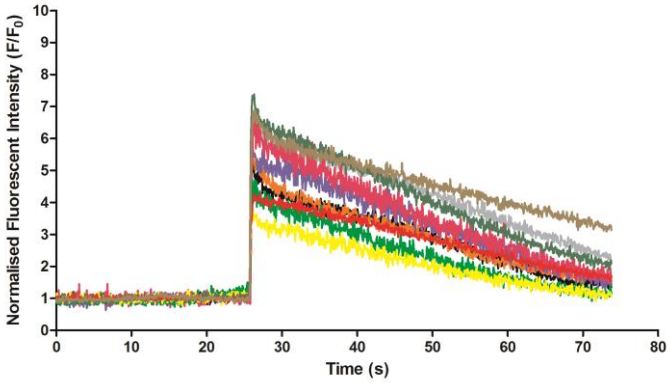


Figure 4.9. Caffeine-induced calcium release assay examining HEK293 cells transfected with conservative hRyR2 mutations. (A) Y4813W, (B) D4829E and (C) Y4839W. Caffeine stimulation induced a rapid increase in fluorescence intensity indicating that conservative mutations formed functional homotetrameric channels.

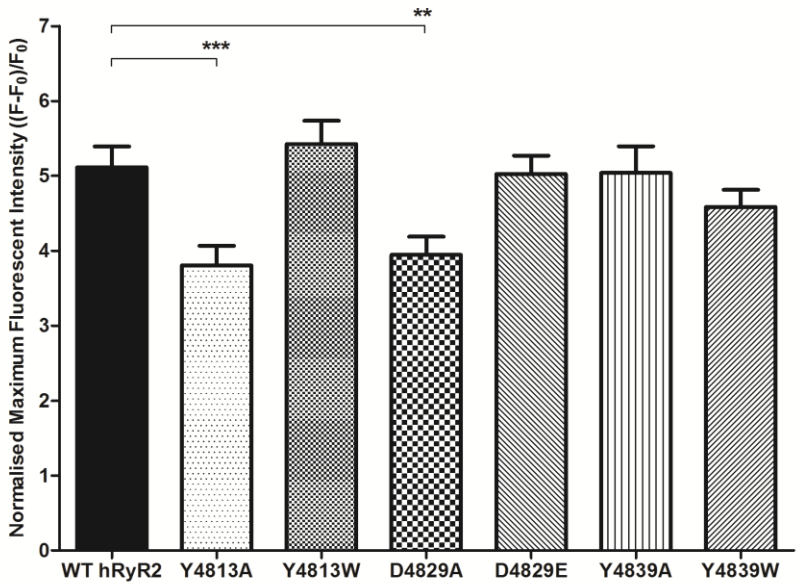


Figure 4.10. Measurement of maximum Ca^{2+} release in HEK293 cells expressing WT and mutant hRyR2 channels. Data are presented as the mean maximum Ca^{2+} release (error bars ± SEM) from at least three separate transfection experiments, acquiring data from a minimum of 39 cells. The total number of experiments and cells (ROIs) are listed in table I (appendix I). Differences between maximum Ca^{2+} release for WT and mutant channels were compared using an unpaired two-tailed *t*-test, *p* values < 0.05 were deemed significant, described in section 4.3.1.1.

4.3.2 Protein expression of hRyR2 mutants – Densitometry analysis

The relative expression of WT and mutant RyR2 channels in membrane preparation fractions was determined by Western blot densitometry analysis, adjusting equivalent quantities of mutant to WT RyR2 membrane fractions in [^{3}H] ryanodine binding assays for valid comparison. RyR2-HEK293 cell transfections were completed on three separate occasions and were subsequently labelled mixed-membrane # 1, 2 and 3. Mutant protein expression was comparable for all six mutations represented in figures 4.11, 4.12 and 4.13 and tables 4.2, 4.3 and 4.4.

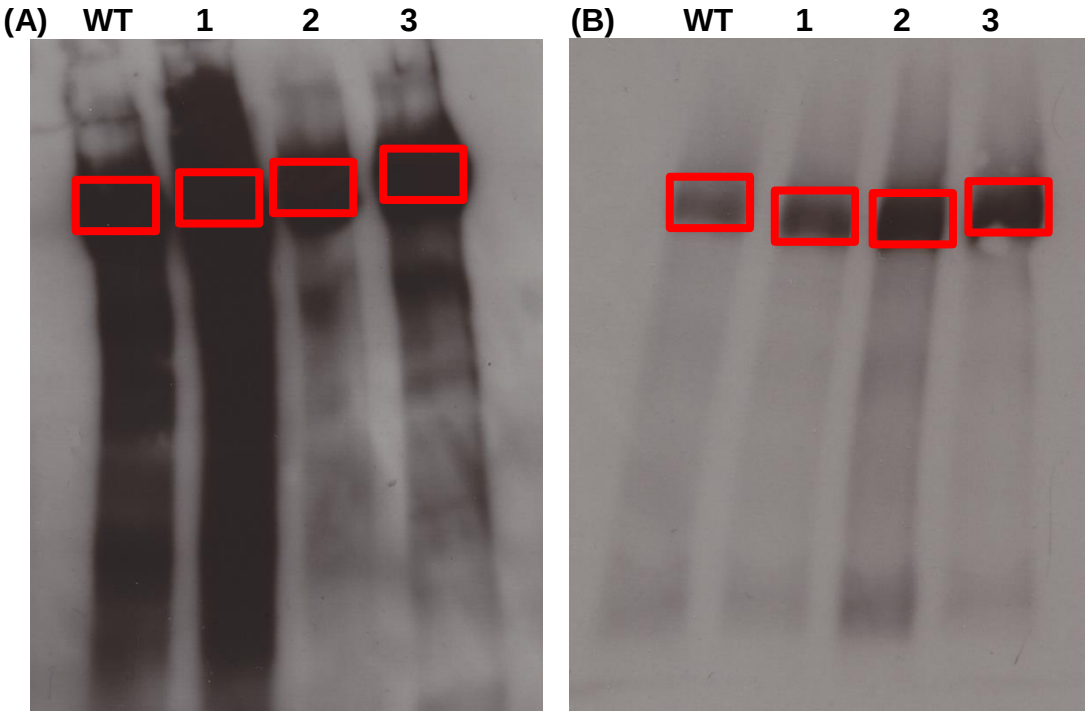


Figure 4.11. Quantification of (A) Y4813A and (B) Y4813W protein expression compared to WT hRyR2 using densitometry analysis. Figure numbering (1, 2 and 3) denotes separate mutant hRyR2 mixed-membrane preparations from HEK293 cell transfections.

	Y4813A			Y4813W	
	IntDen	**Normalised expression (%)**		**IntDen**	**Normalised expression (%)**
WT	40.685	100		89.208	100
MM #1	40.644	100.1		71.741	124.3
MM #2	41.586	97.8		52.376	170.3
MM #3	41.241	98.7		54.205	164.6

Table 4.2. Normalised Y4813A and Y4813W protein expression levels relative to WT hRyR2.

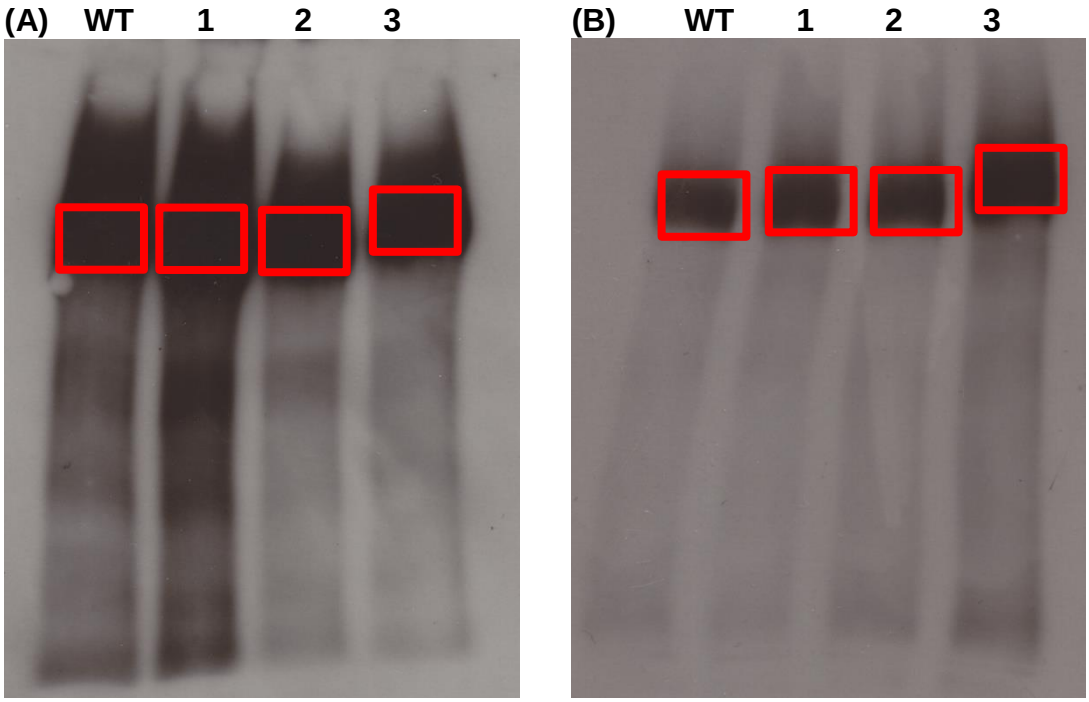


Figure 4.12. Quantification of (A) D4929A and (B) D4829E protein expression compared to WT hRyR2 using Western blot densitometry analysis. Figure numbering (1, 2 and 3) denotes separate mutant hRyR2 mixed-membrane preparations from HEK293 cell transfections.

	D4829A			D4829E	
	IntDen	**Normalised expression (%)**		**IntDen**	**Normalised expression (%)**
WT	42.43	100		60.288	100
MM #1	39.899	106.3		57.177	105.4
MM #2	43.721	97.0		57.678	104.5
MM #3	43.155	98.3		44.13	136.6

Table 4.3. Normalised D4929A and D4829E protein expression levels relative to WT hRyR2.

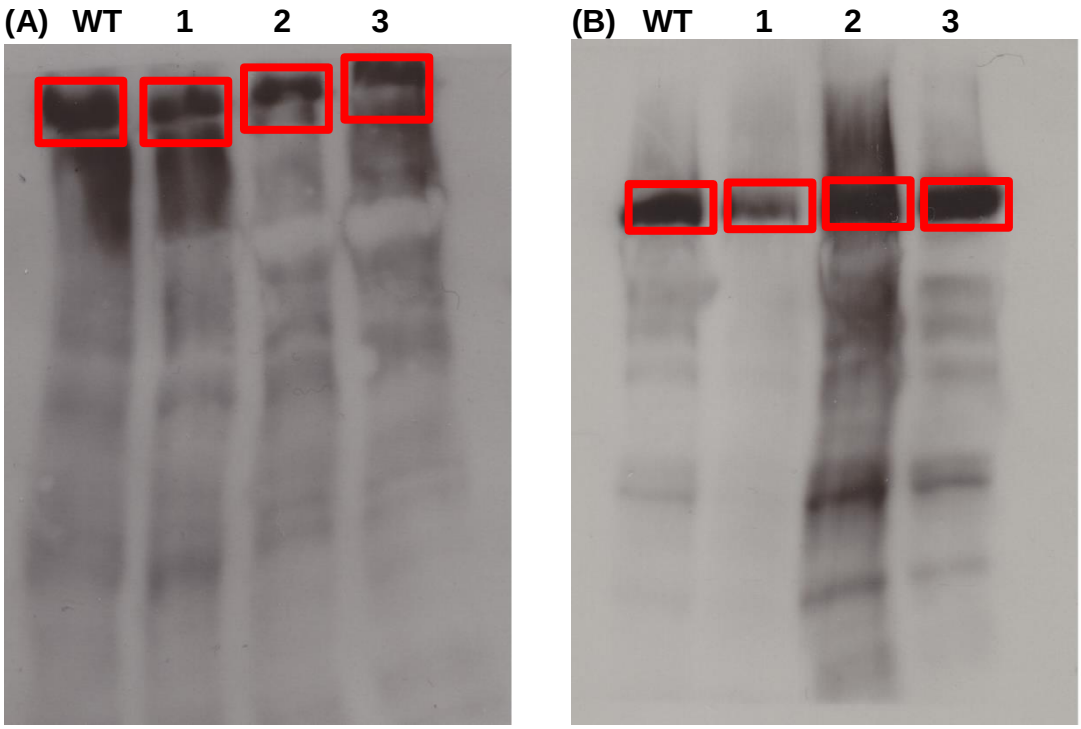


Figure 4.13. Quantification of (A) Y4839A and (B) Y4839W protein expression compared to WT hRyR2 using Western blot densitometry analysis. Figure numbering (1, 2 and 3) denotes separate mutant hRyR2 mixed-membrane preparations from HEK293 cell transfections.

	Y4839A			Y4839W	
	IntDen	**Normalised expression (%)**		**IntDen**	**Normalised expression (%)**
WT	63.335	100		70.882	100
MM #1	72.598	87.2		95.106	74.5
MM #2	82.294	77.0		54.842	129.2
MM #3	74.644	84.8		61.843	114.6

Table 4.4. Normalised Y4839A and Y4839W protein expression levels relative to WT hRyR2.

4.3.3 [^{3}H] ryanodine binding assay

Mutant RyR2 channel activity was assessed and compared quantitatively by determining the ability of mixed-membrane vesicles containing hRyR2 to bind [^{3}H] ryanodine, as the high-affinity binding site is only accessible when the channel is in an open conformation. Figure 4.14 shows an overview of the total values of specific Ca^{2+}-stimulated ryanodine binding to mutant RyR2, expressed as a proportion of the binding to WT hRyR2 protein. Point mutations at the proposed selectivity filter and pore region demonstrated a marked alteration in the ability to bind ryanodine described in sections 4.3.3.1/2/3/4 and listed in table 4.5.

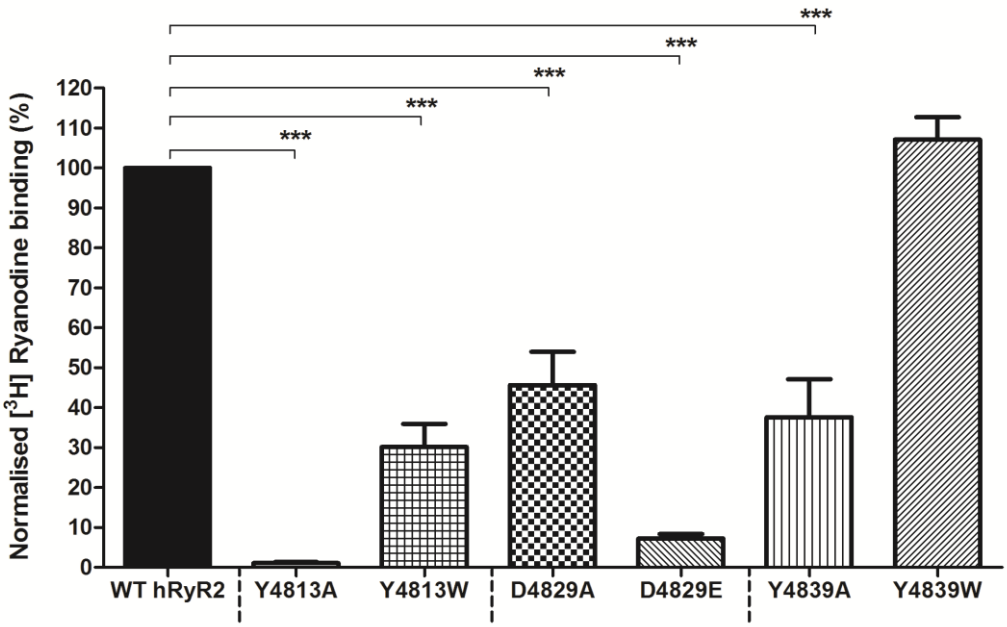


Figure 4.14. An overview of normalised [^{3}H] ryanodine binding of mutant relative to WT hRyR2 mixed-membrane fractions. Normalised binding values are listed in table 4.5.

	Normalised binding (%)		$p < 0.05$
WT hRyR2	100		
Y4813A	1.03	± 0.27	< 0.0001
Y4813W	30.12	± 5.80	< 0.0001
D4829A	45.63	± 8.36	< 0.0001
D4829E	7.18	± 1.18	< 0.0001
Y4839A	37.59	± 9.52	< 0.0001
Y4839W	107.1	± 5.63	ns

Table 4.5. Normalised [^{3}H] ryanodine binding results of mutant relative to WT hRyR2 mixed-membrane fractions. Normalised binding values are means from at least *n*=9 (± SEM), expressed as a percentage. [^{3}H] ryanodine binding results between WT and mutant hRyR2 channels were compared using a one-way ANOVA, Tukey's multiple comparison test, *p* values < 0.05 were deemed significant. Specific [^{3}H] ryanodine binding values, measured in disintegrations per minute (dpm), are listed in table II (appendix II).

4.3.3.1 [^{3}H] ryanodine binding - Y4813A vs Y4813W hRyR2 mutations

As can be seen in figure 4.14, the replacement of Y4813 with alanine produced a significant reduction in the level of ryanodine binding (1.03 %, compared to WT fractions). In contrast, the introduction of a tryptophan at Y4813, a conservative mutation with the ability to form hydrogen-bonding network, partially restored the binding of [^{3}H] ryanodine (30.12 %) compared to WT fractions. The increased binding of ryanodine observed for the conservative Y4813W mutation was significant compared to Y4813A (p<0.0001). However, Y4813W did not restore binding to the equivalent level of WT hRyR2.

4.3.3.2 [^{3}H] ryanodine binding - D4829A vs D4829E hRyR2 mutations

D4829A showed a marked reduction in ryanodine binding, 45.6 %, compared to WT channels shown in figure 4.14. Unlike the tryptophan residue substitution at Y4813W, the conservative mutation D4829E did not improve ryanodine binding (7.18 % compared to WT hRyR2). In fact, the replacement of glutamic acid at D4829E showed a large decrease in [^{3}H] ryanodine binding compared to the alanine hRyR2 mutation at D4829.

4.3.3.3 [^{3}H] ryanodine binding - Y4839A vs Y4839W hRyR2 mutations

Mutating a residue proposed to eliminate a hydrogen-bonding network, Y4839A, reduced ryanodine binding to 37.6 % compared to WT fractions. In contrast to the other two residues at positions Y4813 and D4829, reintroducing similar physicochemical interactions by tryptophan substitution (Y4839W) fully restored ryanodine-RyR2 binding interaction (107.1 %) compared to the WT channel, figure 4.14.

4.3.3.4 [^{3}H] ryanodine binding assay – Y4813A caffeine experiment

An additional assay was performed to examine the observed reduction of Y4813A [^{3}H] ryanodine binding (1.03 %) as described in section 4.3.3.1. Observations from intracellular Ca^{2+} imaging (section 4.3.1.1) confirmed that Y4813A was caffeine-sensitive and formed functional homotetrameric channels, albeit the maximum Ca^{2+} release was reduced by 25.6 % compared to WT hRyR2. [^{3}H] ryanodine binding assays were repeated on three separate occasions using modified buffers, outlined in section 4.2.4, containing caffeine to activate Y4813A channels. Binding buffers supplemented with 10 mM caffeine, the equivalent concentration used for mutant activation during caffeine-induced calcium release assays, did not restore Y4813A ryanodine binding, 1.15 % (caffeine buffer) and 2.03 % (caffeine and $CaCl_2$ buffer) when compared to WT hRyR2, shown in figure 4.15.

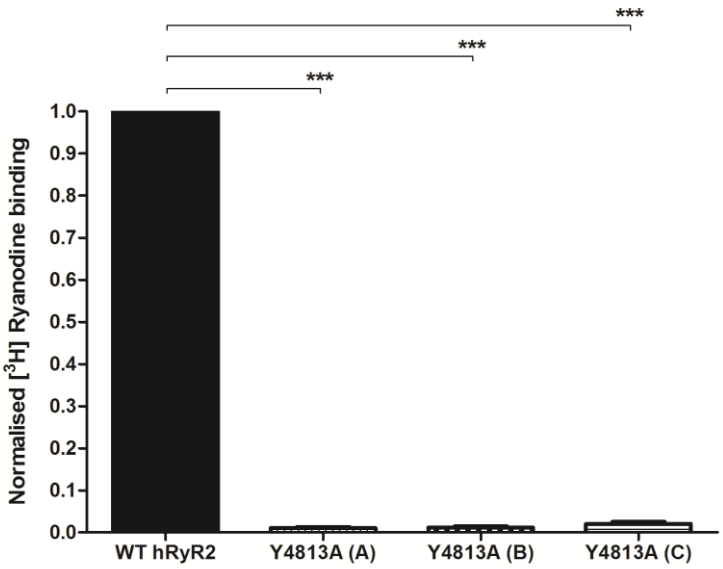


Figure 4.15. Y4813A caffeine [^{3}H] ryanodine binding experiment. Y4813A incubated in (A) $CaCl_2$ buffer, (B) caffeine buffer and (C) caffeine and $CaCl_2$ buffer. The addition of 10 mM caffeine, and or 10 mM caffeine and 100 µM $CaCl_2$ did not significantly increase [^{3}H] ryanodine binding to Y4813A. Buffers are listed in section 4.2.3.

4.4 – Discussion

This study elucidated the effects of point mutations occurring in the PFR on hRyR2 channel function. The constructed selectivity filter and pore helix mutants were examined to assess whether these channels were able to release Ca^{2+} upon caffeine addition, discussed in section 4.4.1, suggesting that mutant channels formed functional homotetramers. In addition to *in situ* function, mutant channel activity was examined by [^{3}H] ryanodine binding to isolated membrane populations, discussed in section 4.4.2.

4.4.1 Caffeine-induced calcium release assay

The process of RyR2 activation, where Ca^{2+} is released from intracellular stores through open channels into the cytosol, was measured using fluorescent Ca^{2+} indicators. Recording changes in fluorescent intensities, upon agonist addition, correlated to the functional status of channels and examined the stability of channels in a cellular context. Previous studies have reported non-functional channels arising from residue substitution in close proximity to the point mutations described in this thesis, such as inner helix mutations outlined in figure 4.16 (Wang *et al.,* 2003) and more recently, G4864V (Euden *et al.,* 2013b). It was therefore important to validate the structural stability of channels harbouring residue substitutions before investigating single-channel gating mechanisms as described in chapters 5 and 6.

The caffeine-induced calcium release assay, using a heterologous RyR-deficient HEK293 cell model, established that all six mutants were able to form functional homotetrameric channels that could release Ca^{2+} from ER stores into the cytoplasm upon activation by caffeine (figures 4.8 and 4.9). Interestingly, point mutations proposed to be in close proximity to the ion permeation pathway, Y4813A in the pore helix and D4829A in the selectivity filter, affected the maximum Ca^{2+} release from HEK293 cells compared to WT hRyR2 channels shown in figure 4.10. The reduction in Ca^{2+} release determined by a reduced ΔF suggested that Y4813A and D4829A had either affected the channel's caffeine sensitivity (and/or channel's Ca^{2+} sensitivity) thereby fewer mutant channels were activated, or alternatively that these mutations physically affected the ability to translocate Ca^{2+} ions through the pore. Determining the maximum Ca^{2+} release provided the first insight into functional

differences resulting from point mutation within the pore that was subsequently useful for evaluating altered [^{3}H] ryanodine binding, discussed in section 4.4.2.

4.4.2 [^{3}H] ryanodine binding assay

The impact of residue mutation on the ryanodine-hRyR2 interaction was assessed by monitoring equilibrium [^{3}H] ryanodine binding to mixed-membrane fractions containing either alanine, or conservative, mutant channels. Binding experiments were carried out in the presence of 100 µM $CaCl_2$, a condition under which hRyR2 has a high open probability (Mukherjee *et al.,* 2012). Using a high Ca^{2+} concentration was optimal for the detection of radioactive binding as access to the ryanodine binding site is limited to when the channel is in an open conformation (Tanna *et al.,* 1998).

Previous studies have demonstrated that mutating residues located in the PFR of RyR modifies the ability of the receptor to bind ryanodine (Zhao *et al.,* 1999; Gao *et al.,* 2000; Du *et al.,* 2001; Li *et al.,* 2002a; Wang *et al.,* 2003; Du *et al.,* 2004; Wang *et al.,* 2004; Ranatunga *et al.,* 2005). These previous investigations are consistent with the proposal that ryanodine binds within the ion conduction pathway of RyR2 within a wide vestibule, as mutations in the S6 region abolish or markedly reduce [^{3}H] ryanodine binding to RyR2 as depicted in figure 4.16 (Wang *et al.,* 2003; Ranatunga *et al.,* 2005). This suggests that the pore region constitutes an essential determinant of ryanodine-RyR2 interaction. Consistent with this proposal, the data presented in this chapter demonstrate that mutation of residues located in the proposed selectivity filter and pore region of hRyR2 reduced the binding of ryanodine, except for the conservative Y4839W channel, shown in figure 4.14. Western blot analysis established that all hRyR2 mutants were expressed at a comparable level to WT hRyR2 in HEK293 cells (figures 4.11, 4.12 and 4.13). Equivalent amounts of WT and mutant protein were used for the binding assays, determined by densitometry analysis, therefore reduced [^{3}H] ryanodine binding to mutant channels was not due to low or altered expression.

(A)

TM10 mutants	[^{3}H]Ryanodine binding	Caffeine response
	%	
RyR2(wt)	100 ± 36	+
I4844A[1]	47 ± 22	+
I4845A[2]	74 ± 14	+
F4846A[3]	5.4 ± 5.0	+
D4847A[4]	0.6 ± 0.8	−
I4848A[5]	59 ± 10	+
T4849A[6]	0.5 ± 0.8	+
F4850A[7]	0.1 ± 0.5	−
F4851A[8]	0.1 ± 0.3	−
F4852A[9]	84 ± 16	+
F4853A[10]	99 ± 28	+
V4854A[11]	36 ± 1.2	+
I4855A[12]	3.8 ± 1.6	+
V4856A[13]	1.0 ± 0.9	+
I4857A[14]	64 ± 2.4	+
L4858A[15]	2.5 ± 1.6	−
L4859A[16]	3.8 ± 1.4	−
A4860G[17]	58 ± 3.5	+
I4861A[18]	98 ± 5.7	+
I4862A[19]	61 ± 2.7	+
Q4863A[20]	0.0 ± 0.0	+
G4864A[21]	93 ± 4.3	+
L4865A[22]	87 ± 7.1	+
I4866A[23]	5.1 ± 1.8	−
I4867A[24]	25 ± 6.7	+

(B)

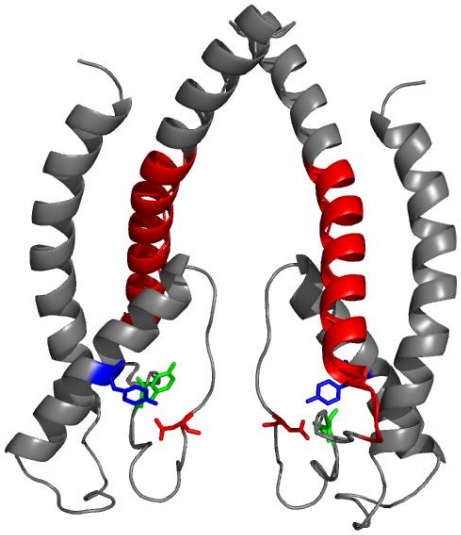


Figure 4.16. Investigating [^{3}H] ryanodine binding and caffeine response of inner (S6) helix RyR2 mutants. (A) The relative percentages of mutant [^{3}H] ryanodine binding were compared to WT RyR2. Caffeine-induced Ca^{2+} response in mutant hRyR2 channels were indicated by "+ or -". Figure adapted from (Wang *et al.,* 2003). (B) The Welch *et al* PFR hRyR2 analogy model highlighting the S6 helix mutations in red relative to the selectivity filter and pore helix mutations in this project, Y4813 (blue), D4829 (red) and Y4839 (green) (Welch *et al.,* 2004).

Once bound to WT hRyR2, the rate of ryanodine dissociation is very slow and binds almost irreversibly to its high affinity site stabilising the channel in an open, reduced conductance, conformation (Lindsay *et al.,* 1994; Needleman and Hamilton, 1997; Mukherjee *et al.,* 2014). Mutation-dependent alterations in ryanodine binding to hRyR2 may occur through several factors such as; the generation of unstable or closed channels, modification of structural components important in the ryanodine-hRyR2 interaction altering the access to, or affinity of, the binding site, or by altering the mutant channel's sensitivity to calcium. Consequently, these considerations were accounted for when interpreting the mutant hRyR2 [^{3}H] ryanodine results and

were assessed in combination with complementary assays such as Ca^{2+} imaging and single-channel bilayers discussed in chapters 5 and 6.

The reduction of [^{3}H] ryanodine binding to Y4813A hRyR2, 1.03 % of that seen in WT, indicated that alanine substitution modified the ryanodine-Y4813A interaction either by altering the properties of the binding site or by affecting the stability of the protein when isolated from whole-cell environment. The functional studies confirmed that Y4813A was caffeine sensitive, i.e. the channel opened in response to agonist, but caffeine failed to increase ryanodine binding to the isolated mixed-membrane preparation as described in section 4.3.3.4. Interestingly, the conservative tryptophan mutation, Y4813W, improved [^{3}H] ryanodine binding in comparison to the alanine mutation Y4813A. This significant increase was however only 30.12 % compared to WT hRyR2. The partial restoration of ryanodine binding by the replacement of tyrosine with tryptophan, a residue with similar aromatic bulk, steric occupancy and physicochemical hydrogen-bonding capabilities, highlights the importance of residue 4813 in this aspect of RyR2 function and provides an interesting insight into a potential hydrogen-bonding network originating from the pore helix to the selectivity filter.

The aspartic acid at position 4829, located at the luminal end of the selectivity filter is highly conserved throughout the RyR isoforms (GGGIG<u>D</u>), IP_3R (GGGVG<u>D</u>) (Taylor and Tovey, 2010) and K^+ channels (TVGYG<u>D</u>) (Heginbotham *et al.,* 1994; McCoy and Nimigean, 2012). Replacing this conserved residue with alanine, D4829A, reduced ryanodine binding to 45.63 % of the level seen in WT hRyR2. In contrast, the extension of the side chain by a methyl group, generating the conserved glutamic acid, reduced the ryanodine-D4829E interaction to 7.18 % compared to WT hRyR2. This observation suggested that the bulk of the residue at 4829 is much more important than its charge in maintaining a conformation that supports ryanodine binding. The reduced ryanodine binding resulting from the substitution of D4829 with either alanine or glutamic acid could be explained if conformational changes resulting from the substitutions either limited the access of ryanodine to its binding site, increased the rate at which bound ryanodine dissociates from its site, or altered the channel's Ca^{2+} sensitivity.

The alanine substitution at Y4839 produced hRyR2 channels that bound 37.59 % of the ryanodine bound to WT hRyR2. This confirmed that the reduction of hydrogen bonding capacity, by alanine substitutions, of all three residues examined in this

thesis reduces the capacity of hRyR2 to bind ryanodine. In addition, unlike the pore helix mutation Y4813W, the conservative mutation at Y4839W fully restored binding to 107.1 % of the WT hRyR2 level.

While all hRyR2 mutations investigated in this thesis reduced the ryanodine binding interaction to hRyR2 (except for Y4839W), only two mutations (Y4813A and D4829A) affected the maximum release of Ca^{2+} from HEK293 cells. This suggests that altered [^{3}H] ryanodine binding to hRyR2 does not exclusively determine channel function as the remaining mutations (Y4813W, D4829E and Y4839A) that reduced binding maintained the functional maximum Ca^{2+} release compared to WT hRyR2 channels. This highlights a limitation of the [^{3}H] ryanodine binding assay, as it can produce misleading results. Previous studies have shown that mutations affect the ability of the channel to bind ryanodine, however without affecting channel gating (Zhao *et al.,* 1999; Gao *et al.,* 2000; Chen *et al.,* 2002). Therefore it is essential to examine the mechanisms underlying altered ryanodine binding and maximum Ca^{2+} release, as a consequence of point mutation, by using the single-channel bilayer technique described in chapter 5.

In summary, two assays were used as an initial screen to examine the effect of point mutations at the selectivity filter and pore helix on channel function. The investigations reported in this chapter demonstrate that all six mutant hRyR2 channels were successfully expressed in HEK293 cells and formed functional Ca^{2+} release channels *in situ* that were able to translocate Ca^{2+} upon stimulation. In accordance to previous studies, [^{3}H] ryanodine binding to alanine substituted channels was altered suggesting that point mutations located in the PFR in this investigation had either affected the sensitivity to activating Ca^{2+} or modified the ryanodine binding site (Gao *et al.,* 2000; Wang *et al.,* 2003; Euden *et al.,* 2013b). The binding results highlighted the significance of side chain interaction properties (valence, hydrophobicity, polarity, hydrogen-bonding ability, and size) in the surrounding PFR environment, as engineering point mutations within PFR resulted in diverse and altered ryanodine-mutant hRyR2 interactions. The stability and gating behaviour of these mutants when purified and incorporated into planar bilayers was determined by single-channel experiments discussed in chapters 5 and 6.

Chapter Five:

Initial Single-Channel Characterisation of Mutant hRyR2 channels

Initial Single-Channel Characterisation of Mutant human Cardiac Ryanodine Receptor (hRyR2) channels

Chapter Five – Aims

To understand the involvement of a gating component in RyR2, formed by a potential hydrogen-bonding network between the selectivity filter and surrounding area, it was essential to characterise mutant hRyR2 proteins at the single-channel level. This chapter discusses the importance of the single-channel electrophysiology technique, and how it was used to determine general biophysical properties of mutant hRyR2 channel conduction, discrimination and permeability. The initial characterisation and ion handling properties established in this chapter set the foundation for investigating single-channel gating mechanisms discussed in chapter 6. The aims of this chapter were as follows:

- To initially screen purified selectivity filter and pore helix mutant hRyR2 channels assessing their stability when isolated, solubilised and incorporated into a planar lipid bilayer.

- To evaluate ryanodine modification and ion conduction of mutant hRyR2 compared to WT hRyR2 channels.

- To assess altered ion conduction properties in mutant hRyR2 channels by a series of ion handling experiments to probe potential mechanistic differences in ion channel discrimination, relative permeability and pore dimensions.

- To examine differences between previous and new structural modelling data in regard to residue positioning around the selectivity filter region.

5.1 – Introduction

5.1.1 The Single-Channel Electrophysiology technique

Ion channels possess three fundamental properties; (1) they translocate ions across the cell membrane, (2) they selectively discriminate between ions and (3) they regulate gating (opening and closing) in response to specific stimuli. These biophysical properties can be quantified by electrophysiological techniques to understand protein function such as mechanisms of channel gating. Conventional electrophysiology techniques such as whole-cell voltage clamp or patch-clamping cannot be used to study the biophysical properties of RyR2 channels due to their inaccessible intracellular SR location (Zhao *et al.,* 2009). The only method to gain biophysical information governing the function of RyR2 and its PFR is to study the behaviour of individual channels using the single-channel planar lipid bilayer technique.

The study of ion channel properties were first demonstrated using the bilayer technique by Miller and Racker, and Alvarez, described in chapter 2.2.4, and enables the investigation of single molecules in a well-controlled *in vitro* environment (Miller and Racker, 1976; Alvarez, 1986; Miller, 1986). The advantage of this technique is that the behaviour of single protein channels can be monitored under defined conditions. The ionic composition of the solutions bathing both faces of the channel can be manipulated either in the presence or absence of particular accessory proteins, modulators and permeant ions thus enabling comprehensive characterisation of channel gating, selectivity and conduction properties.

The single-channel technique is established by an electrical circuit that is formed by two ionic fluid filled chambers separated by an artificial lipid membrane in which a single ion channel is incorporated. Current flowing through the channel from one side of the membrane to another can be measured, depicted in figure 5.1, and interpreted using sophisticated data analysis software, discussed in section 5.2.3.5 and chapter 6.2.2. Idealised raw single-channel data details important measurements such as current amplitudes, frequency of events, dwell time intervals and open probability, revealing fundamental molecular kinetics of ion channel function.

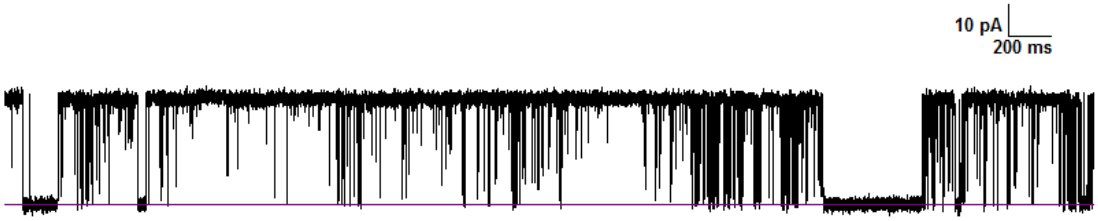


Figure 5.1. Single-channel recording of unitary current fluctuations from a single hRyR2 channel. Single-channel trace depicts clear gating transitions between open and closed states at + 40 mV in symmetrical 210 mM KCl conditions. The purple line denotes the closed state with upward deflections observed as channel openings.

5.1.2 The role of K^+ as the permeant ion for studying hRyR2

Although Ca^{2+} is the physiological permeant ion, single-channel bilayer experiments have been optimised by using K^+ ion as the charge-carrying species (Mukherjee *et al.,* 2012; Euden *et al.,* 2013b; Ramachandran *et al.,* 2013; Mukherjee *et al.,* 2014; Mei *et al.,* 2015; Bannister *et al.,* 2015). RyR2 has a very high unitary conductance when K^+ is the permeant ion, reaching a maximum of ~ 1 nS (Lindsay *et al.,* 1991). Under typical experimental condition (symmetrical 210 mM KCl) the conductance of RyR2 is approximately 789 pS outlined in section 5.3.4. Due to the large conductance of RyR2, K^+ ions offer the greatest signal-to-noise ratio (SNR), improving data accuracy when acquiring current amplitudes, frequency and dwell time interval measurements. The SNR ensures that even brief events are detected and prevents identifying noise as false gating events or disregarding a true event as background noise (Mukherjee *et al*, 2012). K^+ ions are therefore the most favourable cations to use for single-channel bilayer recording of RyR2 activity (Lindsay *et al.,* 1991).

5.1.3 Single-channel characterisation of mutant hRyR2

At present, identifying and altering residues or regions of interest within RyR2 by mutagenesis is the only method of investigating the contribution of these entities to single-channel gating mechanisms. In the absence of accurate structural data the Welch *et al* analogy model of the hRyR2 PFR, discussed in chapter 1.5.2, provides a framework that can be used to predict the involvement of domains and individual

residues in the processes of ion translocation and gating (Welch *et al.,* 2004). Predictions based on known mechanisms in K^+ channels such as a hydrogen-bonding network that regulates channel inactivation are tested by monitoring the function of mutant channels assessing their biophysical characteristics such as conductance, open probability, open and closed times in planar lipid bilayers.

Previous RyR2 studies utilising single-channel planar bilayers have focused on structural gating components and the process of cation discrimination and translocation in the RyR2 PFR. Such studies include investigating the contribution of a putative glycine hinge to RyR2 gating (Euden *et al.,* 2013b), the contribution of hydrophobic residues predicted to line the cytosolic vestibule of the RyR2 PFR (Mason *et al.,* 2012) and identifying acidic residues expected to coat the face both the luminal and cytosolic entrances of the RyR2 PFR (Mead-Savery *et al.,* 2009). The approach of studying the behaviour of single-channels has yielded novel information on the mechanisms underlying ion movement through RyR2.

To understand the involvement of a gating component in RyR2, formed by a potential hydrogen-bonding network between the selectivity filter and surrounding area proposed in chapter 1.5, it was essential to initially characterise mutant hRyR2 proteins at the single-channel level. To study the function of recombinant single hRyR2 channels at the molecular level the protein must be generated in a heterologous cell expression system, isolated and purified to be incorporated into a planar phospholipid bilayer, detailed in chapter 2.2.3. Previous investigation of channel function was confirmed in chapter 4 using Ca^{2+} fluorescent-based imaging. This important assay verified cellular channel function, thus the next logical step was to remove the membrane protein from a cellular environment and, in the absence of accessory proteins, to assess fundamental biophysical properties such as ion conduction and modification of function by ryanodine at the single-channel level.

5.2 – Methods and Materials

5.2.1 Electrophysiology reagents

All buffers and solutions were prepared in bottled dH_2O (AnalaR NORMAPUR®, VWR Chemicals) that were filter sterilised before use. General reagents are listed in chapter 2.1.8. All experiments were completed at RT 20 ± 2 °C.

5.2.2 Ion handling reagents

$BaCl_2$ solution: 205 mM $BaCl_2$ with 20 mM HEPES was prepared and adjusted to pH 7.4 using $Ba(OH)_2$. The addition of hydroxide ions increased the barium concentration by 5 mM. The final $BaCl_2$ concentration was 210 mM.

Monovalent organic cations: 210 mM X^+ ('X' represents monovalent organic cation) and 20 mM HEPES, pH 7.4.
Ethanolamine: 12.68 mL/L (v/v) ≥ 98 % ethanolamine (16.56 M) stock was prepared to obtain a 210 mM working solution, adjusting to pH 7.4 with HCl.
Diethanolamine: 20.19 mL/L (v/v) ≥ 99.5 % diethanolamine (10.4 M) stock was prepared to obtain a 210 mM working solution, adjusting to pH 7.4 with HCl.
Triethanolamine: 28 mL/L (v/v) ≥ 99 % triethanolamine (7.5 M) stock was prepared to obtain a 210 mM working solution, adjusting to pH 7.4 with HCl.

5.2.3 Methods – Single-channel bilayer experiments

5.2.3.1 Initial characterisation of mutant hRyR2

Single-channel bilayer experiments were set up as described in chapter 2.2.4. Upon channel incorporation, symmetrical 210 mM KCl conditions were established. WT and mutant hRyR2 channels were recorded in contaminant Ca^{2+} (~ 1 µM) for 5 min at + 40 mV. Single mutant hRyR2 channels were assessed by the addition of 1 µM ryanodine to the *cis* chamber.

5.2.3.2 Mutant hRyR2 channel conductance - Current-Voltage relationship

Mutant hRyR2 channels were recorded for a minimum of 30 s at each holding potential from ± 10 – 70 mV, in 10 mV increments, with symmetrical 210 mM KCl, unless stated otherwise. On occasion, to increase channel open probability for reliable amplitude idealisation, a caffeine analog, EMD41000, was added (1 µL) from a 50 mM stock to the *cis* chamber at a final concentration of 100 µM (McGarry and Williams, 1994). A minimum of five experiments were completed from each channel. Channel conductance, measured in pico Siemens (pS), was calculated from the slope of the current/voltage (I/V) relationship using linear regression.

5.2.3.3 Ion handling experiments

A series of ion handling experiments were completed to assess altered channel conduction properties in Y4839A hRyR2 channels. Single channels were activated by solutions containing ~ 1 µM Ca^{2+}, measured using a calcium probe (Orion; Thermo Fisher Scientific) (Mukherjee *et al.,* 2012) as outlined in section 6.2.2.1.

5.2.3.3.1 Investigating mutant hRyR2 cation-anion discrimination

Mutant channel discrimination between cation-anions was assessed by establishing asymmetric conditions with 810 mM KCl in the *cis* chamber and 210 mM KCl in the *trans* chamber. A current-voltage relationship, section 5.2.3.2, was completed and reversal potential (E_{rev}) was measured at which no current (0 pA) passed through the channel, determined by the x-intercept.

5.2.3.3.2 Examining mutant hRyR2 monovalent-divalent permeability

The permeability of divalent Ba^{2+} ions relative to monovalent K^+ ions was determined by monitoring reversal potentials under bi-ionic conditions. Conditions were initially established in symmetrical 210 mM KCl before the perfusion of the *trans* chamber with 210 mM $BaCl_2$. Relative permeability (P_X^{2+}/P_Y^{+}) between monovalent (Y^+) and divalent (X^{2+}) was calculated using the equation given by Fatt and Ginsborg stated below (Fatt and Ginsborg, 1958):

$$P_X^{2+}/P_Y^{+} = [Y^+]/(4\cdot[X^{2+}])\cdot\exp(E_{rev}F/RT)\cdot[\exp(E_{rev}F/RT) + 1]$$

RT/F (room temperature/Faraday constant) was 25.2 mV at 20 °C. All reversal potentials were corrected for junction potentials arising between the two solutions using the 'AutoZero' function on the bilayer clamp amplifier BC-535, nullifying any offset.

5.2.3.3.3 Investigating mutant hRyR2 ion conduction with changes in K^+ activity

The effects of mutant hRyR2 ion conduction with varying K^+ concentrations were assessed using symmetrical 25 mM, 50 mM, 100 mM, 150 mM, 210 mM and 610 mM KCl conditions. KCl concentrations that corresponded to K^+ activities of 21.5 mM, 40.8 mM, 76.8 mM, 111.3 mM 149.9 mM and 385.5 mM respectively, were calculated using the activity co-efficient taken from Hamer and Wu as given in Lobo (Hamer and Wu, 1972; Lobo, 1989). Mutant hRyR2 conductance under varying K^+ activities was calculated from current-voltage relationships that were assessed by nonlinear regression derived by Michaelis-Menten-type kinetics. The nonlinear regression determined the maximum saturating conductance (B_{max}) and half maximal conductance (K_D).

5.2.3.3.4 Assessing the dimensions of the pore using monovalent organic cations

Three monovalent organic cations, ethanolamine, diethanolamine and triethanolamine, with varying minimal radii, 2.3 Å, 2.8 Å and 3.6 Å, respectively, determined using a molecular modelling software package (HyperChem Release 2, Autodesk InC, Sausalito, CA) (Tinker and Williams, 1993a), were selected to assess ion conduction and relative permeability to provide information on the dimensions of the mutant hRyR2 pore. Symmetrical 210 mM KCl conditions were initially established for channel incorporation, before perfusing the *cis* chamber with 210 mM of the appropriate organic cation. The reversal potential was measured at which no current passed through the channel in order to determine the relative permeability ratio (P_X^+/P_K^+) between the monovalent organic cation (X^+) and K^+ using the Goldman-Hodgkin-Katz equation (Hodgkin and Katz, 1949) stated below:

$$P_X^+/P_K^+ = [K^+]/[X^+].e^{-ErevF/RT}$$

The *trans* chamber was subsequently perfused with the appropriate test cation to create symmetrical conditions to assess channel conductance, section 5.2.3.2.

5.2.3.4 Western blot analysis assessing Y4813A hRyR2 tetramerisation

Western blot analysis assessing Y4813A hRyR2 tetramerisation was completed as no single channel events were seen for this channel as described in section 5.3.3.1. Purified Y4813A (200 µL) fractions from 28 – 30 % sucrose, detailed in chapter 2.2.3.7.2, were concentrated in a vivaspin 500 (Sartorius Stedim Biotech) 100,000 MWCO column at 15,000 x *g*. The purified protein was concentrated 10 x, centrifuging to a final volume of 20 µL. Prior to protein concentration, dH_2O was eluted through the column to remove residual glycerin. Concentrated samples were loaded onto SDS-PAGE and analysed by Western blot, described in chapter 2.2.3.

5.2.3.5 Single-channel data acquisition and analysis

The Acquire 5.0.1 (Bruxton) oscilloscope was used to visualise the data and the current transitions were saved as .acquire files. The QuB suite, version 2.0.0.9, from the Department of Physiology and Biophysics, State University of New York at Buffalo, was used to analyse single-channel data. QuB is a free-access software package with a user-friendly graphical interface, enabling scientists to import, process, analyse and simulate single-channel data. QuB was used to construct multi-state models to describe single-channel kinetics outlined in chapter 6.2.2. Acquire files were imported into QuB, selected data of interest were extracted in the pre-processing window and saved as .qdf files for subsequent data analysis. An initial two state model, closed ⇌ open, was used for data idealisation, generating key results such as open probability (P_o), open and closed amplitudes (Amp1 and Amp2) and mean open and closed times (T_o and T_c). For current-voltage relationships, 30-60 s (> 1000 events) of single-channel data were extracted over a range of holding potentials, typically from – 70 mV to + 70 mV in 10 mV increments. Channel conductance was assessed as described in section 5.2.3.2.

For presenting single-channel representative traces, current transition data were low-pass 1 kHz filtered in QuB, unless otherwise stated. Traces were presented

with purple line as baseline (closed state) with channel openings determined by upward current deflections at positive holding potentials and downward current deflections at negative holding potentials.

5.2.3.5.1 Statistical analysis

Single-channel data were imported into GraphPad (Prism version 5.01) for figure construction and statistical analysis. Unitary conductance between WT and mutant hRyR2 channels were compared using a one-way ANOVA, Tukey's multiple comparison test, p values < 0.05 were deemed significant. Differences between channel conductance and relative permeability for WT and Y4839A were compared using an unpaired two-tailed t test, p values < 0.05 were deemed significant.

5.3 – Results

5.3.1 Initial single-channel characterisation of mutant hRyR2 channels

The functional stability of mutant hRyR2 channels was assessed in chapter 4 by whole cell fluorescent based imaging, which confirmed that all six hRyR2 mutations formed homotetrameric Ca^{2+}-release channels. Mutant hRyR2 channels were next generated in a recombinant cell expression system and were further isolated and purified as described in chapters 2.2.2 and 2.2.3. The initial characterisation of mutant hRyR2 channels evaluated the stability and integrity of single-channels upon removing these membrane proteins from a whole-cell environment and solubilising in a detergent/lipid mix before incorporation into an artificial planar lipid bilayer. A comprehensive single-channel investigation of mutant channels was completed to assess the effect of constructing point mutations at and around the surrounding area of the selectivity filter on the biophysical function of the channel.

Mutant hRyR2 single-channel traces, shown in figure 5.2, are representative 5 s recordings observing current fluctuations with the primary activating cytosolic ligand as contaminant Ca^{2+} (~ 1 µM) at + 40 mV in symmetrical 210 mM KCl. From initial observations, three hRyR2 mutants, Y4813W, Y4839A and Y4839W formed channels that were comparable to WT hRyR2. These channels were able to incorporate into the bilayer and were therefore suitable for further single-channel analysis, discussed in chapter 6. In contrast, the pore helix mutation Y4813A depicted in figure 5.2B, was non-functional and was further investigated in section 5.3.3.1. The mutations proposed at the luminal mouth of the selectivity filter, D4829A and D4829E, were characterised by drastically altered gating and conductance shown in figures 5.2D and 5.2E that were described in sections 5.3.3.2 and 5.3.3.3, respectively.

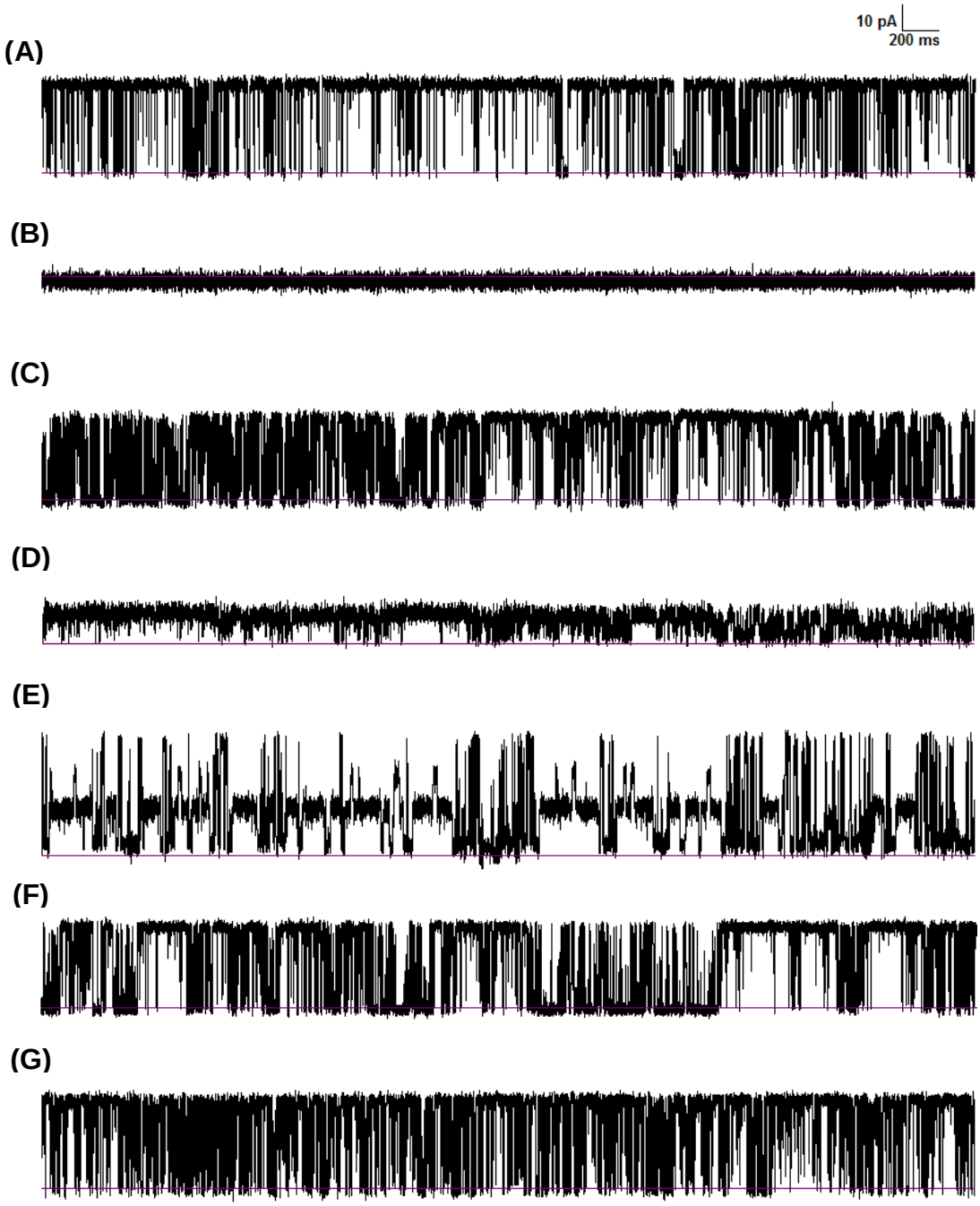


Figure 5.2. Initial characterisation of recombinant purified single WT and mutant hRyR2 channels incorporated into a planar lipid bilayer. Single-channel recording at + 40 mV with baseline (closed) represented as a purple line with upward deflections as channel openings. (A) WT hRyR2, (B) Y4813A, (C) Y4813W, (D) D4829A, (E) D4829E, (F) Y4839A and (G) Y4839W.

5.3.2 Ryanodine modification of mutant hRyR2 channels

The plant alkaloid, ryanodine, which binds with high affinity to hRyR2 was used to assess channel modification to verify mutant hRyR2 channels. Figure 5.3 shows single-channel WT and mutant hRyR2 gating transitions indicating ryanodine binding, illustrated by a red arrow, with channel modification characterised by increased open probability and reduced unitary conductance. Ryanodine modification was confirmed in all mutant channels except Y4813A, detailed in section 5.3.3.1. Gating transitions upon proposed ryanodine modification for D4829A and D4829E were both drastically altered and were uniquely different to modified WT hRyR2 channels, discussed in section 5.4.4.

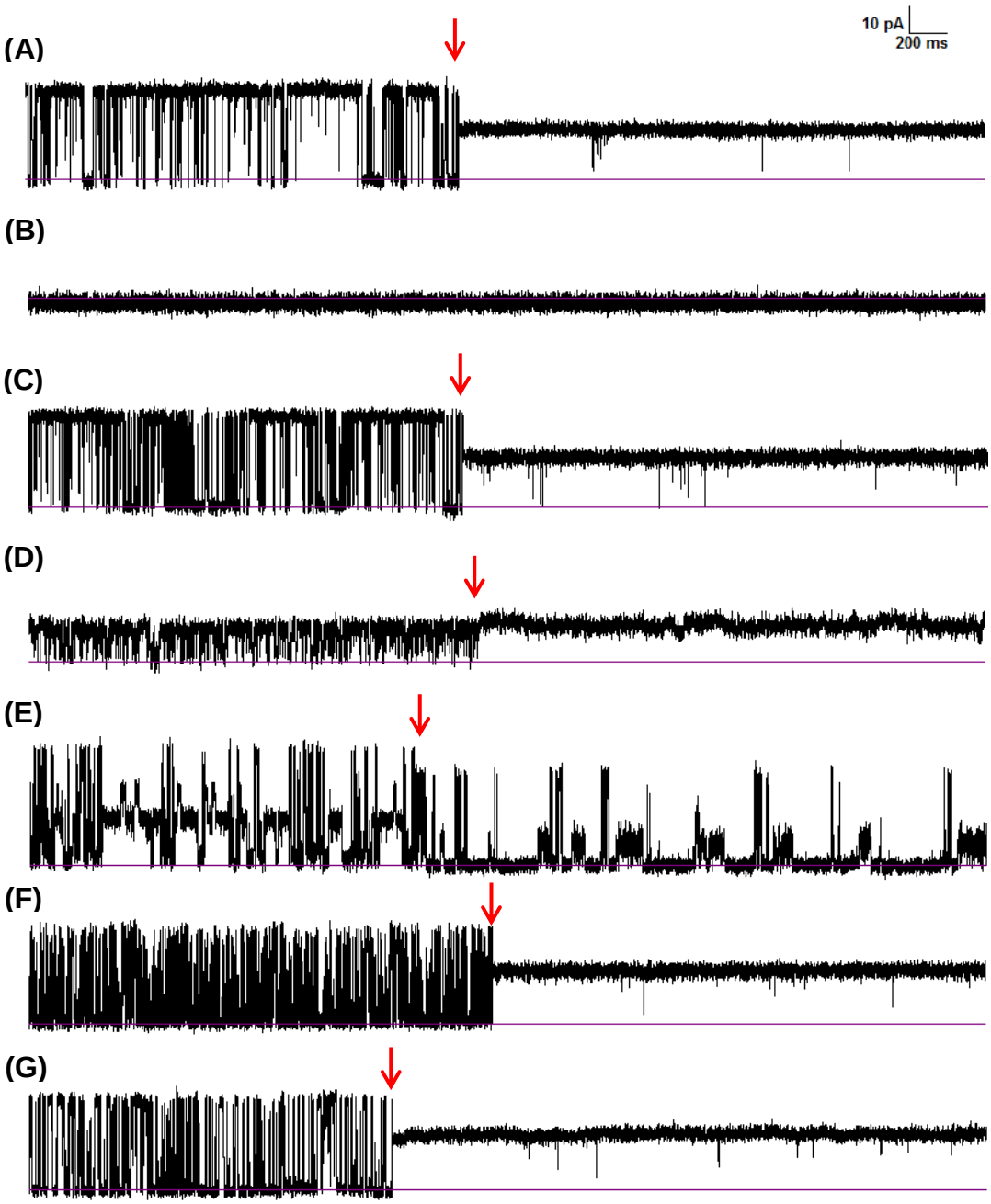


Figure 5.3. Ryanodine modification of mutant hRyR2 channels. Single-channel traces depicting gating transitions prior to ryanodine binding with channel modification, illustrated by a red arrow, were characterised by increased open probability and reduced unitary conductance, except for (E) and (D) respectively. (A) WT hRyR2, (B) Y4813A, (C) Y4813W, (D) D4829A, (E) D4829E, (F) Y4839A and (G) Y4839W. The baseline (closed) is represented by the purple line with upward deflections as channel openings. Traces are 5 s recording at + 40 mV in symmetrical 210 mM KCl.

5.3.3 Investigating altered mutant hRyR2 single-channel function

The initial single-channel characterisation of mutant hRyR2 channels indicated that point mutations at Y4813A, D4829A and D4829E either altered channel stability, gating or conductance while Y4813W, Y4839A and Y4839W were qualitatively comparable to WT hRyR2 channels.

5.3.3.1 Investigating altered mutant hRyR2 single-channel function - Y4813A

From over 100 channel incorporation attempts and from three separate purified preparations, Y4813A, depicted in figure 5.2B, was not detected in bilayers. The stability of Y4813A was assessed by concentrating purified ~ 28 – 30 % sucrose fractions, corresponding to tetramer density, by Western blot analysis. Figure 5.4 demonstrated that Y4813A was present in the concentrated fractions and confirmed that the protein assembled to a tetrameric channel following the purification procedure that was observed as monomers by Western blot following protein dissociation by SDS-PAGE. While the channel tetramer density was confirmed, the absence of channel function in bilayers suggested the alanine point mutation within the pore helix, either prevented channel incorporation or remained permanently closed. Thus, single Y4813A channels were unable to bind ryanodine, figure 5.3B, which supported previous loss of high-affinity [^{3}H] ryanodine binding reported in chapter 4.3.3.

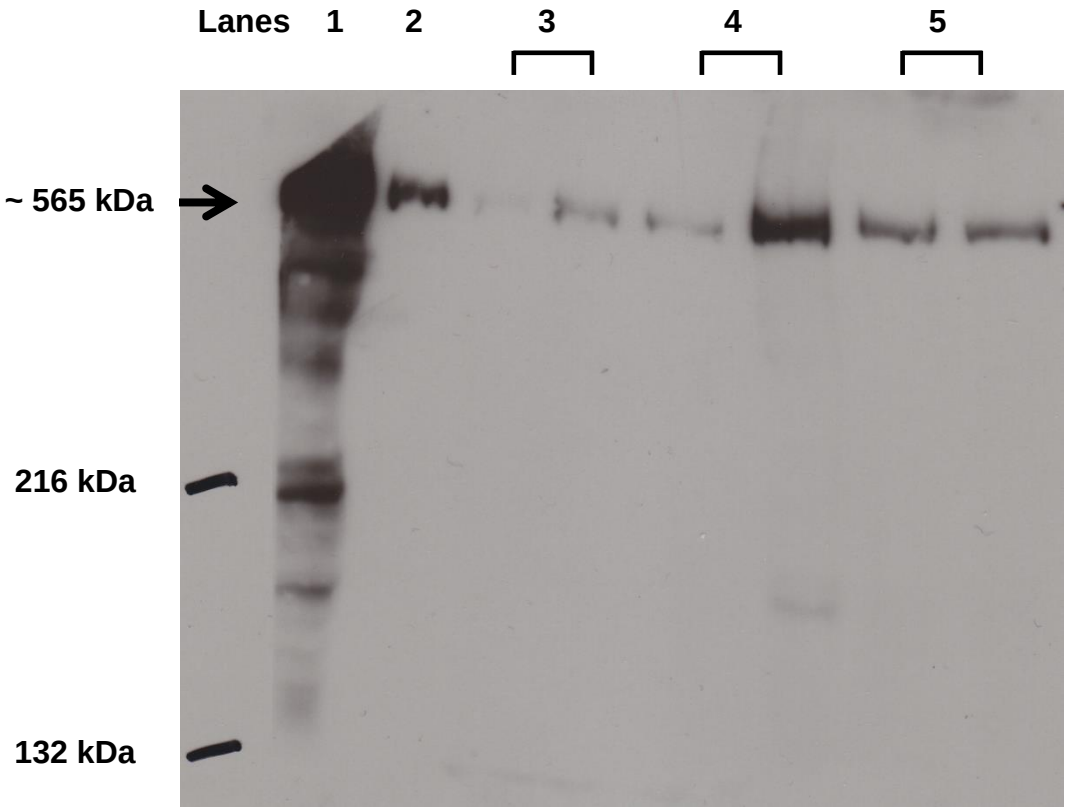


Figure 5.4. Assessing the presence and tetrameric density of Y4813A hRyR2 channels in purified fractions. Concentrated purified sucrose fractions from three separate Y4813A preparations were examined by Western blot analysis. Control samples of (1) WT hRyR2 mixed-membrane and (2) purified WT hRyR2 were compared to Y4813A sucrose fractions containing either ~ 28 or 30 %, left or right lanes, respectively. Purified Y4813A samples were analysed from preparation #1 (Lane 3), preparation #2 (Lane 4) and preparation #3 (Lane 5). Western blot analysis confirmed the presence of Y4813A in sucrose fractions and that the protein maintained the ability to form a channel corresponding to the RyR2 tetramer density following the purification procedure. Y4813A RyR2 monomers (~ 565 kDa) were observed by Western blot, represented by a black arrow, following protein dissociation by SDS-PAGE. Bio-markers corresponding to myosin (216 kDa) and β-galactosidase (132 kDa).

5.3.3.2 Investigating altered mutant hRyR2 single-channel function - D4829A

Single-channel characterisation of D4829A revealed multiple unique channels with altered gating and reduced conductance properties depicted in figure 5.5. When incorporated into a bilayer, purified D4829A did not form channels comparable to WT RyR2, figure 5.2. Abolishing the negative charge and hydrogen-bonding capabilities of the aspartic acid by alanine mutation, proposed to be located at the luminal end of the selectivity filter induced channels with high functional variability. From 85 recorded incorporation attempts, 20 D4829A channels were observed and were confirmed by ryanodine modification, figure 5.3D. Although channels were variable and difficult to quantify, a typically observed D4829A channel depicted in figures 5.5A and 5.5B (n=7) had a reduced unitary conductance at + 40 mV, 195.5 pS, 75 % less than WT hRyR2 (p<0.0001) shown in figure 5.9.

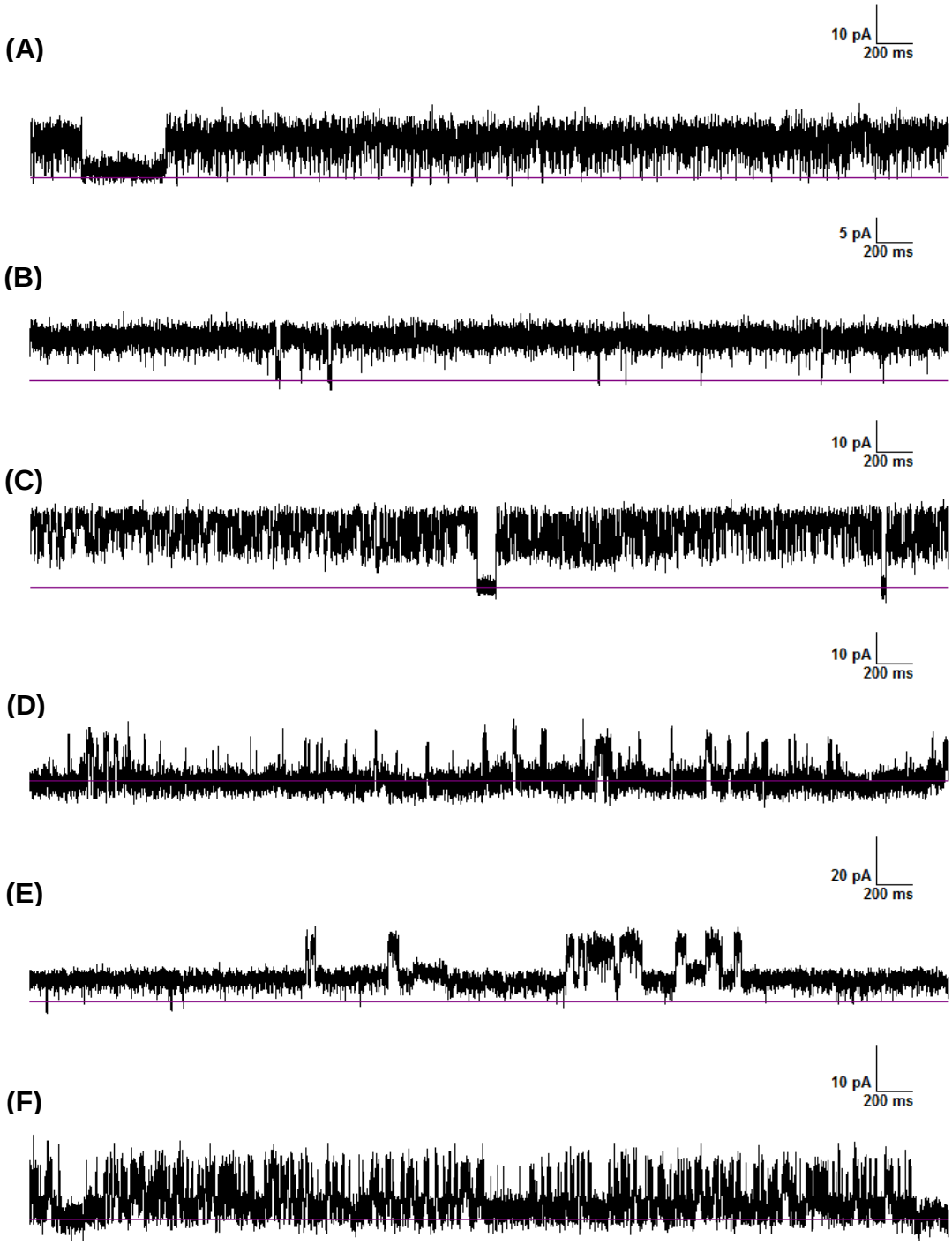


Figure 5.5. Single-channel characterisation of D4829A hRyR2 channels. Single-channel traces of purified D4829A channels (A – F) incorporated into a planar lipid bilayer had high channel-to-channel variability. Alanine point mutation at position D4829 induced multiple unique channels characterised by altered channel gating and conductance. Channels typically observed (A) and (B) were confirmed by ryanodine modification, depicted in figure 5.3D. Differences in current amplitude indicated by scale bar depicted top right.

5.3.3.3 Investigating altered mutant hRyR2 single-channel function - D4829E

From 30 incorporation attempts, 12 single D4829E channel recordings were observed. Similar to D4829A, the conservative D4829E substituted channels were characterised by high channel-to-channel variability shown in figure 5.6. Multiple unique defined sub-conductance states were observed when channels were monitored at + 40 mV in symmetrical 210 mM KCl. Measuring the closed to fully open level at ± 40 mV revealed that D4829E had a reduced unitary full conductance of 627.6 pS that was 20.5 % lower compared to WT hRyR2, depicted in figure 5.9. Introducing a conservative residue substitution with negative charge, D4829E, however had a 68.9 % larger unitary conductance compared to the alanine mutation D4829A, highlighting the importance of residue interactions at the selectivity filter within the proposed luminal mouth of the pore.

Increased open probability and reduced unitary conductance, seen typically in WT hRyR2 following ryanodine interaction, were not observed in D4829E, depicted in figure 5.3E. Prior to the addition of ryanodine, defined sub-conductance states were observed in D4829E channels. The change in D4829E gating, highlighted by the arrow in figure 5.3E, was only seen in the presence of ryanodine suggesting that the observed state was induced by channel modification of ryanodine. Upon this proposed modification, two of the intermediate sub-conductance states were replaced with a defined reduced conductance state. The dissociation of the ryanodine molecule from the channel was observed by changes in gating kinetics and sub-conductance states, shown in figure 5.7. The dissociation of the ryanodine from the proposed modified channels supported previous [^{3}H] ryanodine results that reported reduced binding, 7.18 % compared to WT hRyR2. This indicated that point mutation at D4829E either altered access to, or altered the conformation of the binding site affecting the affinity of ryanodine within the pore.

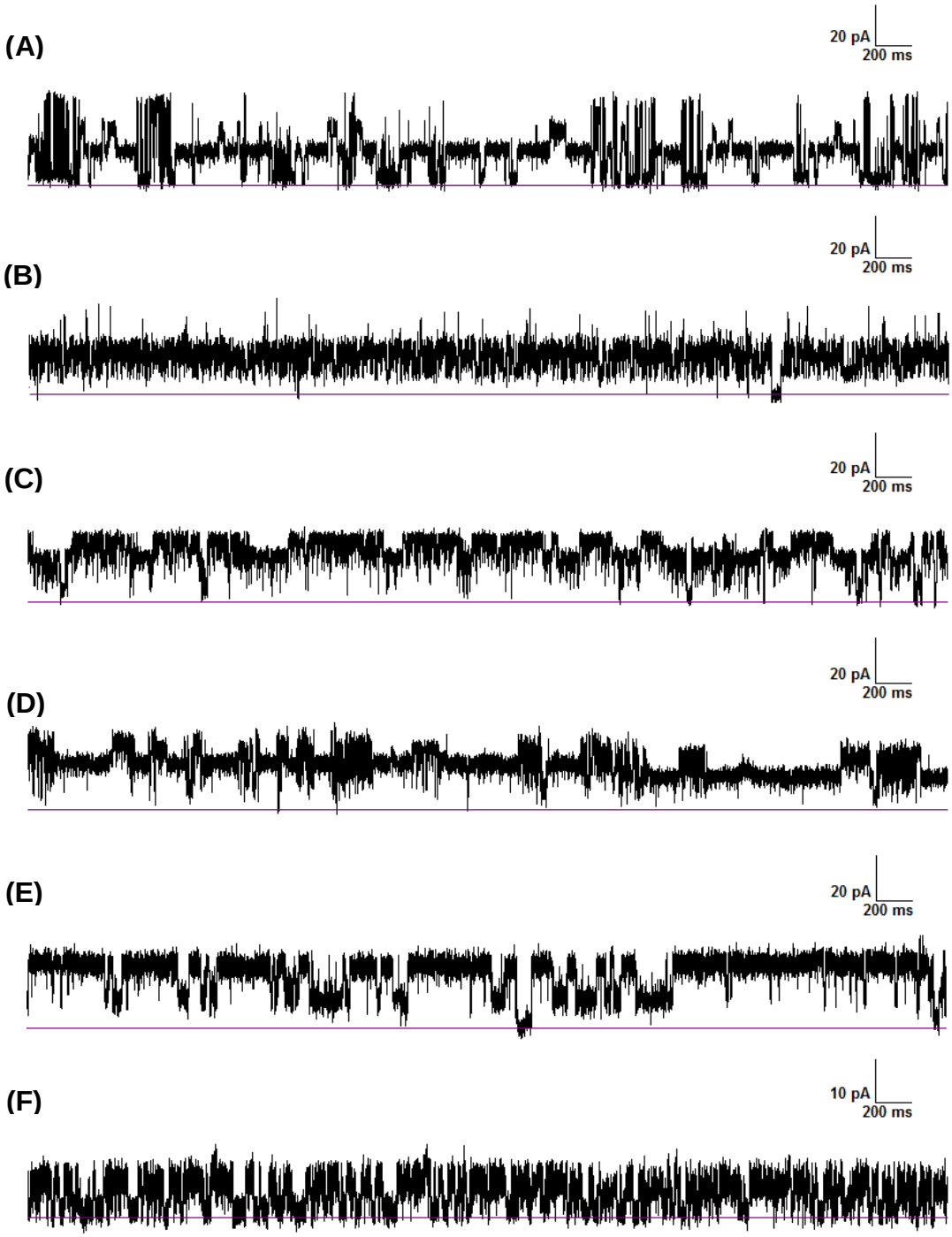


Figure 5.6. Single-channel characterisation of D4829E hRyR2 channels. Observed single-channel recordings of purified D4829E channels (A – F) at + 40 mV in symmetrical 210 mM KCl. The conservative glutamic acid substitution at position D4829E induced high channel-to-channel variability characterised by defined sub-conductance states with altered channel gating and conductance. Differences in current amplitude indicated by scale bar depicted top right.

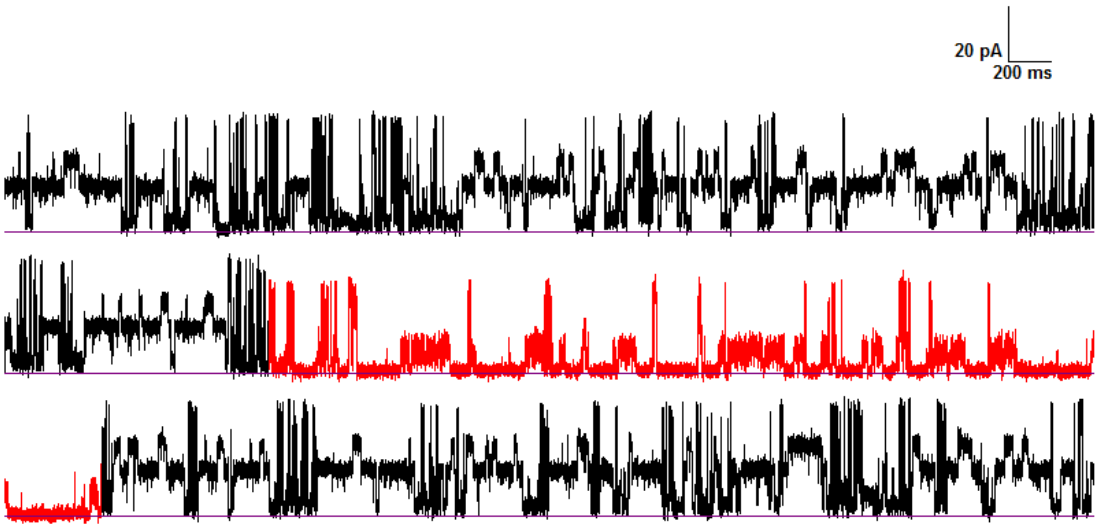


Figure 5.7. Single-channel ryanodine modification of D4829E hRyR2. Single-channel gating events prior to and following the addition of 1 µM ryanodine. Highlighted section in red represents distinct and unique channel modification. Dissociation of ryanodine was observed in the time-scale of a single-channel experiment.

Channel function was drastically altered highlighting the importance of residue properties and their interactions within the proposed selectivity filter region. The initial mutant single-channel characterisation revealed that Y4813A was non-functional for bilayer experiments, and due to the high variability seen in both D4829 mutations it was decided that these three hRyR2 mutations, Y4813A, D4829A and D4829E, were not examined further, however the consequences of these mutations are discussed in sections 5.4.3 and 5.4.4, and in chapter 7.

5.3.4 Ion handling – Assessing mutant hRyR2 channel conductance

Three channels, Y4813W, Y4839A and Y4839W, from the six hRyR2 mutations constructed were suitable for in depth single-channel analysis, detailed in chapter 6. Chapter 6 investigates potential subtle alterations in channel gating kinetics, as a consequence of residue substitution, that are not considered in this chapter. These hRyR2 point mutations produced channels that were qualitatively comparable to WT hRyR2 with similar observable gating transitions as shown in figure 5.2. As a general overview, K^+ conductance was examined in the three hRyR2 mutants and compared with the conductance measured in WT channels. Unitary channel conductance was assessed by monitoring the relationship between current amplitude and holding potential in symmetrical 210 mM KCl. These current/voltage (I/V) relationships shown in figure 5.8 measured slope conductance of WT and mutant hRyR2 channels that were calculated using linear regression, listed in table 5.1.

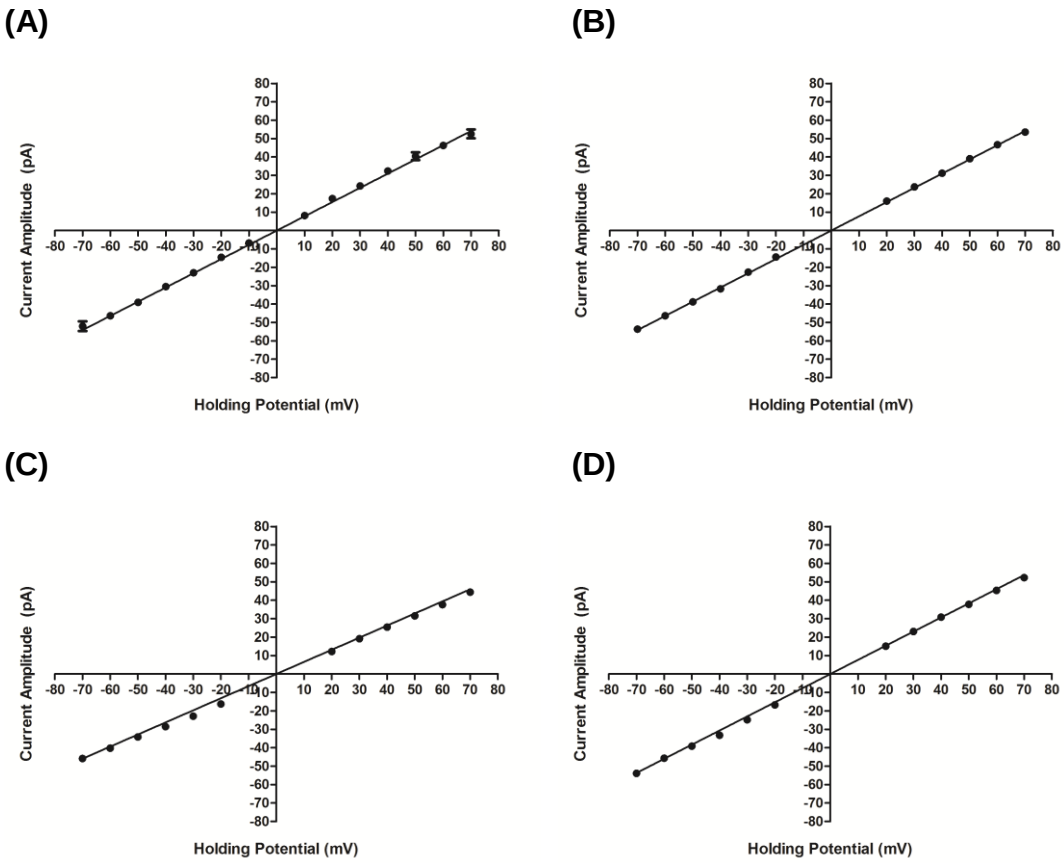


Figure 5.8. Current-Voltage (I/V) relationships of WT and Mutant hRyR2 channels. I/V plots (A) WT hRyR2, (B) Y4813W, (C) Y4839A and (D) Y4839W. Channel conductance was assessed in symmetrical 210 mM KCl recording current amplitude from ± 70 mV in 10 mV increments. Each point is the mean ± SEM from a minimum of five experiments. When no error bars are visible, the SEM is included within the symbol. Slope conductance was calculated by linear regression, listed in table 5.1. Due to high D4829A and D4829E channel-to-channel variability, conductance was calculated from a single holding potential (+ 40 mV). Therefore, D4829A and D4829E were not included in this figure.

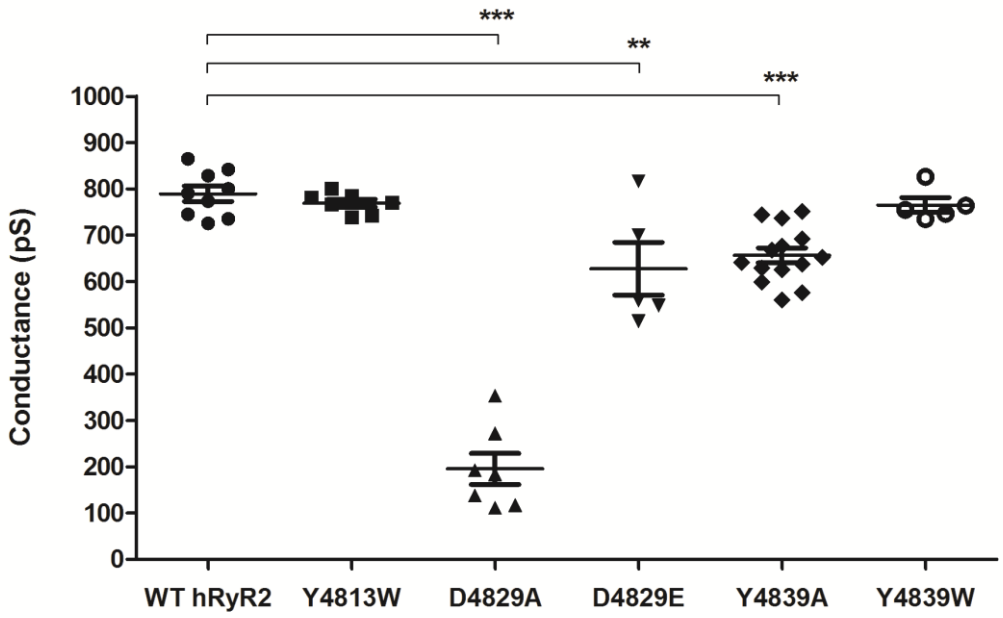


Figure 5.9. Comparing channel conductance between WT and mutant hRyR2. The conductance of D4829A, D4829E and Y4839A were significantly reduced compared to WT by 75 %, 20.5 % and 16.8 %, respectively. Y4813W and Y4839W were comparable to WT hRyR2. Individual channel experiments are plotted with overall mean conductance listed in table 5.1. Bars (where visible) indicate SEMs.

	n	***G* (pS)**	***p* < 0.05**
WT hRyR2	9	789.4 ± 16.42	
Y4813W	7	769.4 ± 8.49	ns
D4829A	7	195.5 ± 33.59	< 0.0001
D4829E	5	627.6 ± 56.84	0.0046
Y4839A	14	656.6 ± 15.98	< 0.0001
Y4839W	5	765.1 ± 15.97	ns

Table 5.1. Assessing WT and mutant hRyR2 channel conductance in symmetrical 210 mM KCl. Mean conductance (± SEM) between WT and mutant hRyR2 channels were compared using a one-way ANOVA, Tukey's multiple comparison test, *p* values < 0.05 were deemed significant. Channel conductance was calculated as described in section 5.2.3.2.

Unitary conductance of the two conservative mutations Y4813W, 769.4 ± 8 pS, and Y4839W, 765.1 ± 15 pS, were comparable to WT hRyR2, 789.4 ± 16 pS. Figure 5.9 compares individual WT and mutant hRyR2 unitary channel conductance revealing that the alanine mutation, Y4839A, conductance was significant reduced by 16.8 % compared to WT hRyR2.

5.3.5 Ion handling – Assessing altered Y4839A ion conduction properties

The reduced unitary conductance in Y4839A compared to WT hRyR2 prompted a series of four additional ion handling investigations to assess potential mechanisms responsible for altered conductance in this channel. These experiments included; channel discrimination between cation and anions, relative permeability of monovalent and divalent cations, examining channel conductance in response to varying K^+ activity and to probing the dimensions and conduction properties of the Y4839A pore using monovalent organic cations.

5.3.5.1 Assessing Y4839A hRyR2 cation-anion discrimination

Purified WT RyR2 is impermeable to anions such as Cl^- (Lindsay and Williams, 1991). An initial ion handling experiment was completed to assess Y4839A cation vs anion discrimination under asymmetric conditions using 810 mM KCl in the *cis* chamber and 210 mM KCl in the *trans* chamber. An I/V plot was completed to measure the reversal potential (E_{rev}), determined by the x-intercept, at which no current passed through the channel (0 pA). Under these conditions using the Nernst equation a selective cation channel (K^+) over anions (Cl^-) had an E_{rev} of - 34 mV (Mead-Savery *et al.,* 2009). The reversal potential value was comparable to both WT - 30 mV and Y4839A - 29 mV shown in figure 5.10 and listed in table 5.2. These experiments demonstrated that alanine mutation at Y4839 did not change the ability of RyR2 to discriminate between cations and anions.

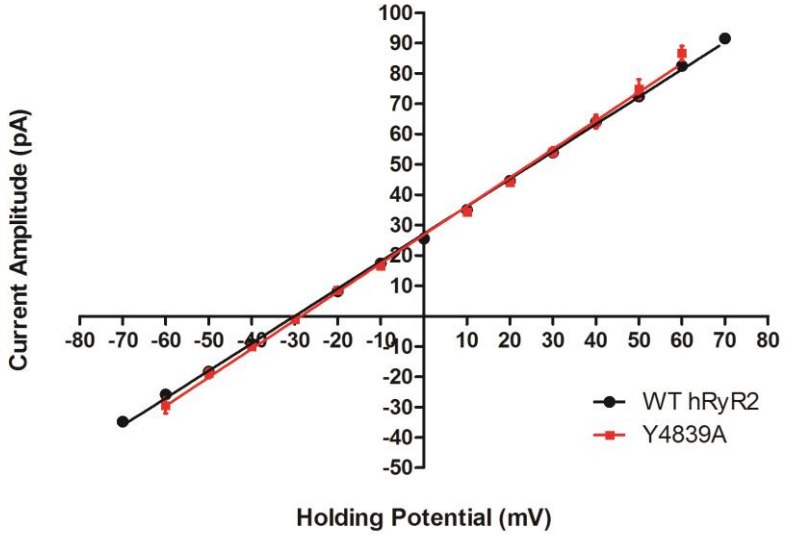


Figure 5.10. Cation-anion discrimination in Y4839A hRyR2. Current/Voltage (I/V) relationship assessing cation-anion discrimination between WT (black) and Y4839A (red) under asymmetric 810 mM KCl (*cis*) and 210 mM KCl (*trans*). Each point is the mean ± SEM from a minimum of five experiments. When no error bars are visible, the SEM is included within the symbol.

	n	***G* (pS)**	**E_{rev} (mV)**
WT hRyR2	5	898.8 ± 14.28	- 30.13 ± 1.21
Y4839A	5	906.9 ± 22.97	- 29.01 ± 1.12

Table 5.2. Cation-anion discrimination of Y4839A hRyR2. Assessing channel conductance (*G*) and E_{rev} between WT and Y4839A hRyR2 in asymmetrical KCl conditions confirmed that alanine mutation retained the ability to discriminate between cations over anions.

5.3.5.2 Examining Y4839A hRyR2 divalent-monovalent cation permeability

Relative permeability between divalent and monovalent cations (P_{Ba}^{2+}/P_{K}^{+}) for Y4839A hRyR2 was assessed under bi-ionic conditions using 210 mM KCl in the *cis* chamber and 210 mM $BaCl_2$ in the *trans* chamber. The permeability of Ba^{2+} ions relative to K^+ ions was calculated using the relationship derived by Fatt and Ginsborg with the equation stated in section 5.2.3.3.2 (Fatt and Ginsborg, 1958). Reversal potentials were manually recorded, filtering at 500 Hz to detect any small

current fluctuations. Previous ion handling experiments on purified sheep RyR2 demonstrated that divalent cations (Ba^{2+}, Sr^{2+} Ca^{2+} and Mg^{2+}) were on average 6.2 times more permeable (5.8 times for Ba^{2+}) than monovalent K^+ ions (Tinker and Williams, 1992). The relative permeability of Ba^{2+} ions, in this study, was 5.3 times more than that of monovalent K^+ ions in recombinant WT hRyR2 channels. For Y4839A hRyR2 however, the relative permeability of Ba^{2+} ions was 4.5 times greater than that of K^+ ions. Relative permeability between divalent and monovalent cations was significantly reduced by 15.1 % in Y4839A compared to WT hRyR2 (p=0.0038), depicted in figure 5.11 and listed in table 5.3.

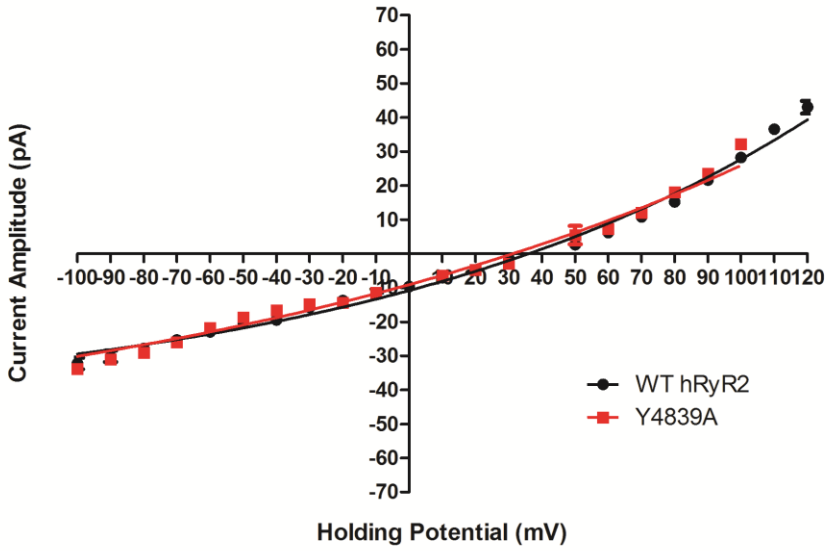


Figure 5.11. Assessing monovalent-divalent permeability between WT and Y4839A hRyR2 channels. Current/Voltage (I/V) relationship showing the response of Y4839A compared to WT hRyR2 in bi-ionic conditions of monovalent 210 mM K^+ (*cis*) and divalent 210 mM Ba^{2+} (*trans*). The E_{rev} and permeability ratios ($P_{Ba}{}^{2+}/P_{K}{}^{+}$) are detailed in table 5.3. All points are mean ± SEM derived from a minimum of four experiments. When no error bars are visible, the SEM is included within the symbol.

	n	E_{rev} Ba^{2+} vs K^+ (mV)	$P_{Ba}{}^{2+}/P_{K}{}^{+}$
WT hRyR2	6	+ 35.67 ± 0.38	5.3
Y4839A	7	+ 33.57 ± 0.42	4.5

Table 5.3. Assessing the reversal potential and permeability ratios of WT and Y4839A hRyR2 channels under bi-ionic conditions using 210 mM KCl in the *cis* chamber and 210 mM $BaCl_2$ in the *trans* chamber.

5.3.5.3 Assessing Y4839A hRyR2 ion conduction with changes in K^+ activity

To investigate the effects of altered Y4839A hRyR2 function, ion conduction was measured under six varying K^+ activities (stated in section 5.2.3.3.3) that were used to determine the maximum saturating conductance (B_{max}) and the activity of K^+ (mM) that yielded half-maximal conductance (K_D) by nonlinear regression derived by Michaelis-Menten-type kinetics, as depicted in figure 5.12. While the K_D was similar for Y4839A compared to WT hRyR2, ~ 23 mM, the B_{max} was reduced by 8.6 %, listed in table 5.4. Differences in B_{max} between the alanine mutation and WT hRyR2 channels was due to reduced unitary conductance at 21.50 mM, 111.3 mM and 149.9 mM K^+ activities in Y4839A, corresponding to symmetrical 25 mM, 150 mM and 210 mM KCl concentrations, respectively.

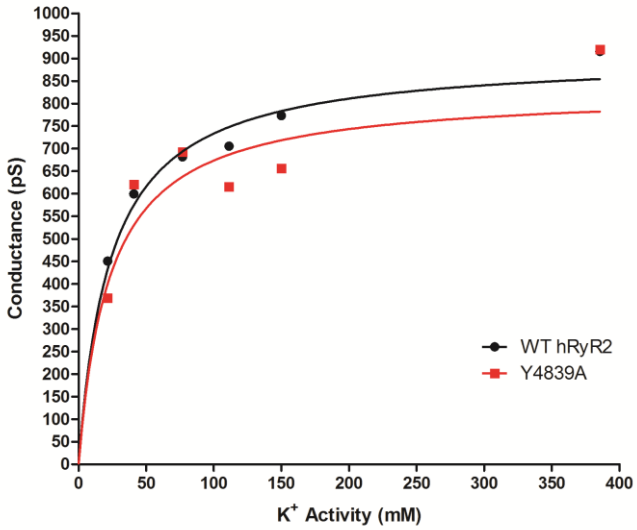


Figure 5.12. Assessing channel conductance between WT and Y4839A hRyR2 in response to increasing K^+ activity. Nonlinear regression derived by Michaelis-Menten-type kinetics determined B_{max} and K_D listed in table 5.4. Each point is the mean conductance ± SEM derived from at least four experiments. When no error bars are visible, the SEM is included within the symbol.

	B_{max} (pS)	K_D (mM)
WT hRyR2	906.5 ± 15.2	23.59 ± 1.9
Y4839A	829.2 ± 37.4	23.10 ± 5.9

Table 5.4. Comparing B_{max} and K_D between WT and Y4839A in response to increasing K^+ activity. Each point is the mean conductance ± SEM derived from at least four experiments.

5.3.5.4 Measuring the pore dimensions and ion conduction properties of Y4839A hRyR2 using monovalent organic cations

Previous investigations demonstrated that RyR2 is permeable to a wide range of monovalent organic cations (Tinker and Williams, 1993a). To assess the dimensions and conduction properties of Y4839A, three monovalent organic cations, ethanolamine, diethanolamine and triethanolamine with similar chemical properties but varying minimal radii were selected. Table 5.5 lists the reversal potential and relative permeability comparing WT and Y4839A. Both Y4839A and

WT hRyR2 channels were impermeable to triethanolamine, with a minimal radius of 3.6 Å. Triethanolamine was unable to pass through the channels at high holding potentials, ≥ + 80 mV, as depicted in figure 5.13. This supported previous studies that established that the narrowest portion of RyR2, proposed to be the selectivity filter, had a minimal radius of ~ 3.5 Å (Tinker and Williams, 1993a). The consequence of reducing the side chain length and interactions at position Y4839A within the PFR did not alter the dimensions of the pore. In addition, the relative permeability and unitary channel conductance for ethanolamine and diethanolamine were comparable to WT hRyR2 channels.

Organic cation	R_xA	E_{rev} (mV)		P_x/P_K		G (pS)	
		WT	**Y4839A**	**WT**	**Y4839A**	**WT**	**Y4839A**
Ethanolamine	2.3	23.4 ± 0.6	25.5 ± 1.1	0.40	0.36	133.6 ± 1.1	131.7 ± 2.0
Diethanolamine	2.8	43.8 ± 0.4	41.7 ± 0.5	0.18	0.19	33.6 ± 1.4	33.6 ± 1.1
Triethanolamine	3.6	≥ 80	≥ 80	≤0.04	≤0.04	-	-

Table 5.5. Probing the dimensions and conduction properties of WT and Y4839A hRyR2 channels using monovalent organic cations. Reversal potentials and single channel conductance were derived from four or more experiments.

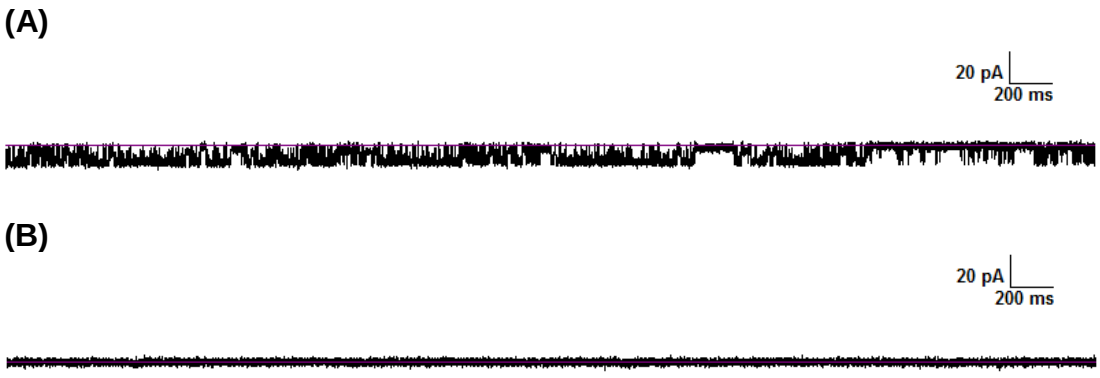


Figure 5.13. Measuring reversal potential for monovalent organic cations. Representative single-channel traces of WT hRyR2 in asymmetric conditions, 210 mM KCl (*cis*) and 210 mM triethanolamine (*trans*) at holding potentials (A) 0 mV and (B) + 80 mV. Both WT and Y4839A were impermeable to triethanolamine (minimum radius 3.6 Å), indicating that reducing the side-chain length with alanine mutation did not alter the pore dimensions in a way that increased aperture radius or permeability of the tertiary amine. Single-channel data were filtered at 500 Hz to visualise small currents.

5.4 – Discussion

5.4.1 Initial single-channel characterisation of mutant hRyR2 channels

The purpose of this investigation was to characterise the single-channel properties of purified hRyR2 channels in which residues in the proposed selectivity filter and pore helix, and hypothesised to play important roles in channel function, have been mutated. Mutant hRyR2 channels were generated recombinantly in a heterologous cell expression system and were isolated and solubilised in conditions that have been used in previous studies to investigate single-channel RyR2 function (Mead-Savery *et al.,* 2009; Mason *et al.,* 2012; Euden *et al.,* 2013b). It was essential to initially screen the novel hRyR2 mutants to assess their single-channel stability and general biophysical properties such as ion conduction.

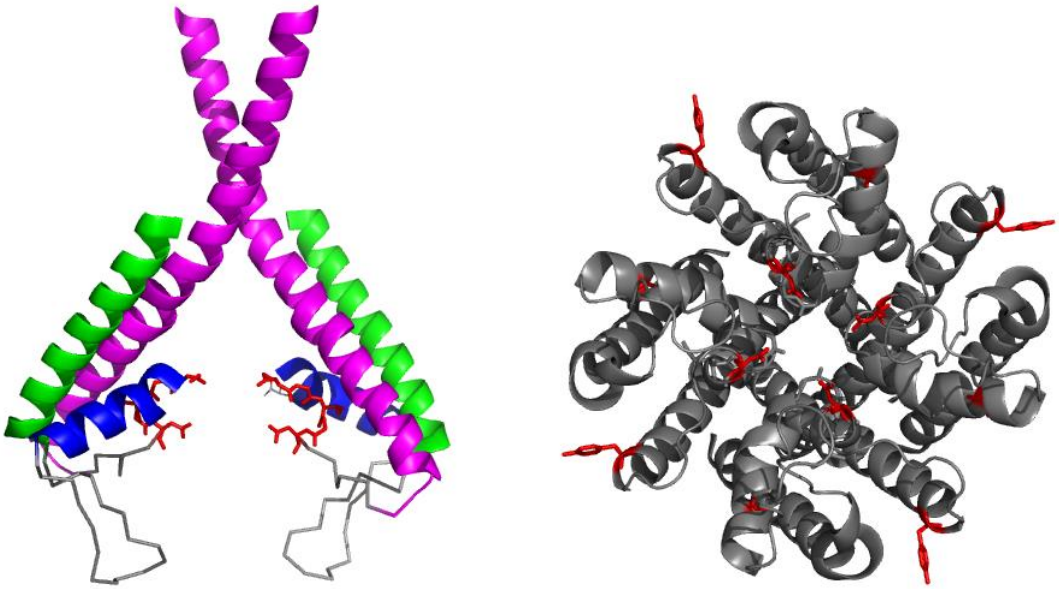
Constructing single point mutations within hRyR2 revealed that residue interactions in the proposed selectivity filter and pore helix are essential for maintaining typical gating and ion conduction discussed in section 5.4.3, 5.4.4 and 5.4.5. Altered single-channel function was assessed by examining structural models of the pore-forming region, in particular, the position and distances of mutated residues in the proposed pore, detailed in sections 5.4.2 and 5.4.6.

5.4.2 Structural models of the RyR pore-forming region

Models of the pore-forming region of RyR1 based on structures obtained by cryo-EM have superseded the original PFR RyR2 model based on the K^+ channel KcsA that was used to make predictions of gating mechanisms stated in the hypotheses (Welch *et al.,* 2004; Zalk *et al.,* 2014; Efremov *et al.,* 2014; Yan *et al.,* 2015). In the absence of high resolution crystal structures of the PFR region resolved in varies conformations, these structural models have been used to predict mechanisms of channel gating that arise from interactions between residues and domains (Welch *et al.,* 2004; Euden *et al.,* 2013b; Ramachandran *et al.,* 2013; Mei *et al.,* 2015). The continual evolution of protein preparation, instrumentation and image processing techniques has improved the accuracy of structural data, and currently the 3.8 Å PFR RyR1 model in a closed conformation is the most accurate structural model shown in figure 5.14A (Yan *et al.,* 2015).

The initial and most striking difference comparing the two models are the dimensions of the selectivity filter and the conformation and length of the S6 and pore helices. Comparing the side and luminal view between models, shown in figure 5.14, the altered conformation of the helices has changed the location and distances between the three residues highlighted in red. A hydrogen-bonding network in the current Yan *et al* model between the three residues would not be possible, discussed in section 5.4.6.

(A)



(B)

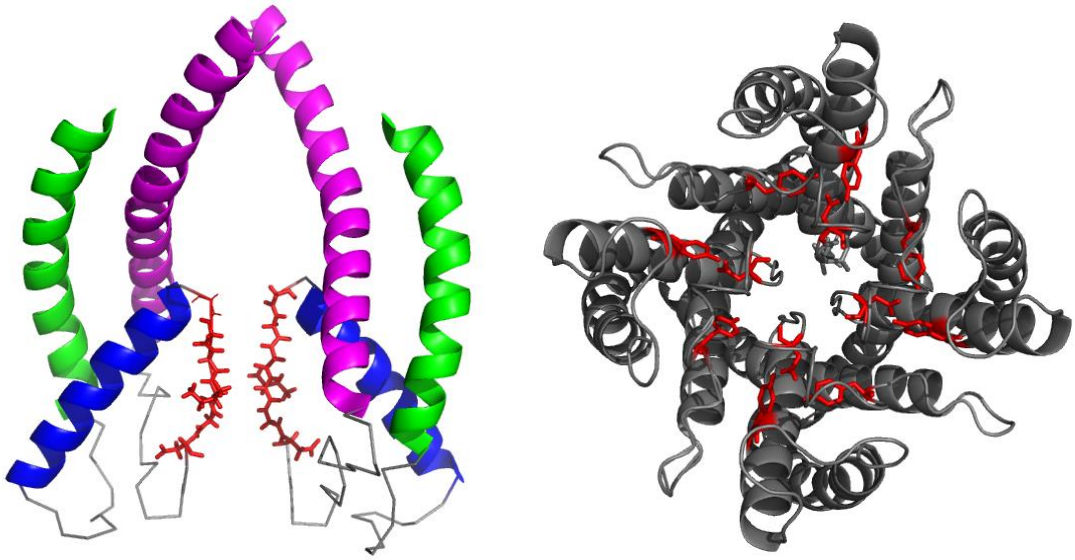


Figure 5.14. Pore-Forming Region models of the ryanodine receptor channel. (A) RyR1 PFR model (Yan *et al.,* 2015) and (B) the analogy PFR RyR2 model (Welch *et al.,* 2004). (*Left*) Side view highlighting the S5 helix (green), pore helix (blue), selectivity filter (red) and S6 helix (purple). (*Right*) Luminal view highlighting the three residues, Y4813, D4829 and Y4839 in red, which depicts the changes in residue position and distance between models. (A) The model of Yan *et al* is unable to support a proposed hydrogen-bonding network. PDB file 3J8H used with permission from Chang-cheng Yin (Yan *et al.,* 2015).

The structural differences between the models are highlighted when aligning the primary sequence of the proposed helix boundary sites depicited in figure 5.15. Of importance, residue Y4839 in the Yan *et al* RyR1 model is located at the start of the S6 helix, in contrast to the analogy model where it is located in a loop-forming region thus explaining potential differences in ion handling and ion conduction, discussed in section 5.4.5.

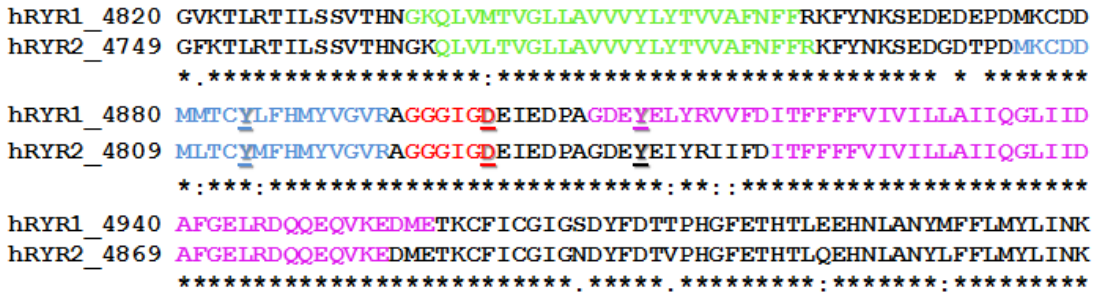


Figure 5.15. Proposed boundary sites of pore-forming region RyR helices. Human RyR1 and RyR2 helice boundary sites based on (Yan *et al.,* 2015) and (Welch *et al.,* 2004), respectively. Highlighted residues form S5 helix (green), pore helix (blue), selectivity filter (red) and S6 helix (purple). Point mutations are underlined. Figure obtained from a web-based software, uniprot, aligning entry codes P21817 (RyR1) and Q92736 (RyR2) (http://www.uniprot.org/align).

In the absense of crystal structures, these models provide a useful structural framework to predict the involvement of residue interactions when assessing the structural-functional relationship. The initial single-channel characterisation of hRyR2 containing point mutations in the proposed selectivity filter and pore helix regions of the channel revealed interesting insights into the importance of residues within the pore. Evaluting the differences in residue distances and orientation, in regard to the orginial Welch *et al* analogy model, with the data obtained by single-channel analysis is explored in the following sections.

5.4.3 Initial single-channel characterisation of mutant hRyR2 channels – Y4813

hRyR2 containing the alanine mutation at residue Y4813A was confirmed to form functional tetramer channels, in a cellular environment, albeit with a 25.6 % reduction in the maximum Ca^{2+} release compared to cells expressing WT hRyR2 channels. The [^{3}H] ryanodine binding assay on mixed-membranes expressing Y4813A, isolated from HEK293 cells, reported 1.03 % binding compared to WT hRyR2 in conditions that favoured high channel open probability that included high Ca^{2+} (100 µM) and caffeine (10 mM) concentrations. While the mutant channels maintained the ability to form tetrameric proteins, confirmed by Western blot following solubilisation and the purification procedure, substituting the tyrosine with an alanine within the pore helix resulted in a channel that was either unable to incorporate into the planar lipid bilayer or remained permanently closed upon incorporation. From over 100 unsuccessful incorporation attempts, from three separate purification preparations, the channel was deemed non-functional at the single-channel level. It was therefore not possible to characterise the mechanism for reduced maximum Ca^{2+} release reported in chapter 4.3.1.1.

Figure 5.16 compares the location of residues between the monomers of both the Yan *et al*, figure 5.16A and Welch *et al* PFR, figure 5.16B, models highlighting Y4813 in blue. In the Welch *et al* analogy model, Y4813 faces inwards into the pore, favouring a hydrogen-bonding network with the selectivity filter. In contrast, in the Yan *et al* RyR1 model, Y4813 is on the opposite side of the helix, rotated 180°, facing away from D4829 and the pore. Substituting the tyrosine with an alanine resulted in a compromised channel, discussed in chapter 7, strongly indicating that a component in the pore helix is essential in maintaining the relative functional characteristics of hRyR2.

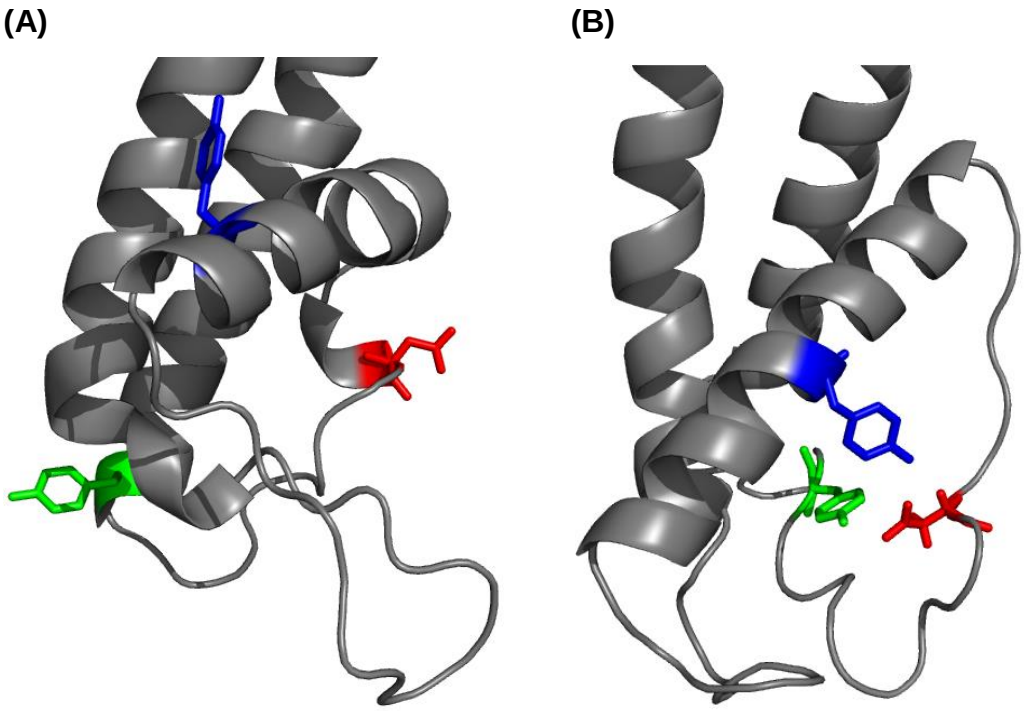


Figure 5.16. Comparing the location of residues between (A) the PFR RyR1 model (Yan *et al.,* 2015) and (B) the analogy PFR RyR2 model (Welch *et al.,* 2004). Highlighted residues are colour coded; Y4813 (blue), D4829 (red) and Y4839 (green), analogous residues highlighted in Yan *et al* RyR1 model. One monomer is shown for clarity.

Several groups investigating RyR channels have reported altered protein function upon the removal of mutant channels from the cellular environment (Gao *et al.,* 2000; Du *et al.,* 2001; Li *et al.,* 2002a; Avila *et al.,* 2004; Wang *et al.,* 2003; Wang *et al.,* 2004; Euden *et al.,* 2013b; Seidel *et al.,* 2014; Mei *et al.,* 2015). These RyR mutations, such as L433P and G4864P in RyR2, and D4899A and G4934V in RyR1, were shown to form tetrameric channels that were caffeine sensitive in HEK293 cells, however the consequence of point mutation affected the function of protein when isolated and solubilised, demonstrated by reduced [^{3}H] ryanodine binding and altered single-channel function. The observations from Y4813A were consistent with these earlier investigations highlighting the challenges of studying single hRyR2 function.

In K^{+} channels, the pore helix plays a critical role in maintaining the structural integrity of the selectivity filter (Doyle *et al.,* 1998; Zhou *et al.,* 2001; Long *et al.,* 2007), and there is also evidence that this region plays a crucial dynamic role during

selectivity filter gating (Clarke *et al.,* 2010; Wang *et al.,* 2011; Raghuraman *et al.,* 2012; Perry *et al.,* 2013). Residue substitution in the pore helix of KcsA (W67A), in a proposed similar position to Y4813, yielded a protein that failed to assemble correctly (Cordero-Morales *et al.,* 2006). Introducing a conservative tyrosine subsitituion to the pore helix at this position, W67Y, interestingly retained channel function similar to WT KcsA and did not affect the overall kinetics and extent of gating as the ability to form hydrogen bonds was preserved (Cordero-Morales *et al.,* 2011). The structure of the PFR of RyR is proposed to resemble a pore architecture similar to K^+ channels (Welch *et al.,* 2004; Samsó *et al.,* 2005; Ludtke *et al.,* 2005; Ramachandran *et al.,* 2009; Ramachandran *et al.,* 2013), suggesting that dynamic rearrangements in the pore domains may occur in RyR analogous to known gating mechanisms in K^+ channels (Cordero-Morales *et al.,* 2006; Cuello *et al.,* 2010a; Cuello *et al.,* 2010b).

In conjunction, the initial single-channel characterisation of Y4813W provided the first novel insight into the importance of residue interactions in the pore helix of hRyR2. In contrast to Y4813A, the conservative mutant Y4813W restored channel function that was comparable to WT hRyR2, which also coincided with the preserved maximum Ca^{2+} release from HEK293 cells, shown in figure 4.10. Maintaining either the steric bulk or the physicochemical properties and hydrogen-bonding capabilities, by replacing the phenol side chain with an indole group, produced a functional channel that was qualitatively comparable to WT hRyR2 with similar ion conductance shown in figure 5.2. Introducing a conservative residue within the pore helix enabled the channel to bind ryanodine at the single-channel level, suggesting that the structural conformation of the Y4813W pore had been restored in contrast to Y4813A. The functional consequence of the conservative tryptophan on channel gating was examined further in chapter 6.

5.4.4 Initial single-channel characterisation of mutant hRyR2 channels – D4829

As discussed in chapter 4, the aspartic acid at position D4829, located at the luminal mouth of the selectivity filter is highly conserved throughout RyR isoforms and other channels (IP_3R and K^+ channels) (Balshaw *et al.,* 1999; Taylor and Tovey, 2010; Heginbotham *et al.,* 1994; McCoy and Nimigean, 2012). The negative charge near the luminal mouth generates an ideal capture radius for cations. Previous

investigations that removed charge and neutralised acidic residues in the luminal mouth produced changes in the electric field in the pore that altered the interaction energies of permeant ions and the stability of the selectivity filter region that ultimately contributed to reduced unitary conductance and changes in ion handling and gating (Mead-Savery *et al.,* 2009). Another investigation focused on D4899 in RyR1 (analogous to D4829 in RyR2) (Gao *et al.,* 2000). Generating alanine (reduced side chain), arginine (positive charged) and asparagine (uncharged with similar side chain length) D4899 mutations resulted in decreased K^+ conductance, shown in figure 5.18, and a loss of high-affinity [^{3}H] ryanodine binding but maintained their response to caffeine in the cellular assay (Gao *et al.,* 2000). The D4829 mutations described in this chapter supported these previous reports by Gao *et al*. In addition, mutation of the analogous residue in the inositol 1,4,5-trisphosphate (IP_3) receptor (IP_3R) (D2550A) resulted in defective Ca^{2+} release activity (van Rossum *et al.,* 2004; Bhanumathy *et al.,* 2006). Together, these results indicate that the conserved selectivity filter residue constitutes an essential part of the ion-conducting pore of both IP_3R and RyR channels.

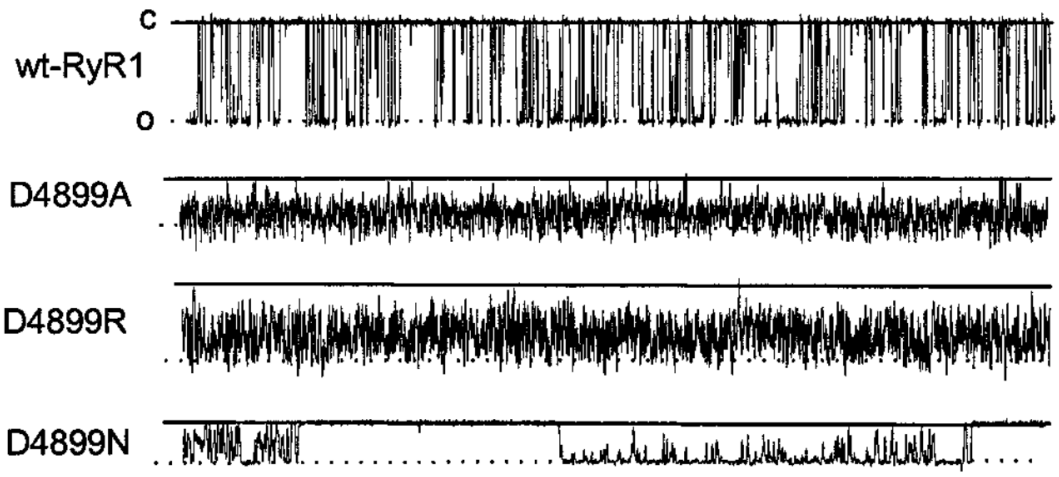


Figure 5.17. Single-channel recordings of WT and mutant D4899 RyR1 in symmetrical 250 mM KCl solution. D4899 in RyR1 is analogous to the D4829 selectivity filter residue in RyR2. Downward single-channel currents are channel openings. Similar channel conductance and gating characteristics were observed in D4829 RyR2 mutations, depicted in figures 5.5 and 5.6, compared to D4899 RyR1 mutations. Figure adapted from Gao *et al.,* (2000).

The architecture of the selectivity filter in K^+ channels ensures strong K^+ ion binding site interactions that provide optimal geometry and close coordination for dehydrated K^+ ions (Doyle *et al.,* 1998). The biophysical structural properties of the selectivity filter, lined by carbonyl oxygen atoms provide closely spaced sites that ensure high selectivity over relevant cations such as Na^+ ions and allows for high ion conduction mediated by electrostatic repulsion (Yellen, 2002; Roux *et al.,* 2011; Nimigean and Allen, 2011; Alam and Jiang, 2011).

The dimensions of the pore in the current Yan *et al* RyR1 model are somewhat different. Comparing the Yan *et al* and the original Welch *et al* models of the PFR RyR depicted in figure 5.18 reveals an altered conformation of the selectivity filter. An arbitrary measurement using PyMol between the two adjacent D4829 residues reported a distance of 12.3 Å in the Welch *et al* analogy RyR2 model shown in figure 5.18B that had increased to 16.9 Å in the Yan *et al* RyR1 model, figure 5.18A (Yan *et al.,* 2015).

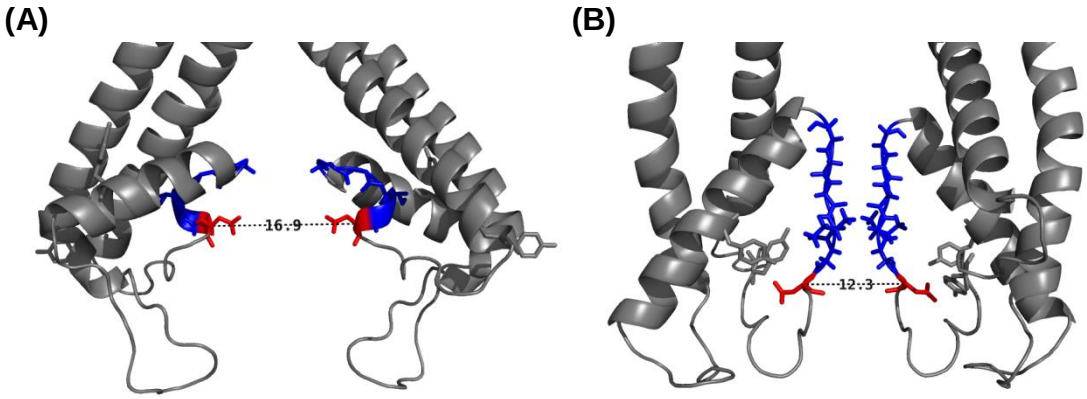


Figure 5.18. Comparing the dimensions of the selectivity filter between structural models. The selectivity filter highlighted in blue with the residue D4829 (D4899 RyR1) in red of (A) the current PFR RyR1 model (Yan *et al.,* 2015) and (B) the analogy PFR RyR2 model (Welch *et al.,* 2004).

While the signature sequence remains the same (GGGIGD) the concave conformation of Yan *et al* PFR model, figure 5.18A, may explain the non-selective and relative permeability to a wide range of monovalent and divalent cations (Lindsay and Williams, 1991; Tinker and Williams, 1992; Tinker and Williams, 1993a). This suggests that the conformation of the filter and the arrangement of residues to accommodate specific cations are less important in RyR than in K^+ channels.

Reducing the side chain length in D4829A, resulted in a channel with reduced unitary conductance, 195.5 pS, 75 % less than WT hRyR2, figure 5.9, and also produced gating kinetics similar to those reported in D4899A RyR1 shown in figures 5.5 and 5.17. In addition, the maximum Ca^{2+} release of HEK293 cells expressing D4829A channels was reduced by 22.7 % compared to cells expressing WT hRyR2 channels (chapter 4.3.1.1). This suggests that the reduced ΔF from a population of D4829A channels may have been a consequence of decreased D4829A single-channel conductance. A mechanism for the reduction in D4829A channel conductance could be due to the loss of negative charge in the luminal region that provides a mechanism for maximising rates of cation delivery to the pore (Welch *et al.,* 2004).

Interestingly, introducing a conservative mutation at this position, D4829E, thus maintaining the negative charge but extending the side chain length by a methyl group, increased unitary conductance compared to D4829A and maintained the maximum Ca^{2+} release compared to WT hRyR2 channels (chapter 4.3.1.1). This suggests that negative charge in the luminal mouth has a functional role for cation delivery and translocation. D4829E did however initiate two well-defined sub-conductance states at the single-channel level. The consequence of conservative residue substitution and flexibility of the filter is likely to have contributed to sub-conductance states that arise from small conformational changes that alter the electric field or affect the ability of this region of the channel to bind ions, discussed in chapter 7.1 (Dani and Fox, 1991; Mead-Savery *et al.,* 2009).

At the single-channel level, a proposed D4829E ryanodine modified channel depicted in figure 5.7, was only observed in the presence of ryanodine. It was therefore likely that the altered gating events, highlighted in red, were due to ryanodine interaction within the channel. Ryanodine was able to dissociate from the proposed modified channel, thus explaining the lower 7.18 % [^{3}H] ryanodine binding results compared to WT hRyR2. Ryanodine dissociation from single-channels and loss of [^{3}H] ryanodine binding has been previously reported in other studies investigating residue substitution within the RyR pore, Q4863A (Wang *et al.,* 2003; Ranatunga *et al.,* 2005). In this study, the single-channel observations from figure 5.7 suggested that the access to, or the conformation of the binding site affected the affinity of ryanodine interaction with D4829E. Further work would be required to assess the consequence of glutamic acid mutation at position 4829 on the altered

affinity of the ryanodine-RyR2 interaction, using reversible ryanoid derivatives such as 21-amino-9alpha-hydroxy-ryanodine (Tanna *et al.,* 1998).

Constructing alanine and glutamic acid point mutations at position D4829 produced channels with reduced ion conductance and high channel-to-channel functional variations. The unique and varied D4829 hRyR2 mutations were ultimately unsuitable for further investigations in the time-scale of this project. However the drastic effect on channel gating and conductance suggested that the negative charge and also the precise side chain length of the conserved aspartic acid is essential in maintaining channel function.

5.4.5 Initial single-channel characterisation of mutant hRyR2 channels – Y4839

As discussed in section 5.4.2 the initial and most striking difference comparing the two models, Yan *et al* and Welch *et al*, was the location of Y4839. Comparing the proposed boundary sites of helices in the primary sequence, depicted in figure 5.15, revealed that in the Welch *et al* model of RyR2, Y4839 is located in a loop-forming region close to the selectivity filter region. In contrast, Y4839 in the PFR RyR1 model by Yan *et al* is located in the S6 helix away from the pore and selectivity filter region, highlighted in green in figure 5.16. The changes in the position of Y4839 are due to the altered helix boundary sites between models. The loop-forming region consists of 18 residues between the selectivity filter and S6 helix in the Welch *et al* model of RyR2, figure 5.16B. In contrast the loop-forming region in the current Yan *et al* model is considerably shorter, with the filter and the start of S6 helix separated by only 6 residues. The increased length of the S6 helix in the Yan *et al* RyR1 model encompasses the residue Y4839, figure 5.16A. The location and orientation of Y4839 within the α-helix means that the residue faces away from the selectivity filter region and a direct interaction of the residue within the pore would be implausible.

Pore-forming region helices are structural domains that pass through numerous conformational changes and are important in the protein's machinery to allow transitions of the channel between closed and open states. Previous investigations based on the activation gate of K^+ channels proposed that the S6 helix in RyR undergoes conformational rearrangements in the gating process (Euden *et al.,*

2013b; Mei *et al.,* 2015). Thus, reducing the side chain length and removing residue interactions with the α-helix in Y4839A hRyR2 may have altered the structure and imposed different constraints within the spiral conformation.

The initial single-channel characterisation of Y4839A revealed a functional channel with similar gating kinetics to WT hRyR2 shown in figures 5.2A, 5.2F and 5.2G. This supported earlier reports of similar maximum Ca^{2+} release in HEK293 cells expressing Y4839A compared to cells expressing WT hRyR2 channels, outlined in chapter 4.3.1.1. However, upon single-channel analysis, under the conditions used in these experiments, the alanine mutation produced a channel with a significant 16.8 % reduction in ion conductance compared to WT hRyR2, thus a series of four ion handling investigations were completed to determine the mechanisms responsible for altered ion conduction.

While the alanine mutation did not alter the ability of hRyR2 to discriminate between cations and anions, the relative permeability between divalent and monovalent cations was significantly lower than in WT hRyR2. This was surprising as in previous reports it had been proposed that a high density of negative charge, either within the pore or within vestibules at either end of the pore, was responsible for discrimination between cations (Tinker *et al.,* 1992; Mead-Savery *et al.,* 2009). However altered cation discrimination, due to disrupted interactions in Y4839A, may have been achieved through an indirect conformational change of the highly electronegative loop-forming region between the selectivity filter and S6 helix. The activity saturation curve also provided interesting insight into the consequence of Y4839A on channel conductance. The unitary conductance was unaltered at all K^+ activities except for 21.50 mM, 111.3 mM and 149.9 mM when compared to WT hRyR2 channels. While the K_D remained the same ~ 23 mM, the reduced B_{max} of Y4839A may have been due to changes in the pore's energy profile.

Probing the dimensions and conduction properties of Y4839A channels using monovalent organic cations demonstrated no significant differences in relative permeability and unitary conductance. This indicates that reducing the size of the side chain of this residue in the S6 helix did not increase the minimum radius of the pore (or its properties) to such an extent as to allow triethanolamine to pass through. The minimal radius of the pore was determined to be < 3.6 Å, this value was in accordance to the minimum pore radius of 3.5 Å established for WT RyR2 in

a previous investigation that employed 23 monovalent organic cations of varying size and properties (Tinker and Williams, 1993a).

As is the case for the pore helix mutation at Y4813, the conservative Y4839W mutation restored single channel conductance to a value comparable with WT hRyR2. The initial single-channel characterisation of Y4839W highlighted the importance of either the steric bulk or residue physicochemical hydrogen-bonding interactions of this residue within the pore region. The single-channel investigation of point mutations occuring at Y4839 indicated that residue interactions at this location are important in ion conduction and to the discrimination of cations. The consequence of residue subsitution at Y4839 on channel gating mechanisms was further examined in chapter 6.

5.4.6 Investigating a potential hydrogen-bonding network in the PFR of RyR

The hypothesis in which it was proposed that a hydrogen-bonding network is established by three residues between the selectivity filter and pore helix that regulates channel gating (chapter 1.5) were assessed. The distances between the ends of the hydroxyl and carboxyl side chains of these three residues were measured in PyMol, depicted in figure 5.19. The distances between Y4813-D4829 and Y4839-D4829 in the Welch *et al* analogy PFR model were 2.5 Å and 3.7 Å respectively as shown in figure 5.19B and are ideal to form hydrogen-bonds (Hubbard and Haider, 2010). However, in the current Yan *et al* model, depicted in figure 5.19A, the distance between the proposed residues Y4813-D4829 and Y4839-D4829, 20 Å and 25.6 Å respectively, would not allow the formation of a hydrogen-bonding network.

Therefore, the close proximity of defined pore residues occurring in K^+ channels, that form a gate by stabilising the selectivity filter may not occur in hRyR2 (Bernèche and Roux, 2005; Cordero-Morales *et al.,* 2006; Ader *et al.,* 2008; Cuello *et al.,* 2010a; Cuello *et al.,* 2010b; van der Cruijsen *et al.,* 2013). However, removing the hydrogen-bonding capacity of two of the hRyR2 mutations, Y4813A and D4829A, significantly affected channel gating and function. This observation suggests that these residues, Y4813 and D4829, are essential and may be involved in stabilising a conformation of the pore helix and selectivity filter.

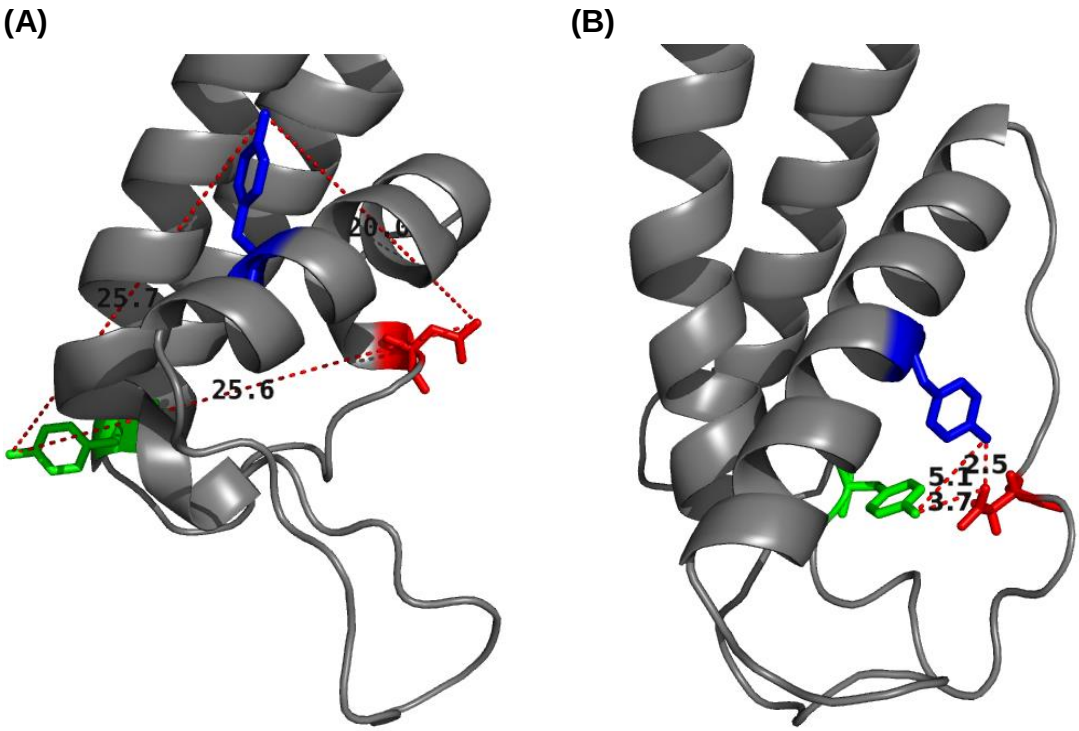


Figure 5.19. Measuring the distances between residues in (A) the PFR RyR1 model (Yan *et al.,* 2015) and (B) the analogy PFR RyR2 model (Welch *et al.,* 2004). Highlighted residues are colour coded; Y4813 (blue), D4829 (red) and Y4839 (green), analogous residues highlighted in RyR1. Labelled distances were determined in PyMol measured in Ångström. (A) The proposed hypothesis of a hydrogen-bonding network between highlighted residues would not be possible in the current Yan *et al* model. One monomer is shown for clarity.

In summary, although the relative position of residues Y4813 and Y4839 have been altered in the current Yan *et al* model, it is important to note that while the resolution of the structure has improved these models represent static structures. Membrane proteins are complicated dynamic molecules that interact continuously with the surrounding environment including lipid, ligands, accessory proteins and modulators that ultimately result in allosteric conformational movements between residues and domains. While in the model published by Yan *et al*, the distances between the three residues proposed in the hypothesis would not permit the formation of hydrogen-bonds due to rearrangement of helices, the selectivity filter region and residues are still of high importance.

Initial single-channel characterisation of selectivity filter and pore helix hRyR2 mutations has revealed interesting insight into the importance of residue properties and their interactions within the pore. Three hRyR2 mutant channels, Y4813W, Y4839A and Y4839W, were suitable for detailed investigations of gating processes of individual channels and these experiments form the basis of chapter 6. The validity of the PFR structural models and the function of residue interactions can only be assessed by measuring biophysical kinetics of mutated proteins at the single-channel level. Examining these gating mechanisms will reveal a potential role of the selectivity filter as a gating component and will assist in the structural-functional relationship of residue interactions in the pore.

Chapter Six:

Single-Channel Gating Mechanisms at the Selectivity Filter of WT and Mutant hRyR2 channels

Single-Channel Gating Mechanisms at the Selectivity Filter of WT and Mutant human Cardiac Ryanodine Receptor (hRyR2) channels

Chapter Six – Aims

The initial single-channel characterisation, outlined in chapter 5, revealed interesting insight into the functional consequence and importance of residue interactions around the proposed selectivity filter region. Three hRyR2 mutant channels, Y4813W, Y4839A and Y4839W, were suitable for detailed investigation of gating processes. This chapter uses the single-channel technique and sophisticated data analysis to assess the role of residue side chain interactions within the pore region and to reveal underlying channel gating mechanisms predicted to occur at the selectivity filter. The aims of this chapter are as follows:

- To investigate the gating mechanism of WT and mutant RyR2 channels in response to activating Ca^{2+} under minimal conditions. This will initially involve calculating the open probabilities (P_o) achieved at different concentrations of free Ca^{2+} and analysing the relationship between dwell times and P_o.

- Following data selection, according to criteria outlined in section 6.3.6, gating behaviour (state occupancy, time and rate constants) was analysed using QuB and compared to previous studies (Mukherjee *et al.,* 2012).

- To identify the prevalence and nature of flicker gating events (thought to originate in the selectivity filter) in mutant hRyR2 channels, to see if substitution has affected this particular conformational transition.

- To discuss and relate novel hRyR2 gating information to recently published RyR1 models to enhance the credibility of these static structures.

6.1 – Introduction

6.1.1 Understanding the mechanisms of hRyR2 channel gating

Ion channels are allosteric proteins that undergo complex structural rearrangements, in response to specific stimuli, to allow ion conduction. The permeation of ions through the channel pore is regulated by distinct structural elements that act as intermittent barriers, or gates, in a process termed channel gating (Perozo *et al.,* 1999; Cordero-Morales *et al.,* 2006; Cuello *et al.,* 2010a; Cuello *et al.,* 2010b; Wang *et al.,* 2011). The precise control of these gating events and the dynamic movement of these structural elements are critical for normal cellular function. Altered RyR2 channel function is a key component in the pathogenesis of arrhythmia in acquired and genetic diseases (Priori *et al.,* 2001; George *et al.,* 2003; Mohamed *et al.,* 2007; Dobrev and Wehrens, 2014), and it is therefore essential to identify these structural elements involved in RyR2 channel gating to gain detailed knowledge of the fundamental processes of RyR2 function in health and disease.

Mechanisms underlying channel gating were initially elucidated in K^+ channels through numerous X-ray crystal structures and experimental data (Doyle *et al.,* 1998; Zhou *et al.,* 2001; Jiang *et al.,* 2002b; Jiang *et al.,* 2003; Long *et al.,* 2005; Uysal *et al.,* 2009; Cuello *et al.,* 2010b). As discussed in chapter 1.5.6, two gates exist in K^+ channels; an activation gate located at the inner-helix bundle crossover (IHBC) and an inactivation gate located at the selectivity filter, depicted in figure 1.22. The coupled interplay between activation and inactivation gating in K^+ channels succinctly controls the flow of ions. The structural basis of K^+ channel gating, and the structural analogy with RyR's (Welch *et al.,* 2004; Ramachandran *et al.,* 2013; Yan *et al.,* 2015) provide a useful template to predict potential mechanisms occurring in RyR2. It has been established that mutations at or near the selectivity filter lead to a variety of gating effects in K^+ channels (Liu *et al.,* 1997; Proks *et al.,* 2001; Alagem *et al.,* 2003; Chapman *et al.,* 2006; Cordero-Morales *et al.,* 2006; Cuello *et al.,* 2010a). However in hRyR2, the identification of a putative structural element at the proposed selectivity filter acting as a gate remains unclear.

Transient elevation of cytosolic Ca^{2+} concentration ($[Ca^{2+}]_{cyt}$) during systole activates hRyR2 channels in a process termed calcium-induced calcium release described in chapter 1.2.1. Ligand interaction with proposed Ca^{2+}-binding sites, distant from the channel pore, must therefore induce a conformational wave of movements between residues and chemical bonds that allow distinct gates within the pore to open. However the dynamic molecular pathway is still unknown. Recent structural studies of rabbit RyR1 have identified EF-hands, acting as a putative Ca^{2+}- binding domain depicted in figure 6.1, on the central domain that are in relatively close proximity to the channel pore (Zalk *et al.,* 2014; Efremov *et al.,* 2014; Yan *et al.,* 2015). This suggests that Ca^{2+} binding may induce conformational changes in the EF-hand that transmit to the pore through contacts with either the S2-S3 loop or central domain, ultimately resulting in changes within the pore aperture (Zalk *et al.,* 2014).

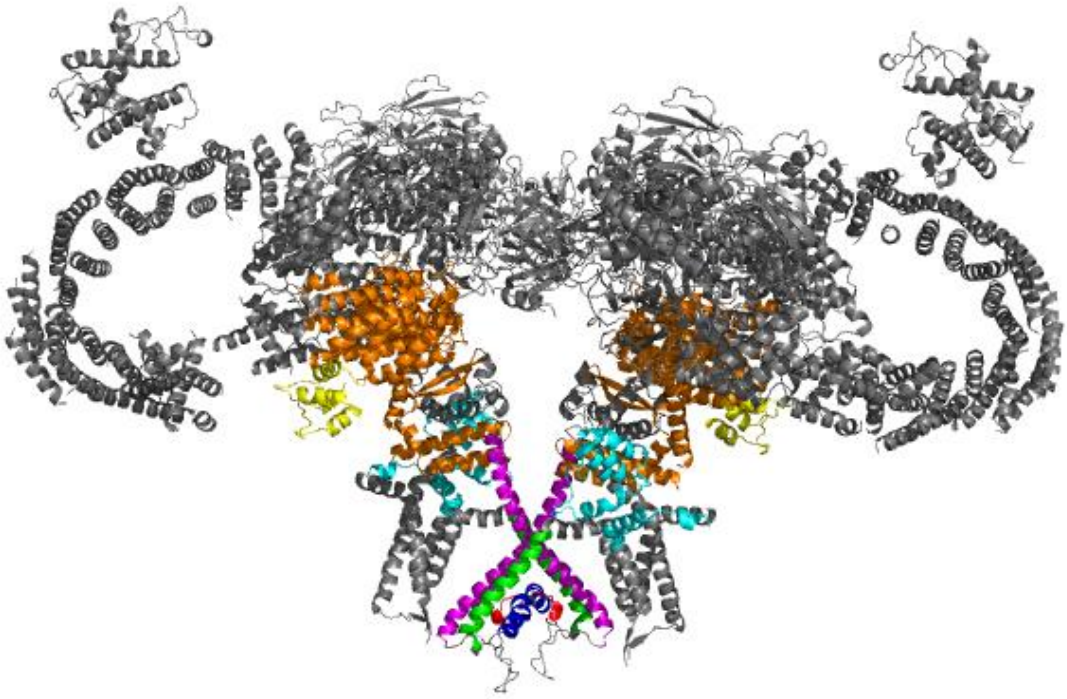


Figure 6.1. Structural model of the rabbit RyR1 channel. Cartoon structure of RyR1 highlighting the EF-hands (4071 - 4132 RyR1), acting as a putative Ca^{2+} binding site, in yellow relative to the PFR colour coded as illustrated in figure 5.14. The EF-hands are in the central domain (highlighted in orange 3668–4251) and are in close proximity to the S2-S3 loop (highlighted in cyan 4675-4790) that are proposed to transmit conformational changes to the pore domain. Two monomers are shown for clarity. Figure was constructed in PyMol using the PDB file, 3J8H, obtained with permission from Chang-cheng Yin (Yan *et al.,* 2015).

It is important to note that the RyR1 structural studies have reported the channel in a closed conformation (Zalk *et al.,* 2014; Yan *et al.,* 2015). Figure 6.2 depicts the constriction site at isoleucine 4937 (I4867 in hRyR2), potentially acting as one of the residues of an 'activation' gate analogous to the IHBC in K^+ channels outlined in chapter 1.5.6.

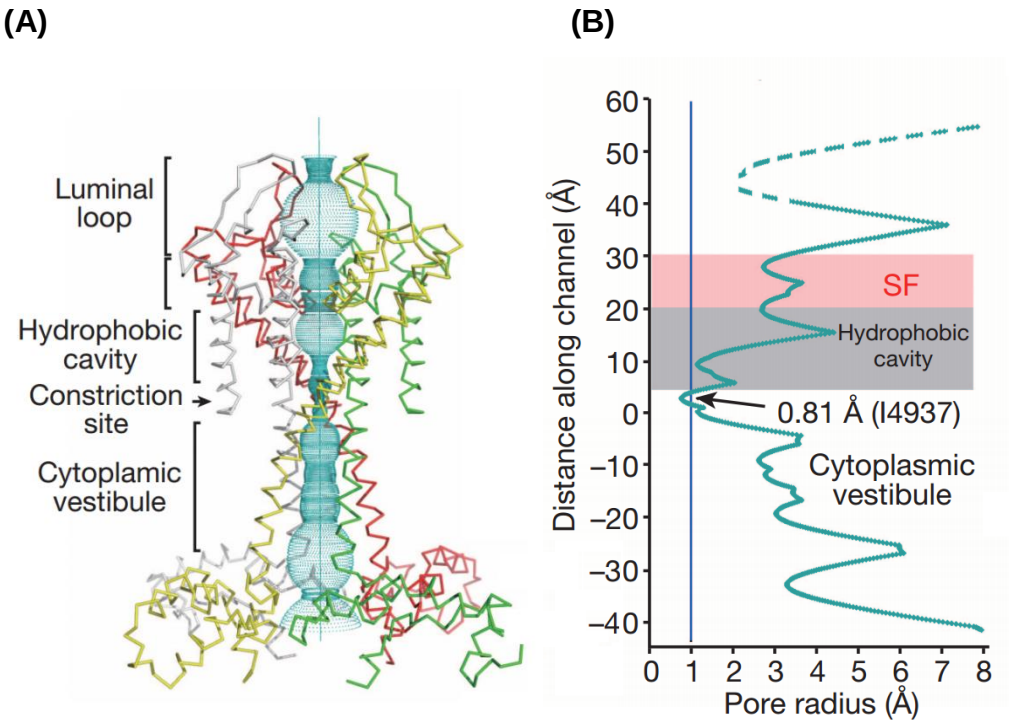


Figure 6.2. Measuring the closed RyR1 channel. (A) The structure of the RyR1 pore and the passage area depicted by cyan dots, calculated by a program HOLE described by Smart *et al.,* (1993). (B) The pore radii along the ion-conducting pathway are tabulated highlighting the selectivity filter (SF) in red (~ 3 Å) and the constriction 'activation gate' site at I4937 (0.81 Å) (I4867 in hRyR2). Figure taken from Yan *et al.,* (2015).

While there is significant indication that Ca^{2+}-mediated activation via an IHBC gate exists in RyR channel isoforms, from recent structural studies (Zalk *et al.,* 2014; Efremov *et al.,* 2014; Yan *et al.,* 2015) and experimental evidence of a proposed glycine hinge in the pore-lining S6 helix (Euden *et al.,* 2013b; Ramachandran *et al.,* 2013; Mei *et al.,* 2015), this project aims to elucidate the potential role of the selectivity filter and residue interactions in hRyR2 gating.

6.1.2 Investigating hRyR2 gating mechanisms using single-channel modelling

At present, RyR2 channel gating can only be quantified using single-channel analysis enabling the investigation of kinetic behaviour in a well-controlled *in vitro* environment (Miller, 1986). RyR2 gating events are resolvable and quantified by measuring single-channel ion currents, depicted in figure 6.3. An essential feature in analysis is the appropriate detection and characterisation of the single-channel gating events known as idealisation. Idealisation of raw single-channel data generates important biophysical parameters such as open probability (P_o), mean amplitudes, frequency of events and dwell-times that are used to characterise hRyR2 channels under defined experimental conditions. The dwell-time measurements of the closed (T_c) and open (T_o) amplitude levels are used to calculate the P_o of the channel, which is expressed as a fraction of the total occupied duration in the open state, outlined in section 6.2.3.1. While P_o is a good indicator of overall channel activity, it does not reveal underlying gating mechanisms.

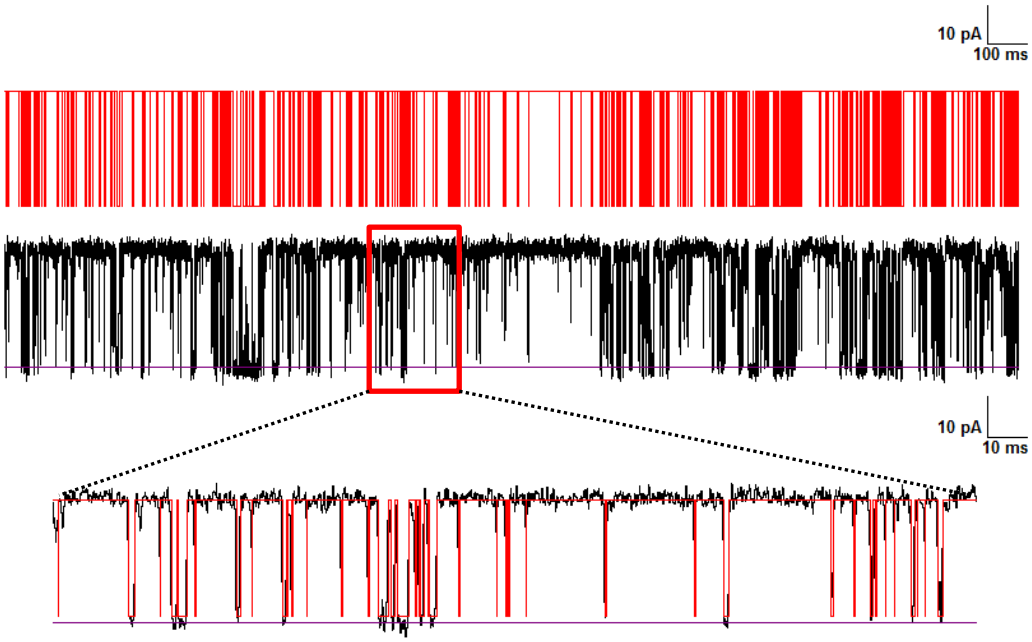


Figure 6.3. Idealisation of single hRyR2 channel gating events. Idealised single-channel data (red trace) generates key biophysical parameters described in text. Lower trace depicts the detection of gating events.

As single-channel gating can be described as a stochastic process (where events are non-deterministic and random) under experimental conditions (Colquhoun and Hawkes, 1977; Colquhoun and Hawkes, 1981), the QuB software, introduced in chapter 5.2.3, utilises probability theory and statistical algorithms to analyse single-channel data. Due to the vast number of interactions that occur within RyR2 at the molecular level during channel gating, it is implausible that an actual sequence of conformational events, such as the chain reaction induced by Ca^{2+} activation, is remembered (Mukherjee, 2014). Therefore, the conformational changes of single-channels are typically modelled as a 'memoryless' Markov process (Qin and Li, 2004). The challenge posed by single-channel kinetic modelling is that ion channels possess multiple states at the same conductance level. These discrete or 'hidden' transitions between states are concealed within the single-channel data therefore putative structural conformations can only be deduced statistically from their dwell-time distributions (Qin *et al.,* 2000).

Constructing kinetic models requires idealised data from which a sequence of open and closed dwell-time histograms are fitted with sums of exponentials based on a given kinetic scheme determined in QuB, detailed in sections 6.3.6 and 6.4.3. A multi-state modelling scheme describes various transitions between states and produces useful kinetic information such as time constants, state occupancy and rate constants that importantly are used to reveal underlying gating mechanisms and assign putative structural conformational states. Modelling single-channel data for channels in which mutations have been made, which are proposed to alter gating kinetics, can therefore be compared to WT hRyR2 channels under defined experimental conditions.

6.1.3 Describing mechanisms of hRyR2 channel gating in minimised conditions

Due to the complex nature of RyR2 channel regulation, with numerous accessory proteins, modulators and ligand interactions discussed in chapter 1.4.1, groups studying RyR2 function have reported varied and inconsistent results (Schiefer *et al.,* 1995; Saftenku *et al.,* 2001; Rosales and Escobar, 2004; Zahradník and Zahradníková, 2005; Laver, 2007). The lack of general consensus between groups was likely due to variable single-channel conditions using different starting material, permeant ions and modulatory factors. This prompted the study by Mukherjee *et al*

to characterise the gating of WT hRyR2 in minimised conditions (Mukherjee *et al.,* 2012). Mukherjee *et al* generated a kinetic scheme, depicted in figure 6.4, that described the gating transitions of WT hRyR2 channels activated by $[Ca^{2+}]_{cyt}$, in the absence of accessory proteins, in a stringently regulated environment. The gating model serves as a template against which the effects of physiological regulatory factors, therapeutic compounds and, in particular for this thesis, point mutations can be tested.

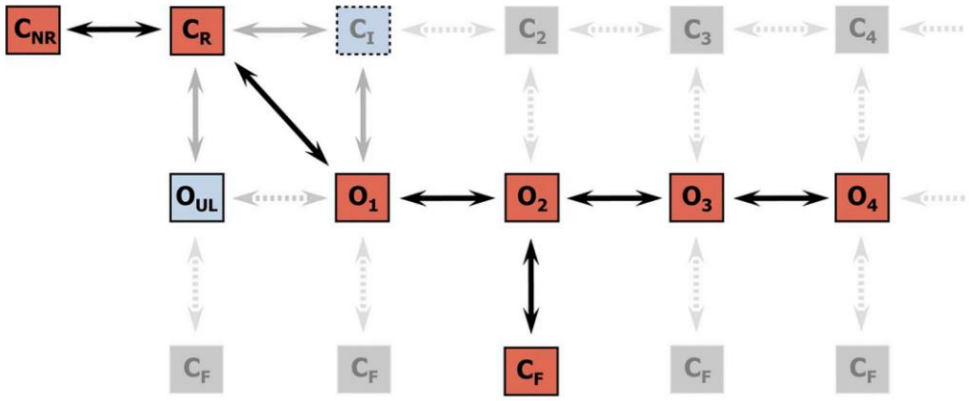


Figure 6.4. A mechanistic description of hRyR2 channel gating. A kinetic gating model of hRyR2, activated by $[Ca^{2+}]_{cyt}$, created under minimised conditions. The kinetic scheme represents a mechanistic network of transitions between different open and closed states describing the behaviour of hRyR2. The kinetic scheme revealed novel aspects of RyR2 gating including non-responsive (C_{NR}) and responsive (C_R) closed states and brief flicker closings (C_F) outlined in section 6.3.6.4. The states and the transitions represented by grey boxes were not discretely resolved from single-channel data analysis. Blue shaded boxes, representing unliganded open state (O_{UL}) and an intermediate Ca^{2+}-bound preopening closed state (C_I) were only resolvable at low Ca^{2+} concentrations, and were not considered in this thesis. Figure obtained from Mukherjee *et al.,* (2012).

6.1.4 Flicker gating transitions at the selectivity filter of the hRyR2 channel

The investigation describing the gating mechanisms of WT hRyR2 in a regulated minimal environment identified very brief closings (~ 0.3 ms), termed 'flicker' gating (Mukherjee *et al.,* 2012), shown in figure 6.5. These flicker transitions observed in the gating scheme, depicted in figure 6.4 as $O_2 \rightleftharpoons C_F$, were resolved during periods of high P_o. The mean dwell time did not change with increasing $[Ca^{2+}]_{cyt}$ (10 – 500 µM) indicating that these very brief flicker closings were Ca^{2+}- independent (Mukherjee *et al.,* 2012).

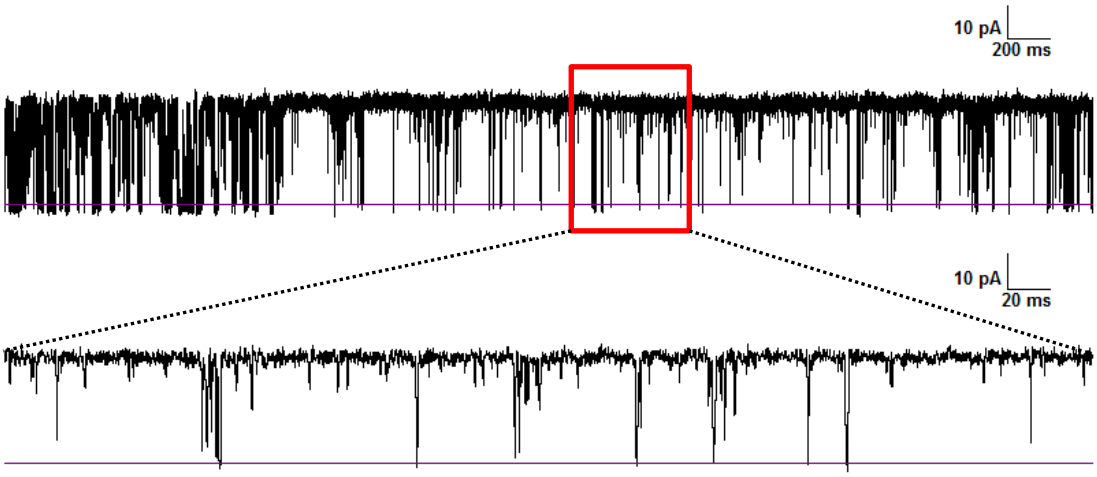


Figure 6.5. Gating of single WT hRyR2 channel highlighting rapid flicker closing transitions occuring during periods of high open probability. The purple baseline represents the closed level, upward deflections are channel openings. The lower 1 kHz trace depicts the very brief 'flicker' closing events as partial (unresolved) downward deflections that do not fully reach the closed level.

Similar flicker events have been observed in other types of channels such as BK, MthK and KcsA where the mechanism in these channels was proposed to occur at the selectivity filter, acting as a gate by rapid switching between conducting and non-conducting states due to the inherent flexibility of the filter (Piskorowski and Aldrich, 2006; Zadek and Nimigean, 2006; Cuello *et al.,* 2010b). Modelling studies reveal that the selectivity filter in hRyR2 is both wider and more flexible than the equivalent region in K^+ channels (Welch *et al.,* 2004), suggesting that flicker closures would be possible.

6.1.5 Purpose of investigating single RyR2 channel gating mechanisms

The high resolution RyR1 models reveal snapshots of the channel structure and provide a valuable resource for predicting channel function. However these static structures do not reflect the dynamic continuum of domain transitions within a single molecule, thus the validity of the PFR structural models and the function of residue interactions can only be assessed by measuring biophysical kinetics of mutated proteins at the single-channel level. While in the recent model published by Yan *et al*, the distances between the three residues proposed in the hypothesis, Y4813, D4829 and Y4839, would not be able to form hydrogen-bonds due to rearrangement of helices, depicted in figure 5.21, the proposed selectivity filter and surrounding region are still of the utmost importance (Yan *et al.,* 2015).

The biophysical characterisation of the six hRyR2 mutant channels outlined in chapter 5 highlighted the significance of residue properties and their interactions within the pore. Mutations investigated in chapter 5 which resulted in channels whose functional behaviour was qualitatively comparable to WT hRyR2 (i.e. Y4813W, Y4839A and Y4839W) were assessed in terms of their effects on gating mechanism. Disruption of interactions at the start of S6 helix by Y4839A was predicted to result in an indirect effect on the stability of the pore region and selectivity filter, thus affecting channel gating such as flicker transitions. The conservative hRyR2 mutations were proposed to be analogous to WT hRyR2 channels by maintaining similar interaction properties, therefore stabilising the pore region such that normal channel gating was preserved. Gating mechanisms were assessed by monitoring WT and mutant hRyR2 channels, activated by 10 µM $[Ca^{2+}]_{cyt}$, in a stringently regulated environment where variables external to the channel were minimised. Biophysical parameters, outlined in section 6.3.1, were assessed and kinetic models, detailed in section 6.3.6, were constructed to describe the behavioural consequence of residue substitution on state transitions.

6.2 – Materials and Methods

6.2.1 Materials

All buffers and solutions were prepared in bottled dH_2O from AnalaR NORMAPUR®, VWR Chemicals that were filter sterilised before use. General reagents are listed in chapter 2.1.8. All experiments were completed at RT 20 ± 2 °C.

6.2.1.1 Ca^{2+} Activation experiment

$CaCl_2$ solution: A 20 mM $CaCl_2$ stock solution was prepared for Ca^{2+} activation experiments.

Ca^{2+} chelating buffers:
***Trans* Ca^{2+} buffer**: 5 mM ethylene glycol tetraacetic acid (EGTA) dissolved in 210 KCl solution buffer.
***Cis* Ca^{2+} buffer**: 90 mM EGTA, 5 mM HEPES and 210 mM KOH adjusted to pH 7.4.
***Cis* Ca^{2+} buffer**: 90 mM *N*-(2-hydroxyethyl)ethylenediamine-*N*,*N'*,*N'*-triacetic acid (HEDTA), 90 mM nitrilotriacetic acid (NTA), 5 mM HEPES and 210 mM KOH, pH adjusted from ~ 8.5 to 7.4 using HCl.

6.2.2 Methods

6.2.2.1 Single-channel experiments – Ca^{2+} Activation

Single hRyR2 channels were generated as outlined in chapter 2.2. The *cis* and *trans* chambers were bathed in symmetrical 210 mM KCl solution with a holding potential of + 40 mV, ensuring appropriate signal-to-noise ratio for gating event detection, for all single-channel Ca^{2+} activation experiments. Ca^{2+} activation experiments were completed in three stages that are outlined below;

Gating in unbuffered contaminant Ca^{2+} solutions: Following chamber perfusion, single hRyR2 channels were recorded for 1 min in symmetrical 210 mM KCl solutions. The free [Ca^{2+}] in KCl solutions were ~ 1 µM (termed contaminant Ca^{2+}), due to trace impurities in the KCl salt, measured using a calcium probe (Orion; Thermo Fisher Scientific) (Mukherjee *et al.,* 2012). The free $[Ca^{2+}]_{cyt}$ was the sole activating ligand.

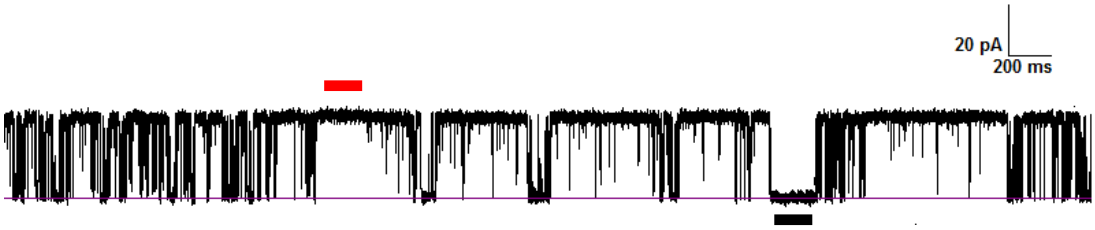
Channel Shutdown: The free [Ca^{2+}] in solutions bathing the channel from both sides of the membrane were stringently regulated. Single hRyR2 channels underwent a shutdown phase where free [Ca^{2+}] was buffered by the addition of Ca^{2+} chelators; EGTA, HEDTA and NTA. From a 90 mM EGTA and 90 mM HEDTA/NTA stock, 5.5 µL was added to the *cis* chamber to a final concentration of 1 mM, to buffer $[Ca^{2+}]_{cyt}$ to nominally 0 Ca^{2+} (~ 0.7 nM). In addition, a 5 mM EGTA stock was added (5 µL) to the *trans* chamber to a final concentration of 25 µM, that ensured the free 'luminal' [Ca^{2+}] was buffered to ~ 50 nM. The concentrations of Ca^{2+} chelators were calculated using a web-based software MaxChelator (http://maxchelator.stanford.edu/index.html), buffering under the following conditions; 22 °C, pH 7.4 and 210 mM KCl. The concentration of Ca^{2+} was verified using a calcium probe (Mukherjee *et al.,* 2012). Both chambers were stirred for a minimum of 1 min following the addition of Ca^{2+} chelators stated above. Chelating the free cytosolic (~ 0.7 nM) and luminal (~ 50 nM) $[Ca^{2+}]_{cyt/lum}$ constituted the shutdown phase. Channel activity was recorded for 1 min under these conditions.

hRyR2 Ca^{2+} Activation: To identify flicker closings, a high channel P_o was required, as these transitions were only resolvable from an open conformation as shown in figure 6.5. The study by Mukherjee *et al* established that hRyR2 channels activated by 10 µM $[Ca^{2+}]_{cyt}$ achieved an open probability above 0.6, that was satisfactory to resolve flicker gating events (Mukherjee *et al.,* 2012). The final concentration of the *cis* chamber was raised to 1.75 mM $CaCl_2$, by the addition of 46.3 µL (20 mM $CaCl_2$ stock) that was stirred for a minimum of 1 min, achieving free 10 µM $[Ca^{2+}]_{cyt}$. WT and mutant single-channel gating behaviour was recorded for up to 20 min under steady-state conditions monitoring activity at + 40 mV in buffered symmetrical 210 mM KCl.

6.2.3 Single-channel data analysis

The single-channel data were low-pass filtered at 5 kHz using a multi-step 8-pole Bessel filter outlined in 2.2.4.1.2. Single-channel ionic current transitions were idealised using the segmental K-means (SKM) algorithm based on hidden Markov modelling (HMM) described by Qin, (2004). Idealisation was initially performed using a two state model, assigning a closed and open level by highlighting regions of defined and continuous sequence of data points, depicted in figure 6.6. Class 1 (black) was assigned the closed current level and Class 2 (red) was assigned the open current level, shown in figure 6.6B. The output is an idealised trace (red) of the raw trace depicted in figure 6.3.

(A)



(B)

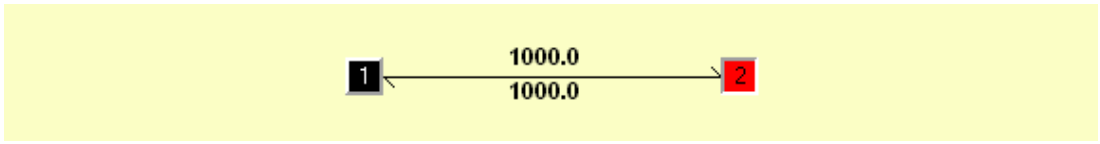


Figure 6.6. Assigning closed and open current levels for single-channel idealisation. (A) A single-channel trace that contains clear closed (black bar) and open (red bar) data point sequence. (B) The continuous closed and open levels were assigned to their Class 1 (black) and Class 2 (red), respectively.

For consistency, data analysis and figure presentation was completed in order of residue sequence i.e. (1) WT hRyR2, (2) Y4813W, (3) Y4839A and (4) Y4839W. For presenting single-channel representative traces, current transition data were low-pass 1 kHz filtered in QuB, unless otherwise stated. The purple baseline in traces denoted the closed level with channel openings determined by upward current deflections at positive holding potentials. Single-channel artifacts such as baseline drifts, user noise and capacitance spikes were removed from the extracted segment prior to analysis.

6.2.3.1 Calculating single-channel open probability

Single channel P_o is the fraction of the time that the channel is in the open state. The probability was calculated following single-channel data idealisation in QuB by measuring the total open time divided by the total time of the extracted recording, stated in the equation below (total open (T_o) and closed (T_c) time);

$$P_o = T_o / (T_o + T_c)$$

Twenty minute single-channel recordings were chopped into 15 s sequential segments using the "Chop Data" tool in the pre-processing tab. Data segments were idealised with a two state model (closed ⇌ open), calculating channel open probabilities that were subsequently plotted against time to generate Ca^{2+} activation distributions.

The relationship between channel dwell-time and P_o was assessed by chopping single-channel data files (20 min) into 30 s sequential segments. The idealised data generated mean T_c and T_o that were plotted against open probability.

6.2.3.2 Single-channel modelling

The comprehensive application of the QuB software and its modelling theory was used to construct kinetic models that describe hRyR2 gating. This thesis does not attempt to explain the mathematical algorithms used in the process of generating the kinetic models as it is not the focus of this project and can be reviewed elsewhere (Colquhoun and Hawkes, 1995; Colquhoun and Sigworth, 1995; Qin and Li, 2004; Qin, 2004; Sigg, 2014; Mukherjee, 2014).

6.2.3.3 Data selection for modelling analysis

An aim of this investigation was to resolve flicker gating transitions by building a model to best describe the gating behaviour of WT and mutant hRyR2 channels. To identify these very brief flicker closing events a high P_o was required. Based on the results obtained from the Ca^{2+} activation experiments, defined criteria were imposed for data selection, listed in section 6.3.6. Periods of single-channel data that contained 30 s of homogenous gating events ranging from P_o 0.6 - 0.8 were

extracted. The criteria ensured that data segments contained comparable general biophysical parameters (P_o, T_c, T_o and number of events) between WT and mutant hRyR2 channels, therefore, any subtle differences in kinetics (time constants, state occupancy or rate constants) resulted as a consequence of residue substitution.

6.2.3.4 Idealisation parameters for modelling analysis

QuB settings were altered to ensure that brief events were resolved and distinguished from noise, and that as few as possible were missed. A certain cut-off duration was imposed, termed dead time (T_d), which ensured that all events with durations longer than T_d were considered as true events and those shorter were missed. As the single-channel data were digitised at 20 kHz (i.e. 50 µs sampling interval), a T_d of 125 µs, 2.5 x the sampling rate was adequate for event detection (Mukherjee, 2014).

6.2.3.5 Constructing kinetic models to describe single-channel gating mechanisms

The Maximum Interval Likelihood (MIL) function in QuB was used to optimise the rate constants of the kinetic model according to the dwell times calculated by the SKM idealisation, generating a log likelihood (LL). Individual closed and open states were assigned and added to the model until further state addition did not increase the LL by more than 5 as shown in figure 6.20. Optimising the LL by more than 5 ensured that the kinetic model suitably fitted the dwell time data. The model provided information on time constants of states, expressed in milliseconds, and the relative area under the exponential fit, converted into a percentage, that indicated the likelihood of a state being occupied.

6.3 – Results

6.3.1 Ca^{2+} activation of single WT and mutant hRyR2 channels – Open probability

The Ca^{2+} activation experiments, described in section 6.2.2.1, were completed in three stages; (1) unbuffered contaminant [Ca^{2+}], (2) regulated Ca^{2+} chelated channel shutdown and (3) 10 µM $[Ca^{2+}]_{cyt}$ activation for WT and mutant Y4813W, Y4839A and Y4839W hRyR2 channels. As an initial biophysical marker, open probability was compared between WT and mutant hRyR2 channels.

6.3.1.1 Stage #1 – Gating in unbuffered contaminant [Ca^{2+}] solutions

The open probability of individual WT and mutant hRyR2 channels activated by contaminant [Ca^{2+}], shown in figure 6.7, was calculated for 1 min immediately following the establishment of symmetrical 210 mM KCl conditions. Individual WT hRyR2 (*n*=23) channel-to-channel open probabilities were variable across the range, P_o 0 – 1, and were characterised by either high, intermediate or low channel activity. A similar trend in mutant hRyR2 channel P_o was observed. WT and mutant hRyR2 channels exhibited similar mean channel P_o, listed in table 6.1, in unbuffered containing ~ 1 µM [Ca^{2+}] with similar spread in the data shown in figure 6.7.

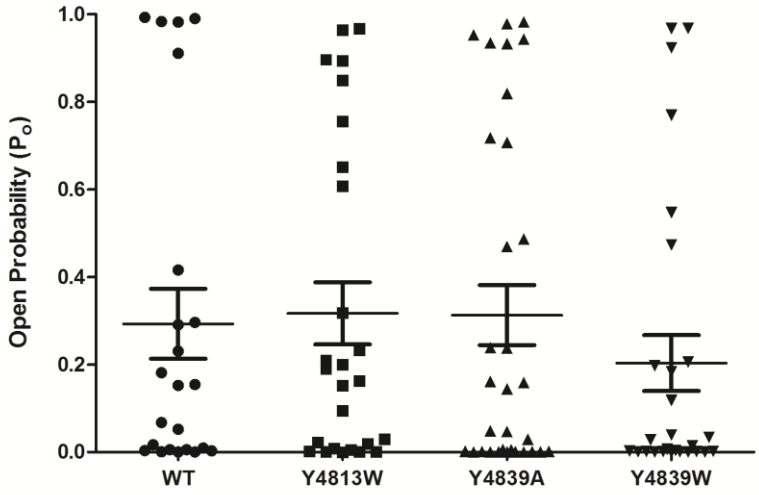


Figure 6.7. Comparing the open probability of individual WT and mutant hRyR2 channels in unbuffered contaminant [Ca^{2+}]. Single-channels were recorded at + 40 mV for 1 min in symmetrical 210 mM KCl. Each data point is a separate channel P_o; there was no significant difference between WT and mutant channel P_o. Bars indicate SEMs and are listed in table 6.1. Individual channel P_o varied from high, intermediate and low.

6.3.1.2 Stage #2 – hRyR2 channel shutdown

A combination of Ca^{2+} buffers, described in section 6.2.2.1, was added to regulate free cytosolic and luminal [Ca^{2+}] in the KCl solutions. Channel shutdown was recorded for 1 min immediately following homogenous mixing of Ca^{2+} buffers. Chelating free [Ca^{2+}] from the KCl solutions resulted in a significant reduction in channel P_o, depicted in figure 6.8, when compared to monitoring channels in contaminant [Ca^{2+}] solutions. A small proportion of very brief hRyR2 opening events was observed in WT and mutant channels, and is discussed in section 6.4.1. The open probability during channel shutdown was consistently low, $P_o < 0.01$, for WT and mutant hRyR2 channels except for Y4813W, listed in table 6.1. The conservative pore helix mutant, Y4813W (*n*=23), revealed five outlier channels that remained active ($P_o > 0.05$) in ~ 0.7 nM $[Ca^{2+}]_{cyt}$ and 50 nM $[Ca^{2+}]_{lum}$. Although the majority of channels (78.3 %) did shutdown in response to chelating Ca^{2+}, the mean open probability (P_o 0.04) was significantly higher when compared to WT, Y4839A and Y4839W hRyR2 channels.

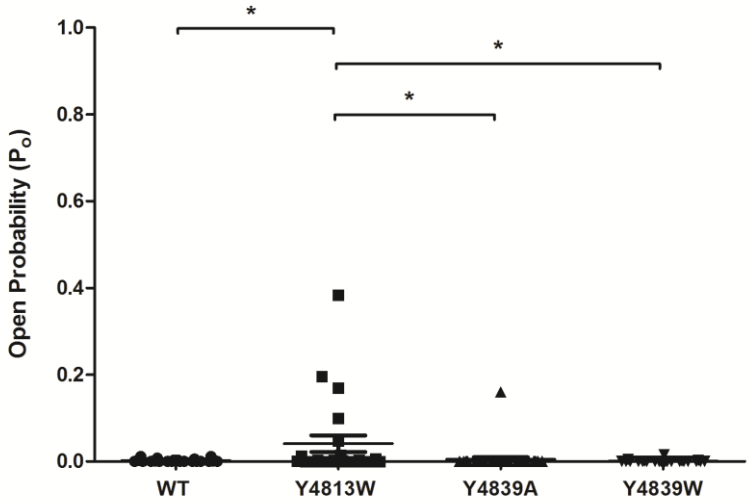


Figure 6.8. Comparing the open probability of individual WT and mutant hRyR2 channels during shutdown. Following stage #1, the same single-channels were recorded in ~ 0.7 nM and 50 nM $[Ca^{2+}]_{cyt}/_{lum}$, respectively, at + 40 mV for 1 min in symmetrical 210 mM KCl solutions. The P_o of Y4813W was significantly higher compared to WT, Y4839A and Y4839W hRyR2 channels (p<0.05). Bars (where visible) indicate SEMs and are listed in table 6.1.

6.3.1.3 Stage #3 – hRyR2 Ca^{2+} activation

Chelating *cis* (cytosolic) and *trans* (luminal) free $[Ca^{2+}]$ significantly reduced channel P_o. In these regulated, minimised, conditions single-channels were activated by 10 µM $[Ca^{2+}]_{cyt}$. WT and mutant hRyR2 channels were subsequently monitored under steady-state conditions for 20 min to evaluate the consequence of point mutations on the proteins biophysical function.

Channel P_o increased upon the addition of 10 µM $[Ca^{2+}]_{cyt}$, depicted in figure 6.9, however the mean P_o of the channel during the 20 min recording was lower than monitoring channels in unbuffered contaminant Ca^{2+} conditions (Stage #1). Mutant channel open probabilities were not significantly different and were comparable to WT hRyR2 (P_o ~ 0.1) during the 20 min recording, listed in table 6.1. Similar to recording channels in KCl solutions that were unbuffered, open probability was variable and not consistent during steady-state conditions.

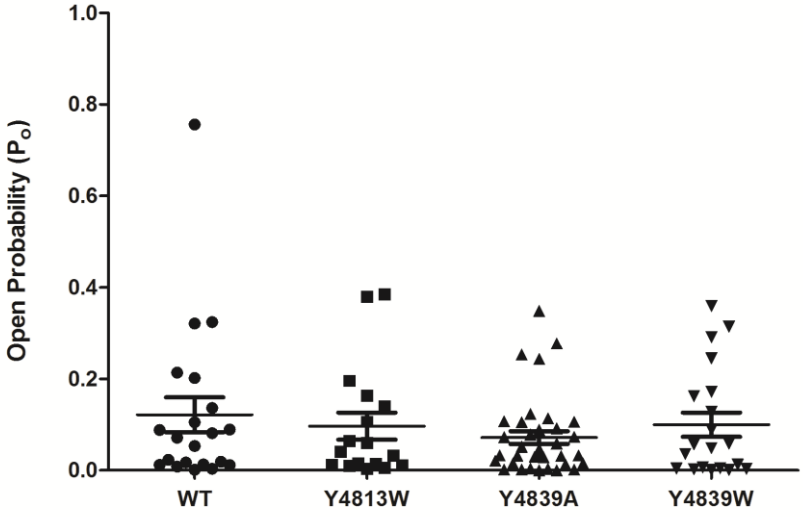


Figure 6.9. Comparing the open probability of individual WT and mutant hRyR2 channels during Ca^{2+} activation. Following stages #1 and 2, the same single-channels were activated by 10 µM $[Ca^{2+}]_{cyt}$ and recorded under steady-state conditions at + 40 mV for 20 min in symmetrical 210 mM KCl. Each data point is a separate channel P_o; there was no significant difference between WT and mutant channel P_o. Bars indicate SEMs and are listed in table 6.1.

	Contaminant $[Ca^{2+}]$			Shutdown			Ca^{2+} Activation		
	n	**(P_o)**		***n***	**(P_o)**		***n***	**(P_o)**	
WT hRyR2	23	0.293 ± 0.08		23	0.001 ± 0.001		21	0.121 ± 0.04	
Y4813W	26	0.316 ± 0.07	ns	23	0.041 ± 0.019	*	17	0.097 ± 0.03	ns
Y4839A	32	0.312 ± 0.07	ns	32	0.004 ± 0.005	ns	33	0.072 ± 0.01	ns
Y4839W	28	0.203 ± 0.06	ns	24	0.001 ± 0.001	ns	20	0.099 ± 0.03	ns

Table 6.1. Comparing the mean open probability of WT and mutant hRyR2 channels during Ca^{2+} activation experiment. Open probability values are means (± SEM). No statistically significant difference in mean P_o was observed between hRyR2 channels activated by contaminant ~ 1 µM $[Ca^{2+}]$ or 10 µM $[Ca^{2+}]_{cyt}$ during Ca^{2+} activation (ns), due to large variation in channel activity depicted in figures 6.7 and 6.9. Y4813W channel P_o during shutdown was significantly increased (P_o 0.041) compared to WT hRyR2 channels (P_o 0.001) indicated by a single asterisk (* p=0.0495).

6.3.2 Ca^{2+} activation open probability distributions

Distribution histograms were generated by analysing single WT hRyR2 channel P_o in sequential 15 s segments, depicted in figure 6.10, that were extracted over the 20 min experiment. Monitoring hRyR2 proteins for extended periods, revealed an intriguing phenomenon: WT hRyR2 channels switched between different gating modes represented by fluctuations in open probability. On occasion, the addition of 10 µM $[Ca^{2+}]_{cyt}$ did not induce typical channel activation ($P_o > 0.6$) (Mukherjee *et al* 2012), where channel P_o remained consistently low ($P_o < 0.2$) represented in figure 6.10(ii). In contrast, the addition of cytosolic $[Ca^{2+}]$ induced modal channel gating on a macro 'minute-to-minute' scale that randomly shifted between periods of low and high P_o and was represented by distributions termed 'skyscrapers', shown in figures 6.10 (i) (iii) and (vi). Similar open probability distributions were observed when analysing the three hRyR2 mutant channels, depicted in figures 6.11, 6.12 and 6.13.

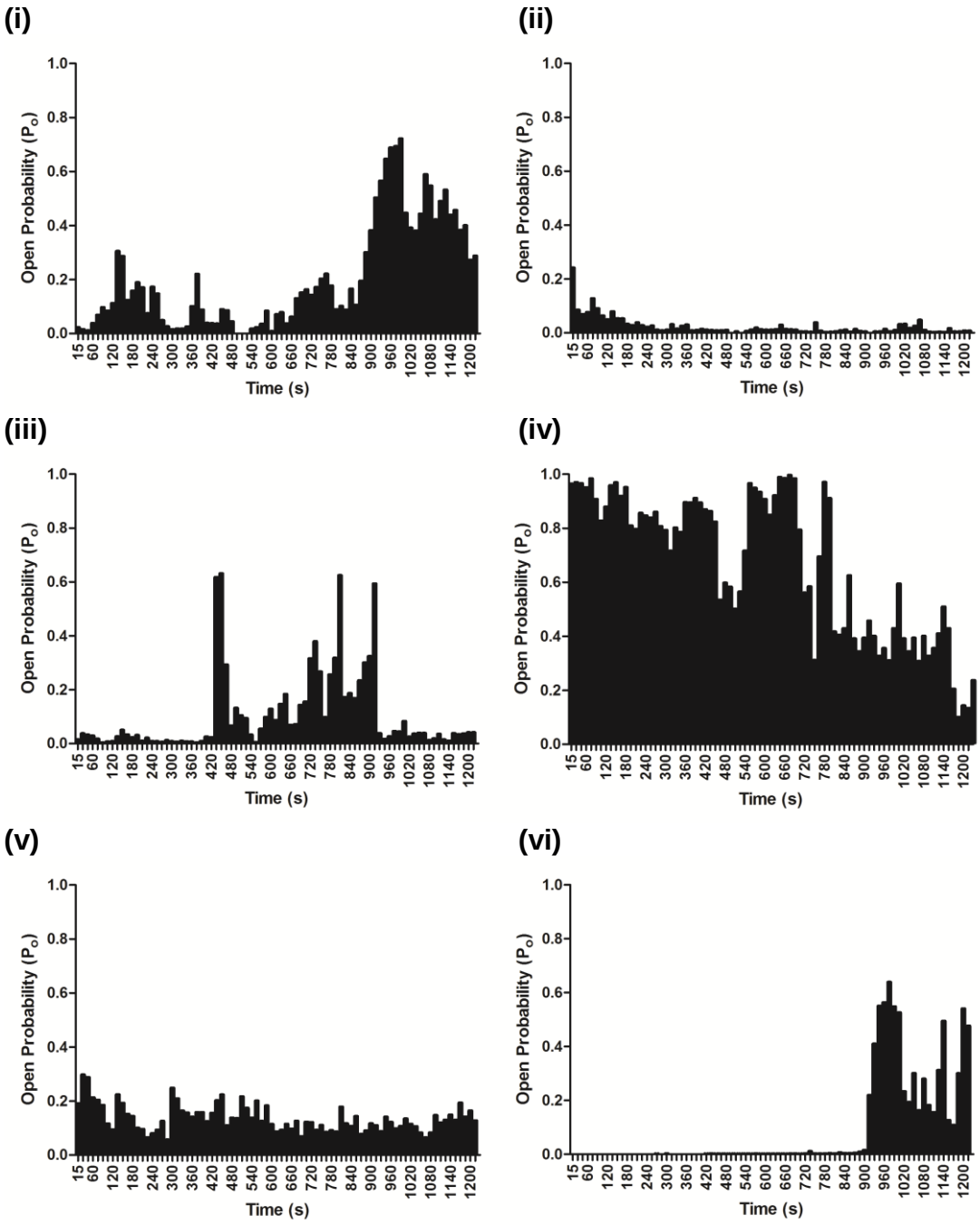


Figure 6.10. Ca^{2+} activation distribution histograms of WT hRyR2 channels. Six representative (i-vi) single WT hRyR2 channel distribution histograms (total *n*=21), analysing open probability under steady-state conditions in sequential 15 s segments over a 20 min recording. Distributions depict high channel-to-channel variation and modal fluctuations in open probability. A representative single-channel long recording is shown in appendix IV.

6.3.3 Categorising the population of WT and mutant hRyR2 channel experiments by open probability threshold

Assessing timed segments over the 20 min recording, revealed the unique and varied nature of studying single-channels at the molecular level. The population of WT and mutant hRyR2 channels were categorised into subsets that were defined by open probability thresholds; high ($P_o \geq 0.6$), figure 6.11, intermediate (P_o 0.2 – 0.6) figure 6.12 and low ($P_o \leq 0.2$) figure 6.13. The proportion of these subset channels, which reached a particular threshold during any 15 s segment, were expressed as a percentage and were listed in table 6.2. A chi-squared contingency test was used to compare the threshold subset distributions and revealed that mutant hRyR2 channels were distributed significantly different to WT hRyR2 (p<0.001). The distribution of WT hRyR2 channel subsets were similar and had the highest proportion of channels that exceeded P_o 0.6 (38 %) compared to mutant hRyR2 channels. The likelihood of mutant hRyR2 channels reaching high P_o was less than 24 %. Both conservative Y4813W and Y4839W mutations favoured the low P_o threshold 53 % and 55 %, respectively, whereas the alanine Y4839 mutation had the highest proportion of channels in the intermediate subset (55 %).

		Single-channel subset proportion (%)		
	n	**High $P_o \geq 0.6$**	**Int P_o 0.2 – 0.6**	**Low $P_o \leq 0.2$**
WT hRyR2	21	38	29	33
Y4813W	17	24	24	53
Y4839A	33	18	55	27
Y4839W	20	15	30	55

Table 6.2. Categorising the population of WT and mutant hRyR2 channel Ca^{2+} activation experiments by high, intermediate and low open probability thresholds. Percentage values were rounded to the nearest integer.

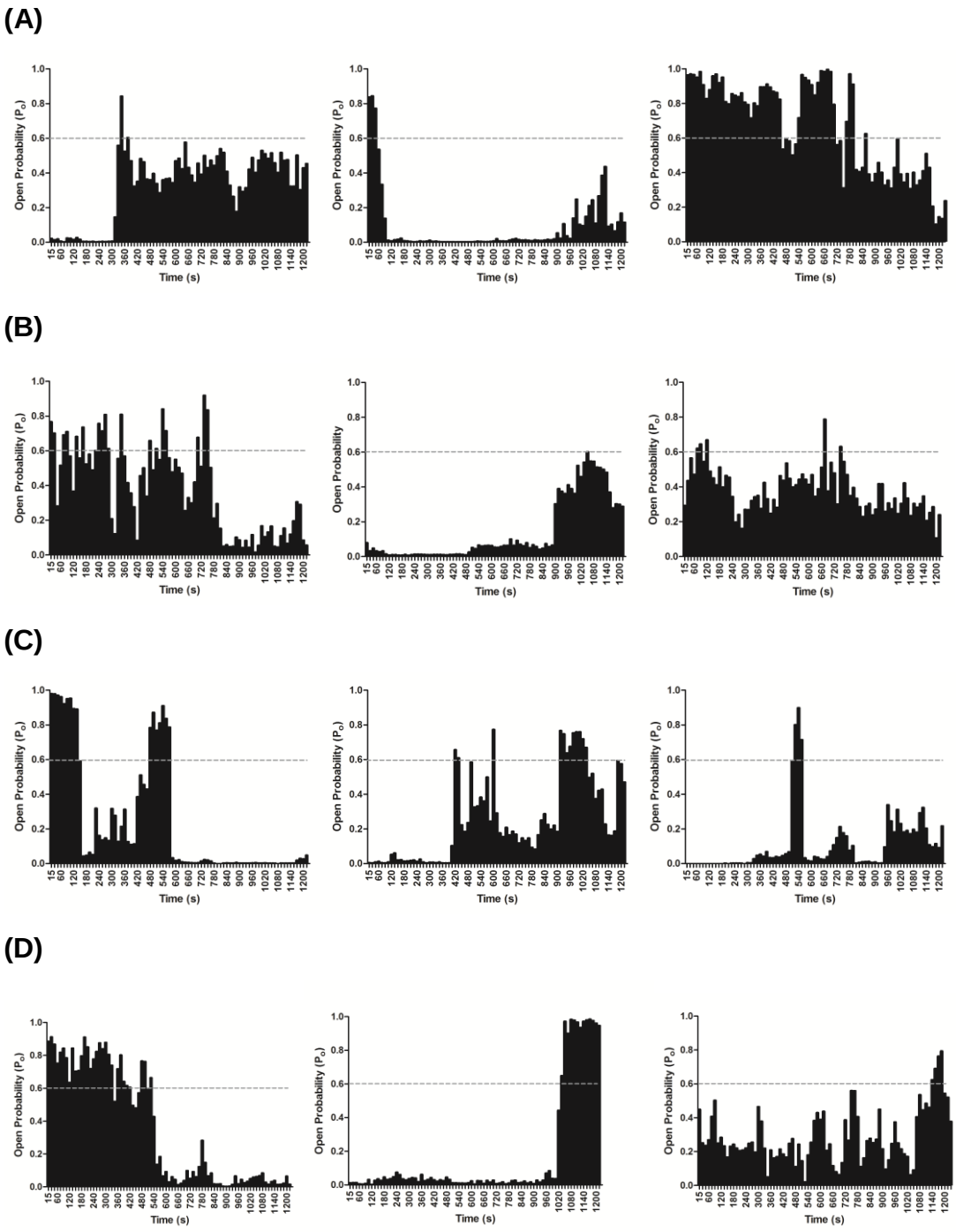


Figure 6.11. Ca^{2+} activation distribution histograms of single WT and mutant hRyR2 channels representing high open probability. Open probability was measured in sequential 15 s segments for 20 min. Three representative individual distribution histograms from (A) WT hRyR2, (B) Y4813W, (C) Y4839A and (D) Y4839W channels depict a 'skyscraper' distribution with large modal fluctuations in channel activity. The grey dotted line denotes high P_o threshold ($P_o \geq 0.6$).

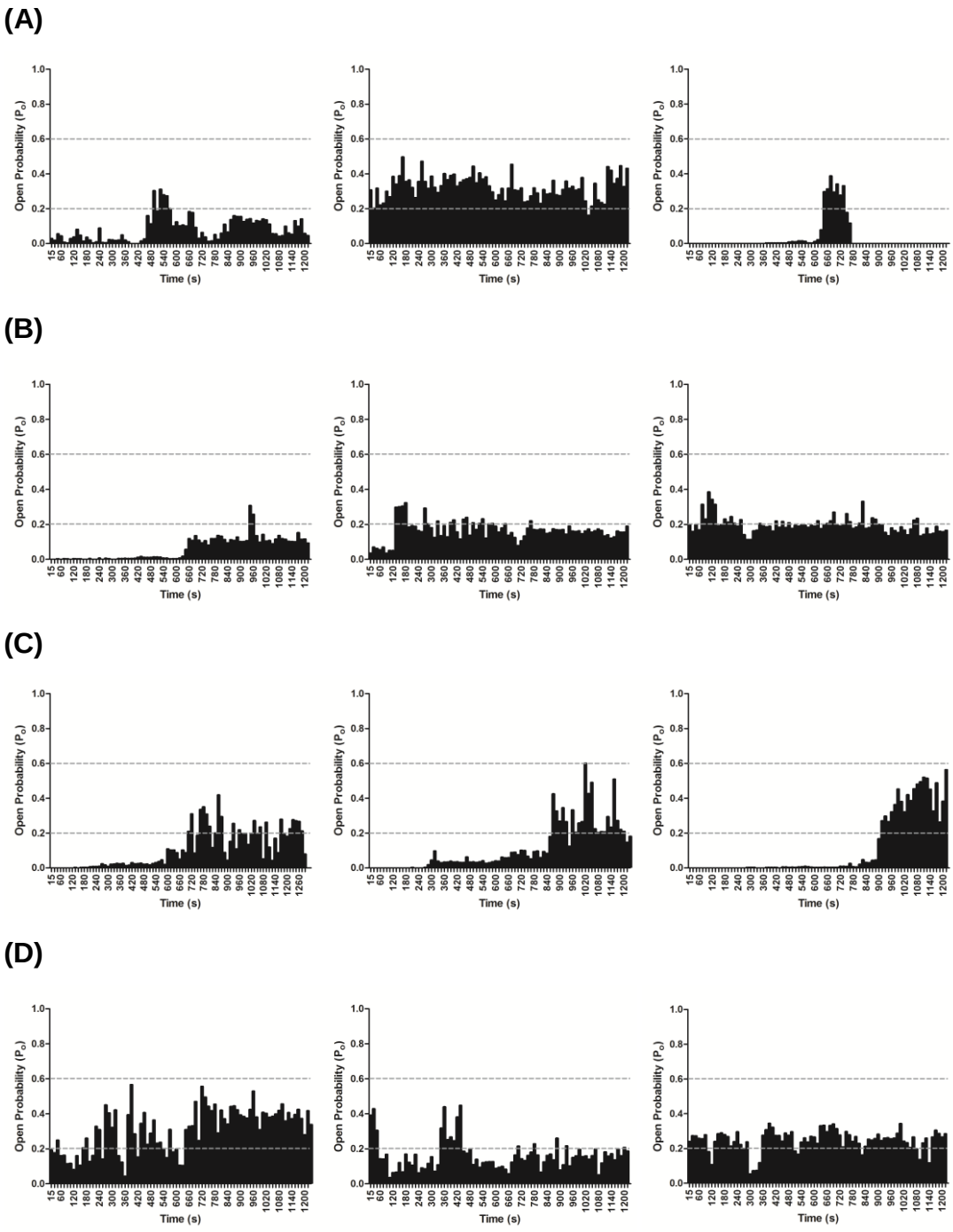


Figure 6.12. Ca^{2+} activation distribution histograms of single WT and mutant hRyR2 channels representing intermediate open probability. Open probability was measured in sequential 15 s segments for 20 min. Three representative individual distribution histograms from (A) WT hRyR2, (B) Y4813W, (C) Y4839A and (D) Y4839W channels depict a 'skyscraper' distribution with modal fluctuations in channel activity. The grey dotted line denotes intermediate P_o threshold (P_o 0.2 - 0.6).

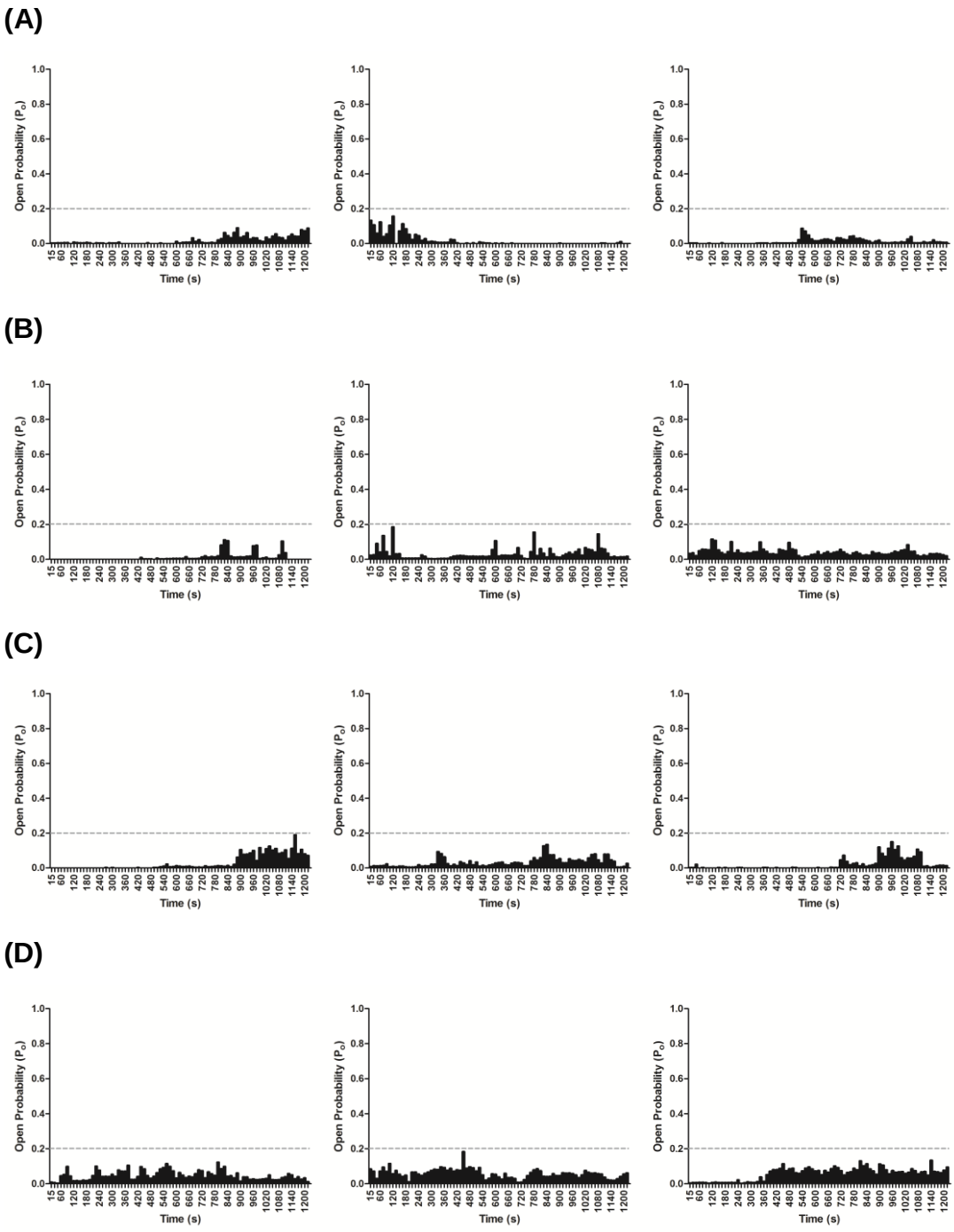


Figure 6.13. Ca^{2+} activation distribution histograms of single WT and mutant hRyR2 channels representing low open probability. Open probability was measured in sequential 15 s segments for 20 min. Three representative individual distribution histograms from (A) WT hRyR2, (B) Y4813W, (C) Y4839A and (D) Y4839W channels. The grey dotted line denotes low P_o threshold ($P_o \leq 0.2$).

The purpose of this investigation was to assess any difference in open probability between WT and mutant hRyR2 channels. While there were no differences in channel P_o, this study identified several important features of studying hRyR2 channels by Ca^{2+} activation under regulated minimised conditions:

(1) Recording single hRyR2 channels for short 1 min periods in unbuffered KCl solutions containing ~ 1 µM [Ca^{2+}], revealed varied snapshots of channel activity.
(2) Chelating cytosolic and luminal free [Ca^{2+}] from KCl solutions induced 'shutdown' in all hRyR2 channels except for a proportion of Y4813W (*n*=5) which remained relatively active (P_o > 0.05) in response to nominal 0 [Ca^{2+}] (~ 0.7 nM and 50 nM $[Ca^{2+}]_{cyt}/_{lum}$ respectively).
(3) WT and mutant hRyR2 channel P_o, activated by 10 µM $[Ca^{2+}]_{cyt}$ over long periods, were lower than channels in unbuffered solutions, listed in table 6.1, however were not significantly different to each other due to high variability in channel activity.
(4) Channel open probabilities for WT and mutant hRyR2 varied with time during the Ca^{2+} activation experiment under defined conditions.
(5) Modal gating was observed in hRyR2 channels on a micro 'second-to-second' scale, described in section 6.3.4, during periods of high P_o under steady-state conditions.
(6) Large fluctuations in channel activity were observed with periods of high, intermediate and low P_o, illustrated by the 'skyscraper' distribution histograms, during long recordings. This supported the observed variation of channel activity 'snapshots' during short 1 min recordings, stated in (1).
(7) Only a small subset of the channel population reached threshold P_o 0.6, therefore 10 µM $[Ca^{2+}]_{cyt}$ did not guarantee hRyR2 activation under the experimental conditions.
(8) The population of conservative Y4813W and Y4839W mutations had the highest proportion of low P_o channel subsets, whereas the alanine mutation favoured the intermediate threshold. However overall, there were no significant differences between mean open probabilities compared to WT hRyR2.

6.3.4 hRyR2 Ca^{2+} activation – Modal gating

An extraction of single-channel WT hRyR2 data, during high P_o ($P_o > 0.6$) from the Ca^{2+} activation experiment, depicted in figure 6.14, shows the shift between different gating modes. Two types of modal gating were observed in all WT and mutant hRyR2 channels and were characterised by random switching ('gear shifting') between high and low P_o (long dwell times and increased frequency of events) during steady-state conditions. Firstly, modal gating was observed on a macro 'minute-to-minute' scale observed as the 'skyscraper' distributions during the 20 min recordings and secondly on a micro 'second-to-second' scale observed in the minute extraction.

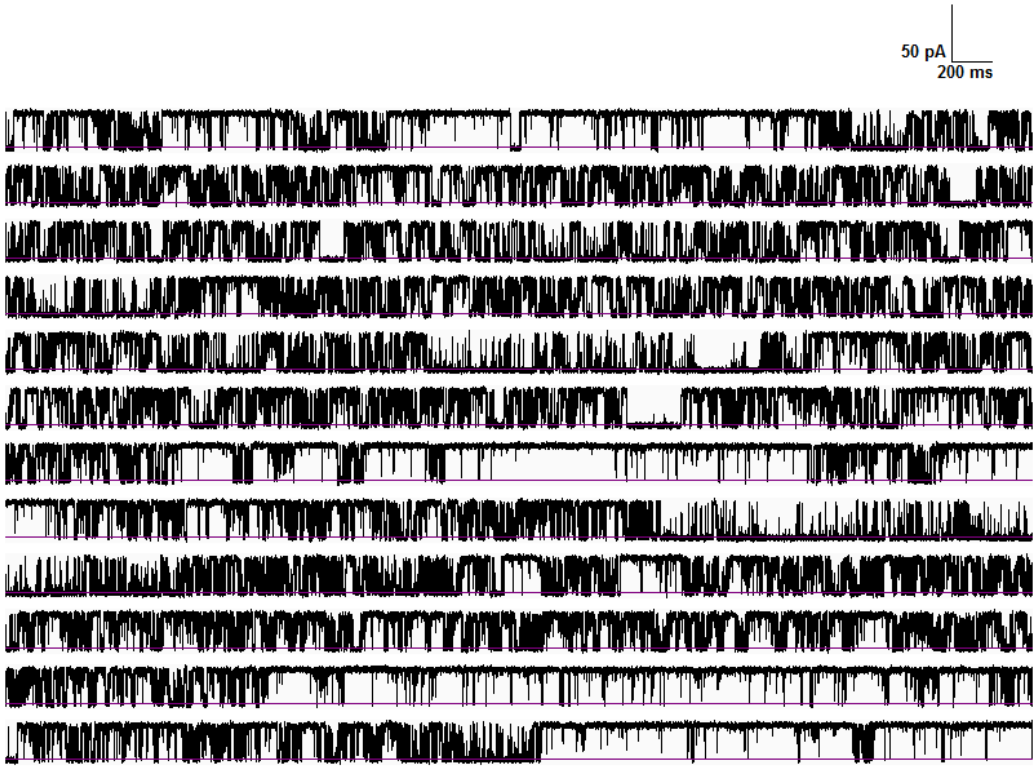


Figure 6.14. Single WT hRyR2 channel modal gating under steady-state conditions. The behaviour of a single WT hRyR2 channel, extracted from a Ca^{2+} activation experiment, was monitored for 1 min during high P_o. The channel randomly switched between different low, intermediate and high gating modes on a micro 'second-to-second' scale under steady-state conditions. Each line represents 5 s of data. The closed level is denoted by the purple baseline with upward deflections as channel openings.

6.3.5 Assessment of hRyR2 mean closed and open times

Open probability is a useful biophysical parameter to assess the overall activity of single channels during a set period; however it does not reveal channel gating kinetics and their mechanism. While investigating the mean P_o did not reveal differences between WT and mutant hRyR2 channels, the 'skyscraper' distributions provided an ideal template for further in-depth analysis described here and in section 6.3.6.

To access differences in channel gating kinetics, mean closed and open times (T_c and T_o), were calculated for WT and mutant hRyR2 channels. Ca^{2+} activation experiments that contained periods of high channel P_o, exceeding P_o 0.6, were selected (WT (*n*=8), Y4813W (*n*=4), Y4839A (*n*=9) and Y4839W (*n*=4)). These distributions contained periods of low, intermediate and high channel activities, therefore dwell-times were examined across the whole range of open probabilities (P_o 0 – 1). The long recordings were chopped into sequential 30 s segments over 20 min recording generating ~ 40 data point values for each experiment. The extracted data segments were idealised to generate mean T_c and $T_{o,}$ and subsequently the relationship between these dwell-times and their open probability were compared in figures 6.15 and 6.16, respectively.

A similar trend between WT (black dots) and mutant (red squares) hRyR2 channel mean dwell times were observed. As the open probability increased, the mean closed time decreased, figure 6.15, whereas the mean open time increased depicted in figure 6.16. There were no differences between overall mean open and closed times in mutant channels compared to WT hRyR2 across the P_o range 0 - 1, however the relationship between dwell-time during periods of very high P_o > 0.8 were assessed in the following section 6.3.5.1.

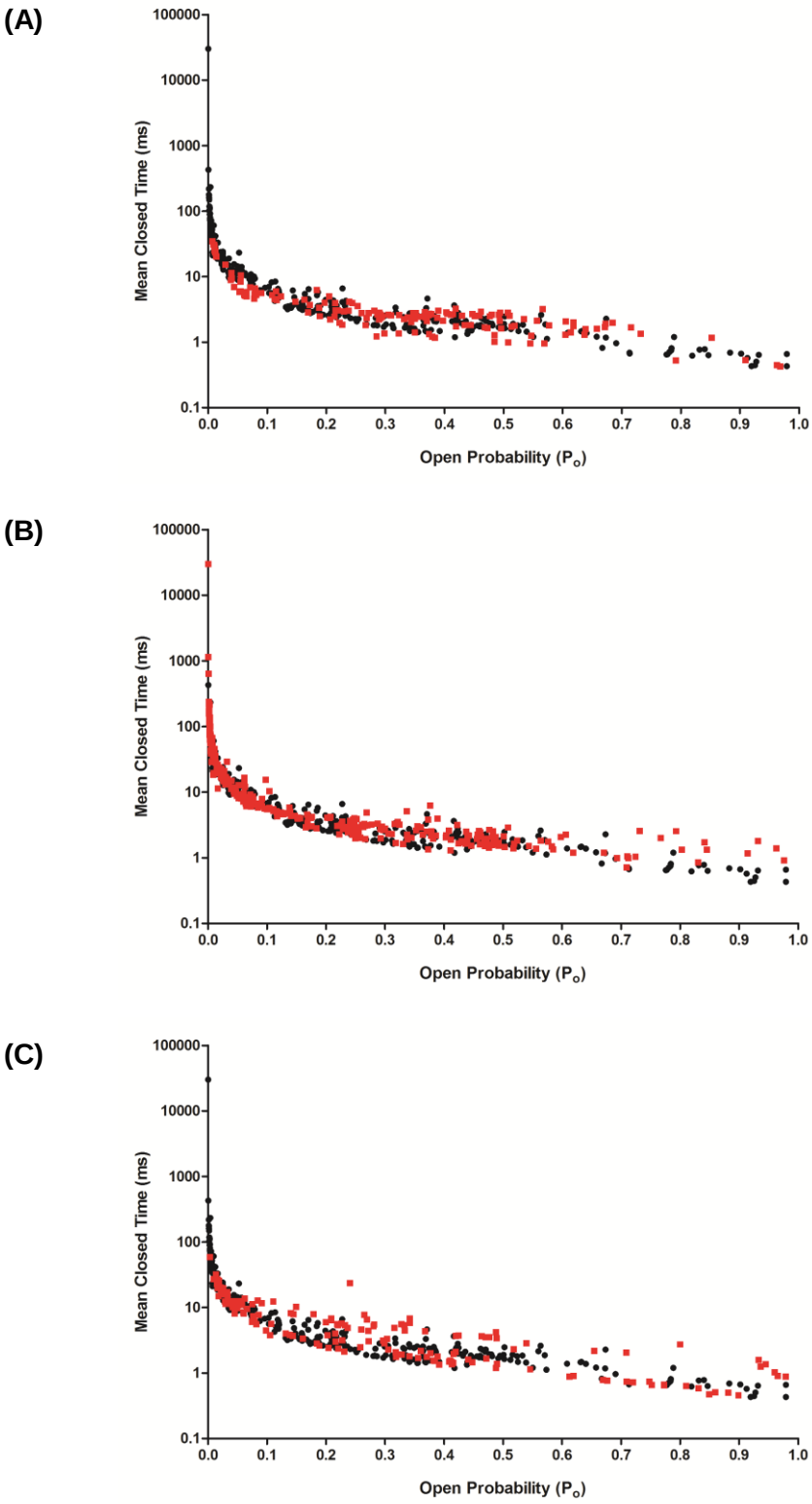


Figure 6.15. The relationship between open probability and mean closed times of WT and mutant hRyR2 channels. Each data point represents a 30 s segment from the 20 min Ca^{2+} activation experiment. WT hRyR2 (*n*=8) data points (black) overlay mutant (A) Y4813W (*n*=4), (B) Y4839A (*n*=9) and (C) Y4839W (*n*=4) highlighted in red.

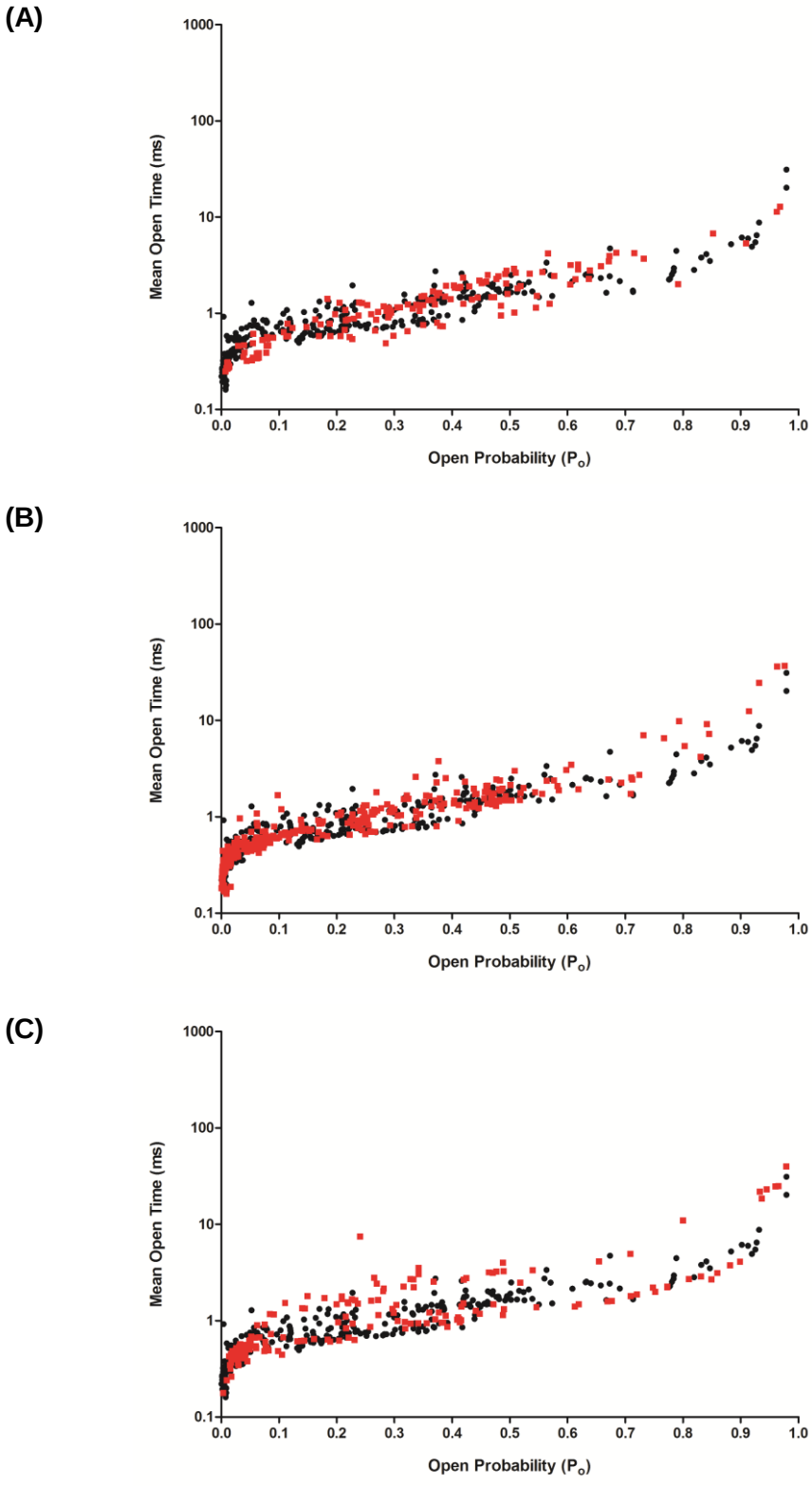


Figure 6.16. The relationship between open probability and mean open times of WT and mutant hRyR2 channels. Each data point represents a 30 s segment from the 20 min Ca^{2+} activation experiment. WT hRyR2 (*n*=8) data points (black) overlay mutant (A) Y4813W (*n*=4), (B) Y4839A (*n*=9) and (C) Y4839W (*n*=4) highlighted in red.

6.3.5.1 The relationship between dwell-time and periods of very high open probability for WT and mutant hRyR2 channels

The relationship between mean T_c and T_o and periods of very high open probability, $P_o > 0.8$ are listed in table 6.3. There were no differences in mean P_o ($P_o \sim 0.89$) from the idealised 30 s single-channel data between WT and mutant hRyR2 channels. The mean time closed for Y4839A (1.46 ms) was longer than WT hRyR2 (0.6 ms) however the duration of the mean time open was not significantly different. There were no differences in T_c and T_o at high P_o when comparing the conservative Y4813W and Y4839W mutations to WT hRyR2 channels.

	WT hRyR2 (*n*=13)	**Y4813W** (*n*=5)	**Y4839A** (*n*=9)	**Y4839W** (*n*=13)
P_o	0.899 ± 0.01	0.896 ± 0.03	0.877 ± 0.02	0.896 ± 0.02
T_c (ms)	0.603 ± 0.03	0.624 ± 0.14	1.46 ± 0.17*	0.998 ± 0.18
T_o (ms)	8.354 ± 2.26	7.695 ± 1.99	16.26 ± 4.33	14.13 ± 3.39

Table 6.3. The relationship between dwell-time and P_o (0.8 – 1) for WT and mutant hRyR2 channels. Open probability was comparable for all channel types. Y4839A had a significantly longer mean T_c compared to WT hRyR2, indicated by an asterisk. All other dwell times were not significantly different to those achieved for WT hRyR2.

6.3.6 Investigating single-channel gating mechanisms at the selectivity filter of hRyR2 channels

6.3.6.1 Justification of hRyR2 modelling analysis

The inherent fluctuations in channel activity and the highlighted modal gating in hRyR2 during stringently regulated steady-state conditions presented challenges in data analysis. To avoid selection bias and to resolve the aims of this project, listed in chapter 1.6.2, particular segments of data were selected in accordance with the specific criteria listed in section 6.3.6.2.

To test the importance of interactions within the proposed pore region, and in particular on flicker closings occurring from the open state, a high P_o (P_o 0.6 – 0.8) was required. Using the open probability 'skyscraper' distribution histograms as a template shown in figure 6.17, 30 s segments were extracted. Only single-channel segments with homogenous gating events, i.e. similar dwell-times, were analysed depicted in figure 6.18, thus avoiding modal shifts between periods of long closings and openings, which satisfied the essential Markov assumption that the rate constants of state transitions do not change with time in a memoryless system (Qin, 2004; Mukherjee *et al.,* 2012). The 30 s duration of single-channel transitions at P_o 0.6 – 0.8 ensured that the number of events exceeded 3000, which was considered to be statistically sufficient for modelling analysis (Colquhoun and Sigworth, 1995; Qin, 2004).

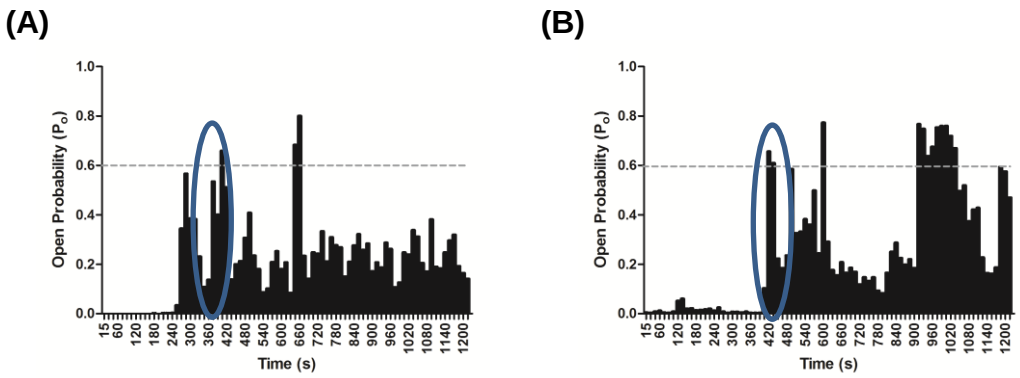


Figure 6.17. Utilising the open probability distribution histograms as a template for modelling data selection. A blue oval region highlights representative extraction of (A) WT and (B) mutant hRyR2 channel data. Where appropriate, multiple 30 s segments were extracted from a single 20 min recording and used for modelling analysis.

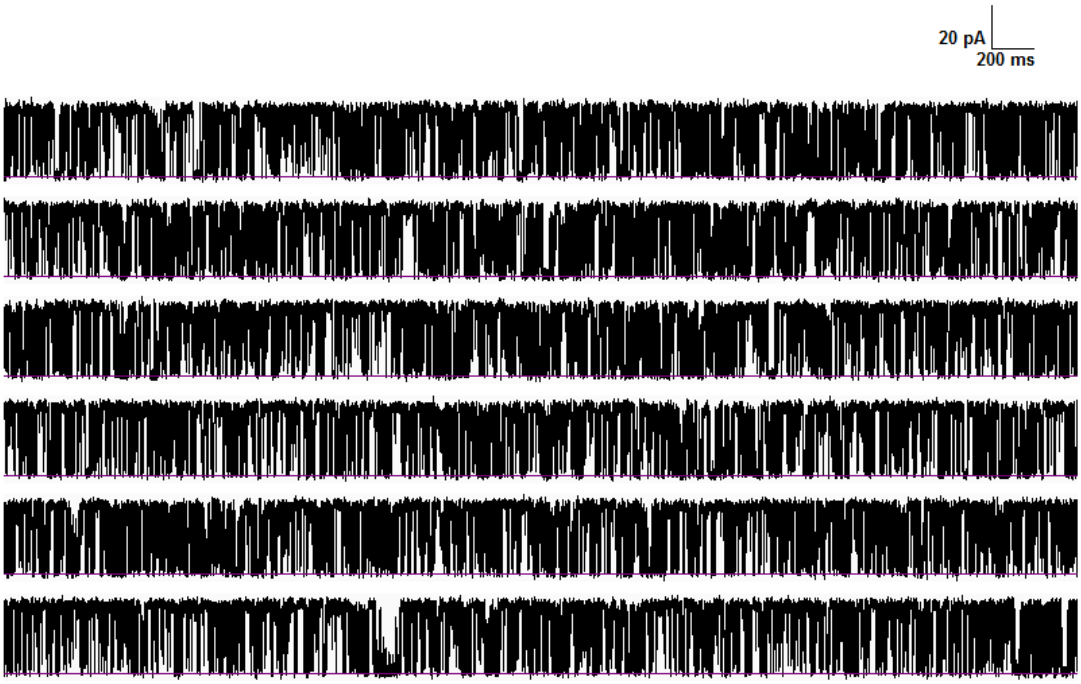


Figure 6.18. Representative 30 s extraction of homogenous WT single hRyR2 channel gating for modelling analysis. Each line represents 5 s of data. The closed state is denoted by purple baseline with upward deflections as channel openings. The idealised trace (not shown) generated biophysical parameters: P_o 0.68, T_c 0.92 ms, T_o 1.98 ms and total number of events 20604.

6.3.6.2 Data selection criteria for modelling analysis

- Data from the Ca^{2+} activation experiments were analysed.
- Extraction of 30 s of single-channel data.
- Open probability between 0.6 - 0.8.
- Homogenous single-channel gating events.
- Modal gating indicated by atypical periods of long open or closed dwell-times was excluded from analysis.
- Number of events per segment exceeded 3000.

6.3.6.3 Homogenous single-channel data

Prior to constructing the kinetic models, the extracted single-channel data were idealised and compared to ensure the data were homogenous for valid comparison. It was confirmed that there were no significant differences in the general biophysical markers (mean open probability, dwell-times and total number of events), listed in table 6.4, between WT and mutant hRyR2 data segments, thus satisfying the criteria for data selection.

	WT hRyR2 (*n*=7)	**Y4813W** (*n*=7)	**Y4839A** (*n*=8)	**Y4839W** (*n*=9)
P_o	0.69 ± 0.04	0.66 ± 0.02	0.74 ± 0.02	0.71 ± 0.02
T_c (ms)	0.87 ± 0.14	1.08 ± 0.12	1.02 ± 0.14	0.99 ± 0.14
T_o (ms)	2.06 ± 0.34	1.99 ± 0.29	3.70 ± 0.93	2.45 ± 0.36
Events	22689 ± 3023	21943 ± 2903	20371 ± 2220	19559 ± 2116

Table 6.4. Key biophysical parameters for modelling analysis. Homogenous gating data indicated by no significant differences between open probability (P_o), mean time closed (T_c) and open (T_o) and total dwell count (events). Values are means (± SEM).

6.3.6.4 Constructing kinetic models to describe the gating behaviour of mutant hRyR2 channels

In order to describe the behavioural consequence of residue substitutions within the proposed pore region of hRyR2 a kinetic model, using HMM, was constructed to reveal underlying channel gating mechanisms. For each WT and mutant hRyR2 selected data set a kinetic model was constructed in QuB. The process of constructing the models by state additions, to maximise the log likelihood (LL), is shown in figure 6.20. In all cases, except for Y4839W (*n*=1), the three closed and four open state model depicted in figure 6.19 achieved the highest LL. Further additions of closed or open states did not affect the LL by more than 5 and in some cases produced rate constants that were unrealistic, and were therefore not included in the scheme.

The model generated in this investigation was consistent with a previous study describing hRyR2 channel gating (Mukherjee *et al.,* 2012). The states were named according to Mukherjee *et al*, non-responsive closed (C_{NR}), responsive closed (C_R), flicker closed (C_F), open state 1, 2, 3 and 4, and are discussed in section 6.4.3.

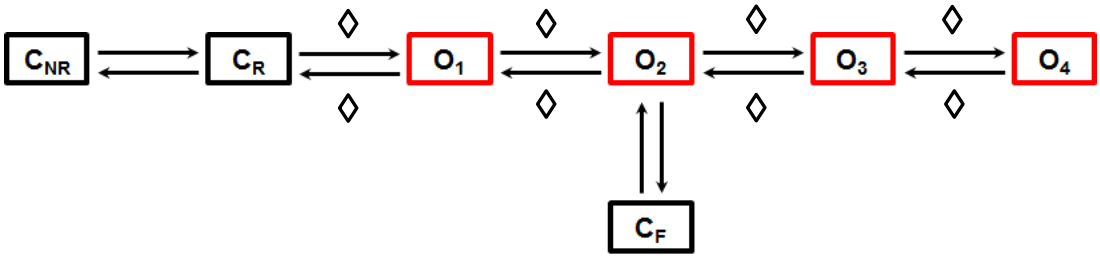
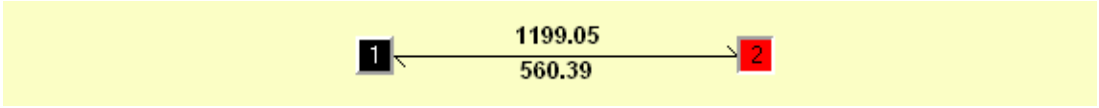
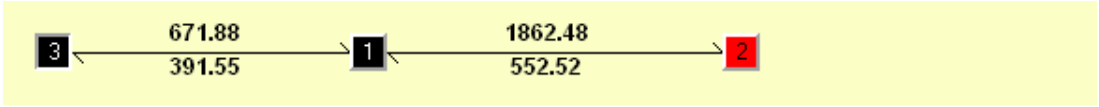


Figure 6.19. Highest ranked kinetic model describing the behaviour of hRyR2 gating when activated by 10 μM $[Ca^{2+}]_{cyt}$. Black boxes represent class 1 closed states; C_{NR} (non-responsive), C_R (responsive) and C_F (flicker). Red boxes represent class 2 open states; O_1, O_2, O_3 and O_4. Arrows represent forward and backward state transition rate constants, listed in table 6.7. $[Ca^{2+}]_{cyt}$-dependent transitions are labeled by ◊ above and below the rate constant arrows (μM^{-1} s^{-1}), the remaining transitions are $[Ca^{2+}]_{cyt}$-independent (s^{-1}).

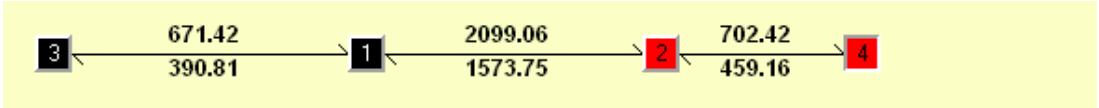
LL: 94432.74



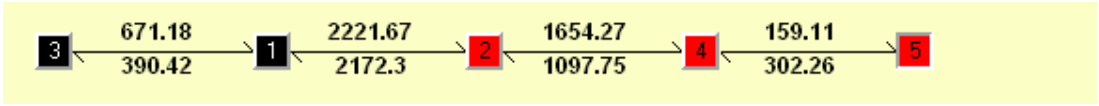
LL: 94866.28



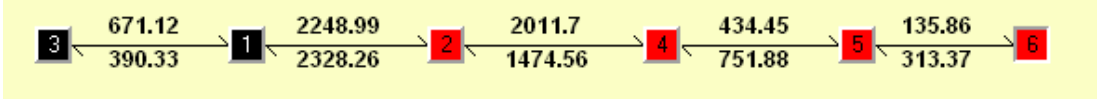
LL: 96099.12



LL: 96172.8



LL: 96184.46



LL: 96535.65

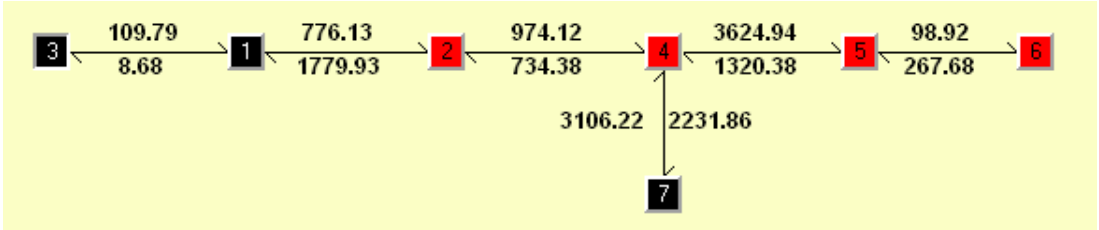


Figure 6.20. Constructing a kinetic model to describe the gating behaviour of hRyR2. The addition of states increased the log likelihood (LL) by more than 5. Black and red squares denote closed and open states, respectively, the numbers within states refer to the sequence of state addition, state names were referred to as described in figure 6.19. Rate constants depicted in figure are representative of modelling a single WT hRyR2 channel using the data selection criteria outlined in section 6.3.6.2. The directions of forward and backward rate constants are denoted by arrows (units are s^{-1} or μM^{-1} s^{-1} as shown in figure 6.19).

6.3.6.5 Comparing WT and mutant hRyR2 dwell-time distribution histograms

The three closed and four open state model depicted in figure 6.19, achieved the highest LL and fitted both the WT and mutant hRyR2 data segments suitably. Dwell-time distribution histograms were generated and representative closed (black) and open (red) histograms are shown in figures 6.21 and 6.22, respectively. Due to the thousands of events and dwell-time intervals from extracted data segments, single-channel distributions were expressed as the square-root of the count divided by the total intervals, using a log10 scale for duration (ms). The models provided important kinetic information on time constants and state transitions that were used to describe the gating behaviour and to speculate on putative structural conformations discussed in section 6.4.3.

The time constants and relative area underneath the exponential from the three closed states, C_F, C_R and C_{NR}, were assessed and listed in table 6.5. There were no differences in mean closed times between WT and mutant channels. Mean flicker (C_F) times were ~ 0.30 ms under the defined conditions when hRyR2 channels were activated by 10 µM $[Ca^{2+}]_{cyt}$. The most visited and stable conformations, determined by the relative area, were the C_F (~ 48 %) and C_R (~ 42 %) states. Under the criteria selected in this analysis, the non-responsive closed (C_{NR}) state with long closed dwell duration during high single-channel P_o were the least occupied (~ 10 %). There were no differences in closed state occupancies (C_F, C_R and C_{NR}) between WT and mutant hRyR2 channels discussed in sections 6.4.3 and 6.4.4.

The time constants and relative area underneath the exponential from the four open states, O_1, O_2, O_3 and O_4, were assessed and listed in table 6.6. As is the case with the closed states, there were no significant differences in kinetics between mutant and WT hRyR2 channels. Channel opening switched between various conformations with variable occupancy. The most probable states visited when channels were activated by 10 µM $[Ca^{2+}]_{cyt}$ were the O_2 (~ 38 %) and O_3 (~ 45 %) that had mean open times of ~ 0.62 ms and ~ 3.04 ms, respectively. The very brief open (O_1) and longer open (O_4) times were the least occupied under the criteria selected in this analysis and are discussed in sections 6.4.3 and 6.4.4.

Closed States		WT hRyR2 (*n*=7)	Y4813W (*n*=7)	Y4839A (*n*=8)	Y4839W (*n*=8)
C_F	τ (ms)	0.29 ± 0.03	0.29 ± 0.03	0.38 ± 0.05	0.30 ± 0.02
	Area (%)	49.1 ± 7.6	36.7 ± 9.2	51.8 ± 1.0	49.9 ± 1.9
C_R	τ (ms)	1.09 ± 0.28	1.13 ± 0.14	1.45 ± 0.19	1.18 ± 0.14
	Area (%)	37.4 ± 1.6	47.4 ± 3.8	45.6 ± 1.2	42.2 ± 1.1
C_{NR}	τ (ms)	5.79 ± 1.30	4.91 ± 0.45	9.25 ± 1.50	6.53 ± 1.47
	Area (%)	13.5 ± 7.7	15.9 ± 5.7	2.6 ± 0.4	7.9 ± 1.2

Table 6.5. Time constants and relative areas for exponential fits of closed dwell-time distributions. Values are means (± SEM). Representative examples are depicted in figure 6.21.

Open States		WT hRyR2 (*n*=7)	Y4813W (*n*=7)	Y4839A (*n*=8)	Y4839W (*n*=8)
O_1	τ (ms)	0.26 ± 0.04	0.22 ± 0.04	0.41 ± 0.08	0.23 ± 0.03
	Area (%)	2.8 ± 0.6	7.9 ± 4.4	5.9 ± 3.6	4.8 ± 2.3
O_2	τ (ms)	0.49 ± 0.07	0.56 ± 0.13	0.92 ± 0.22	0.51 ± 0.07
	Area (%)	38.7 ± 3.2	34.7 ± 2.5	38.9 ± 2.3	40.1 ± 2.7
O_3	τ (ms)	2.51 ± 0.47	2.69 ± 0.52	4.13 ± 0.76	2.86 ± 0.33
	Area (%)	46.2 ± 1.7	45.4 ± 2.8	44.8 ± 3.9	42.9 ± 1.8
O_4	τ (ms)	10.86 ± 2.44	9.88 ± 1.69	23.71 ± 7.29	14.93 ± 3.66
	Area (%)	12.4 ± 3.3	11.9 ± 2.3	11.8 ± 1.7	12.3 ± 1.7

Table 6.6. Time constants and relative areas for exponential fits of open dwell-time distributions. Values are means (± SEM). Representative examples are depicted in figure 6.22.

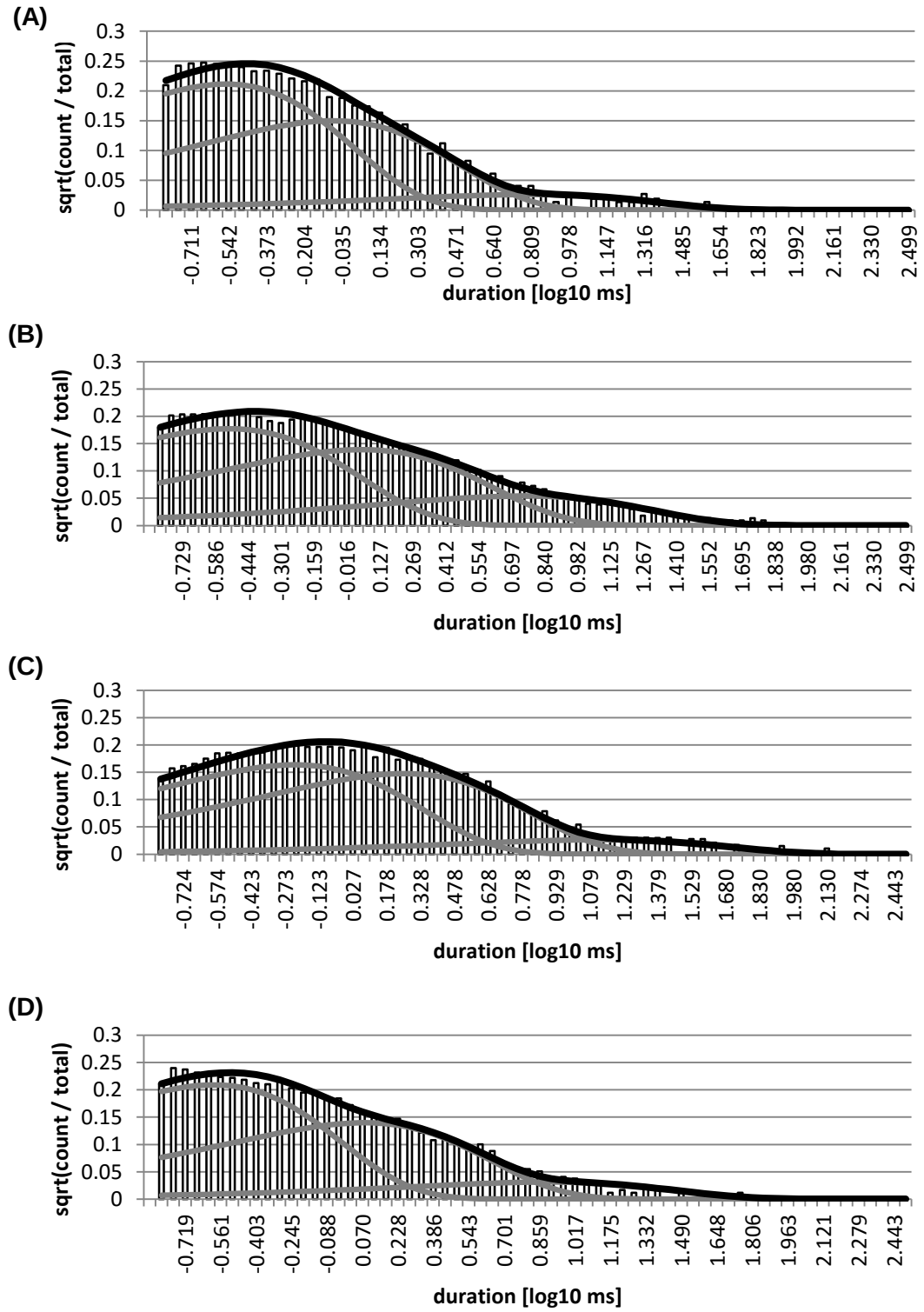


Figure 6.21. Closed dwell-time histograms from a single representative hRyR2 channel activated by 10 μM $[Ca^{2+}]_{cyt}$. (A) WT hRyR2, (B) Y4813W, (C) Y4839A and (D) Y4839W. Histograms fitted with sums of exponential curves, the black curve on each histogram represents the overall fit and the three grey curves underneath show the relative area for individual closed fits (C_F, C_R and C_{NR} listed in table 6.5).

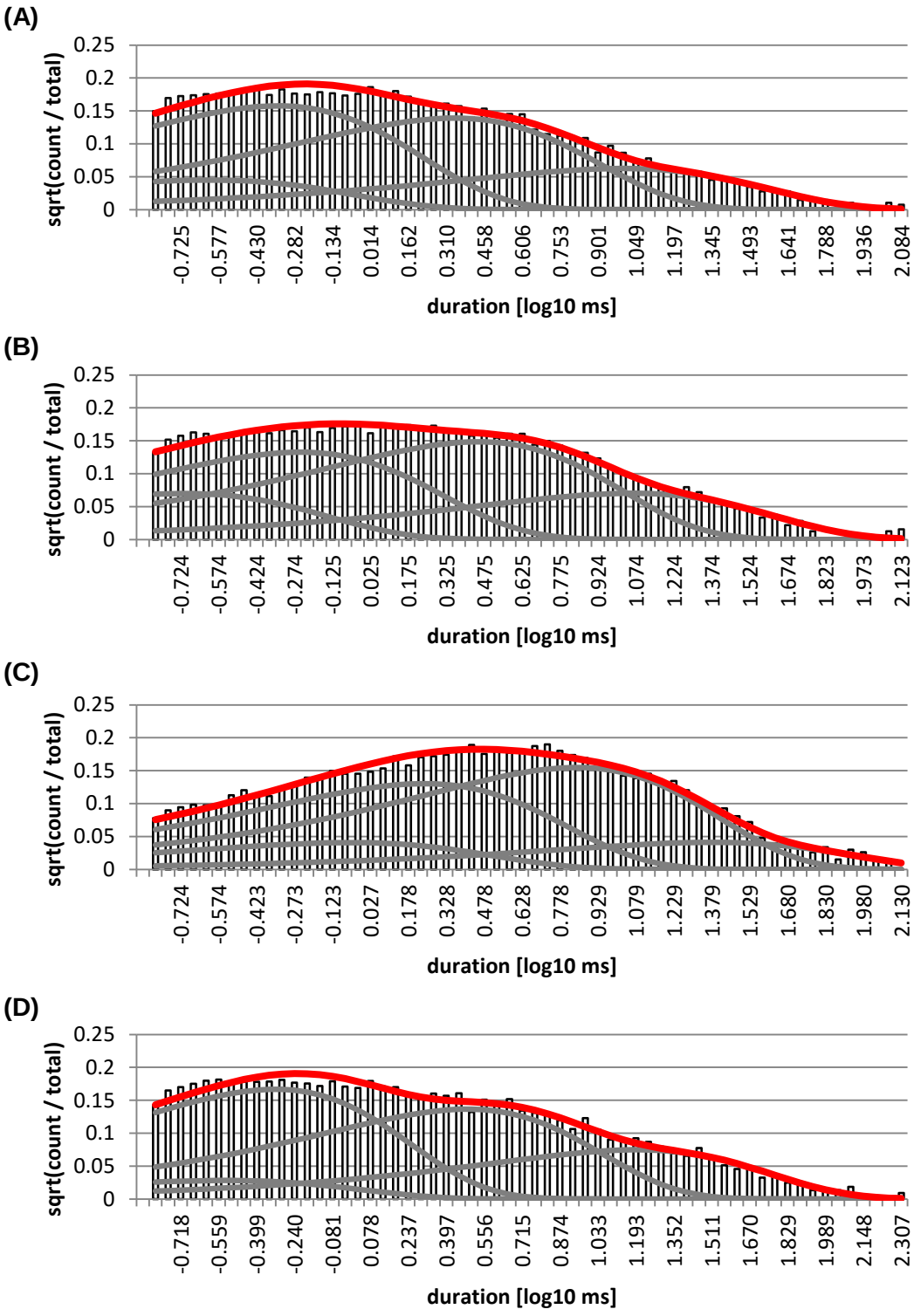


Figure 6.22. Open dwell-time histograms from a single representative hRyR2 channel activated by 10 μM $[Ca^{2+}]_{cyt}$. (A) WT hRyR2, (B) Y4813W, (C) Y4839A and (D) Y4839W. Histograms fitted with sums of exponential curves, the red curve on each histogram represents the overall fit and the four grey curves underneath show the relative area for individual open fits (O_1, O_2, O_3 and O_4 listed in table 6.6).

6.3.6.6 Assessing individual state transitions between WT and mutant hRyR2 channels

The highest ranked kinetic model, depicted in figure 6.19, consisted of a total of 12 state transitions. The mean rate constants for WT and mutant hRyR2 experiments were tabulated in table 6.7. Overall there were no differences in rate constants between channels, except for one state transition highlighted by the asterisk sign. When comparing the transition from the second open (O_2) state to the very brief flicker closed (C_F) state ($O_2 \rightarrow C_F$), the rate constant for the alanine mutation, Y4839A, was significantly lower compared to WT and conservative Y4813W and Y4839W hRyR2 channels, depicted in figure 6.23. The kinetic model for WT and Y4839A hRyR2 is shown in figure 6.25 and discussed in section 6.4.4.

	WT hRyR2 (*n*=7)	**Y4813W** (*n*=7)	**Y4839A** (*n*=8)	**Y4839W** (*n*=8)
$C_{NR} \rightarrow C_R$	222.4 ± 54.5	202 ± 11.1	137.7 ± 23.3	263.6 ± 44.4
$C_R \rightarrow C_{NR}$	68.9 ± 23.6	52.4 ± 13.2	23.4 ± 3.5	79.9 ± 15.2
$C_R \rightarrow O_1$	1390 ± 267.1	1147 ± 173.6	930.4 ± 155.8	1074 ± 115.9
$O_1 \rightarrow C_R$	2057 ± 276.6	2128 ± 256.9	1887 ± 227.9	2046 ± 84.2
$O_1 \rightarrow O_2$	553.1 ± 113.8	645.5 ± 81.3	486.2 ± 120.1	611.9 ± 63.1
$O_2 \rightarrow O_1$	317.4 ± 75.7	424.9 ± 107.4	267.8 ± 77.1	397.1 ± 88.4
$O_2 \rightarrow C_F$	2183 ± 472.2	1920 ± 203.2	805.6 ± 210*****	1991 ± 230.9
$C_F \rightarrow O_2$	4294 ± 836.1	3116 ± 366.3	3336 ± 437.5	4306 ± 418.8
$O_2 \rightarrow O_3$	2093 ± 351.2	2899 ± 486.4	1362 ± 181.2	2777 ± 492.5
$O_3 \rightarrow O_2$	1309 ± 173.5	1301 ± 311.2	852.3 ± 127.4	1052 ± 130.3
$O_3 \rightarrow O_4$	74.8 ± 16.4	65.5 ± 14.7	47.9 ± 11.4	61.1 ± 11.4
$O_4 \rightarrow O_3$	151 ± 34.8	163.5 ± 48.7	86.3 ± 19.8	114.4 ± 17.3

Table 6.7. Rate constants derived from the highest ranked kinetic model. Transitions between states are given as rate constants means (± SEM) with units s^{-1} or μM^{-1} s^{-1}, as shown in figure 6.19. State transition between $O_2 \rightarrow C_F$ was significantly lower in Y4839A compared to WT hRyR2 channels, indicated by an asterisks (p<0.05).

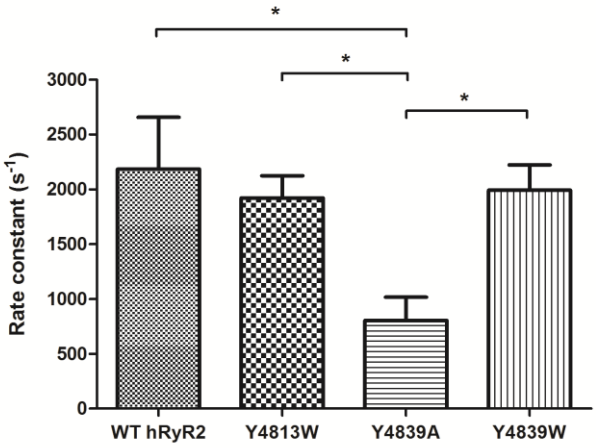
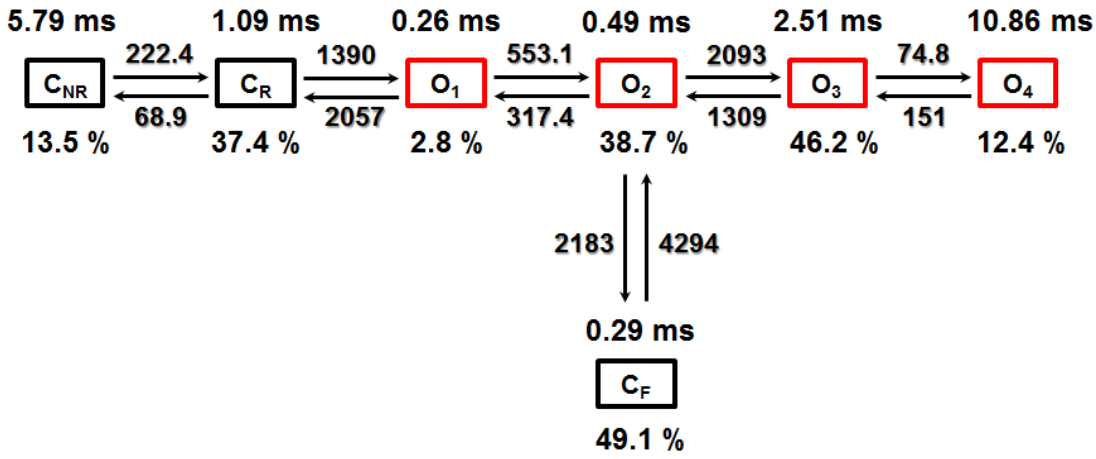


Figure 6.23. Rate constant from open (O_2) to closed (C_F) between WT and mutant hRyR2. Entry from the O_2 to C_F ($O_2 \rightarrow C_F$) was significantly lower in the alanine mutant Y4839A compared to WT and conservative mutant hRyR2 channels as listed in table 6.7 (p=0.0104).

(A)



(B)

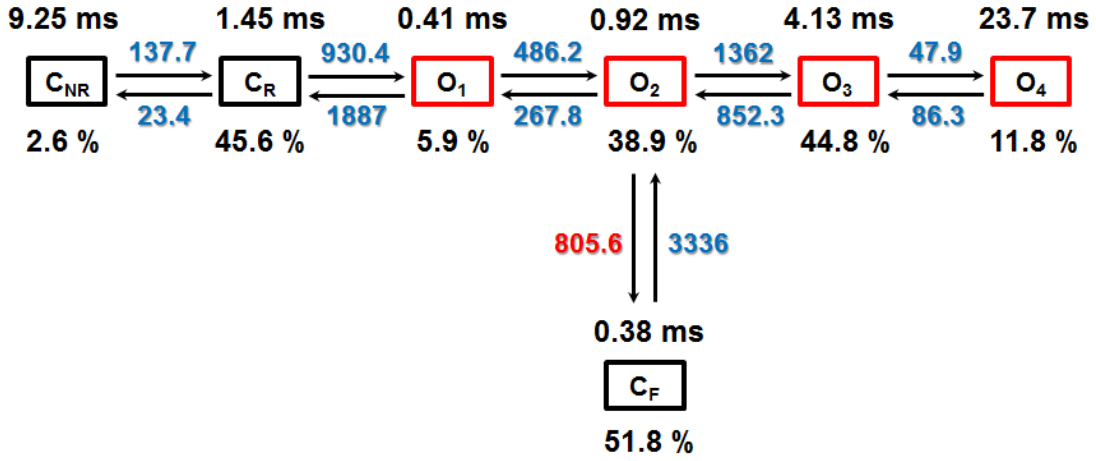


Figure 6.24. Comparing the kinetic information between (A) WT and (B) Y4839A hRyR2 channels. Time constants (ms) and state occupancies (%) are indicated above and below individual states, respectively. The direction of the mean rate constants are shown by the arrows (units s^{-1} or μM^{-1} s^{-1} as shown in figure 6.19). A subtle trend in Y4839A kinetics was observed with longer time constants and slower rate constants (highlighted in blue) compared to WT hRyR2, although only one of these transitions ($O_2 \rightarrow C_F$) was significant slower highlighted in red. SEMs are listed in tables 6.5, 6.6 and 6.7.

6.4 – Discussion

The biophysical characterisation of the six hRyR2 mutant channels outlined in chapter 5 highlighted the significance of residue properties and their interactions within the pore. The drastic alteration in Y4813A, D4829A and D4829E channel function made these mutants unsuitable for further investigation and the consequences of these mutations are discussed in chapter 7. Mutations which resulted in channels whose functional behaviour was qualitatively comparable to WT hRyR2 (i.e. Y4813W, Y4839A and Y4839W) were assessed in terms of their effects on gating mechanisms. This was the first investigation to record hRyR2 channels for a prolonged length of time (20 min) to evaluate the proteins' biophysical properties and to identify any quantitative differences in open probability, dwell-time and gating kinetics between WT and mutant hRyR2 channels.

A total of 91 hRyR2 Ca^{2+} activated long recording experiments were analysed in this chapter. The duration of hRyR2 gating events were typically milliseconds, thus an enormous amount of continuous steady-state data was acquired (~ 30 h). Previous studies investigating gating mechanisms in RyRs typically monitored channels for short 2 – 3 min periods (Mukherjee *et al.,* 2012; Euden *et al.,* 2013b; Ramachandran *et al.,* 2013; Mei *et al.,* 2015), therefore this chapter revealed intriguing insight into the biophysical characteristics and behaviour of single-channel kinetics, discussed in sections 6.4.1, 6.4.2 and 6.4.4.

6.4.1 Single-channel Ca^{2+} activation experiments – Biophysical parameters

This investigation highlighted the biophysical variability of recombinantly-generated purified hRyR2 channel gating under regulated conditions. The open probability distributions revealed unique fluctuations in channel activity on a macro 'minute-to-minute' scale switching between high and low periods that were observed as skyscraper landscapes.

It is a well-documented phenomenon that the gating behaviour of single ion channels is random with 'gear shifting' between several different levels of activity (long dwell-times and frequency of events) under constant experimental conditions. Modal gating has been observed in many channels such as G protein-activated K^+

(GIRK) (Yakubovich *et al.,* 2000), $Ca_v2.1$ (Luvisetto *et al.,* 2004), KcsA (Chakrapani *et al.,* 2010) and IP_3R channels (Ullah *et al.,* 2012), and has also been observed previously in sheep RyR2 (Saftenku *et al.,* 2001; Galfré *et al.,* 2012). It has been demonstrated that variation in P_o exists and that this phenomenon is not limited to RyR2, however the exact mechanism underlying modal gating in RyR2 is unknown.

The mean P_o for both WT and mutant hRyR2 channels during the Ca^{2+} activation experiment in unbuffered KCl solutions containing ~ 1 µM [Ca^{2+}] (Stage #1) had a P_o ~ 0.3, compared to channels activated by 10 µM $[Ca^{2+}]_{cyt}$ (Stage #3) that had a P_o ~ 0.1. This was a surprising difference, a higher activating $[Ca^{2+}]_{cyt}$ would have been predicted to augment open probability as previous studies have reported a steep dependence of P_o on cytosolic Ca^{2+} from 1-500 µM (Chu *et al.,* 1993; Mukherjee *et al.,* 2012). This observation may have occurred due to the timescale of the recording (20 min), as modal fluctuations in channel gating were reported, thus periods of long low channel activity may have affected the overall mean P_o. In addition, this may have been due to chelating free luminal Ca^{2+} from ~ 1 µM to 50 nM following the channel shutdown stage. Previous studies have shown that luminal Ca^{2+} increases channel P_o (albeit with much higher $[Ca^{2+}]_{lum}$ (mM) and in the presence of other factors such as ATP or Mg^{2+}) (Tencerova *et al.,* 2012; Chen *et al.,* 2014). The effect of luminal Ca^{2+} on hRyR2 in these regulated experimental conditions remains to be determined.

The distributions of mutant channel population subsets (low, intermediate and high P_o) were significantly different to WT hRyR2. It was more likely for WT to reach a threshold above P_o 0.6 during the 20 min recording than mutants, which favoured intermediate and low P_o thresholds. The difference in distributions may have been due to $[Ca^{2+}]_{cyt}$ sensitivity. Previous [^{3}H] ryanodine assays, described in chapter 4, reported lower binding in mutant Y4813W and Y4839A hRyR2 channels (~ 30 %) compared to WT hRyR2, while binding in Y4839W was unaltered. The proposed altered Ca^{2+} sensitivity would need to be confirmed by monitoring [^{3}H] ryanodine binding and single-channel gating at a range of activating cytosolic [Ca^{2+}].

While removing cytosolic and luminal free [Ca^{2+}] from KCl solutions induced ‘channel shutdown’, a small proportion of very brief hRyR2 opening events were observed in WT and mutant channels, described in section 6.3.1.2. These rare opening events were identified in a previous study by Mukherjee *et al*, and also in other ion channels (CNG, AChR and BK channels), and have been attributed to

spontaneous openings in absence of agonist occurring as a result of intrinsic thermodynamic fluctuations in the protein molecule, termed unliganded gating (Tibbs *et al.,* 1997; Talukder and Aldrich, 2000; Grosman and Auerbach, 2000; Mukherjee *et al.,* 2012). Interestingly, a proportion of Y4813W (~ 20 %) remained relatively active (P_o > 0.05) in response to nominal zero [Ca^{2+}], the mechanism underlying the increased channel openings remains unclear. There were no differences in Y4813W channel P_o compared to WT hRyR2 during stage #1 and #3 of the Ca^{2+} activation experiment, however in the absence of cytosolic [Ca^{2+}] these augmented spontaneous unliganded 'leaky' channel openings would be expected to occur in disease-linked point mutations (Guerrero-Hernández *et al.,* 2014; Eisner, 2014).

6.4.2 Comparing WT and mutant hRyR2 channel biophysical properties

Overall there were no differences in Y4813W, Y4839A and Y4839W mutant channel P_o and dwell-times compared to WT hRyR2 in the Ca^{2+} activation experiment. A similar trend of channel-to-channel open probability variation akin to WT hRyR2 was observed in mutant channels indicating that the point mutations had not drastically altered channel function. One of the key findings was that conservative side chain properties in the proposed pore helix at position Y4813W fully restored biophysical single-channel properties comparable to WT hRyR2, in contrast to the alanine mutation Y4813A that was non-functional in bilayers as described in chapter 5. As the pore helix in K^+ channels undergoes complex and dynamic rearrangements during gating (Cuello *et al.,* 2010b; Wang *et al.,* 2011), the results in this chapter implicate a role for aromatic pore helix residues and their side chain properties in hRyR2 channel function.

Assessing hRyR2 open probability was a useful tool to evaluate overall single-channel activity; however it does not reveal information regarding channel gating kinetics and their mechanism. The open and closed dwell times were therefore analysed and revealed no significant changes between mutant and WT hRyR2 channels except that at very high P_o (P_o > 0.8) the Y4839A mutation increased the duration of the mean closed time. Reducing the side chain length and disrupting local interactions of Y4839A, proposed to be located at the start of the S6 helix, may have altered the flexibility or the conformation of the α-helix, such that during high channel P_o Y4839A may destabilise the Ca^{2+}-mediated IHBC S6 activation gate

favouring channel closings. However in the absence of crystal structures these predictions of channel function are speculative. Previous studies that have attempted to identify the RyR activation gate by alanine scanning (Wang *et al.,* 2003) and other residue substitutions (valine, isoleucine and proline) (Euden *et al.,* 2013b; Ramachandran *et al.,* 2013; Mei *et al.,* 2015) established that a degree of flexibility at the S6 helix is required. The location of Y4839A distant from the proposed activation gate had minor effects on channel function and, in general, channels containing this mutation had similar biophysical parameters compared to WT hRyR2. A current RyR activation model may simply entail twisting of the S6 bundle, as depicted in figure 6.25, thus the residue at the start of the helix may be less important than centrally aligned residues in close proximity to the proposed IHBC gate (Yan *et al.,* 2015).

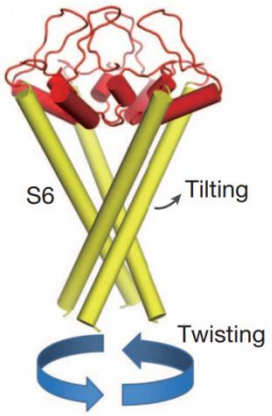


Figure 6.25. Putative conformational twisting of the S6 helices occurring during opening of the activation gate. Figure adapted from Yan *et al.,* (2015).

The open and closed dwell-times of the S6 helix conservative tryptophan mutant, Y4839W, were similar to WT hRyR2 and were in accordance with the conservative pore helix mutant in this chapter highlighting the significance of these aromatic residues and their side chain properties in maintaining high P_o by potentially stabilising the pore region.

6.4.3 Modelling single-channel gating kinetics and assigning putative structural conformations

Due to the inherent variability of hRyR2 channels, to assess the consequence of residue substitution on flicker closing transitions specific criteria were imposed on the single-channel data to avoid selection bias, as outlined in section 6.3.6.2. Thus, only a small proportion, less than 1 % (15 min), of the total single-channel data were analysed. These criteria ensured that data segments contained comparable general biophysical parameters (P_o, T_c, T_o and number of events) for both WT and mutant hRyR2 channels. This ensured, as a consequence, that any subtle differences in kinetics (time constants, state occupancy or rate constants) resulted as an outcome of residue side chain substitution.

The purpose of modelling single-channel data was to begin to investigate possible putative structural conformations based on the kinetic information generated by the gating scheme. RyR channels have multiple conformations with the same conductance, concealing their transitions between states (Mukherjee *et al.,* 2012). These 'hidden' transitions among channel conformations can only be deduced statistically from their dwell-time distributions (Qin *et al.,* 2000). As the transitions within channels occur in a continuum, due to the dynamic rearrangement and conformational wave of residues and domains (Qin, 2004), the kinetic model first constructed by Mukherjee *et al* and used as a template in this chapter, was composed of the minimum number of conformational states that were stable enough to be discretely resolved (Mukherjee *et al.,* 2012). The kinetic model constructed in this chapter was composed of three closed and four open states, depicted in figure 6.19, and fitted the single-channel data for WT and mutant hRyR2 generating important kinetic information that could explain, in mechanistic terms, the channel gating behavior during 10 µM $[Ca^{2+}]_{cyt}$ activation. The effects of mutations on channel gating kinetics are compared in section 6.4.4. Constructing the multi-state scheme, originally to investigate flicker gating, resolved seven states and 12 state transitions. The rate constants in conjunction with the time constants of each state and the probability of a particular state occuring, determined by the area underneath the exponential fit, were used to assign putative conformations of the hRyR2 structure. A representation of proposed structural conformations during channel gating is shown in figure 6.26.

A particular closed conformation (C_{NR}) was characterised by a long closed time (5.79 ms), was rarely visited in high activating 10 µM $[Ca^{2+}]_{cyt}$ conditions. In addition, a relatively stable pre-opening closed conformation (C_R) termed 'responsive' was resolved (37.4 %) and characterised by a short mean closed time (1.09 ms). From the C_R, binding of cytosolic Ca^{2+} induced a proposed structural conformational change that opened the putative IHBC gate, transitioning into different Ca^{2+} bound open states (O_1, O_2, O_3 and O_4) that were characterised by variable open time occupancy. The structural rearrangements that underlie these transitions are unknown. The putative conformations, shown in figure 6.26, resolved from the kinetic model that describes the gating behaviour of hRyR2 are predictions and the actual conformations during channel gating must be validated by future high-resolution structural information.

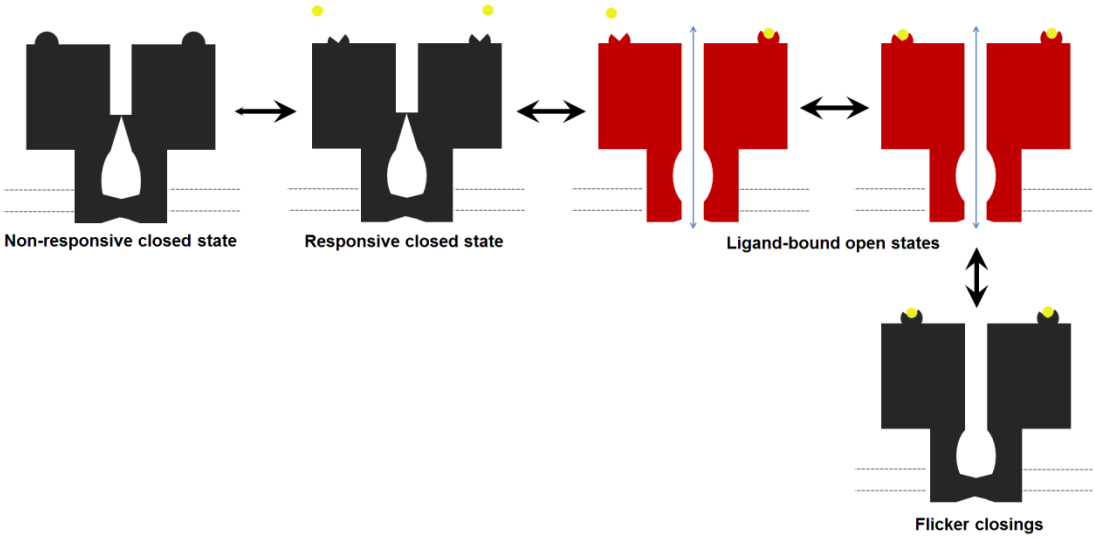


Figure 6.26. Schematic representation of putative hRyR2 channel conformation transitions when activated by 10 µM $[Ca^{2+}]_{cyt}$. Transitions between resolvable closed (black) and open (red) states are indicated by the direction of the black arrow. The least likely transition, under the stated conditions, occurred from the responsive to the non-responsive closed state ($C_R \rightarrow C_{NR}$) highlighted by a reduced arrow head. Two putative gates are shown, one at the IHBC located at the entrance to the cytosolic vestibule and another at the selectivity filter located at the luminal entrance to the pore. Ca^{2+} ions are indicated by a yellow circle. Only two of the four monomers are shown, each of which is proposed to contain a Ca^{2+} binding site. The diagram does not depict the actual conformational structures of hRyR2 or the number of Ca^{2+}-binding sites and are represented purely for illustration purposes. Figure constructed using a template from Mukherjee *et al.,* (2012).

6.4.4 Comparing gating kinetics and flicker closing transitions between WT and mutant hRyR2 channels

The kinetic information from the conservative Y4813W and Y4839W mutation models (time constants, state occupancy and rate constants) were comparable to WT hRyR2. These pieces of evidence in conjunction with the comparable biophysical parameters discussed in sections 6.4.1 and 6.4.2, were in accordance with the original hypotheses in this thesis that retaining the physicochemical properties and hydrogen-bonding capabilities of residues maintained the functional characteristics of WT hRyR2.

The alanine mutant, Y4839A, did not significantly alter the brief flicker mean closed time (0.38 ms) compared to WT hRyR2 (0.29 ms). However, interestingly, the forward state transition entering into the flicker state from the second open state ($O_2 \rightarrow C_F$) was significantly slower (805 s^{-1}) compared to WT and the conservative hRyR2 mutations (~ 2000 s^{-1}), shown in figure 6.27.

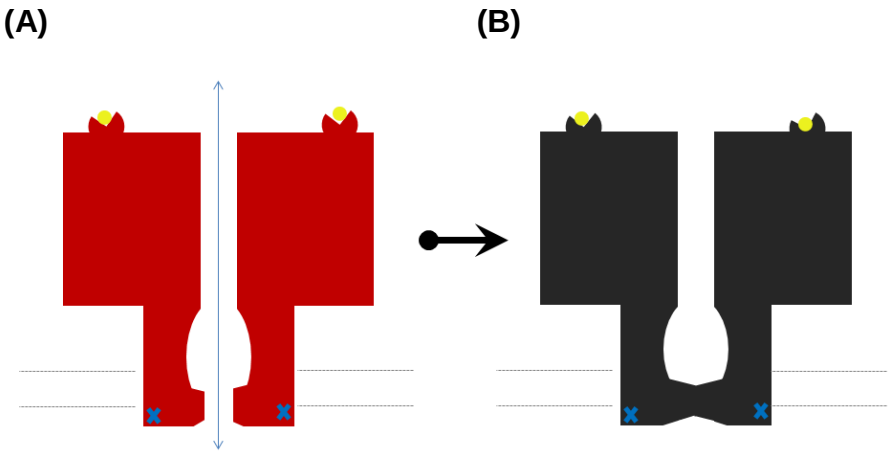


Figure 6.27. Schematic representation of putative Y4839A hRyR2 channel conformation transitions during flicker gating. (A) Putative open ligand-bound state (O_2 in red and Ca^{2+} in yellow) and (B) brief flicker closing event (C_F in black) at a putative gate proposed to occur at the selectivity filter in a Ca^{2+}-independent manner. Rate constant transition between $O_2 \rightarrow C_F$ indicated by the direction of the black arrow occurred slower in Y4839A compared to WT hRyR2 channels. The Y4839A point mutations in the pore region (S6 helix) are indicated by a blue cross.

The open and closed time constants for Y4839A were all longer than WT and conservative hRyR2 mutation channels, however were not significantly different. In addition, comparing the kinetic models and their rate constants shown in figure 6.24 revealed that all 12 state transitions in Y4839A were slower than WT hRyR2, although only one of these transitions ($O_2 \rightarrow C_F$) was significantly different. The subtle kinetic trends of longer time constants and slower state transitions for Y4839A implies that alanine mutation induced a type of channel rigidity or stiffness, however with the lack of statistical significance it remains unclear whether the Y4839A mutation had affected channel gating and this is discussed further in chapter 7.

The overall comparable biophysical parameters (open probability and dwell-times) and kinetic information for Y4839A and WT hRyR2 may be due to the position of the mutated residue and the relative distance of this residue away from the proposed selectivity filter and IHBC gate shown in figure 6.28. Therefore disrupting local interactions at a distance from critical regions of the pore may be less important in regulating channel gating and function.

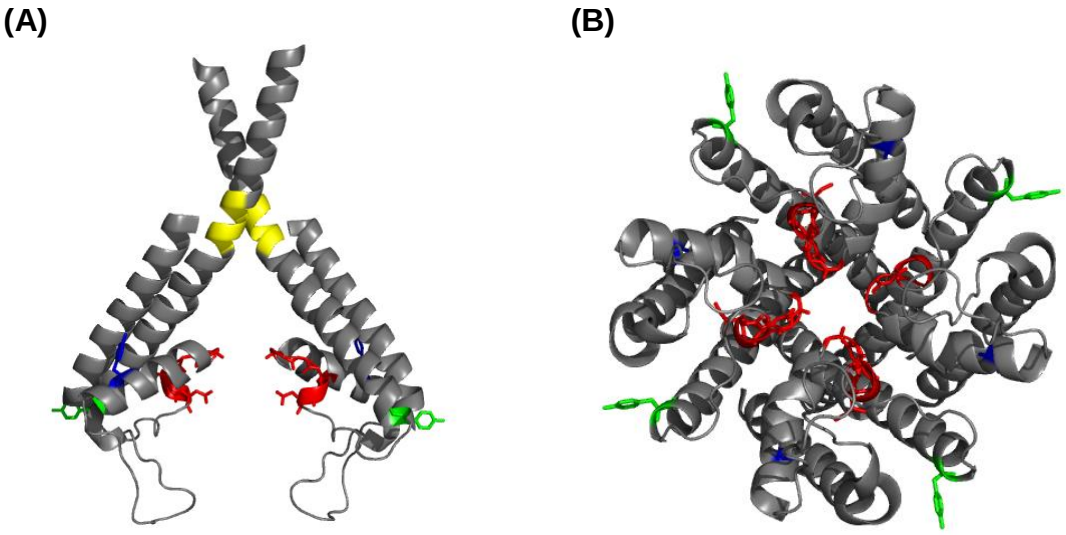


Figure 6.28. Structural model of the RyR1 pore-forming region. (A) Side and (B) luminal view of the PFR RyR1 model of Yan *et al.,* (2015) with helices coloured in grey and Y4813 highlighted in blue and Y4839 in green. The proposed selectivity filter is shown in red and the putative IHBC gate in yellow. The relative distance of residues (highlighted) away from the selectivity filter and IHBC gate may mean that they are less important in facilitating channel gating and function than initially proposed in the hypotheses tested in this thesis.

In summary, this was the first study to demonstrate the inherent variability of single hRyR2 channel gating in stringently regulated minimised conditions over periods of several minutes. Due to channel-to-channel variation, challenges were faced in establishing criteria for data analysis that avoided selection bias in the assessment of the consquences of residue substitution on channel gating. Analysing comparable WT and mutant single-channel data unsurprisingly generated similar kinetic results. However this was a necessary condition for the reliable assessment of subtle differences in channel gating.

While data selection criteria were required to investigate flicker gating, acquiring an enormous amount of data provides the possibility for future analyses on different aspects of hRyR2 channel gating. It may be interesting, therefore, to investigate and compare different gating parameters such as inter- and intra-burst length and P_o, prolonged closures and segments of intermediate and low P_o between WT and mutant hRyR2 single-channel data.

The conservative hRyR2 mutations reinstated the functional characteristics of the WT hRyR2 channel and confirmed the significance of residue side chain interactions within the pore region of the channel as originally hypothesised. The alanine mutant channel, Y4839A, had similar biophysical properties to WT hRyR2; however detailed analysis of gating revealed subtle alterations in gating kinetics that may indicate a role for Y4839 located at the start of the S6 helix in hRyR2 channel gating. The significance of this thesis and future work is discussed in chapter 7.

Chapter Seven:

General Discussion

7.1 Investigating structural mechanisms of gating at the selectivity filter of the hRyR2 channel

This thesis focused on investigating the structure-function relationship of hRyR2 to reveal gating mechanisms proposed to occur at the selectivity filter. The recent publication of high-resolution RyR1 structural models during the latter stage of this project provided detailed structural organisation and an exceptional opportunity to determine functional mechanisms (Zalk *et al.,* 2014; Efremov *et al.,* 2014; Yan *et al.,* 2015). The PFR in RyR1 and RyR2 isoforms share almost identical homology (93.4 %), providing a valid model to compare structure and functional mechanisms. However, in the absence of these near-atomic models at the beginning of this project, predictions on putative structural elements were developed using the RyR2 model based on the K^+ channel, KcsA (Welch *et al.,* 2004).

In KcsA, a network of hydrogen-bonding interactions between the pore helix and selectivity filter forms a structural element that stabilises a conformation of the selectivity filter, regulating channel gating (Cordero-Morales *et al.,* 2006; Cuello *et al.,* 2010a; Cuello *et al.,* 2010b; Cordero-Morales *et al.,* 2011). Three residues (Y4813, D4829 and Y4839) were identified in the Welch *et al* RyR2 PFR model in positions analogous to KcsA (W67, E71 and D80) (Welch *et al.,* 2004). The location of these residues in RyR2 and their side chain properties were predicted to be ideal to form a multipoint network of hydrogen-bonding interactions, therefore altering the properties of these residues by mutation would disrupt the proposed network affecting hRyR2 channel gating.

In addition, previous studies in K^+ channels identified very brief flicker closing events occurring at the selectivity filter due to its dynamic meta-stable nature (Piskorowski and Aldrich, 2006; Zadek and Nimigean, 2006; Cuello *et al.,* 2010b). Structural modelling of the selectivity filter in hRyR2 suggested that this region was wider and more flexible than the K^+ channel selectivity filter (Welch *et al.,* 2004) and previous investigations of single hRyR2 channel gating have identified rapid flicker transitions (Mukherjee *et al.,* 2012), suggesting that these closings may occur at the selectivity filter in hRyR2.

Six full-length mutant hRyR2 channels were constructed using a cassette-based strategy to disrupt (Y4813A, D4829A and Y4839A) or retain (Y4813W, D4829E and

Y4839W) functional side chain interactions, outlined in chapter 3. No deleterious effects on transfection efficiency or protein expression were reported for mutant hRyR2 channels when compared to WT hRyR2. Therefore the successful generation of the six channels permitted downstream cellular and molecular functional assays to be undertaken to evaluate the consequence of residue interaction in the pore region.

As an initial screen, the functional status of a population of mutant hRyR2 channels was examined *in situ* by intracellular Ca^{2+} imaging. Ca^{2+} was released from HEK293 ER stores through the six mutant hRyR2 channels upon the addition of caffeine. This was indicated by a fluorescent intensity increase, suggesting that hRyR2 containing these mutations occurring in the pore region formed functional homotetrameric channels that maintained the ability to translocate Ca^{2+} ions through the pore. However interestingly, the maximum Ca^{2+} release from HEK293 cells expressing Y4813A and D4829A was reduced by 25.6 % and 22.7 % compared to cells expressing WT hRyR2 channels, respectively. The remaining four hRyR2 mutations (Y4813W, D4829E, Y4839A and Y4839W) maintained the maximal Ca^{2+} release compared to WT hRyR2, suggesting that alanine substitution within the proposed pore helix, Y4813A, and selectivity filter, D4829A, either affected the channel's sensitivity to caffeine and/or calcium, or that these mutations physically affected Ca^{2+} release through the pore.

The investigation of mutant hRyR2 channels using [^{3}H] ryanodine binding and single-channel techniques provided insight into the significance of residue side chain properties in the pore region. The drastic reduction of [^{3}H] ryanodine binding in the alanine pore helix mutant, Y4813A, in conditions favouring channel opening (10 mM caffeine and 100 µM $CaCl_2$) and the absence of purified channels in bilayers, prompted the examination of Y4813A homotetramer stability when removed from the cellular environment. Western blot analysis of sucrose fractions of density at which the homotetramer would sediment, confirmed that Y4813A formed tetrameric channels upon isolation. This observation indicated that the absence of channel function in bilayers either occurred because channels did not incorporate or because Y4813A remained permanently closed following incorporation. The latter option was favoured as [^{3}H] ryanodine binding to Y4813A channels was only 1.03 % of that seen with WT hRyR2. The consequence of disrupting hydrogen bond interactions at the pore helix may have resulted in a collapsed non-conductive selectivity filter, analogous to the collapsed filter seen in K^+ channel crystal

structures resolved in low permeant K^+ concentrations (Zhou *et al.,* 2001; Cuello *et al.,* 2010a). However, the proposal that hRyR2 Y4813A channels remained permanently closed was surprising as these channels were caffeine sensitive *in situ*, opening and facilitating the release of Ca^{2+} upon agonist addition.

These aforementioned findings highlight limitations of the [^{3}H] ryanodine binding assay, as altered binding results may have been a consequence of the mutation itself, producing misleading results. Mutation-dependent alterations in ryanodine binding to hRyR2 may occur through several factors such as; the generation of unstable or closed channels, modification of structural components important in the ryanodine-hRyR2 interaction altering the access to, or affinity of, the binding site, or by altering the mutant channel's sensitivity to calcium. Therefore, altered binding does not exclusively determine channel function, and thus it is essential to interpret mutant hRyR2 [^{3}H] ryanodine results in combination with complementary assays such as intracellular Ca^{2+} imaging and single-channel bilayers, however for Y4813A, the latter was not possible.

Interestingly hRyR2 containing the conservative tryptophan mutation, Y4813W, had improved [^{3}H] ryanodine binding (30.12 % of WT binding) compared to channels containing the Y4813A mutation. At the molecular level, the biophysical properties of ion conduction, ryanodine modification, dwell-time occupancy and gating kinetics of Y4813W were all comparable to WT hRyR2 channels. The replacement of tyrosine with tryptophan, a residue with similar steric bulk and physicochemical hydrogen-bonding capabilities, provided interesting insight into the importance of an aromatic residue at position 4813 that restored RyR2 function compared to Y4813A.

The aspartic acid at position 4829, located at the luminal end of the selectivity filter is a highly conserved residue throughout the RyR isoforms (Welch *et al.,* 2004; Lanner *et al.,* 2010; Yan *et al.,* 2015), IP_3R (Taylor and Tovey, 2010) and K^+ channels (Heginbotham *et al.,* 1994; McCoy and Nimigean, 2012). Replacing this residue with either an alanine, D4829A, or conservative glutamic acid, D4829E, reduced ryanodine binding to 45.63 % and 7.18 % compared to WT hRyR2, respectively. This was surprising as retaining the negative charge by D4829E, however extending the side chain by a methyl group significantly reduced binding compared to the alanine mutation. This observation suggests that the bulk of the residue at 4829 is much more important than its charge in maintaining a conformation that supports ryanodine binding. Both mutant D4829 channels were

characterised by channel-to-channel variability in gating and sub-conductance states when assessing their biophysical properties in bilayers. The full unitary conductance of single D4829A and D4829E channels was reduced by 75 % and 20.5 % compared to WT hRyR2, respectively. Yan *et al*, (2015) proposed that the selectivity filter of RyR1 may constitute two cation-binding sites (AGGGIGDE), with one site located at the luminal mouth formed by D4899 and E4900 (equivalent to D4829 and E4830 in hRyR2) and another at A4893, G4894 and G4895 (equivalent to A4823, G4824 and G4825 in hRyR2) shown in figure 7.1A (Yan *et al.,* 2015). In addition, the highly electronegative luminal loop (containing 8 aspartic acid and glutamic acid residues out of 16) between the S5 and pore helix above the entrance to the selectivity filter in the Yan *et al* RyR1 model provides a mechanism for maximising rates of cation delivery to the pore shown in figure 7.1B. A similar mechanism was proposed previously in the Welch *et al* RyR2 model, that contains a smaller electronegative luminal loop (Welch *et al.,* 2004), therefore the drastic reduction in D4829A channel conductance may have been due to the net loss of negative charge within the luminal mouth region. The unique and varied biophysical properties of hRyR2 channels with mutations at D4829 were ultimately unsuitable for further investigations. The drastic effect on channel gating and conductance supports the proposal that D4829 may contribute to a cation-binding site, and suggests that the negative charge and also the precise side chain length of the conserved aspartic acid is essential for maintaining channel function.

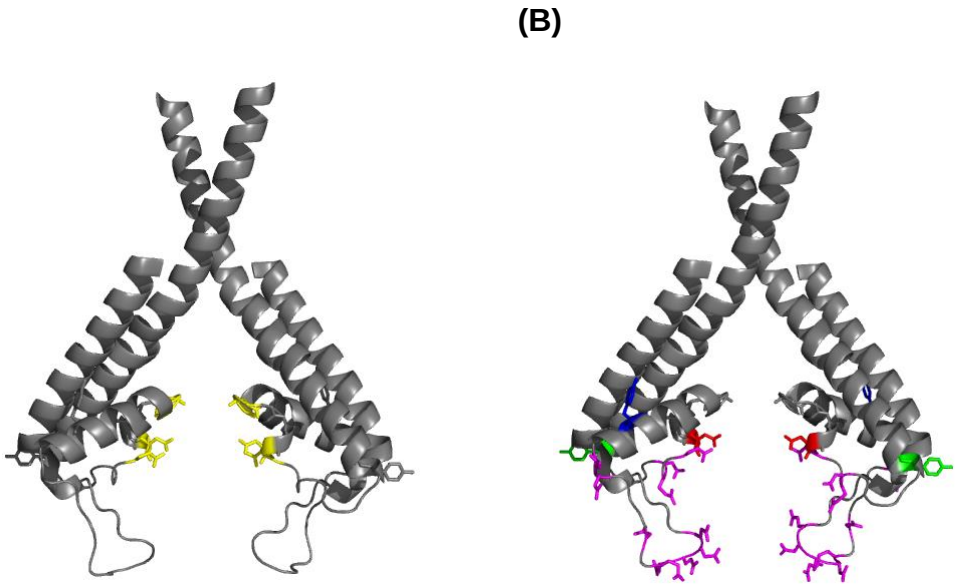


Figure 7.1. A proposed cation-binding site at the luminal mouth of the selectivity filter of RyR1. (A) Two proposed cation-binding sites (AGGGIGDE) are highlighted in yellow. D4899 and E4900 are located at the luminal mouth and are equivalent to D4829 and E4830 in RyR2. (B) A highly electronegative luminal loop between the S5 and pore helix contains 8 aspartic and glutamic acid residues, highlighted in magenta. Residues are colour-coded as stated in figure 5.16. The figures were constructed in PyMol using the PDB file 3J8H from Yan *et al.,* (2015).

The alanine mutation at position Y4839 affected channel function, reducing [^{3}H] ryanodine binding and unitary ion conductance at 210 mM KCl by 62.5 % and 16.8 % compared to WT hRyR2, respectively. Altered ion conduction properties in Y4839A hRyR2 channels were assessed by a series of ion handling experiments to probe potential mechanistic differences in ion channel discrimination, relative permeability and pore dimensions. While the alanine mutation did not alter the ability of hRyR2 to discriminate between cations and anions, the relative permeability between divalent (Ba^{2+}) and monovalent (K^+) cations was 15.1 % lower than in WT hRyR2. This was surprising as in previous reports it had been proposed that a high density of negative charge, either within the pore or within vestibules at either end of the pore, was responsible for discrimination between cations (Tinker *et al.,* 1992; Mead-Savery *et al.,* 2009). The small changes in cation discrimination and ion conductance at particular K^+ activities may have therefore been achieved through Y4839A indirectly altering the conformation of the electronegative luminal loop at the mouth of the selectivity filter. The radius of the narrowest region of the Y4839A hRyR2 channel pore was determined by monitoring the relative

permeability of monovalent organic cations and was found to be equivalent to that of WT hRyR2 channels. The assessment of the ion handling properties of Y4839A supported the credibility of the recent RyR1 model of Yan *et al* (2015), as, while in the Welch *et al* (2004) RyR2 model Y4839 is located in the loop-forming region in close proximity to the filter, in the more recent model it is located at the luminal end of the S6 helix, distant from critical regions of the pores ion permeation pathway (Welch *et al.,* 2004; Yan *et al.,* 2015).

Y4839A hRyR2 channels had very minor changes in channel gating and function. A noticeable, but not statistically significant, trend in Y4839A gating kinetics (longer time constants and slower state transitions) was observed and may have been achieved through a type of channel stiffness by imposing different constraints within the S6 helix conformation. However, in general, the similarity in maximum Ca^{2+} release, open probabilities and dwell-time parameters in Y4839A compared to WT hRyR2 may have been due to the relative distance of Y4839 away from the proposed selectivity filter region as indicated by the Yan *et al* RyR1 model. Therefore disrupting local interactions distant from proposed critical regions of the pore may have less influence on channel gating.

The conservative tryptophan mutation Y4839W fully restored both [^{3}H] ryanodine binding and ion conductance, at 210 mM KCl, to values equivalent to WT hRyR2. In addition, the gating parameters of Y4839W (open probability, dwell time intervals, time constants, state occupancy and transitions) were comparable to WT hRyR2. The data obtained from both alanine and tryptophan substitutions at residue 4839 are in accordance with the original hypothesis that retaining physicochemical properties and hydrogen-bonding capabilities of this aromatic residue is essential for hRyR2 function.

7.2 Is there a gate at the selectivity filter of hRyR2?

It remains unclear whether the selectivity filter, stabilised by a network of residue interactions, has a role in hRyR2 channel gating. In the RyR1 model published recently by Yan *et al* (2015), the distance between the proposed residues selected in this thesis, Y4813-D4829 and Y4839-D4829, ~ 20 Å and ~ 25.6 Å respectively, would not be compatible with the formation of a hydrogen-bonding network. Therefore the three residues (Y4813, D4829 and Y4839) would not be involved in stabilising the selectivity filter region in a manner similar to the equivalent residues in K^+ channels.

However, removing the hydrogen-bonding capacity of two of the hRyR2 mutations, Y4813A and D4829A, significantly affected channel gating and function. This observation suggests that these residues, Y4813 and D4829, are essential and may be involved in stabilising a conformation of the pore helix and selectivity filter. Furthermore, it is important to note that while the resolution of the Yan *et al* RyR1 model has improved compared to the Welch *et al* RyR2 model, these models represent static structures and do not reveal the nature of a functioning channel. The models do not account for the dynamic rearrangements of residues and domains, and further underlies the importance of functional single-channel experiments to test these models and assess their credibility.

7.3 Future work

7.3.1 Identifying alternative residue candidates to assess the role of hRyR2 selectivity filter gating

The altered conformation and rearrangement of helix boundary sites in the RyR1 model by Yan *et al*, raises the question of whether a network of hydrogen-bonding interactions exists between different residues in the pore. An initial screen of the RyR1 PDB file (Yan *et al.,* 2015) and sequence alignment of the RyR isoforms, shown in figure 5.16, indicate that tyrosine residues on the pore helix, Y4818, and in the luminal loop-forming region, Y4793, using RyR2 residue numbering, are in close proximity to the selectivity filter depicted in figure 7.2. These residues may prove to be alternative candidates for site-directed mutagenesis and functional assays to examine the role of selectivity filter regulated gating.

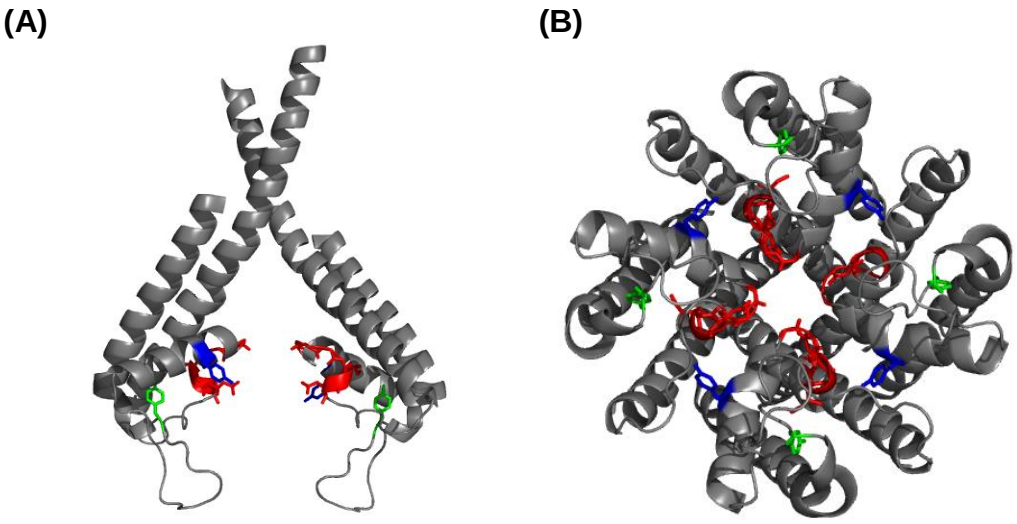


Figure 7.2. Identifying alternative residue candidates to assess the role of side chain interactions to stabilise a putative selectivity filter gate. Y4818 in the pore helix is highlighted in blue and Y4793 located in the luminal loop-forming region in green are in close proximity to the proposed selectivity filter (GGGIGD) highlighted red.

7.3.2 What is the physiological relevance of flicker closings in RyR2?

The physiological relevance of flicker closings (0.30 ms) remains to be established in RyR2 channels. The effect of altered flicker gating has not been documented in the literature and is a relatively novel area of RyR2 functional studies.

Kinetic models were constructed to describe the gating behaviour of WT and mutant hRyR2 to identify the prevalence and nature of flicker gating events (thought to originate in the selectivity filter) and to examine if substitution had affected this particular conformational transition. Flicker gating is one of the main closing events (~ 49 % state occupancy) to occur during Ca^{2+} activation experiments, suggesting that these closings may regulate, to some extent, the release of stored SR Ca^{2+}. It has been shown that channel open time determines the spread of Ca^{2+} sparks from individual RyR2 channels into Ca^{2+} waves (Sato and Bers, 2011), suggesting that decreasing channel open times as a consequence of flicker events may play a role in Ca^{2+} termination. However due to the brief nature of these events, it remains unknown whether flicker events are sufficient to affect Ca^{2+} release.

Preliminary data suggests that flicker closing events in hRyR2 occur less with saturating permeant monovalent cations and increase as the concentration of cations are decreased. It may therefore be interesting to speculate on the effect of permeant ions on the prevalence of flicker closings. As $[Ca^{2+}]_{lum}$ is depleted from the SR during CICR the occurrence of these flicker closings may increase.

The identification of structural elements involved in flicker closings is one part of the jigsaw puzzle in the overall gating process of RyR2 channels. It is essential to continually improve our knowledge of the mechanisms underpinning RyR2 channel gating to therefore understand how these systems are affected in pathological conditions.

7.4 Concluding remarks

The kinetic models constructed in this thesis to examine hRyR2 channel gating can be used as a framework for a long term research strategy. Monitoring WT and mutant hRyR2 behaviour revealed unique fluctuations in channel activity switching between different modes of gating under steady-state conditions. Future investigations must therefore provide clear criteria for data selection to justifiably compare the effect of prospective point mutations, potential therapeutic compounds and physiological regulatory factors on hRyR2 channel gating, as it is essential to distinguish between the inherent variability of the channel and the influence of external factors on gating.

7.5 Final summary of findings

It remains unclear whether hRyR2 channel gating is regulated by the proposed selectivity filter stabilised by a hydrogen-bonding network due to altered residue distances between Y4813, D4829 and Y4839 in the recently published RyR1 structural model by Yan *et al*, (2015). However, data from intracellular Ca^{2+} imaging, [^{3}H] ryanodine binding and single-channel assays revealed that residues located in the pore region, and their side chain interactions, are essential in maintaining hRyR2 channel gating and function. Together these results indicate that the selectivity filter region is an important component for RyR2 function.

Appendix I – Measuring the maximum Ca^{2+} release from HEK293 cells expressing hRyR2 channels

	Exp (*n*)	Cells (*n*)	Maximum Ca^{2+} release $((F-F_0)/F_0)$	$p < 0.05$
WT hRyR2	6	55	5.113 ± 0.278	
Y4813A	3	56	3.806 ± 0.261	0.0009
Y4813W	3	44	5.424 ± 0.311	ns
D4829A	3	53	3.947 ± 0.243	0.0022
D4829E	3	40	5.024 ± 0.246	ns
Y4839A	3	39	5.038 ± 0.358	ns
Y4839W	3	61	4.587 ± 0.227	ns

Table I. Measurement of maximum Ca^{2+} release in HEK293 cells expressing WT and mutant hRyR2 channels. Total number of experiments (Exp) and ROIs (cells) were analysed to determine maximum Ca^{2+} release ($(F-F_0)/F_0$), detailed in section 4.3.1.1. HEK293 cells expressing Y4813A and D4829A had a significantly reduced maximal Ca^{2+} release than cells expressing WT hRyR2 channels by 25.6 % and 22.7 %, respectively.

Appendix II – Specific [^{3}H] ryanodine binding values

	n	Specific [^{3}H] ryanodine binding (dpm)	$p < 0.05$
WT hRyR2	19	2695 ± 293.9	
Y4813A	11	27.76 ± 20.75	< 0.0001
Y4813W	9	811.74 ± 197.9	< 0.0001
D4829A	16	1229.7 ± 413.1	0.0197
D4829E	9	193.50 ± 25.09	< 0.0001
Y4839A	11	1013.05 ± 268.1	0.0041
Y4839W	9	2886.35 ± 523.8	ns

Table II. Specific [^{3}H] ryanodine binding values. Point mutations at the proposed selectivity filter and pore region of hRyR2 resulted in a marked reduction in the ability to bind ryanodine, except for Y4839W. Normalised binding results are listed in table 4.5.

Appendix III – hRyR2 channel gating at negative holding potentials.

Following the Ca^{2+} activation experiments described in chapter 6, single hRyR2 channels were held at negative holding potentials (- 40 mV) for a further 20 min. There were no differences in mean P_o for WT and mutant hRyR2 channels between positive and negative holding potentials, shown in table III. The proportion of channel P_o thresholds measured at negative were categorised and compared with channel subsets at positive, listed in table IV. A significantly lower proportion of channels exceeded high ($P_o \geq 0.6$) during – 40 mV for WT and mutant hRyR2 (~ 11 %) compared to + 40 mV. Therefore, there were insufficient data for modelling analysis using the criteria set (section 6.3.6) at – 40 mV.

	Ca^{2+} Activation (P_o)			
	n	**+ 40 mV**	***n***	**- 40 mV**
WT hRyR2	21	0.121 ± 0.038	18	0.109 ± 0.028
Y4813W	17	0.097 ± 0.029	14	0.041 ± 0.009
Y4839A	33	0.072 ± 0.014	26	0.076 ± 0.017
Y4839W	20	0.099 ± 0.026	12	0.084 ± 0.027

Table III. Comparing the mean open probability for WT and mutant hRyR2 between positive and negative holding potentials from Ca^{2+} activation experiments.

	Single-channel subset proportion (%)					
	High $P_o \geq 0.6$		**Int P_o 0.2 - 0.6**		**Low $P_o \leq 0.2$**	
	+ 40 mV	**- 40 mV**	**+ 40 mV**	**- 40 mV**	**+ 40 mV**	**- 40 mV**
WT hRyR2	38	**11**	29	**44**	33	**44**
Y4813W	24	**0**	24	**29**	53	**71**
Y4839A	28	**12**	55	**46**	27	**42**
Y4839W	15	**16**	30	**42**	55	**42**

Table IV. Comparing the proportion of open probability threshold subsets between positive and negative holding potentials. Significantly lower proportion of channels exceeded high ($P_o \geq 0.6$) during – 40 mV. There were insufficient data for modelling analysis at – 40 mV.

Mean open probability distributions for WT and mutant hRyR2 channels at +/- 40 mV were generated shown in figure I, and revealed consistent channel activity with no time dependent trend in P_o. There was no evidence of a decline in P_o from recording channels over 40 min.

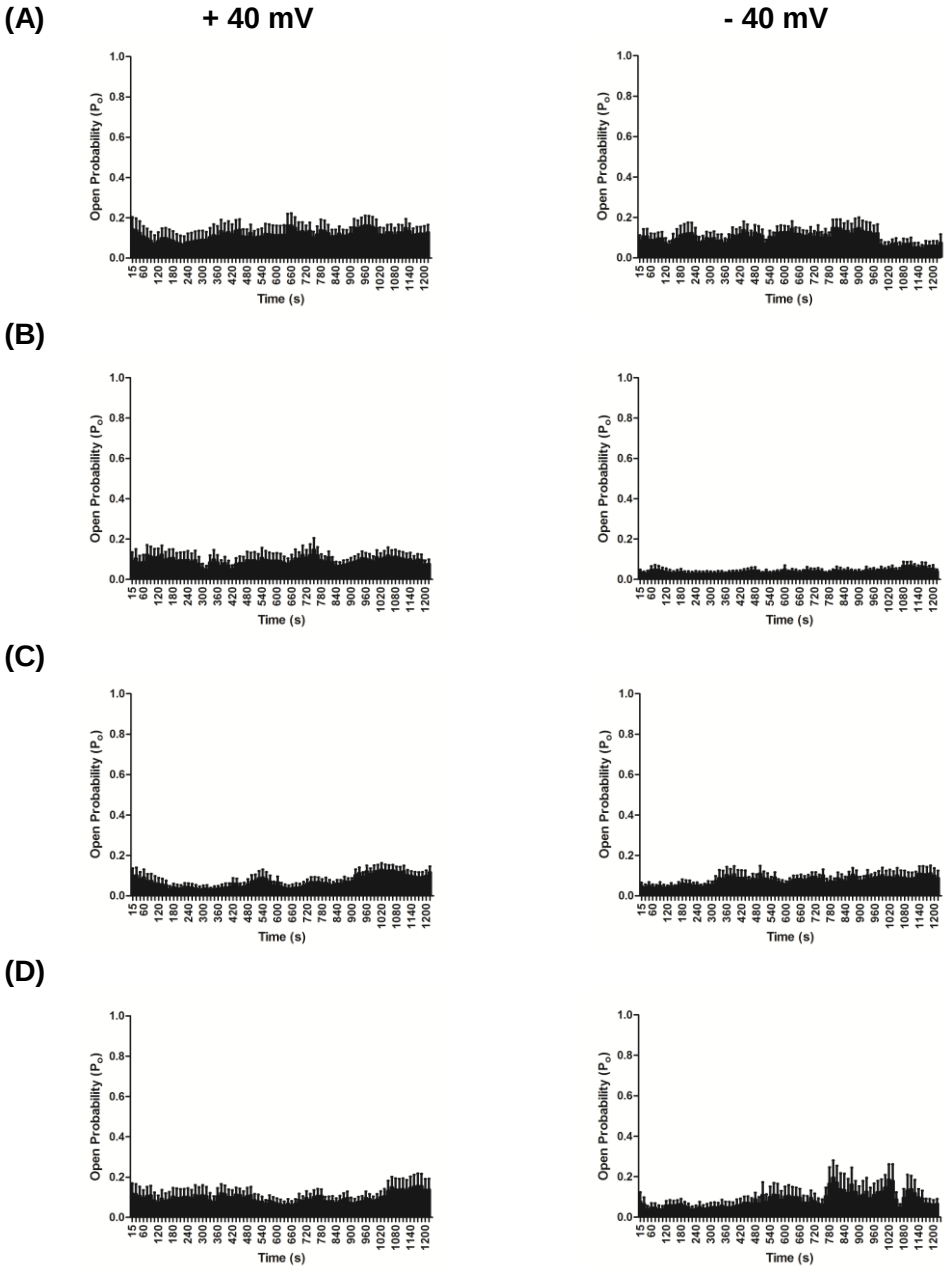
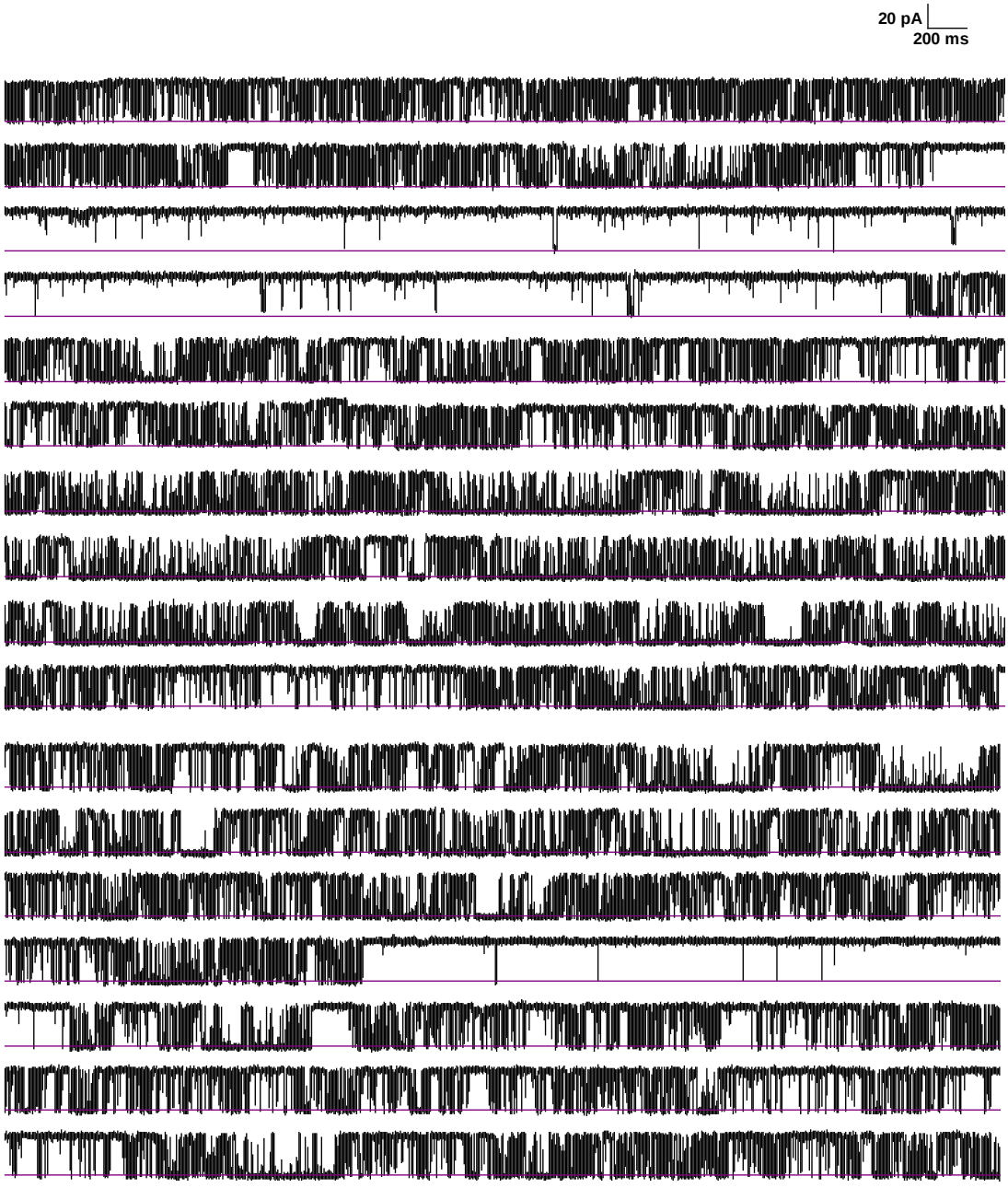
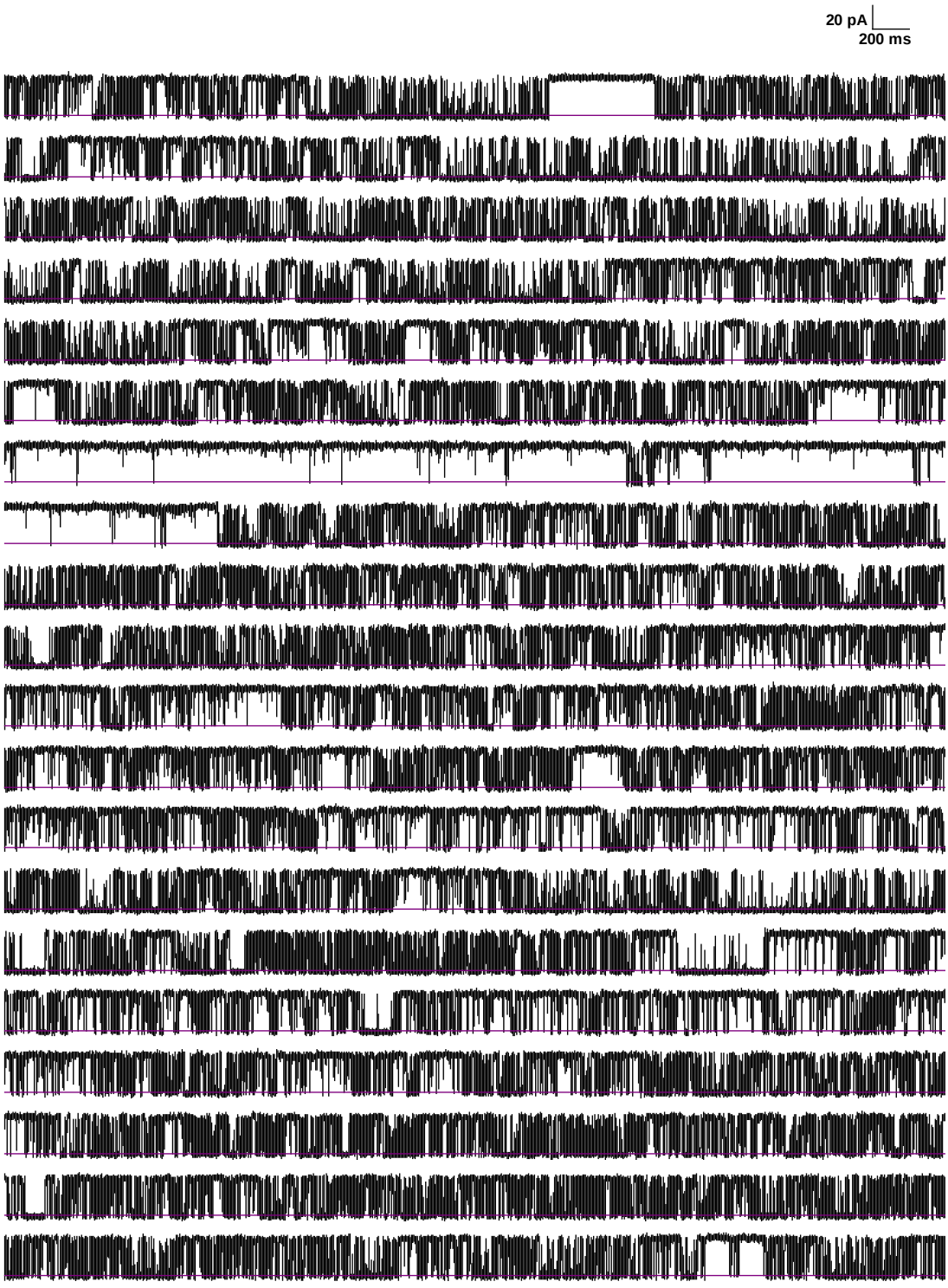
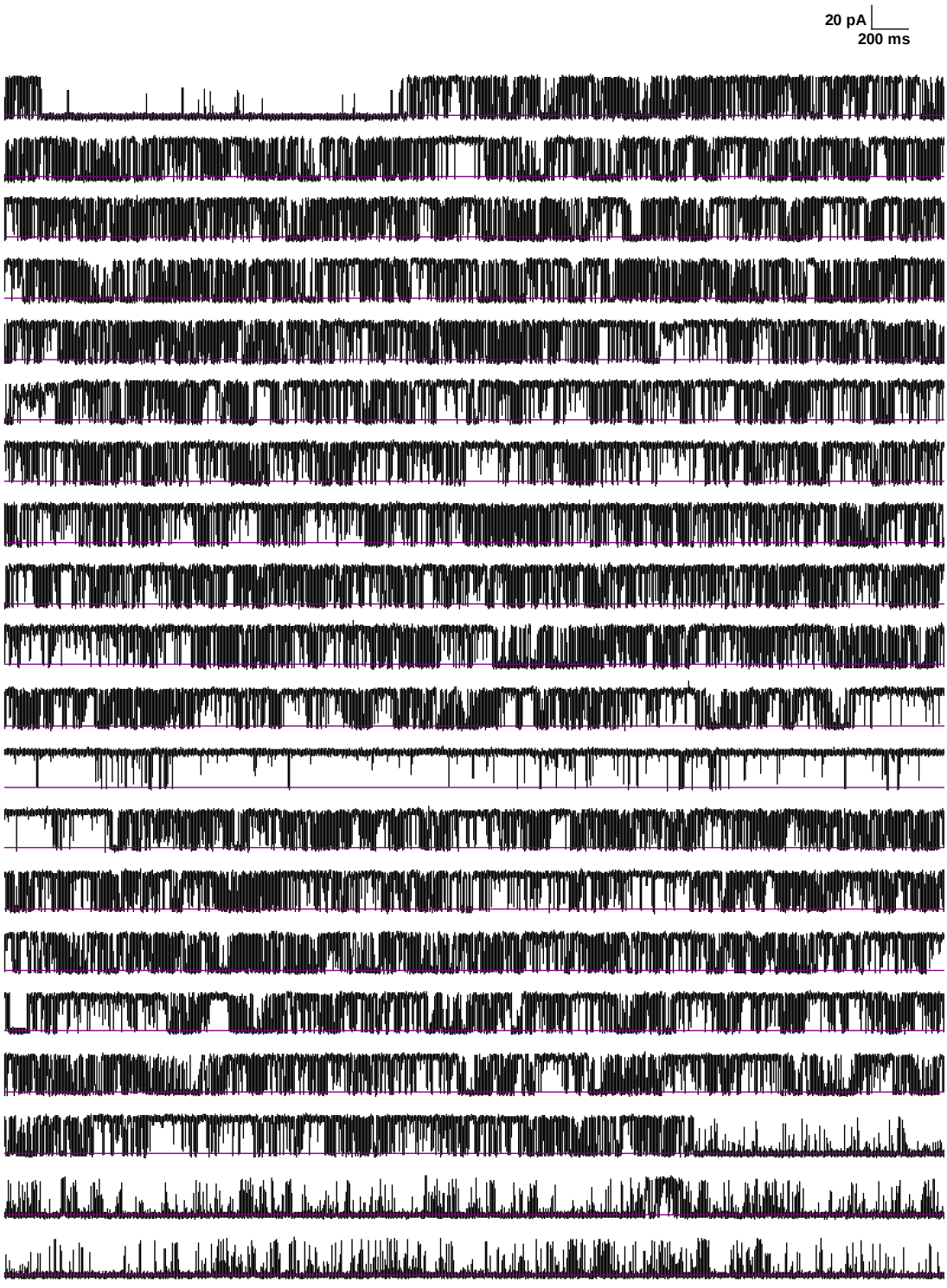


Figure I. Mean open probability distributions from Ca^{2+} activation experiments. Figures represent the combined P_o distributions of (A) WT hRyR2, (B) Y4813W, (C) Y4839A and (D) Y4839W channels recorded at + 40 mV (*left*) and - 40 mV (*right*), analysing the mean P_o in sequential 15 s segments over 20 mintues. Mean P_o are listed in table III.

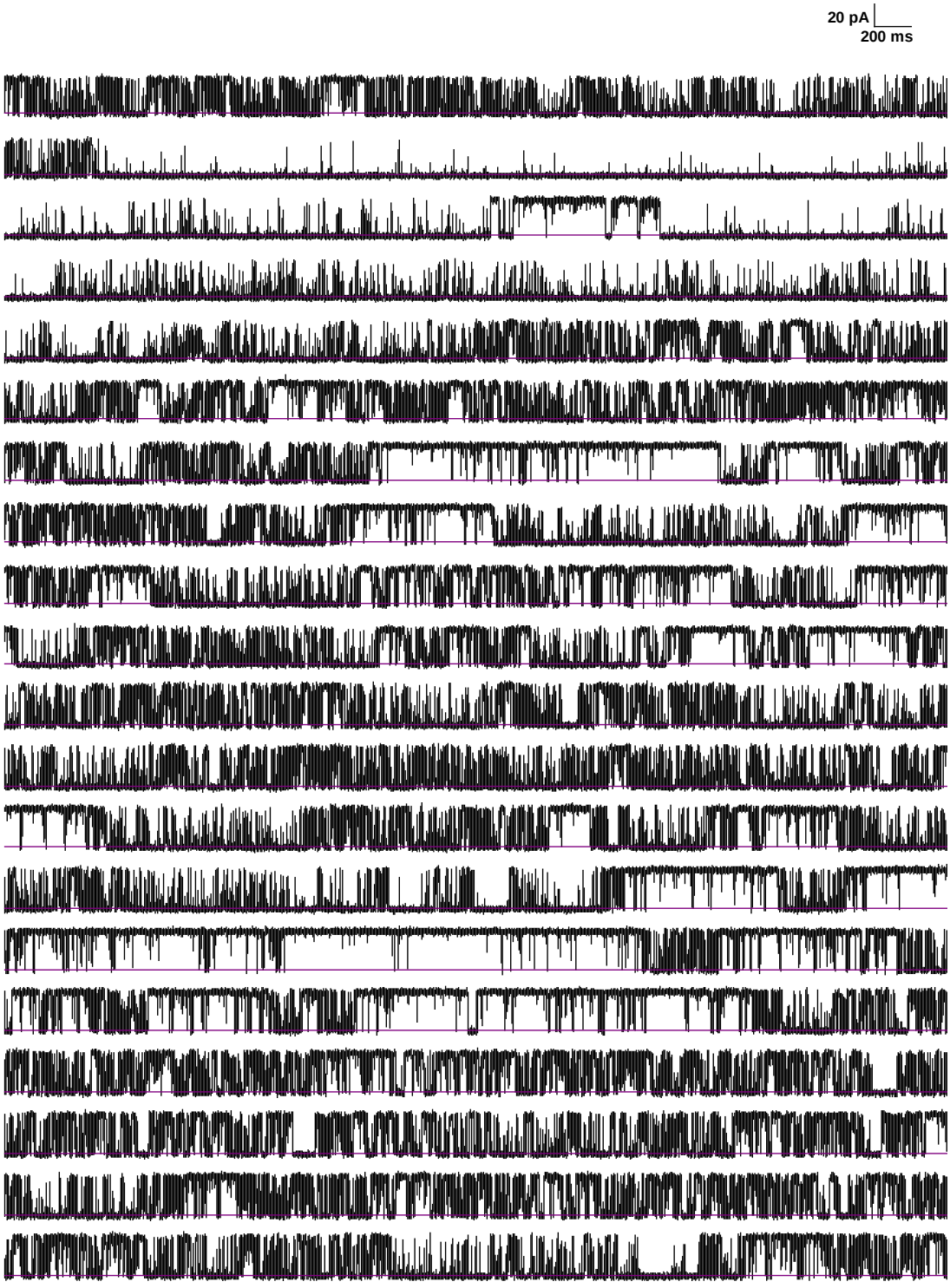
Appendix IV - Monitoring a representative single WT hRyR2 channel at + 40 mV during a Ca^{2+} activation experiment under steady-state conditions. The single-channel trace is a continuous 20 min recording depicting the gating transitions between open and closed states. The purple line denotes the closed state with upward deflections observed as channel openings.

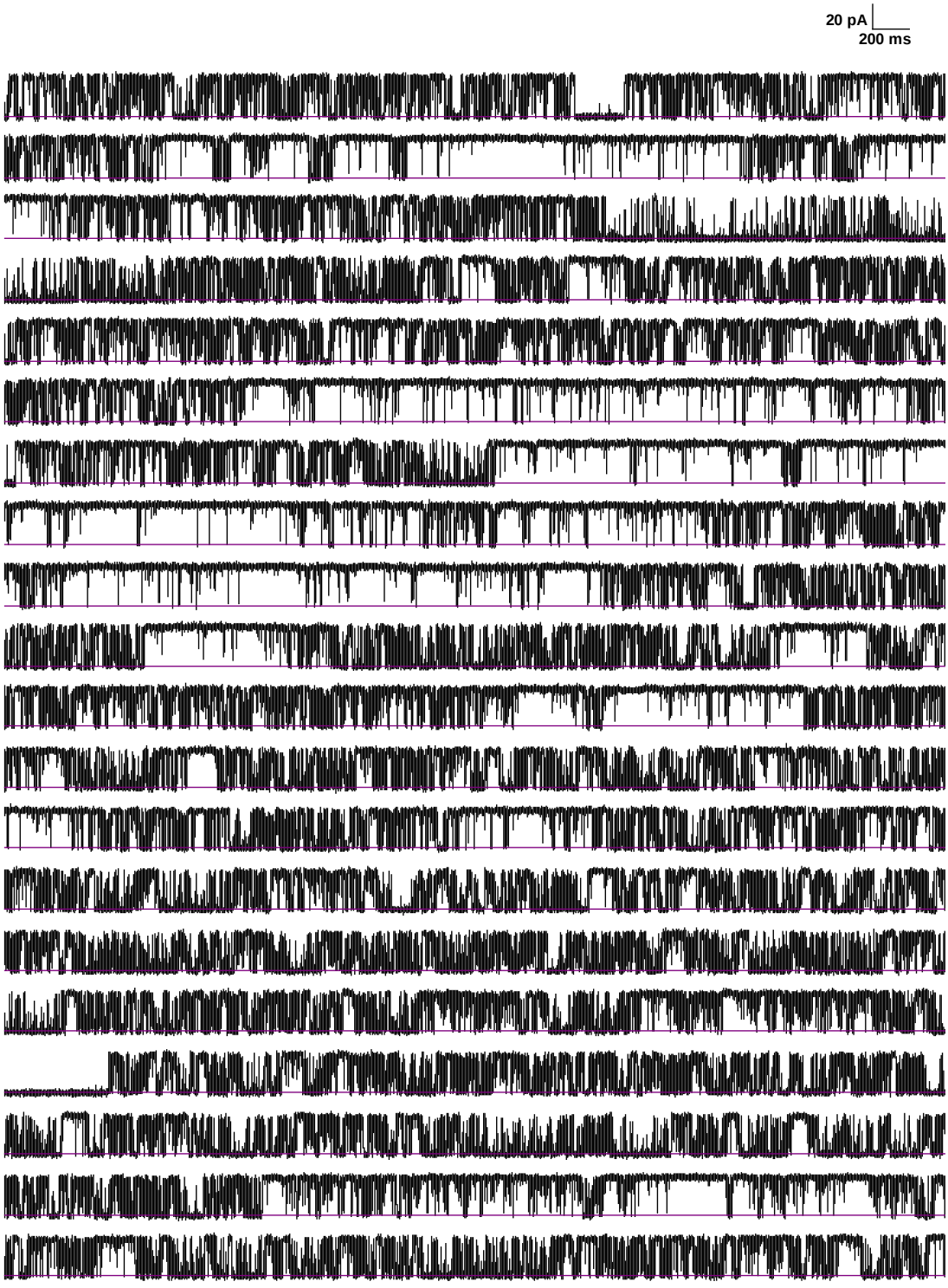



20 pA
200 ms

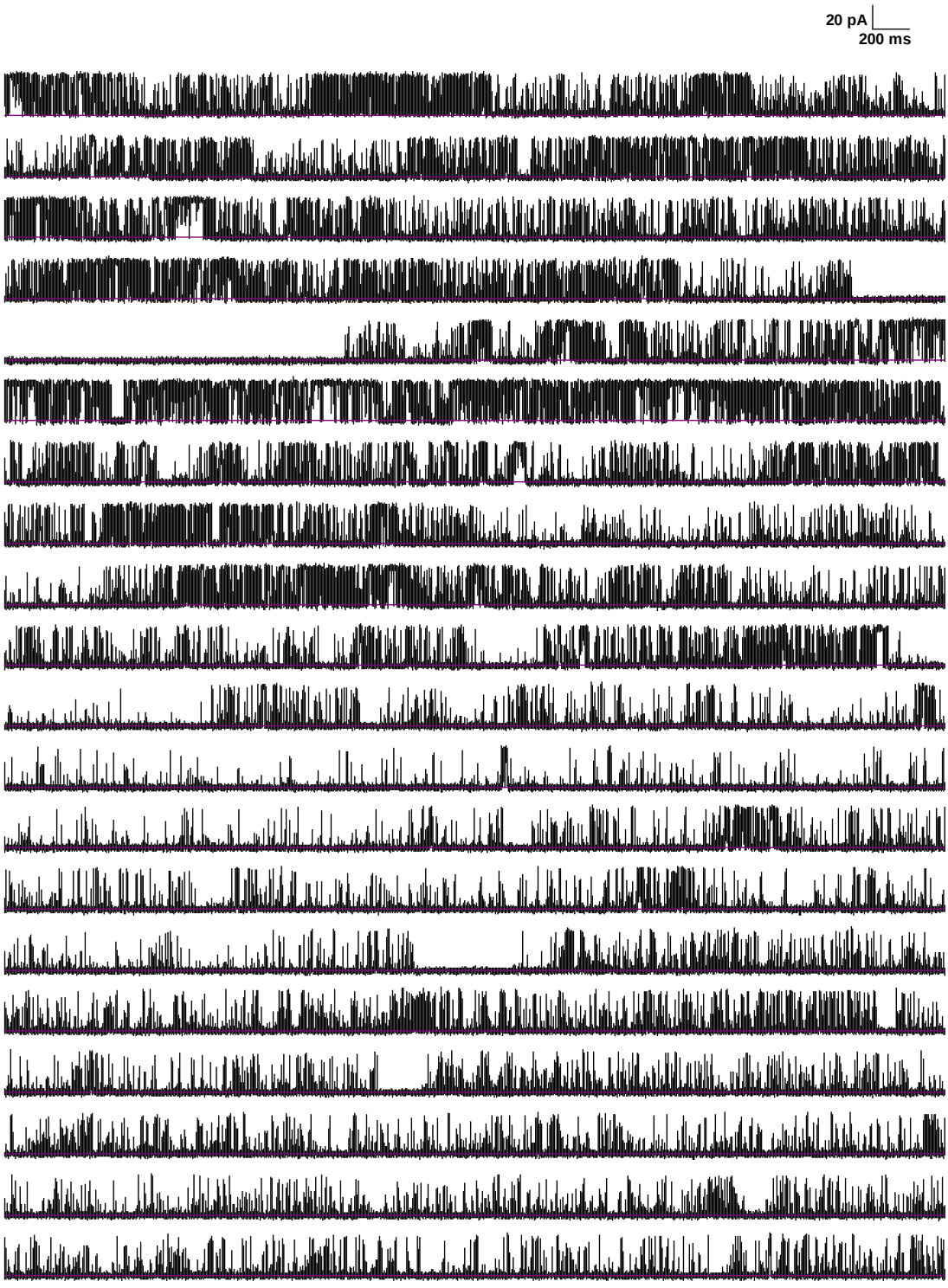

20 pA
200 ms

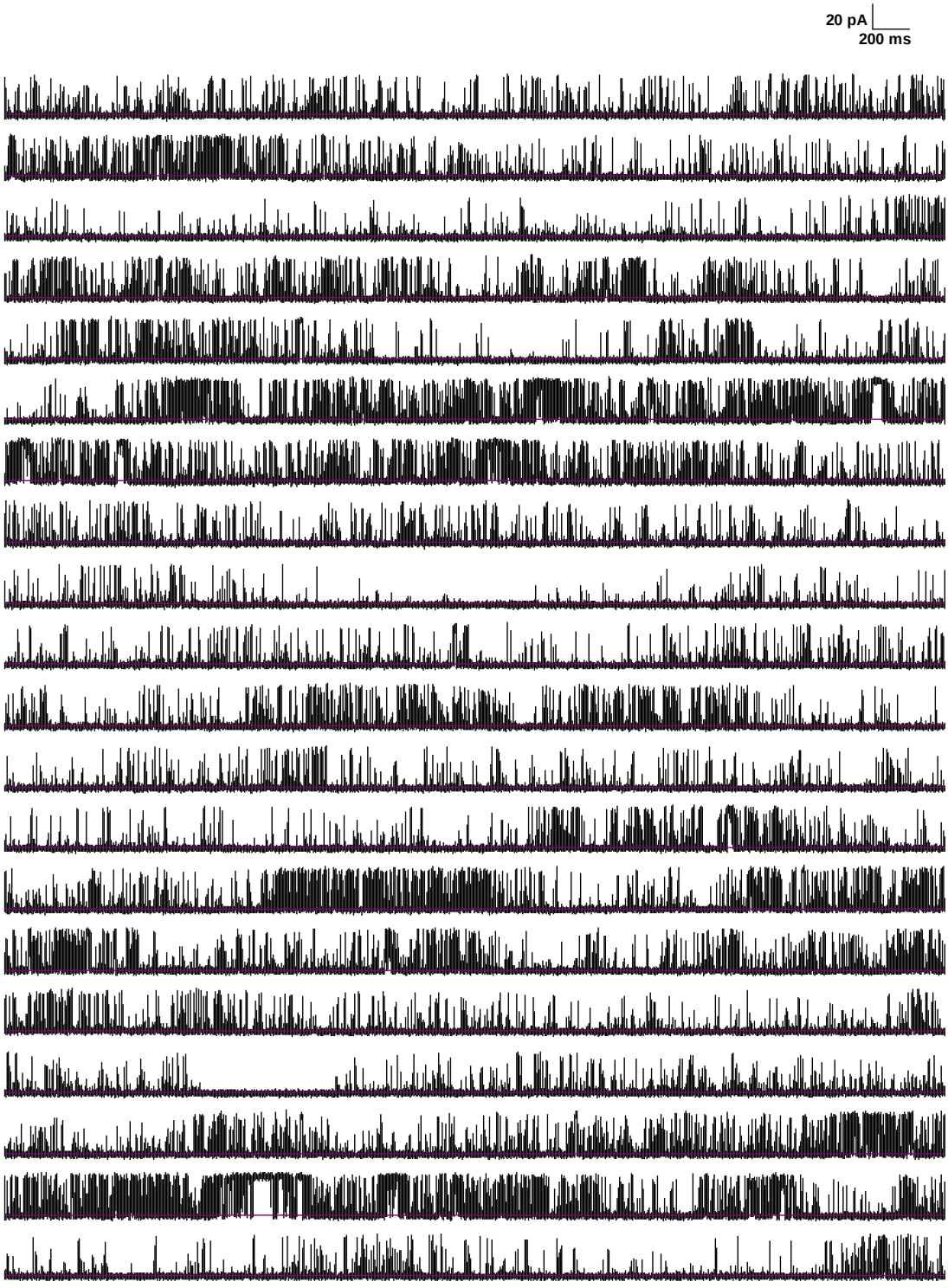

20 pA
200 ms

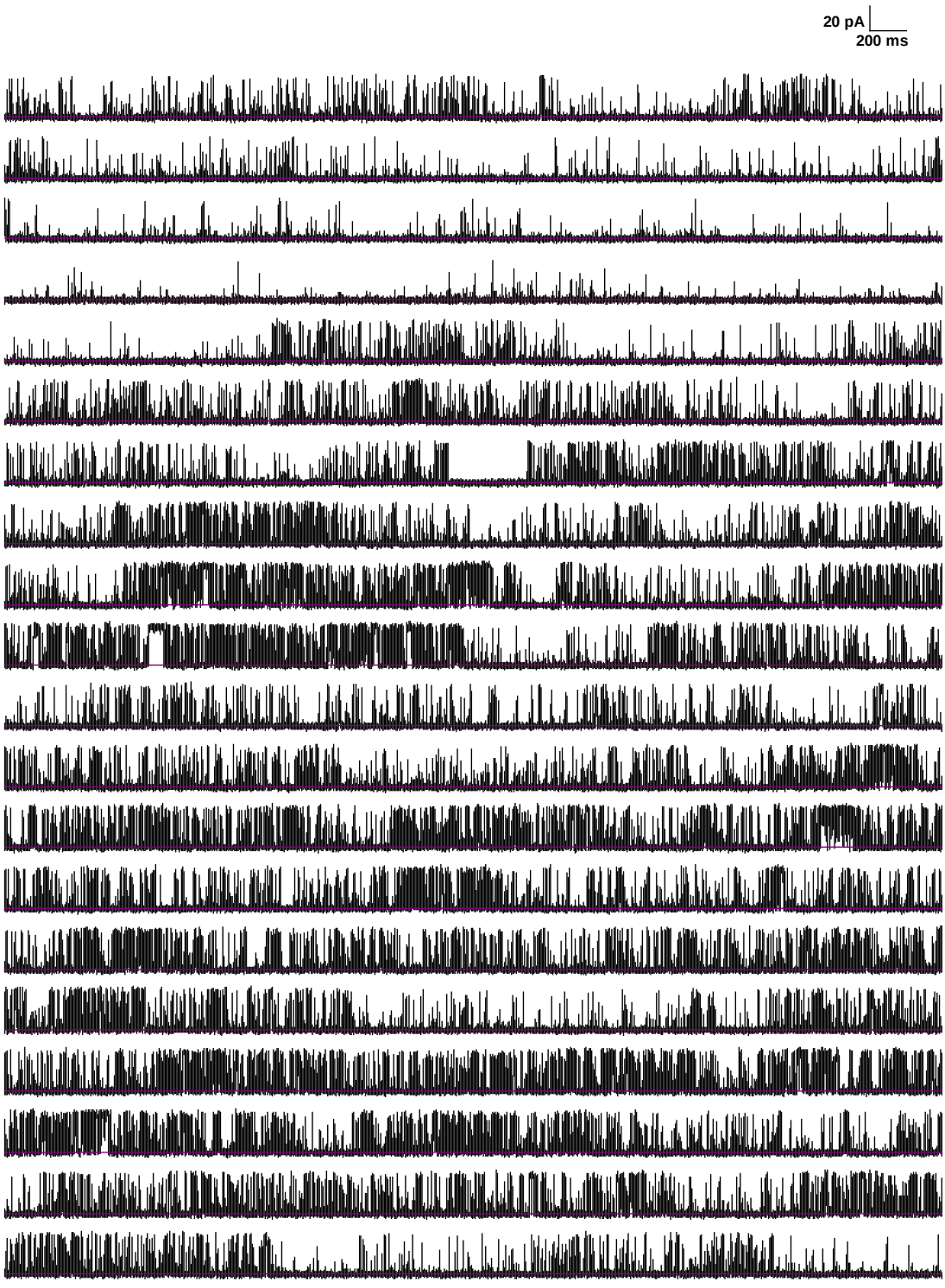

20 pA
200 ms

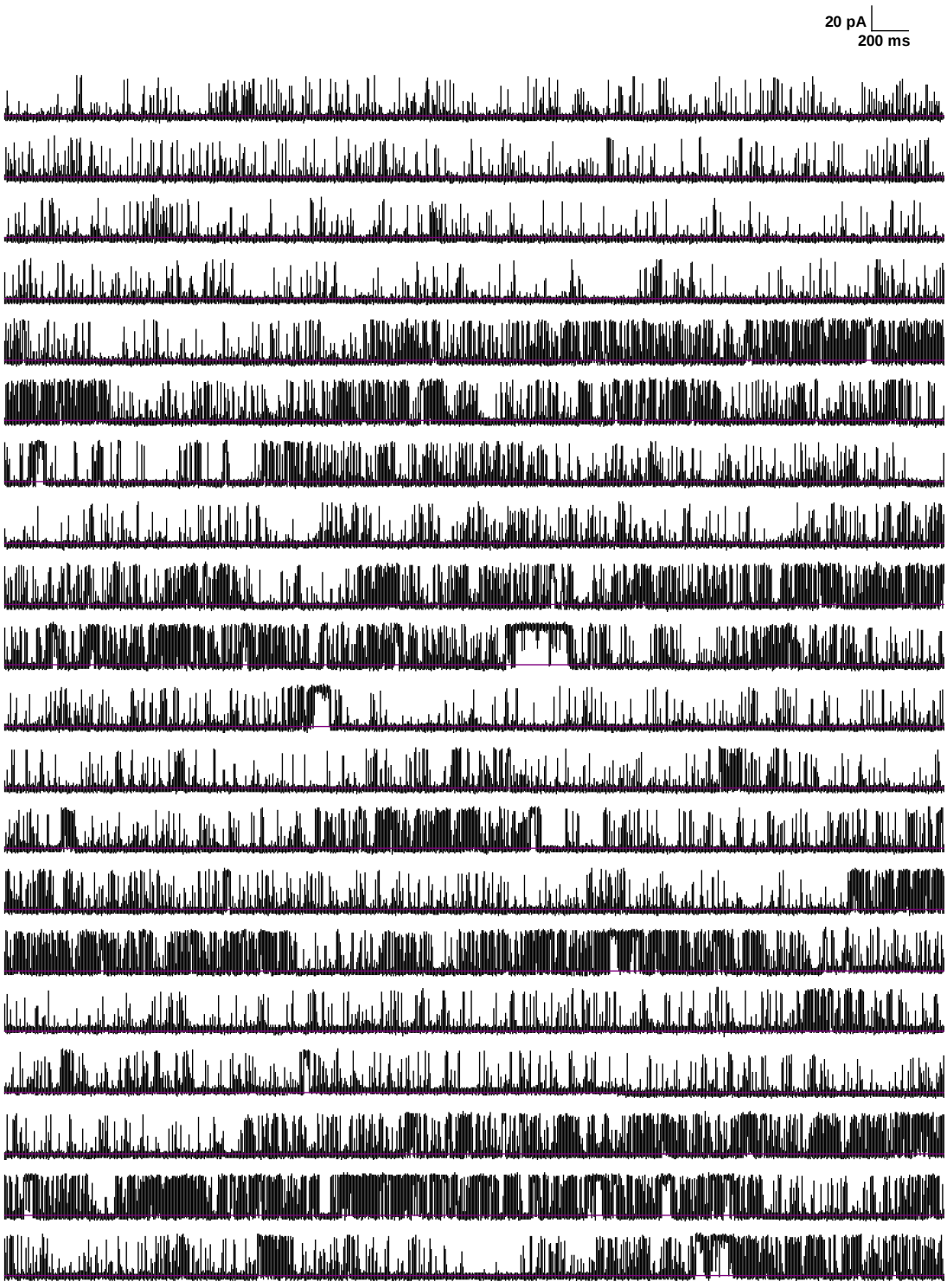

20 pA
200 ms


20 pA
200 ms


20 pA
200 ms


20 pA
200 ms


20 pA
200 ms


20 pA
200 ms

References

Abriel, H. and Zaklyazminskaya, E.V. 2013. Cardiac channelopathies: Genetic and molecular mechanisms. *Gene* 517(1), pp. 1-11.

Ader, C., Schneider, R., Hornig, S., Velisetty, P., Wilson, E.M., Lange, A., Giller, K., Ohmert, I., Becker, S., Pongs, O. and Baldus, M. 2008. A structural link between inactivation and block of a K^+ channel. *Nature Structural & Molecular Biology* 15(6), pp. 605-12.

Ai, X., Curran, J.W., Shannon, T.R., Bers, D.M. and Pogwizd, S.M. 2005. Ca^{2+}/calmodulin-dependent protein kinase modulates cardiac ryanodine receptor phosphorylation and sarcoplasmic reticulum Ca^{2+} leak in heart failure. *Circulation Research* 97(12), pp. 1314-1322.

Alagem, N., Yesylevskyy, S. and Reuveny, E. 2003. The pore helix is involved in stabilizing the open state of inwardly rectifying K^+ channels. *Biophysical Journal* 85(1), pp. 300-12.

Alam, A. and Jiang, Y. 2011. Perspectives on: Ion selectivity: Structural studies of ion selectivity in tetrameric cation channels. *The Journal of General Physiology* 137(5), pp. 397-403.

Alvarez, O. 1986. How to set up a bilayer system. *In: Ion Channel Reconstitution,* New York: Plenum. pp. 115-130.

Andersson, D.C. and Marks, A.R. 2010. Fixing ryanodine receptor Ca^{2+} leak–a novel therapeutic strategy for contractile failure in heart and skeletal muscle. *Drug discovery today. Disease mechanisms* 7(2), pp. 151-157.

Ather, S., Respress, J.L., Li, N., X, Wehrens, X.H.T. and Wehrens, E.H.T. 2013. Alterations in ryanodine receptors and related proteins in heart failure. *Biochimica et biophysica acta* 1832(12), pp. 2425-31.

Avila, G., Sharma, P., Khanna, V.K., Dirksen, R.T. and MacLennan, D.H. 2004. Role of the sequence surrounding predicted transmembrane helix M4 in membrane association and function of the Ca^{2+} release channel of skeletal muscle sarcoplasmic reticulum (ryanodine receptor isoform 1). *Journal of Biological Chemistry* 279(36), pp. 37566-74.

Backx, P.H. 2014. Complexity, confusion and controversy continue complicating the contribution of RyR2 channel phosphorylation to heart function. *The Journal of Physiology* 592(Pt 9), pp. 1911-2.

Baddeley, D., Jayasinghe, I.D., Lam, L., Rossberger, S., Cannell, M.B. and Soeller, C. 2009 Optical single-channel resolution imaging of the ryanodine receptor distribution in rat cardiac myocytes. *Proceedings of the National Academy of Sciences of the United States of America* 106(52), pp. 22275-80.

Baines, D., Mallon, B.S. and Love, S. 1992. Effects of sodium butyrate on the expression of sodium channels by neuronal cell lines derived from the rat CNS. *Brain research. Molecular brain research* 16(3-4), pp. 330-8.

Baker, M.L., Baker, M.R. and Cong, Y. 2012. Computational methods for interpretation of EM maps at subnanometer resolution. *eLS Chichester: John Wiley & Sons, Ltd*.

Baker, M.R., Fan, G. and Serysheva, I.I. 2015. Single-particle cryo-EM of the ryanodine receptor channel in an aqueous environment. *European Journal of Translational Myology* 25(1), pp. 35-48.

Balshaw, D., Gao, L. and Meissner, G. 1999. Luminal loop of the ryanodine receptor: a pore-forming segment? *Proceedings of the National Academy of Sciences of the United States of America* 96(7), pp. 3345-7.

Balshaw, D.M., Xu, L., Yamaguchi, N., Pasek, D.A. and Meissner, G. 2001. Calmodulin binding and inhibition of cardiac muscle calcium release channel (ryanodine receptor). *The Journal of biological chemistry* 276(23), pp. 20144-53.

Bannister, M.L., Thomas, N.L., Sikkel, M.B., Mukherjee, S., Maxwell, C.E., MacLeod, K.T., George, C.H. and Williams, A.J. 2015. The mechanism of flecainide action in CPVT does not involve a direct effect on RyR2. *Circulation Research*, 116(8) pp. 1324-35.

Baylor, S.M. and Hollingworth, S. 2003. Sarcoplasmic reticulum calcium release compared in slow-twitch and fast-twitch fibres of mouse muscle. *The Journal of Physiology* 551(Pt 1), pp. 125-38.

Bean, B.P. 2007. The action potential in mammalian central neurons. *Nature reviews. Neuroscience* 8(6), pp. 451-65.

Belevych, A., Kubalova, Z., Terentyev, D., Hamlin, R.L. and Carnes, C.A. 2007. Enhanced ryanodine receptor-mediated calcium leak determines reduced sarcoplasmic reticulum calcium content in chronic canine heart failure. *Biophysical Journal* 93(11), pp. 4083-92.

Belevych, A.E., Radwanski, P.B., Carnes, C.A. and Gyorke, S. 2013. 'Ryanopathy': causes and manifestations of RyR2 dysfunction in heart failure. *Cardiovascular Research* 98(2), pp. 240-247.

Benkusky, N.A., Weber, C.S., Scherman, J.A., Farrell, E.F., Hacker, T.A., John, M.C., Powers, P.A., *et al.,* 2007. Intact beta-adrenergic response and unmodified progression toward heart failure in mice with genetic ablation of a major protein kinase A phosphorylation site in the cardiac ryanodine receptor. *Circulation Research* 101(8), pp. 819-29.

Bernas, T., Zarebski, M., Cook, R.R., Dobrucki, J.W. and Cook, P.R. 2004. Minimizing photobleaching during confocal microscopy of fluorescent probes bound to chromatin: role of anoxia and photon flux. *Journal of microscopy* 215(Pt 3), pp. 281-96.

Bernèche, S. and Roux, Benoît 2005. A gate in the selectivity filter of potassium channels. *Structure* 13(4), pp. 591-600.

Berridge, M.J., Bootman, M.D. and Roderick, H.L. 2003. Calcium signalling: dynamics, homeostasis and remodelling. *Nature reviews. Molecular cell biology* 4(7), pp. 517-29.

Bers, D.M. 2000. Calcium fluxes involved in control of cardiac myocyte contraction. *Circulation Research* 87(4), pp. 275-81.

Bers, D.M. 2008. Calcium cycling and signaling in cardiac myocytes. *Annual review of physiology* 70, pp. 23-49.

Bers, D.M. 2010. CaMKII inhibition in heart failure makes jump to human. *Circulation Research* 107(9), pp. 1044-6.

Bers, D.M. 2002. Cardiac excitation-contraction coupling. *Nature* 415(6868), pp. 198-205.

Bers, D.M. 2014. Cardiac sarcoplasmic reticulum calcium leak: basis and roles in cardiac dysfunction. *Annual review of physiology* 76, pp. 107-27.

Bers, D.M. 2004. Macromolecular complexes regulating cardiac ryanodine receptor function. *Journal of molecular and cellular cardiology* 37(2), pp. 417-29.

Bers, D.M. 2012. Ryanodine receptor S2808 phosphorylation in heart failure: smoking gun or red herring. *Circulation Research* 110(6), pp. 796-99

Betzenhauser, M.J. and Marks, A.R. 2010. Ryanodine receptor channelopathies. *Pflügers Archiv : European journal of physiology* 460(2), pp. 467-80.

Bhanumathy, C.D., Nakao, S.K. and Joseph, S.K. 2006. Mechanism of proteasomal degradation of inositol trisphosphate receptors in CHO-K1 cells. *The Journal of biological chemistry* 281(6), pp. 3722-30.

Bhat, M.B., Zhao, J., Takeshima, H. and Ma, J. 1997. Functional calcium release channel formed by the carboxyl-terminal portion of ryanodine receptor. *Biophysical Journal* 73(3), pp. 1329-36.

Bhuiyan, Z.A., Hamdan, M.A., Shamsi, E.T., Postma, A.V., Mannens, M.M., Wilde, A.A. and Al-Gazali, L. 2007. A novel early onset lethal form of catecholaminergic polymorphic ventricular tachycardia maps to chromosome 7p14-p22. *Journal of Cardiovascular Electrophysiology* 18(10), pp. 1060-6.

Blayney, L.M. and Lai, F.A. 2009. Ryanodine receptor-mediated arrhythmias and sudden cardiac death. *Pharmacology & Therapeutics* 123(2), pp. 151-177.

Bootman, M., Niggli, E., Berridge, M. and Lipp, P. 1997. Imaging the hierarchical Ca^{2+} signalling system in HeLa cells. *The Journal of Physiology* 499 (Pt 2), pp. 307-14.

Bootman, M.D., Higazi, D.R., Coombes, S. and Roderick, H.L. 2006. Calcium signalling during excitation-contraction coupling in mammalian atrial myocytes. *Journal of cell science* 119(Pt 19), pp. 3915-25.

Brini, M., Manni, S., Pierobon, N., Guang, du, G., Sharma, P., MacLennan, D.H. and Carafoli, E. 2005. Ca^{2+} signaling in HEK-293 and skeletal muscle cells expressing recombinant ryanodine receptors harboring malignant hyperthermia and central core disease mutations. *The Journal of biological chemistry* 280(15), pp. 15380-9.

Bull, R. and Marengo, J.J. 1993. Sarcoplasmic reticulum release channels from frog skeletal muscle display two types of calcium dependence. *FEBS letters* 331(3), pp. 223-7.

Callaway, C., Seryshev, A., Wang, J.P., Slavik, K.J., Needleman, D.H., 3rd, C.C., Wu, Y., *et al.,* 1994. Localization of the high and low affinity [^{3}H]ryanodine binding sites on the skeletal muscle Ca^{2+} release channel. *The Journal of biological chemistry* 269(22), pp. 15876-84.

Campbell, K.P., Franzini-Armstrong, C. and Shamoo, A.E. 1980. Further characterization of light and heavy sarcoplasmic reticulum vesicles. Identification of the 'sarcoplasmic reticulum feet' associated with heavy sarcoplasmic reticulum vesicles. *Biochimica et biophysica acta* 602(1), pp. 97-116.

Campbell, K.P., Knudson, C.M., Imagawa, T., Leung, A.T., Sutko, J.L., Kahl, S.D., Raab, C.R., *et al.,* 1987. Identification and characterization of the high affinity [^{3}H]ryanodine receptor of the junctional sarcoplasmic reticulum Ca^{2+} release channel. *The Journal of biological chemistry* 262(14), pp. 6460-3.

Capes, E.M., Loaiza, R. and Valdivia, H.H. 2011. Ryanodine receptors. *Skeletal Muscle* 1(1), pp. 1-18.

Carrigan, P.E., Ballar, P. and Tuzmen, S. 2011. Site-directed mutagenesis. *Methods in molecular biology (Clifton, N.J.)* 700, pp. 107-24.

Chakrapani, S., Cordero-Morales, J.F. and Perozo, E. 2007. A quantitative description of KcsA gating II: Single-channel currents. *The Journal of General Physiology* 130(5), pp. 479-496.

Chakrapani, S., Cordero-Morales, J.F., Jogini, V., Pan, A.C., Cortes, D.M. and Roux, B. 2010. On the structural basis of modal gating behavior in K^+ channels. *Nature Structural & Molecular Biology* 18(1), pp. 67-74.

Chapman, M.L., Blanke, M.L., Krovetz, H.S. and VanDongen, A.M.J. 2006. Allosteric effects of external K^+ ions mediated by the aspartate of the GYGD signature sequence in the $K_v2.1$ K^+ channel. *Pflügers Archiv : European journal of physiology* 451(6), pp. 776-92.

Chen, W., Wang, R., Chen, B., Zhong, X., Kong, H., Bai, Y., Zhou, Q., *et al.,* 2014. The ryanodine receptor store-sensing gate controls Ca^{2+} waves and Ca^{2+}-triggered arrhythmias. *Nature Medicine* 20(2), pp. 184-192.

Cheng, H., Lederer, M.R., Lederer, W.J. and Cannell, M.B. 1996. Calcium sparks and $[Ca^{2+}]_i$ waves in cardiac myocytes. *The American journal of physiology* 270(1 Pt 1), pp. 148-59.

Cheng, H., Lederer, W.J. and Cannell, M.B. 1993. Calcium sparks: elementary events underlying excitation-contraction coupling in heart muscle. *Science (New York, N.Y.)* 262(5134), pp. 740-4.

Chu, A., Díaz-Muñoz, M., Hawkes, M.J., Brush, K. and Hamilton, S.L. 1990. Ryanodine as a probe for the functional state of the skeletal muscle sarcoplasmic reticulum calcium release channel. *Molecular Pharmacology* 37(5), pp. 735-41.

Chu, A., Fill, M., Stefani, E. and Entman, M.L. 1993. Cytoplasmic Ca^{2+} does not inhibit the cardiac muscle sarcoplasmic reticulum ryanodine receptor Ca^{2+} channel, although Ca^{2+}-induced Ca^{2+} inactivation of Ca^{2+} release is observed in native vesicles. *The Journal of membrane biology* 135(1), pp. 49-59.

Clapham, D.E. 1995. Calcium signaling. *Cell* 80(2), pp. 259-68.

Clarke, O.B., Caputo, A.T., Hill, A.P., Vandenberg, J.I., Smith, B.J. and Gulbis, J.M. 2010. Domain reorientation and rotation of an intracellular assembly regulate conduction in K_{ir} potassium channels. *Cell* 141(6), pp. 1018-29.

Cline, J., Braman, J.C. and Hogrefe, H.H. 1996. PCR fidelity of pfu DNA polymerase and other thermostable DNA polymerases. *Nucleic acids research* 24(18), pp. 3546-51.

Colquhoun, D. and Hawkes, A. 1995. The principles of the stochastic interpretation of ion-channel mechanisms. *In: Sakmann, B. and Neher, E. ed 2.* Springer US, *Single-Channel Recording*, pp 397 - 482.

Colquhoun, D. and Hawkes, A.G. 1981. On the stochastic properties of single ion channels. *Proceedings of the Royal Society of London. Series B, Biological sciences* 211(1183), pp. 205-35.

Colquhoun, D. and Hawkes, A.G. 1977. Relaxation and fluctuations of membrane currents that flow through drug-operated channels. *Proceedings of the Royal Society of London. Series B, Biological sciences* 199(1135), pp. 231-62.

Colquhoun, D. and Sigworth, F.J. 1995. Fitting and statistical analysis of single-channel records. *In: Sakmann, B. and Neher, E. ed 2.* Springer US. *Singe-Channel Recording*, pp 483 - 587.

Copello, J.A, Barg, S., Onoue, H. and Fleischer, S. 1997. Heterogeneity of Ca^{2+} gating of skeletal muscle and cardiac ryanodine receptors. *Biophysical Journal* 73(1), pp. 141-56.

Cordero-Morales, J.F., Jogini, V., Chakrapani, S. and Perozo, E. 2011. A multipoint hydrogen-bond network underlying KcsA C-Type inactivation. *Biophysical Journal* 100, pp. 2387-2393.

Cordero-Morales, J.F., Cuello, L.G., Zhao, Y., Jogini, V., Cortes, D.M. and Roux, B. 2006. Molecular determinants of gating at the potassium-channel selectivity filter. *Nature Structural & Molecular Biology* 13(4), pp. 311-318.

Cordero-Morales, J.F., Jogini, V., Lewis, A., Vásquez, V., Cortes, D.M. and Roux, B. 2007. Molecular driving forces determining potassium channel slow inactivation. *Nature Structural & Molecular Biology* 14(11), pp. 1062-1069.

Coumel, P., Fidelle, J., Lucet, V., Attuel, P. and Bouvrain, Y. 1978. Catecholamine-induced severe ventricular arrhythmias with Adams-Stokes syndrome in children: report of four cases. *British Heart Journal* 40, pp. 28-37.

Cuello, L.G., Jogini, V., Cortes, D.M. and Perozo, E. 2010a. Structural mechanism of C-type inactivation in K^+ channels. *Nature* 466(7303), pp. 203-8.

Cuello, L.G., Jogini, V., Cortes, D.M., Pan, A.C., Gagnon, D.G., Dalmas, O., Cordero-Morales, J.F., Chakrapani, S., Roux, B. and Perozo, E. 2010b. Structural basis for the coupling between activation and inactivation gates in K^+ channels. *Nature* 466(7303), pp. 272-5.

Currie, S., Loughrey, C.M., Craig, M.A. and Smith, G.L. 2004. Calcium/calmodulin-dependent protein kinase II delta associates with the ryanodine receptor complex and regulates channel function in rabbit heart. *Biochemical Journal* 377(Pt 2), pp. 357-366.

Dani, J.A. and Fox, J.A. 1991. Examination of subconductance levels arising from a single ion channel. *Journal of theoretical biology* 153(3), pp. 401-23.

Despa, S. and Bossuyt, J. 2006. Regulation of Ca^{2+} and Na^{+} in normal and failing cardiac myocytes. *Annals of the New York Academy of Sciences* 1080, pp. 165-77.

di Barletta, M.R., Viatchenko-Karpinski, S., Nori, A., Memmi, M., Terentyev, D., Turcato, F., Valle, G., *et al.,* 2006. Clinical phenotype and functional characterization of CASQ2 mutations associated with catecholaminergic polymorphic ventricular tachycardia. *Circulation* 114(10), pp. 1012-1019.

Dirksen, R.T. and Avila, G. 2002. Altered ryanodine receptor function in central core disease: leaky or uncoupled Ca^{2+} release channels? *Trends in Cardiovascular Medicine* 12(5), pp. 189-97.

Dobrev, D. and Wehrens, X.H.T. 2014. Role of RyR2 phosphorylation in heart failure and arrhythmias: Controversies around ryanodine receptor phosphorylation in cardiac disease. *Circulation Research* 114(8), pp. 1311-1319.

Domeier, T.L., Maxwell, J.T. and Blatter, L.A. 2012. Beta-Adrenergic stimulation increases the intra-sarcoplasmic reticulum Ca^{2+} threshold for Ca^{2+} wave generation. *The Journal of Physiology* 590(23), pp. 6093-6108.

Dorn, G. and Molkentin, J.D. 2004. Manipulating cardiac contractility in heart failure: data from mice and men. *Circulation* 109, pp. 150-158.

Doyle, D.A., Cabral, J.M., Pfuetzner, R.A., Kuo, A., Gulbis, J.M., Cohen, S.L., Chait, B.T., *et al.,* 1998. The structure of the potassium channel: molecular basis of K^{+} conduction and selectivity. *Science (New York, N.Y.)* 280(5360), pp. 69-77.

Du, G.G., Guo, X., Khanna, V.K. and MacLennan, D.H. 2001. Functional characterization of mutants in the predicted pore region of the rabbit cardiac muscle Ca^{2+} release channel (ryanodine receptor isoform 2). *The Journal of biological chemistry* 276(34), pp. 31760-71.

Du, G.G, Khanna, V., Guo, X. and MacLennan, D. 2004. Central core disease mutations R4892W, I4897T and G4898E in the ryanodine receptor isoform 1 reduce the Ca^{2+} sensitivity and amplitude of Ca^{2+}-dependent Ca^{2+} release. *Biochemical Journal* 382(Pt 2), pp. 557-64.

Du, G.G., Sandhu, B., Khanna, V.K., Guo, X.H. and MacLennan, D.H. 2002. Topology of the Ca^{2+} release channel of skeletal muscle sarcoplasmic reticulum (RyR1). *Proceedings of the National Academy of Sciences of the United States of America* 99(26), pp. 16725-30.

Efremov, R.G., Leitner, A., Aebersold, R. and Raunser, S. 2014. Architecture and conformational switch mechanism of the ryanodine receptor. *Nature* 517(7532), pp. 39-43.

Eisner, D. 2014. Calcium in the heart: from physiology to disease. *Experimental Physiology* 99(10), pp. 1273-1282.

Endo, M., Tanaka, M. and Ogawa, Y. 1970. Calcium induced release of calcium from the sarcoplasmic reticulum of skinned skeletal muscle fibres. *Nature* 228(5266), pp. 34-6.

Euden, J., Mason, S.A. and Williams, A.J. 2013a. Functional characterization of the cardiac ryanodine receptor pore-forming region. *PloS one* 8(6), p. e66542.

Euden, J., Mason, S.A., Viero, C., Thomas, N.L. and Williams, A.J. 2013b. Investigations of the contribution of a putative glycine hinge to ryanodine receptor channel gating. *The Journal of biological chemistry* 288(23), pp. 16671-9.

Fabiato, A. 1983. Calcium-induced release of calcium from the cardiac sarcoplasmic reticulum. *The American journal of physiology* 245(1), pp. C1-14.

Fairhurst, A.S. 1973. Effect of ryanodine on skeletal muscle reticulum calcium adenosine triphosphatase (CaATPase). *Biochemical pharmacology* 22(22), pp. 2815-27.

Fatt, P. and Ginsborg, B.L. 1958. The ionic requirements for the production of action potentials in crustacean muscle fibres. *The Journal of Physiology* 142(3), pp. 516-43.

Fearnley, C.J., Roderick, H.L. and Bootman, M.D. 2011. Calcium signaling in cardiac myocytes. *Cold Spring Harbor perspectives in biology* 3(11), p. a004242.

Ferguson, W.B., McManus, O.B. and Magleby, K.L. 1993. Opening and closing transitions for BK channels often occur in two steps via sojourns through a brief lifetime subconductance state. *Biophysical Journal* 65(2), pp. 702-14.

Fernández, I.S., Bai, X., Hussain, T., Kelley, A.C., Lorsch, J.R., Ramakrishnan, V. and Scheres, S.H.W. 2013. Molecular architecture of a eukaryotic translational initiation complex. *Science (New York, N.Y.)* 342(6160), p. 1240585.

Fill, M. and Copello, J.A. 2002. Ryanodine receptor calcium release channels. *Physiological Reviews* 82(4), pp. 893-922.

Franzini-Armstrong, C. 1970. Studies of the triad: I. Structure of the junction in frog twitch fibers. *The Journal of cell biology* 47(2), pp. 488-99.

Franzini-Armstrong, C., Protasi, F. and Ramesh, V. 1999. Shape, size, and distribution of Ca^{2+} release units and couplons in skeletal and cardiac muscles. *Biophysical Journal* 77(3), pp. 1528-39.

Fu, Y., Westenbroek, R.E., Scheuer, T. and Catterall, W.A. 2013. Phosphorylation sites required for regulation of cardiac calcium channels in the fight-or-flight response. *Proceedings of the National Academy of Sciences of the United States of America* 110(48), pp. 19621-6.

Gaburjakova, J. and Gaburjakova, M. 2013. Coupled gating modifies the regulation of cardiac ryanodine receptors by luminal Ca^{2+}. *Biochimica et biophysica acta* 1838(3), pp. 867-73.

Galfré, E., Pitt, S.J., Venturi, E., Sitsapesan, M., Zaccai, N.R., Tsaneva-Atanasova, K., O'Neill, S. and Sitsapesan, R. 2012. FKBP12 activates the cardiac ryanodine receptor Ca^{2+}-release channel and is antagonised by FKBP12.6. *PLoS ONE* 7(2), p. e31956.

Gao, L., Balshaw, D., Tripathy, A., Xin, C. and Meissner, G. 2000. Evidence for a role of the lumenal M3-M4 loop in skeletal muscle Ca^{2+} release channel (ryanodine receptor) activity and conductance. *Biophysical Journal* 79(2), pp. 828-40.

George, C.H. 2007. Sarcoplasmic reticulum Ca^{2+} leak in heart failure: mere observation or functional relevance? *Cardiovascular Research* 77(2), pp. 302-314.

George, C.H., Higgs, G.V. and Lai, F.A. 2003. Ryanodine receptor mutations associated with stress-induced ventricular tachycardia mediate increased calcium release in stimulated cardiomyocytes. *Circulation Research* 93(6), pp. 531-540.

George, C.H., Jundi, H., Fry, D.L. and Lai, F.A. 2007. Ryanodine receptors and ventricular arrhythmias: Emerging trends in mutations, mechanisms and therapies. *Journal of Molecular and Cellular Cardiology* 42(1), pp. 34-50.

Gerçeker, A.A., Zaidi, T., Marks, P., Golan, D.E. and Pier, G.B. 2000. Impact of heterogeneity within cultured cells on bacterial invasion: analysis of *Pseudomonas aeruginosa* and *Salmonella enterica* serovar typhi entry into MDCK cells by using a green fluorescent protein-labelled cystic fibrosis transmembrane conductance regulator receptor. *Infection and immunity* 68(2), pp. 861-70.

Giannini, G., Conti, A., Mammarella, S., Scrobogna, M. and Sorrentino, V. 1995. The ryanodine receptor/calcium channel genes are widely and differentially expressed in murine brain and peripheral tissues. *The Journal of cell biology* 128(5), pp. 893-904.

Golob, M., Moss, R.L. and Chesler, N.C. 2014. Cardiac tissue structure, properties, and performance: a materials science perspective. *Annals of biomedical engineering* 42(10), pp. 2003-13.

Grosman, C. and Auerbach, A. 2000. Kinetic, mechanistic, and structural aspects of unliganded gating of acetylcholine receptor channels: a single-channel study of second transmembrane segment 12' mutants. *The Journal of General Physiology* 115(5), pp. 621-35.

Grunwald, R. and Meissner, G 1995. Lumenal sites and C terminus accessibility of the skeletal muscle calcium release channel (ryanodine receptor). *The Journal of biological chemistry* 270(19), pp. 11338-47.

Grynkiewicz, G., Poenie, M. and Tsien, R.Y. 1985. A new generation of Ca^{2+} indicators with greatly improved fluorescence properties. *The Journal of biological chemistry* 260(6), pp. 3440-50.

Guerrero-Hernández, A., Ávila, G. and Rueda, A. 2014. Ryanodine receptors as leak channels. *European journal of pharmacology* 739, pp. 26-38.

Guzadhur, L. 2009. The characterization of the recombinant human cardiac ryanodine receptor. Ph.D. Thesis, Imperial College London.

Györke, I. and Györke, S. 1998. Regulation of the cardiac ryanodine receptor channel by luminal Ca^{2+} involves luminal Ca^{2+} sensing sites. *Biophysical Journal* 75(6), pp. 2801-10.

Györke, S. and Terentyev, D. 2008. Modulation of ryanodine receptor by luminal calcium and accessory proteins in health and cardiac disease. *Cardiovascular Research* 77(2), pp. 245-255.

Hakamata, Y., Nakai, J., Takeshima, H. and Imoto, K. 1992. Primary structure and distribution of a novel ryanodine receptor/calcium release channel from rabbit brain. *FEBS letters* 312(2-3), pp. 229-35.

Hamer, W. and Wu, Y. 1972. Osmotic coefficients and mean activity coefficients of uni-univalent electrolytes in water at 25 ˚C. *Journal of Physical and Chemical Reference Data* 1(4), pp. 1047-1100.

Hamill, S.J., Cota, E., Chothia, C. and Clarke, J. 2000. Conservation of folding and stability within a protein family: the tyrosine corner as an evolutionary cul-de-sac. *Journal of Molecular Biology* 295(3), pp. 641-9.

Hamilton, S. L. and Serysheva, I.I. 2009. Ryanodine receptor structure: Progress and challenges. *Journal of Biological Chemistry* 284(7), pp. 4047-4051.

Haugaa, K.H., Leren, I.S., Berge, K.E., Bathen, J., Loennechen, J.P., Anfinsen, O., Früh, A., *et al.,* 2010. High prevalence of exercise-induced arrhythmias in catecholaminergic polymorphic ventricular tachycardia mutation-positive family members diagnosed by cascade genetic screening. *Europace : European pacing, arrhythmias, and cardiac electrophysiology : journal of the working groups on cardiac pacing, arrhythmias, and cardiac cellular electrophysiology of the European Society of Cardiology* 12(3), pp. 417-23.

Hayashi, M., Denjoy, I., Extramiana, F., Maltret, A., Buisson, N.R., Klug, D., Takatsuki, S., *et al.,* 2009a. Incidence and risk factors of arrhythmic events in catecholaminergic polymorphic ventricular tachycardia. *Circulation* 119(18), pp. 2426-2434.

Hayashi, T., Martone, M.E., Yu, Z., Thor, A., Doi, M., Holst, M.J., Ellisman, M.H., *et al.,* 2009b. Three-dimensional electron microscopy reveals new details of membrane systems for Ca^{2+} signaling in the heart. *Journal of cell science* 122(Pt 7), pp. 1005-13.

Heginbotham, L., Lu, Z., Abramson, T. and MacKinnon, R. 1994. Mutations in the K^+ channel signature sequence. *Biophysical Journal* 66(4), pp. 1061-1067.

Hell, J.W. 2010. Beta-adrenergic regulation of the L-type Ca^{2+} channel $Ca_V1.2$ by PKA rekindles excitement. *Science signaling* 3(141), pp. e33.

Hoch, B., Meyer, R., Hetzer, R., Krause, E.G. and Karczewski, P. 1999. Identification and expression of delta-isoforms of the multifunctional Ca^{2+}/calmodulin-dependent protein kinase in failing and nonfailing human myocardium. *Circulation Research* 84(6), pp. 713-21.

Hodgkin, A.L. and Katz, B. 1949. The effect of sodium ions on the electrical activity of giant axon of the squid. *The Journal of Physiology* 108(1), pp. 37-77.

Holmberg, S.R. and Williams, A.J. 1989. Single channel recordings from human cardiac sarcoplasmic reticulum. *Circulation Research* 65(5), pp. 1445-9.

Hoshi, T., Zagotta, W.N. and Aldrich, R.W. 1991. Two types of inactivation in *Shaker* K^+ channels: effects of alterations in the carboxy-terminal region. *Neuron* 7(4), pp. 547-56.

Hubbard, R.E. and Haider, M.K. 2010. Hydrogen bonds in proteins: Role and strength. *Encyclopedia of Life Sciences*, pp. 1-7.

Hunt, D.J., Jones, P.P., Wang, R., Chen, W., Bolstad, J., Chen, K., Shimoni, Y., *et al.,* 2007. K201 (JTV519) suppresses spontaneous Ca^{2+} release and [^{3}H]ryanodine binding to RyR2 irrespective of FKBP12.6 association. *The Biochemical journal* 404(3), pp. 431-8.

Hymel, L., Inui, M., Fleischer, S. and Schindler, H. 1988. Purified ryanodine receptor of skeletal muscle sarcoplasmic reticulum forms Ca^{2+}-activated oligomeric Ca^{2+} channels in planar bilayers. *Proceedings of the National Academy of Sciences of the United States of America* 85(2), pp. 441-5.

Hyndman, D.L. and Mitsuhashi, M. 2003. PCR primer design. *Methods in molecular biology (Clifton, N.J.)* 226, pp. 81-8.

Imredy, J.P. and MacLennan, D.H. 1998. Characterization of recombinant rabbit cardiac and skeletal muscle Ca^{2+} release channels (ryanodine receptors) with a novel [^{3}H]ryanodine binding assay. *Journal of Biological Chemistry* 273(50), pp. 33259-66.

Ishikawa, Y. and Homcy, C.J. 1997. The adenylyl cyclases as integrators of transmembrane signal transduction. *Circulation Research* 80(3), pp. 297-304.

Jenden, D.J. and Fairhurst, A.S. 1969. The pharmacology of ryanodine. *Pharmacological Reviews* 21(1), pp. 1-25.

Jiang, D., Xiao, B., Yang, D., Wang, R., Choi, P., Zhang, L., Cheng, H., *et al.,* 2004. RyR2 mutations linked to ventricular tachycardia and sudden death reduce the threshold for store-overload-induced Ca^{2+} release (SOICR). *Proceedings of the National Academy of Sciences* 101(35), pp. 13062-7.

Jiang, M.T., Lokuta, A.J., Farrell, E.F., Wolff, M.R., Haworth, R.A. and Valdivia, H.H. 2002a. Abnormal Ca^{2+} release, but normal ryanodine receptors, in canine and human heart failure. *Circulation Research* 91(11), pp. 1015-1022.

Jiang, Y., Lee, A., Chen, J., Cadene, M., Chait, B.T. and MacKinnon, R. 2002b. The open pore conformation of potassium channels. *Nature* 417(6888), pp. 523-6.

Jiang, Y., Lee, A., Chen, J., Ruta, V., Cadene, M., Chait, B.T. and MacKinnon, R. 2003. X-ray structure of a voltage-dependent K^+ channel. *Nature* 423(6935), pp. 33-41.

Jiang, Z. and Sharfstein, S.T. 2008. Sodium butyrate stimulates monoclonal antibody over-expression in CHO cells by improving gene accessibility. *Biotechnology and Bioengineering* 100(1), pp. 189-94.

Johnson, J.N., Tester, D.J., Bass, N.E. and Ackerman, M.J. 2010. Cardiac channel molecular autopsy for sudden unexpected death in epilepsy. *Journal of Child Neurology* 25(7), pp. 916-921.

Jones, J., Reynolds, D.F., Lai, F.A. and Blayney, L.M. 2005. Ryanodine receptor binding to FKBP12 is modulated by channel activation state. *Journal of cell science* 118(Pt 20), pp. 4613-9.

Kamer, K.J. and Mootha V.K. 2015. The molecular era of the mitochondrial calcium uniporter. *Nature Reviews Molecular Cell Biology*. AOP, pp. 1-9

Kirchhefer, U., Schmitz, W., Scholz, H. and Neumann, J. 1999. Activity of cAMP-dependent protein kinase and Ca^{2+}/calmodulin-dependent protein kinase in failing and nonfailing human hearts. *Cardiovascular Research* 42(1), pp. 254-61.

Koh, X., Srinivasan, B., Ching, H.S. and Levchenko, A. 2005. A 3D Monte Carlo analysis of the role of dyadic space geometry in spark generation. *Biophysical Journal* 90(6), pp. 1999-2014.

Kong, H., Jones, P.P., Koop, A., Zhang, L., Duff, H.J. and Chen, S.R.W. 2008. Caffeine induces Ca^{2+} release by reducing the threshold for luminal Ca^{2+} activation of the ryanodine receptor. *The Biochemical journal* 414(3), pp. 441-52.

Kranias, E.G. and Hajjar, R.J. 2012. Modulation of cardiac contractility by the phospholamban/SERCA2a regulatome. *Circulation Research* 110(12), pp. 1646-60.

Krebs, J. and Michalak, M. 2007. *Calcium : A matter of life or death*. Amsterdam: Elsevier.

Kushnir, A., Shan, J., Betzenhauser, M.J., Reiken, S. and Marks, A.R. 2010. Role of CaMKIIdelta phosphorylation of the cardiac ryanodine receptor in the force frequency relationship and heart failure. *Proceedings of the National Academy of Sciences* 107(22), pp. 10274-10279.

Lahat, H., Eldar, M., Levy-Nissenbaum, E., Bahan, T., Friedman, E., Khoury, A., Lorber, A., *et al.,* 2001a. Autosomal recessive catecholamine- or exercise-induced polymorphic ventricular tachycardia: clinical features and assignment of the disease gene to chromosome 1p13-21. *Circulation* 103(23), pp. 2822-7.

Lahat, H., Pras, E., Olender, T., Avidan, N., Ben-Asher, E., Man, O., Levy-Nissenbaum, E., *et al.,* 2001b. A missense mutation in a highly conserved region of CASQ2 is associated with autosomal recessive catecholamine-induced polymorphic ventricular tachycardia in Bedouin families from Israel. *American journal of human genetics* 69(6), pp. 1378-84.

Lai, F.A. and Meissner, G. 1989. The muscle ryanodine receptor and its intrinsic Ca^{2+} channel activity. *Journal of bioenergetics and biomembranes* 21(2), pp. 227-46.

Lai, F.A., Erickson, H.P., Rousseau, E., Liu, Q.Y. and Meissner, G. 1988. Purification and reconstitution of the calcium release channel from skeletal muscle. *Nature* 331(6154), pp. 315-9.

Laitinen, P.J., Brown, K.M., Piippo, K., Swan, H., Devaney, J.M., Brahmbhatt, B., Donarum, E.A., *et al.,* 2001. Mutations of the cardiac ryanodine receptor (RyR2) gene in familial polymorphic ventricular tachycardia. *Circulation* 103(4), pp. 485-90.

Lanner, J.T., Georgiou, D.K., Joshi, A.D. and Hamilton, S.L. 2010. Ryanodine receptors: structure, expression, molecular details, and function in calcium release. *Cold Spring Harbor perspectives in biology* 2(11), p. a003996.

Lau, K. and van Petegem, F. 2014. Crystal structures of wild type and disease mutant forms of the ryanodine receptor SPRY2 domain. *Nature Communications* 5, p. 5397.

Laude, A.J. and Simpson, A.W.M. 2009. Compartmentalized signalling: Ca^{2+} compartments, microdomains and the many facets of Ca^{2+} signalling. *FEBS Journal* 276(7), pp. 1800-1816.

Laver, D.R. 2007. Ca^{2+} stores regulate ryanodine receptor Ca^{2+} release channels via luminal and cytosolic Ca^{2+} sites. *Clinical and experimental pharmacology & physiology* 34(9), pp. 889-96.

Laver, D.R. 2009. Luminal Ca^{2+} activation of cardiac ryanodine receptors by luminal and cytoplasmic domains. *European Biophysics Journal* 39(1), pp. 19-26.

LeMasurier, M., Heginbotham, L. and Miller, C. 2001. KcsA: it's a potassium channel. *The Journal of General Physiology* 118(3), pp. 303-14.

Leenhardt, A., Lucet, V., Denjoy, I., Grau, F., Ngoc, D.D. and Coumel, P. 1995. Catecholaminergic polymorphic ventricular tachycardia in children. A 7-year follow-up of 21 patients. *Circulation* 91(5), pp. 1512-9.

Lehnart, S.E., Wehrens, X.H.T., Reiken, S., Warrier, S., Belevych, A.E., Harvey, R.D., Richter, W., *et al.,* 2005. Phosphodiesterase 4D deficiency in the ryanodine-receptor complex promotes heart failure and arrhythmias. *Cell* 123(1), pp. 25-35.

Leonard, T.R. and Herzog, W. 2010. Regulation of muscle force in the absence of actin-myosin-based cross-bridge interaction. *American journal of physiology. Cell physiology* 299(1), pp. C14-20.

Leri, A., Rota, M., Pasqualini, F.S., Goichberg, P. and Anversa, P. 2015. Origin of cardiomyocytes in the adult heart. *Circulation Research* 116(1), pp. 150-66.

Li, N., Wang, T., Wang, W., Cutler, M.J., Wang, Q., Voigt, N., Rosenbaum, D.S., Dobrev, D. and Wehrens, X.H. 2012. Inhibition of CaMKII phosphorylation of RyR2 prevents induction of atrial fibrillation in FKBP12.6 knockout mice. *Circulation Research* 110(3), pp. 465-70.

Li, P., Zhao, M., Li, X. and Zhang, L. 2002a. Role of the proposed pore-forming segment of the Ca^{2+} release channel (ryanodine receptor) in ryanodine interaction. *Biophysical Journal* 82(5), pp. 2436-47.

Li, Y., Kranias, E.G. and Mignery, G.A. 2002b. Protein kinase A phosphorylation of the ryanodine receptor does not affect calcium sparks in mouse ventricular myocytes. *Circulation Research* 90(3), pp. 309-16.

Lindsay, A.R. and Williams, A.J. 1991. Functional characterisation of the ryanodine receptor purified from sheep cardiac muscle sarcoplasmic reticulum. *Biochimica et biophysica acta* 1064(1), pp. 89-102.

Lindsay, A.R., Manning, S.D. and Williams, A.J. 1991. Monovalent cation conductance in the ryanodine receptor-channel of sheep cardiac muscle sarcoplasmic reticulum. *The Journal of Physiology* 439, pp. 463-80.

Lindsay, A.R., Tinker, A. and Williams, A.J. 1994. How does ryanodine modify ion handling in the sheep cardiac sarcoplasmic reticulum Ca^{2+}-release channel? *The Journal of General Physiology* 104(3), pp. 425-47.

Liu, Y, Holmgren, M., Jurman, M.E. and Yellen, G. 1997. Gated access to the pore of a voltage-dependent K^+ channel. *Neuron* 19(1), pp. 175-84.

Liu, Y., Porta, M., Qin, J., Ramos, J., Nani, A. and Shannon, T.R. 2010. Flux regulation of cardiac ryanodine receptor channels. *The Journal of General Physiology* 135(1), pp. 15-27.

Lobo, P.A. and van Petegem, F. 2009. Crystal structures of the N-terminal domains of cardiac and skeletal muscle ryanodine receptors: insights into disease mutations. *Structure (London, England : 1993)* 17(11), pp. 1505-14.

Lobo, V. 1989. *Handbook of electrolyte solutions*. Amsterdam Elsevier.

Long, S.B., Campbell, E.B. and Mackinnon, R. 2005. Crystal structure of a mammalian voltage-dependent Shaker family K^+ channel. *Science (New York, N.Y.)* 309(5736), pp. 897-903.

Long, S.B., Tao, X., Campbell, E.B. and MacKinnon, R. 2007. Atomic structure of a voltage-dependent K^+ channel in a lipid membrane-like environment. *Nature* 450(7168), pp. 376-82.

Lu, T., Ting, A.Y., Mainland, J., Jan, L.Y., Schultz, P.G. and Yang, J. 2001. Probing ion permeation and gating in a K^+ channel with backbone mutations in the selectivity filter. *Nature neuroscience* 4(3), pp. 239-46.

Ludtke, S.J., Serysheva, I.I., Hamilton, S.L. and Chiu, W. 2005. The pore structure of the closed RyR1 channel. *Structure (London, England : 1993)* 13(8), pp. 1203-11.

Luvisetto, S., Fellin, T., Spagnolo, M. and Hivert, B. 2004. Modal gating of human $Ca_V2.1$ (P/Q-type) calcium channels. I. The slow and the fast gating modes and their modulation by β Subunits. *The Journal of General Physiology* 124(5) pp. 445-61.

MacDonnell, S.M., García-Rivas, G., Scherman, J.A., Kubo, H., Chen, X., Valdivia, H. and Houser, S.R. 2008. Adrenergic regulation of cardiac contractility does not involve phosphorylation of the cardiac ryanodine receptor at serine 2808. *Circulation Research* 102(8), pp. e65-72.

MacLennan, D.H. and Chen, S.R.W. 2009. Store overload-induced Ca^{2+} release as a triggering mechanism for CPVT and MH episodes caused by mutations in *RYR* and *CASQ* genes. *The Journal of Physiology* 587(Pt 13), pp. 3113-5.

Marian, A.J., Salek, L. and Lutucuta, S. 2001. Molecular genetics and pathogenesis of hypertrophic cardiomyopathy. *Minerva medica* 92(6), pp. 435-51.

Marks, A.R., Tempst, P., Hwang, K.S., Taubman, M.B., Inui, M., Chadwick, C., Fleischer, S., *et al.,* 1989. Molecular cloning and characterization of the ryanodine receptor/junctional channel complex cDNA from skeletal muscle sarcoplasmic reticulum. *Proceedings of the National Academy of Sciences of the United States of America* 86(22), pp. 8683-7.

Marx, S.O, Gaburjakova, J., Gaburjakova, M., Henrikson, C., Ondrias, K. and Marks, A.R. 2001. Coupled gating between cardiac calcium release channels (ryanodine receptors). *Circulation Research* 88(11), pp. 1151-8.

Marx, S.O, Reiken, S., Hisamatsu, Y., Jayaraman, T., Burkhoff, D., Rosemblit, N. and Marks, A.R. 2000. PKA phosphorylation dissociates FKBP12.6 from the calcium release channel (ryanodine receptor): defective regulation in failing hearts. *Cell* 101(4), pp. 365-76.

Marx, S.O. and Marks, A.R. 2013. Dysfunctional ryanodine receptors in the heart: New insights into complex cardiovascular diseases. *Journal of molecular and cellular cardiology* 58, pp. 225-231.

Marziali, G., Rossi, D., Giannini, G., Charlesworth, A. and Sorrentino, V. 1996. cDNA cloning reveals a tissue specific expression of alternatively spliced transcripts of the ryanodine receptor type 3 (RyR3) calcium release channel. *FEBS letters* 394(1), pp. 76-82.

Mason, S.A., Viero, C., Euden, J., Bannister, M., West, D., Chen, S.R.W. and Williams, A.J. 2012. The contribution of hydrophobic residues in the pore-forming region of the ryanodine receptor channel to block by large tetraalkylammonium cations and Shaker B inactivation peptides. *The Journal of General Physiology* 140(3), pp. 325-339.

McCoy, J.G. and Nimigean, C.M. 2012. Structural correlates of selectivity and inactivation in potassium channels. *Biochimica et biophysica acta* 1818(2), pp. 272-85.

McGarry, S.J. and Williams, A.J. 1994. Activation of the sheep cardiac sarcoplasmic reticulum Ca^{2+}-release channel by analogues of sulmazole. *British Journal of Pharmacology* 111(4), pp. 1212-20.

Mead-Savery, F.C., Wang, R., Tanna-Topan, B., Chen, S.R.W., Welch, W. and Williams, A.J. 2009. Changes in negative charge at the luminal mouth of the pore alter ion handling and gating in the cardiac ryanodine-receptor. *Biophysical Journal* 96(4), p. 1374.

Medeiros-Domingo, A., Bhuiyan, Z.A., Tester, D.J., Hofman, N., Bikker, H., van Tintelen, J.P., Mannens, M.M.A.M., *et al.,* 2009. The RyR2-encoded ryanodine receptor/calcium release channel in patients diagnosed previously with either catecholaminergic polymorphic ventricular tachycardia or genotype negative, exercise-induced long QT syndrome. *Journal of the American College of Cardiology* 54(22), pp. 2065-2074.

Mei, Y., Le Xu, Mowrey, D.D., Giraldez, R.M., Wang, Y., Pasek, D.A., Dokholyan, N.V., *et al.,* 2015. Channel gating dependence on pore lining helix glycine residues in skeletal muscle ryanodine receptor. *The Journal of biological chemistry* 290(28), pp. 17535-45.

Meissner, G. 1994. Ryanodine receptor/Ca^{2+} release channels and their regulation by endogenous effectors. *Annual review of physiology* 56, pp. 485-508.

Meissner, G., Darling, E. and Eveleth, J. 1986. Kinetics of rapid Ca^{2+} release by sarcoplasmic reticulum. Effects of Ca^{2+}, Mg^{2+}, and adenine nucleotides. *Biochemistry* 25(1), pp. 236-44.

Meissner, G. 2002. Regulation of mammalian ryanodine receptors. *Frontiers in bioscience : a journal and virtual library* 7, pp. d2072-80.

Miller, C. 1986. *Ion channel reconstitution*. Springer Science & Business Media.

Miller, C. and Racker, E. 1976. Ca^{2+}-induced fusion of fragmented sarcoplasmic reticulum with artificial planar bilayers. *The Journal of membrane biology* 30(3), pp. 283-300.

Mohamed, U., Gollob, M.H., Gow, R.M. and Krahn, A.D. 2006. Sudden cardiac death despite an implantable cardioverter-defibrillator in a young female with catecholaminergic ventricular tachycardia. *Heart rhythm : the official journal of the Heart Rhythm Society* 3(12), pp. 1486-9.

Mohamed, U., Napolitano, C. and Priori, S.G. 2007. Molecular and electrophysiological bases of catecholaminergic polymorphic ventricular tachycardia. *Journal of cardiovascular electrophysiology* 18(7), pp. 791-7.

Mongan, L.C., Gormally, J., Hubbard, A.R., d'Lacey, C. and Ockleford, C.D. 1999. Confocal microscopy. Theory and applications. *Methods in molecular biology (Clifton, N.J.)* 114, pp. 51-74.

Morrison, K.L. and Weiss, G.A. 2001. Combinatorial alanine-scanning. *Current opinion in chemical biology* 5(3), pp. 302-7.

Mukherjee, S., Thomas, N.L. and Williams, A.J. 2012. A mechanistic description of gating of the human cardiac ryanodine receptor in a regulated minimal environment. *The Journal of General Physiology* 140(2), pp. 139-158.

Mukherjee, S. 2014. *The human cardiac ryanodine receptor gating behaviour: a study of mechanisms.* Ph.D. Thesis, Cardiff University.

Mukherjee, S., Thomas, N.L. and Williams, A.J. 2014. Insights into the gating mechanism of the ryanodine-modified human cardiac Ca^{2+}-release channel (ryanodine receptor 2). *Molecular pharmacology* 86(3), pp. 318-29.

Nakai, J., Dirksen, R.T., Nguyen, H.T., Pessah, I.N., Beam, K.G. and Allen, P.D. 1996. Enhanced dihydropyridine receptor channel activity in the presence of ryanodine receptor. *Nature* 380(6569), pp. 72-5.

Nakai, J., Imagawa, T., Hakamat, Y., Shigekawa, M., Takeshima, H. and Numa, S. 1990. Primary structure and functional expression from cDNA of the cardiac ryanodine receptor/calcium release channel. *FEBS letters* 271(1-2), pp. 169-77.

Napolitano, C. and Priori, S.G. 2007. Diagnosis and treatment of catecholaminergic polymorphic ventricular tachycardia. *Heart Rhythm* 4(5), pp. 675-678.

Napolitano, C., Bloise, R., Memmi, M. and Priori, S.G. 2014. Clinical utility gene card for: Catecholaminergic polymorphic ventricular tachycardia (CPVT). *European journal of human genetics* 22(1), pp. e1-3.

Nayler, W.G., Daile, P., Chipperfield, D. and Gan, K. 1970. Effect of ryanodine on calcium in cardiac muscle. *The American journal of physiology* 219(6), pp. 1620-6.

Needleman, D.H. and Hamilton, S.L. 1997. Factors influencing [^{3}H]ryanodine binding to the skeletal muscle Ca^{2+} release channel. *Analytical biochemistry* 248(1), pp. 173-9.

Nimigean, C.M. and Allen, T.W. 2011. Perspectives on: Ion selectivity: Origins of ion selectivity in potassium channels from the perspective of channel block. *The Journal of General Physiology* 137(5), pp. 405-413.

Nimigean, C.M and Miller, C. 2002. Na^+ block and permeation in a K^+ channel of known structure. *The Journal of General Physiology* 120(3), pp. 323-35.

Nio, A.Q.X., Stöhr, E.J. and Shave, R. 2015. The female human heart at rest and during exercise: A review. *European journal of sport science* 15(4), pp. 286-95.

Noskov, S.Y., Bernèche, S. and Roux, B. 2004. Control of ion selectivity in potassium channels by electrostatic and dynamic properties of carbonyl ligands. *Nature* 431(7010), pp. 830-4.

Nyegaard, M., Overgaard, M.T., Sondergaard, M.T., Vranas, M., Behr, E.R., Hildebrandt, L.L., Lund, J., Hedley, P.L., Camm, A.J., Wettrell, G., Fosdal, I., Christiansen, M. and Borglum, A.D. 2012. Mutations in calmodulin cause ventricular tachycardia and sudden cardiac death. *American Journal of Human Genetics* 91(4), pp. 703-12.

Ogawa, Y. 1994. Role of ryanodine receptors. *Critical reviews in biochemistry and molecular biology* 29(4), pp. 229-74.

Ogawa, Y., Kurebayashi, N. and Murayama, T. 1999. Ryanodine receptor isoforms in excitation-contraction coupling. *Advances in biophysics* 36, pp. 27-64.

Ondrias, K. and Mojzisová, A. 2002. Coupled gating between individual cardiac ryanodine calcium release channels. *General physiology and biophysics* 21(1), pp. 73-84.

Ono, K., Yano, M., Ohkusa, T., Kohno, M., Hisaoka, T., Tanigawa, T., Kobayashi, S., *et al.,* 2000. Altered interaction of FKBP12.6 with ryanodine receptor as a cause of abnormal Ca^{2+} release in heart failure. *Cardiovascular Research* 48(2), pp. 323-31.

Ostmeyer, J., Chakrapani, S., Pan, A.C. and Roux, B. 2013. Recovery from slow inactivation in K^{+} channels is controlled by water molecules. *Nature* 501(7465), pp. 121-124.

Otsu, K., Fujii, J., Periasamy, M., Difilippantonio, M., Uppender, M., Ward, D.C. and MacLennan, D.H. 1993. Chromosome mapping of five human cardiac and skeletal muscle sarcoplasmic reticulum protein genes. *Genomics* 17(2), pp. 507-9.

Otsu, K., Willard, H.F., Khanna, V.K., Zorzato, F., Green, N.M. and MacLennan, D.H. 1990. Molecular cloning of cDNA encoding the Ca^{2+} release channel (ryanodine receptor) of rabbit cardiac muscle sarcoplasmic reticulum. *The Journal of biological chemistry* 265(23), pp. 13472-83.

Panama, B.K., McLerie, M. and Lopatin, A.N. 2007. Heterogeneity of IK1 in the mouse heart. *American journal of physiology. Heart and circulatory physiology* 293(6), pp. 3558-67.

Paredes, R.M., Etzler, J.C., Watts, L.T., Zheng, W. and Lechleiter, J.D. 2008. Chemical calcium indicators. *Methods (San Diego, Calif.)* 46(3), pp. 143-51.

Pellicena, P. and Schulman, H. 2014. CaMKII inhibitors: from research tools to therapeutic agents. *Frontiers in pharmacology* 5:21.

Periasamy, M. and Kalyanasundaram, A. 2007. SERCA pump isoforms: their role in calcium transport and disease. *Muscle & nerve* 35(4), pp. 430-42.

Perozo, E, Cortes, D.M. and Cuello, L.G. 1999. Structural rearrangements underlying K^+-channel activation gating. *Science (New York, N.Y.)* 285(5424), pp. 73-8.

Perry, M.D., Ng, C.A. and Vandenberg, J.I. 2013. Pore helices play a dynamic role as integrators of domain motion during K_v11.1 channel inactivation gating. *Journal of Biological Chemistry* 288(16), pp. 11482-11491.

Piacentino, V., Weber, C.R., Chen, X., Weisser-Thomas, J., Margulies, K.B. and Houser, S.R. 2003. Cellular basis of abnormal calcium transients of failing human ventricular myocytes. *Circulation Research* 92(6), pp. 651-8.

Pinnell, J., Turner, S. and Howell, S. 2007. Cardiac muscle physiology. *Continuing Education in Anaesthesia, Critical Care & Pain* 7(3), pp. 85-88.

Piskorowski, R.A. and Aldrich, R. W. 2006. Relationship between pore occupancy and gating in BK potassium channels. *The Journal of General Physiology* 127(5), pp. 557-576.

Pizzale, S., Gollob, M.H., Gow, R. and Birnie, D.H. 2008. Sudden death in a young man with catecholaminergic polymorphic ventricular tachycardia and paroxysmal atrial fibrillation. *Journal of Cardiovascular Electrophysiology* 19(12), pp. 1319-21.

Pless, S.A. and Ahern, C.A. 2013. Unnatural amino acids as probes of ligand-receptor interactions and their conformational consequences. *Annual Review of Pharmacology and Toxicology* 53(1), pp. 211-229.

Porta, M., Diaz-Sylvester, P.L., Neumann, J.T., Escobar, A.L. and Fleischer, S. 2012. Coupled gating of skeletal muscle ryanodine receptors is modulated by Ca^{2+}, Mg^{2+}, and ATP. *American journal of physiology. Cell physiology* 303(6), pp. 682-97.

Priori, S.G., Napolitano, C., Tiso, N., Memmi, M., Vignati, G., Bloise, R., Sorrentino, V., *et al.,* 2001. Mutations in the cardiac ryanodine receptor gene (hRyR2) underlie catecholaminergic polymorphic ventricular tachycardia. *Circulation* 103(2), pp. 196-200.

Priori, S.G. and Chen, S.R.W. 2011. Inherited dysfunction of sarcoplasmic reticulum Ca^{2+} handling and arrhythmogenesis. *Circulation Research* 108(7), pp. 871-83.

Priori, S.G. and Napolitano, C. 2005. Cardiac and skeletal muscle disorders caused by mutations in the intracellular Ca^{2+} release channels. *The Journal of clinical investigation* 115(8), pp. 2033-8.

Priori, S.G., Napolitano, C., Memmi, M., Colombi, B., Drago, F., Gasparini, M., DeSimone, L., *et al.,* 2002. Clinical and molecular characterization of patients with catecholaminergic polymorphic ventricular tachycardia. *Circulation* 106(1), pp. 69-74.

Proks, P., Capener, C.E., Jones, P. and Ashcroft, F.M. 2001. Mutations within the P-loop of $K_{ir}6.2$ modulate the intraburst kinetics of the ATP-sensitive potassium channel. *The Journal of General Physiology* 118(4), pp. 341-53.

Qin, F. 2004. Restoration of single-channel currents using the segmental k-means method based on hidden Markov modeling. *Biophysical Journal* 86(3), pp. 1488-501.

Qin, F. and Li, L. 2004. Model-based fitting of single-channel dwell-time distributions. *Biophysical Journal* 87(3), pp. 1657-71.

Qin, F., Auerbach, A. and Sachs, F. 2000. A direct optimization approach to hidden Markov modeling for single channel kinetics. *Biophysical Journal* 79(4), pp. 1915-27.

Radwański, P.B., Belevych, A.E., Brunello, L., Carnes, C.A. and Györke, S. 2013. Store-dependent deactivation: cooling the chain-reaction of myocardial calcium signaling. *Journal of Molecular and Cellular Cardiology* 58, pp. 77-83.

Raghuraman, H., Cordero-Morales, J.F., Jogini, V., Pan, A.C., Kollewe, A. and Roux, B. 2012. Mechanism of Cd^{2+} coordination during slow inactivation in potassium channels. *Structure (London, England : 1993)* 20(8), pp. 1332-42.

Ramachandran, S., Chakraborty, A., Mei, Y., Samsó, M., Dokholyan, N.V. and Meissner, G. 2013. Structural determinants of skeletal muscle ryanodine receptor gating. *The Journal of biological chemistry* 288(9), pp. 6154-65.

Ramachandran, S., Serohijos, A.W.R., Xu, L.L., Meissner, G. and Dokholyan, N.V. 2009. A structural model of the pore-forming region of the skeletal muscle ryanodine receptor (RyR1). *PLoS Computational Biology* 5(4), p. e1000367.

Ranatunga, K.M., Moreno-King, T.M., Tanna, B., Wang, R., Chen, S.R.W., Ruest, L., Welch, W. and Williams A.J. 2005. The Gln4863Ala mutation within a putative, pore-lining trans-membrane helix of the cardiac ryanodine receptor channel alters both the kinetics of ryanoid interaction and the subsequent fractional conductance. *Molecular Pharmacology* 68(3), pp. 840-6.

Reid, D.S., Tynan, M., Braidwood, L. and Fitzgerald, G.R. 1975. Bidirectional tachycardia in a child. A study using His bundle electrography. *British heart journal* 37(3), pp. 339-44.

Respress, J.L., van Oort, R.J., Li, N., Rolim, N., Dixit, S.S., De Almeida, A., Voigt, N., Lawrence, W.S., Skapura, D.G., Skårdal, K., Wisløff, U., Wieland, T., Ai, X., Pogwizd, S.M., Dobrev, D. and Wehrens, X.H. 2012. Role of RyR2 phosphorylation at S2814 during heart failure progression. *Circulation Research* 110(11), pp. 1474-83.

Reuter, H., Han, T., Motter, C., Philipson, K.D. and Goldhaber, J.I. 2004. Mice overexpressing the cardiac sodium-calcium exchanger: defects in excitation-contraction coupling. *The Journal of Physiology* 554(Pt 3), pp. 779-89.

Rijkers, G.T., Justement, L.B., Griffioen, A.W. and Cambier, J.C. 1990. Improved method for measuring intracellular Ca^{2+} with fluo-3. *Cytometry* 11(8), pp. 923-7.

Robinson, R., Carpenter, D., Shaw, M., Halsall, J. and Hopkins, P. 2006. Mutations in RyR1 in malignant hyperthermia and central core disease. *Human mutation* 27(10), pp. 977-89.

Rosales, R.A. and Escobar, A.L. 2004. Calcium regulation of single ryanodine receptor channel gating analyzed using HMM/MCMC statistical methods. *The Journal of General Physiology* 123(5), pp. 533-53.

Rousseau, E., Smith, J.S. and Meissner, G. 1987. Ryanodine modifies conductance and gating behavior of single Ca^{2+} release channel. *The American journal of physiology* 253(3 Pt 1), pp. 364-8.

Roux, B., Bernèche, S., Egwolf, B., Lev, B., Noskov, S.Y., Rowley, C.N. and Yu, H. 2011. Perspectives on: Ion selectivity: Ion selectivity in channels and transporters. *The Journal of General Physiology* 137(5), pp. 415-426.

Roux-Buisson, N., Cacheux, M., Fourest-Lieuvin, A., Fauconnier, J., Brocard, J., Denjoy, I., Durand, P., Guicheney, P., Kyndt, F., Leenhardt, A., Le Marec, H., Lucet, V., Mabo, P., Probst, V., Monnier, N., Ray, P.F., Santoni, E., Tremeaux, P., Lacampagne, A., Faure, J., Lunardi, J. and Marty, I. 2012. Absence of triadin, a protein of the calcium release complex, is responsible for cardiac arrhythmia with sudden death in human. Human Molecular Genetics 21(12), pp. 2759-67.

Saftenku, E., Williams, A.J. and Sitsapesan, R. 2001. Markovian models of low and high activity levels of cardiac ryanodine receptors. *Biophysical Journal* 80(6), pp. 2727-41.

Samsó, M., Feng, W., Pessah, I.N. and Allen, P.D. 2009. Coordinated movement of cytoplasmic and transmembrane domains of RyR1 upon gating. *PLoS biology* 7(4), p. e85.

Samsó, M., Shen, X. and Allen, P.D. 2006. Structural characterization of the RyR1-FKBP12 interaction. *Journal of Molecular Biology* 356(4), pp. 917-27.

Samsó, M., Wagenknecht, T. and Allen, P.D. 2005. Internal structure and visualization of transmembrane domains of the RyR1 calcium release channel by cryo-EM. *Nature Structural & Molecular Biology* 12(6), pp. 539-44.

Sato, D. and Bers, D.M. 2011. How does stochastic ryanodine receptor-mediated Ca leak fail to initiate a Ca spark? *Biophysical Journal* 101(10), pp. 2370-9.

Schiefer, A., Meissner, G. and Isenberg, G. 1995. Ca^{2+} activation and Ca^{2+} inactivation of canine reconstituted cardiac sarcoplasmic reticulum Ca^{2+}-release channels. *The Journal of physiology* 489 (Pt 2)(2), pp. 337-48.

Schmidt, U., Hajjar, R.J., Helm, P.A., Kim, C.S., Doye, A.A. and Gwathmey, J.K. 1998. Contribution of abnormal sarcoplasmic reticulum ATPase activity to systolic and diastolic dysfunction in human heart failure. *Journal of Molecular and Cellular Cardiology* 30(10), pp. 1929-37.

Schmitt, N., Grunnet, M. and Olesen, S. 2014. Cardiac potassium channel subtypes: new roles in repolarization and arrhythmia. *Physiological Reviews* 94(2), pp. 609-53.

Schrempf, H., Schmidt, O., Kümmerlen, R., Hinnah, S., Müller, D., Betzler, M., Steinkamp, T., *et al.,* 1995. A prokaryotic potassium ion channel with two predicted transmembrane segments from *Streptomyces lividans*. *The EMBO Journal* 14(21), pp. 5170-8.

Scoote, M. and Williams, A.J. 2004. Myocardial calcium signalling and arrhythmia pathogenesis. *Biochemical and Biophysical Research Communications* 322(4), pp. 1286-1309.

Seidel, M., Thomas, N.L., Williams, A.J., Lai, F.A. and Zissimopoulos, S. 2014. Dantrolene rescues aberrant N-terminus intersubunit interactions in mutant pro-arrhythmic cardiac ryanodine receptors. *Cardiovascular Research* 105(1), pp. 118-128.

Shan, J., Betzenhauser, M.J., Kushnir, A., Reiken, S., Meli, A.C., Wronska, A., Dura, M., *et al.,* 2010. Role of chronic ryanodine receptor phosphorylation in heart failure and β-adrenergic receptor blockade in mice. *The Journal of clinical investigation* 120(12), pp. 4375-87.

Shannon, T.R, Pogwizd, S.M. and Bers, D.M. 2003. Elevated sarcoplasmic reticulum Ca^{2+} leak in intact ventricular myocytes from rabbits in heart failure. *Circulation Research* 93(7), pp. 592-4.

Shrivastava, I.H., Tieleman, D.P., Biggin, P.C. and Sansom, M.S.P. 2002. K^+ versus Na^+ ions in a K^+ channel selectivity filter: a simulation study. *Biophysical Journal* 83(2), pp. 633-45.

Sigg, D. 2014. Modeling ion channels: past, present, and future. *The Journal of General Physiology* 144(1), pp. 7-26.

Sitsapesan, R. and Williams, A.J. 1990. Mechanisms of caffeine activation of single calcium-release channels of sheep cardiac sarcoplasmic reticulum. *The Journal of physiology* 423, pp. 425-39.

Sitsapesan, R. and Williams, A.J. 1994. Regulation of the gating of the sheep cardiac sarcoplasmic reticulum Ca^{2+}-release channel by luminal Ca^{2+}. *The Journal of membrane biology* 137(3), pp. 215-26.

Sitsapesan, R. and Williams, A.J. 1995. The gating of the sheep skeletal sarcoplasmic reticulum Ca^{2+}-release channel is regulated by luminal Ca^{2+}. *The Journal of membrane biology* 146(2), pp. 133-44.

Smart, O.S., Goodfellow, J.M. and Wallace, B.A. 1993. The pore dimensions of gramicidin A. *Biophysical Journal* 65(6), pp. 2455-60.

Smith, P.K., Krohn, R.I., Hermanson, G.T., Mallia, A.K., Gartner, F.H., Provenzano, M.D., Fujimoto, E.K., *et al.,* 1985. Measurement of protein using bicinchoninic acid. *Analytical biochemistry* 150(1), pp. 76-85.

Smith, P.L., Baukrowitz, T. and Yellen, G. 1996. The inward rectification mechanism of the HERG cardiac potassium channel. *Nature* 379(6568), pp. 833-6.

Spector, P.S., Curran, M.E., Zou, A., Keating, M.T. and Sanguinetti, M.C. 1996. Fast inactivation causes rectification of the IKr channel. *The Journal of General Physiology* 107(5), pp. 611-9.

Stange, M., Le Xu, Balshaw, D., Yamaguchi, N. and Meissner, G. 2003. Characterization of recombinant skeletal muscle (Ser-2843) and cardiac muscle (Ser-2809) ryanodine receptor phosphorylation mutants. *The Journal of biological chemistry* 278(51), pp. 51693-702.

Stewart, R., Zissimopoulos, S. and Lai, F.A. 2003. Oligomerization of the cardiac ryanodine receptor C-terminal tail. *The Biochemical journal* 376(Pt 3), pp. 795-9.

Sumitomo, N., Harada, K., Nagashima, M., Yasuda, T., Nakamura, Y., Aragaki, Y., Saito, A., *et al.,* 2003. Catecholaminergic polymorphic ventricular tachycardia: electrocardiographic characteristics and optimal therapeutic strategies to prevent sudden death. *Heart (British Cardiac Society)* 89(1), pp. 66-70.

Sutko, J.L., Airey, J.A., Welch, W. and Ruest, L. 1997. The pharmacology of ryanodine and related compounds. *Pharmacological Reviews* 49(1), pp. 53-98.

Swaminathan, P.D., Purohit, A., Hund, T.J. and Anderson, M.E. 2012. CaMKII: linking heart failure and arrhythmias. *Circulation Research* 110(12), pp. 1661-77.

Swan, H., Piippo, K., Viitasalo, M., Heikkilä, P., Paavonen, T., Kainulainen, K., Kere, J., *et al.,* 1999. Arrhythmic disorder mapped to chromosome 1q42-q43 causes malignant polymorphic ventricular tachycardia in structurally normal hearts. *Journal of the American College of Cardiology* 34(7), pp. 2035-42.

Swan, J.S., Dibb, K., Negretti, N., O'Neill, S.C. and Sitsapesan, R. 2003. Effects of eicosapentaenoic acid on cardiac SR Ca^{2+}-release and ryanodine receptor function. *Cardiovascular Research* 60(2), pp. 337-46.

Tada, M. and Katz, A.M. 1982. Phosphorylation of the sarcoplasmic reticulum and sarcolemma. *Annual review of physiology* 44, pp. 401-23.

Takeshima, H., Nishimura, S., Matsumoto, T., Ishida, H., Kangawa, K., Minamino, N., Matsuo, H., *et al.,* 1989. Primary structure and expression from complementary DNA of skeletal muscle ryanodine receptor. *Nature* 339(6224), pp. 439-45.

Talukder, G. and Aldrich, R.W. 2000. Complex voltage-dependent behavior of single unliganded calcium-sensitive potassium channels. *Biophysical Journal* 78(2), pp. 761-72.

Tank, A.W. and Wong, D.L. 2015. Peripheral and central effects of circulating catecholamines. *Comprehensive Physiology* 5(1), pp. 1-15.

Tanna, B., Welch, W., Ruest, L., Sutko, J.L. and Williams, A.J. 1998. Interactions of a reversible ryanoid (21-amino-9alpha-hydroxy-ryanodine) with single sheep cardiac ryanodine receptor channels. *The Journal of General Physiology* 112(1), pp. 55-69.

Taylor, C.W. and Tovey, S.C. 2010. IP(3) receptors: toward understanding their activation. *Cold Spring Harbor perspectives in biology* 2(12), p. a004010.

Tencerova, B., Zahradnikova, A., Gaburjakova, J. and Gaburjakova, M. 2012. Luminal Ca^{2+} controls activation of the cardiac ryanodine receptor by ATP. *The Journal of General Physiology* 140(2), pp. 93-108.

Thomas, N.L., George, C.H. and Lai, F.A. 2004. Functional heterogeneity of ryanodine receptor mutations associated with sudden cardiac death. *Cardiovascular Research* 64(1), pp. 52-60.

Thomson, A.S. and Rothberg, B.S. 2010. Voltage-dependent inactivation gating at the selectivity filter of the MthK K^+ channel. *The Journal of General Physiology* 136(5), pp. 569-579.

Thorpe, G.H., Kricka, L.J., Moseley, S.B. and Whitehead, T.P. 1985. Phenols as enhancers of the chemiluminescent horseradish peroxidase-luminol-hydrogen peroxide reaction: application in luminescence-monitored enzyme immunoassays. *Clinical chemistry* 31(8), pp. 1335-41.

Tibbs, G.R., Goulding, E.H. and Siegelbaum, S.A. 1997. Allosteric activation and tuning of ligand efficacy in cyclic-nucleotide-gated channels. *Nature* 386(6625), pp. 612-5.

Tinker, A. and Williams, A.J. 1992. Divalent cation conduction in the ryanodine receptor channel of sheep cardiac muscle sarcoplasmic reticulum. *The Journal of General Physiology* 100(3), pp. 479-93.

Tinker, A. and Williams, A.J. 1995. Measuring the length of the pore of the sheep cardiac sarcoplasmic reticulum calcium-release channel using related trimethylammonium ions as molecular calipers. *Biophysical Journal* 68(1), pp. 111-20.

Tinker, A. and Williams, A.J. 1993a. Probing the structure of the conduction pathway of the sheep cardiac sarcoplasmic reticulum calcium-release channel with permeant and impermeant organic cations. *The Journal of General Physiology* 102(6), pp. 1107-29.

Tinker, A. and Williams, A.J. 1993b. Using large organic cations to probe the nature of ryanodine modification in the sheep cardiac sarcoplasmic reticulum calcium release channel. *Biophysical Journal* 65(4), pp. 1678-83.

Tinker, A., Lindsay, A.R. and Williams, A.J. 1992. A model for ionic conduction in the ryanodine receptor channel of sheep cardiac muscle sarcoplasmic reticulum. *The Journal of General Physiology* 100(3), pp. 495-517.

Tinker, A., Sutko, J.L., Ruest, L., Deslongchamps, P., Welch, W., Airey, J.A., Gerzon, K., *et al.,* 1996. Electrophysiological effects of ryanodine derivatives on the sheep cardiac sarcoplasmic reticulum calcium-release channel. *Biophysical Journal* 70(5), pp. 2110-9.

Trafford, A.W., Díaz, M.E., Negretti, N. and Eisner, D.A. 1997. Enhanced Ca^{2+} current and decreased Ca^{2+} efflux restore sarcoplasmic reticulum Ca^{2+} content after depletion. *Circulation Research* 81(4), pp. 477-84.

Tu, Q., Velez, P., Cortes-Gutierrez, M. and Fill, M. 1994. Surface charge potentiates conduction through the cardiac ryanodine receptor channel. *The Journal of General Physiology* 103(5), pp. 853-67.

Tung, C., Lobo, P.A., Kimlicka, L. and van Petegem, F. 2010. The amino-terminal disease hotspot of ryanodine receptors forms a cytoplasmic vestibule. *Nature* 468(7323), pp. 585-588.

Tunwell, R.E., Wickenden, C., Bertr, B.M., Bertrand, B.M., Shevchenko, V.I., Walsh, M.B., Allen, P.D., *et al.,* 1996. The human cardiac muscle ryanodine receptor-calcium release channel: identification, primary structure and topological analysis. *The Biochemical journal* 318 (Pt 2), pp. 477-87.

Ullah, G., Mak, D.D. and Pearson, J.E. 2012. A data-driven model of a modal gated ion channel: the inositol 1,4,5-trisphosphate receptor in insect Sf9 cells. *The Journal of General Physiology* 140(2), pp. 159-73.

Uysal, S., Vásquez, V., Tereshko, V., Esaki, K., Fellouse, F.A., Sidhu, S.S., Koide, S., *et al.,* 2009. Crystal structure of full-length KcsA in its closed conformation. *Proceedings of the National Academy of Sciences of the United States of America* 106(16), pp. 6644-9.

van Oort, R.J., McCauley, M.D., Dixit, S.S., Pereira, L., Yang, Y., Respress, J.L., Wang, Q., De Almeida, A.C., Skapura, D.G., Anderson, M.E., Bers, D.M. and Wehrens X.H. 2010. Ryanodine receptor phosphorylation by calcium/calmodulin-dependent protein kinase II promotes life-threatening ventricular arrhythmias in mice with heart failure. *Circulation* 122(25), pp. 2669-2679.

van Petegem, F. 2014. Ryanodine receptors: Allosteric ion channel giants. *Journal of Molecular Biology* 427(1), pp. 31-53.

van Petegem, F. 2012. Ryanodine receptors: structure and function. *The Journal of biological chemistry* 287(38), pp. 31624-32.

van Rossum, D.B., Patterson, R.L., Kiselyov, K., Boehning, D., Barrow, R.K., Gill, D.L. and Snyder, S.H. 2004. Agonist-induced Ca^{2+} entry determined by inositol 1,4,5-trisphosphate recognition. *Proceedings of the National Academy of Sciences of the United States of America* 101(8), pp. 2323-7.

van der Cruijsen, E.A.W., Nand, D., Weingarth, M., Prokofyev, A., Hornig, S., Cukkemane, A.A., Bonvin, A.M.J.J., *et al.,* 2013. Importance of lipid-pore loop interface for potassium channel structure and function. *Proceedings of the National Academy of Sciences of the United States of America* 110(32), pp. 13008-13.

van der Werf, C., Kannankeril, P.J., Sacher, F., Krahn, A.D., Viskin, S., Leenhardt, A., Shimizu, W., *et al.,* 2011. Flecainide therapy reduces exercise-induced ventricular arrhythmias in patients with catecholaminergic polymorphic ventricular tachycardia. *Journal of the American College of Cardiology* 57(22), pp. 2244-2254.

Verkerk, A.O., Wilders, R., van Borren, M.M., Peters, R.J., Broekhuis, E., Lam, K., Coronel, R., de Bakker, J.M. and Tan, H.L. 2007. Pacemaker current (I_f) in the human sinoatrial node. *European Heart Journal* 28(20), pp. 2472-8.

Viero, C., Thomas, N.L., Euden, J., Mason, S.A., George, C.H. and Williams, A.J. 2012. Techniques and methodologies to study the ryanodine receptor at the molecular, subcellular and cellular level. *Advances in experimental medicine and biology* 740, pp. 183-215.

Viskin, S. and Belhassen, B. 1998. Polymorphic ventricular tachyarrhythmias in the absence of organic heart disease: classification, differential diagnosis, and implications for therapy. *Progress in cardiovascular diseases* 41(1), pp. 17-34.

Wagenknecht, T. and Samsó, M. 2002. Three-dimensional reconstruction of ryanodine receptors. *Frontiers in Bioscience : a journal and virtual library* 7, pp. 1464-74.

Wang, D.T., Hill, A.P., Mann, S.A., Tan, P.S. and Vandenberg, J.I. 2011. Mapping the sequence of conformational changes underlying selectivity filter gating in the K_v11.1 potassium channel. *Nature Structural & Molecular Biology* 18(1), pp. 35-41.

Wang, J.P., Needleman, D.H. and Hamilton, S.L. 1993. Relationship of low affinity [^{3}H]ryanodine binding sites to high affinity sites on the skeletal muscle Ca^{2+} release channel. *Journal of Biological Chemistry* 268(28), pp. 20974-82.

Wang, R., Zhang, L., Bolstad, J., Diao, N., Brown, C., Ruest, L., Welch, W., Williams, A.J. and Chen, S.R.W. 2003. Residue Gln4863 within a predicted transmembrane sequence of the Ca^{2+} release channel (ryanodine receptor) is critical for ryanodine interaction. *Journal of Biological Chemistry* 278(51), pp. 51557-65.

Wang, R., Bolstad, J., Kong, H., Zhang, L., Brown, C. and Chen, S.R.W. 2004. The predicted TM10 transmembrane sequence of the cardiac Ca^{2+} release channel (ryanodine receptor) is crucial for channel activation and gating. *The Journal of biological chemistry* 279(5), pp. 3635-42.

Wang, S.Q., Song, L.S., Lakatta, E.G. and Cheng, H. 2001. Ca^{2+} signalling between single L-type Ca^{2+} channels and ryanodine receptors in heart cells. *Nature* 410(6828), pp. 592-6.

Webb, R.H. 1996. Confocal optical microscopy. *Reports on Progress in Physics* 59, pp.427-471.

Wehrens, X.H.T., Lehnart, S.E., Reiken, S.R. and Marks, A.R. 2004. Ca^{2+}/calmodulin-dependent protein kinase II phosphorylation regulates the cardiac ryanodine receptor. *Circulation Research* 94(6), pp. 61-70.

Wehrens, X.H.T., Wehrens, E.H.T. and Lehnart, S.E. 2005. Intracellular calcium release and cardiac disease. *Annual review of physiology* 67, pp. 69-98.

Welch, W., Rheault, S., West, D.J. and Williams, A.J. 2004. A model of the putative pore region of the cardiac ryanodine receptor channel. *Biophysical Journal* 87(4), pp. 2335-51.

Williams, A.J. 1994. An introduction to the methods available for ion channel reconstitution. In: Ogden D, editor. *Microelectrode techniques: the plymouth workshop handbook.* Company of Biologists; Cambridge, pp. 79-99.

Williams, A.J., West, D.J. and Sitsapesan, R. 2001. Light at the end of the Ca^{2+}-release channel tunnel: structures and mechanisms involved in ion translocation in ryanodine receptor channels. *Quarterly reviews of biophysics* 34(1), pp. 61-104.

Williams, E.S. and Viswanathan, M.N. 2013. Current and emerging antiarrhythmic drug therapy for ventricular tachycardia. *Cardiology and therapy* 2(1), pp. 27-46.

Witcher, D.R., McPherson, P.S., Kahl, S.D., Lewis, T., Bentley, P., Mullinnix, M.J., Windass, J.D., *et al.,* 1994. Photoaffinity labeling of the ryanodine receptor/Ca^{2+} release channel with an azido derivative of ryanodine. *The Journal of biological chemistry* 269(18), pp. 13076-9.

Xia, Y., Chu, W., Qi, Q. and Xun, L. 2014. New insights into the QuikChangeTM process guide the use of Phusion DNA polymerase for site-directed mutagenesis. *Nucleic acids research*, pp. 1-9

Xiao, B., Zhong, G., Obayashi, M., Yang, D., Chen, K., Walsh, M.P., Shimoni, Y., *et al.,* 2006. Ser-2030, but not Ser-2808, is the major phosphorylation site in cardiac ryanodine receptors responding to protein kinase A activation upon beta-adrenergic stimulation in normal and failing hearts. *The Biochemical journal* 396(1), pp. 7-16.

Xin, M., Olson, E.N. and Bassel-Duby, R. 2013. Mending broken hearts: cardiac development as a basis for adult heart regeneration and repair. *Nature Reviews Molecular Cell Biology* 14(8), pp. 529-41.

Yakubovich, D., Pastushenko, V., Bitler, A., Dessauer, C.W. and Dascal, N. 2000. Slow modal gating of single G protein-activated K^+ channels expressed in Xenopus oocytes. *The Journal of Physiology* 524(Pt3), pp. 737-55.

Yan, Z., Bai, X., Yan, C., Wu, J., Li, Z., Xie, T., Peng, W., Yin, C.C., Li, X., Scheres, S.H.W., Shi, Y. and Yan, N. 2015. Structure of the rabbit ryanodine receptor RyR1 at near-atomic resolution. *Nature* 517(7532), pp. 50-5.

Yano, M., Ono, K., Ohkusa, T., Suetsugu, M., Kohno, M., Hisaoka, T., Kobayashi, S., *et al.,* 2000. Altered stoichiometry of FKBP12.6 versus ryanodine receptor as a cause of abnormal Ca^{2+} leak through ryanodine receptor in heart failure. *Circulation* 102(17), pp. 2131-6.

Yano, M., Kobayashi, S., Kohno, M., Doi, M., Tokuhisa, T., Okuda, S., Suetsugu, M., *et al.,* 2003. FKBP12.6-mediated stabilization of calcium-release channel (ryanodine receptor) as a novel therapeutic strategy against heart failure. *Circulation* 107(3), pp. 477-84.

Yellen, G. 1998. The moving parts of voltage-gated ion channels. *Quarterly Reviews of Biophysics* 31(3), pp. 239-95.

Yellen, G. 2002. The voltage-gated potassium channels and their relatives. *Nature* 419(6902), pp. 35-42.

Yin, C., Blayney, L.M. and Lai, F.A. 2005. Physical coupling between ryanodine receptor-calcium release channels. *Journal of Molecular Biology* 349(3), pp. 538-46.

Ylänen, K., Poutanen, T., Hiippala, A., Swan, H. and Korppi, M. 2010. Catecholaminergic polymorphic ventricular tachycardia. *European journal of pediatrics* 169(5), pp. 535-42.

Zadek, B. and Nimigean, C.M. 2006. Calcium-dependent gating of MthK, a prokaryotic potassium channel. *The Journal of General Physiology* 127(6), pp. 673-685.

Zagotta, W.N., Hoshi, T. and Aldrich, R.W. 1990. Restoration of inactivation in mutants of Shaker potassium channels by a peptide derived from ShB. *Science* 250(4980), pp. 568-71.

Zahradník, I. and Zahradníková, A. 2005. Calcium activation of ryanodine receptor channels-reconciling RyR gating models with tetrameric channel structure. *The Journal of General Physiology* 126(5), pp. 515-27.

Zalewska, M., Siara, M. and Sajewicz, W. 2014. G protein-coupled receptors: abnormalities in signal transmission, disease states and pharmacotherapy. *Acta poloniae pharmaceutica* 71(2), pp. 229-43.

Zalk, R., Clarke, O.B., Georges, A.D., Grassucci, R.A., Reiken, S., Mancia, F., Hendrickson, W.A., Frank, J. and Marks A.R. 2014. Structure of a mammalian ryanodine receptor. *Nature* 517(7532), pp. 44-9.

Zhao, M., Li, P., Li, X., Zhang, L., Winkfein, R.J. and Chen, S.R.W. 1999. Molecular identification of the ryanodine receptor pore-forming segment. *The Journal of biological chemistry* 274(37), pp. 25971-4.

Zhao, Y., Inayat, S., Dikin, D.A., Singer, J.H., Ruoff, R.S. and Troy, J.B. 2009. Patch clamp technique: review of the current state of the art and potential contributions from nanoengineering. *Journal of Nanoengineering and Nanosystems* 222(149), pp. 1-11.

Zhou, Y., Morais-Cabral, J.H., Kaufman, A. and MacKinnon, R. 2001. Chemistry of ion coordination and hydration revealed by a K^+ channel-Fab complex at 2.0 A resolution. *Nature* 414(6859), pp. 43-8.

Zimányi, I., Buck, E., Abramson, J.J., Mack, M.M. and Pessah, I.N. 1992. Ryanodine induces persistent inactivation of the Ca^{2+} release channel from skeletal muscle sarcoplasmic reticulum. *Molecular Pharmacology* 42(6), pp. 1049-57.

Zissimopoulos, S., Seifan, S., Maxwell, C., Williams, A.J. and Lai, F.A. 2012. Disparate ryanodine receptor association with the FK506-binding proteins in mammalian heart. *Journal of Cell Science*, pp. 1-38.

Zorzato, F., Fujii, J., Otsu, K., Phillips, M., Green, N.M., Lai, F.A., Meissner, G. and MacLennan, D.H. 1990. Molecular cloning of cDNA encoding human and rabbit forms of the Ca^{2+} release channel (ryanodine receptor) of skeletal muscle sarcoplasmic reticulum. *The Journal of biological chemistry* 265(4), pp. 2244-56.